DOCTOR OF PHILOSOPHY

# The nature of remotely-sensed surface turbidity in U.K. and Atlantic French Waters

Griffiths, Joshua

*Award date:*
2016

*Awarding institution:*
Bangor University

# THE NATURE OF REMOTELY-SENSED SURFACE TURBIDITY IN U.K. AND ATLANTIC FRENCH WATERS


Joshua William Griffiths

*Bangor University, Ifremer, DSTL & DGA*

A thesis in partial fulfilment of the requirements of Bangor University for the degree of Doctor of Philosophy

December 2016

# 1 Thesis rationale

The concentration of sediments suspended within the surface of the water column may be estimated using remotely-sensed reflectance from satellites (Froidefrond et al., 2002; Gohin et al., 2002; Gohin et al., 2005). Suspended sediments inhibit light visibility through the water column, referred to as turbidity or water clarity. Highly turbid waters are often perceived to be cloudy with little light passing through them. Using the Hydrolight model, Mobley estimated that all but 0.1% of visible light would be attenuated by 10m of depth in coastal waters (Mobley et al., 1993; Mobley, 1994; Mobley et al., 2015). Satellite observations of the suspended sediment concentration have been taken for almost half a century, allowing a detailed perspective to be made upon their spatial and temporal variability in surface waters (Simpson & Brown, 1987; Binding et al., 2005; Bowers et al., 2007). Taking advantage of such sets of archived satellite observations, statistical models of suspended sediment concentration (Rivier et al., 2012; Gohin et al., 2015; Saulquin et al., 2015) have been utilised to form prediction tools in regions where satellite coverage is poor. Presently, these models have been developed in small geographic regions, such as the English Channel (Rivier et al., 2012; Gohin et al., 2015) and the Bay of Biscay (Saulquin et al., 2015).

Remote-sensing algorithms for suspended sediment concentration depend upon the relationship between the observed mass of suspended sediments and the resulting backscattering and absorption of light. Mass-specific backscattering, $b^*_{bp}$, is used to describe variation in backscattering with concentration of suspended sediments (Bowers & Mitchelson-Jacob, 1996; Babin et al., 2003). Present algorithms assume that mass-specific backscattering is constant, an assumption that backscattering increases linearly with suspended sediment concentration (Gohin et al., 2005). However, field observations of the backscattering of light found that the efficiency of a particle to scatter light is largely controlled by particle composition and cross-sectional area (Neukermans et al., 2012; Bowers et al., 2014). Mineral particles were shown to have a higher refractive index than more organic particles, therefore they backscatter light more effectively (Bowers et al., 2014). Flocculation of particles, which is related to both their composition and cross-sectional area, is effected by the level of turbulence within the water

column. Smaller particles are assumed to be more resistant to turbulent activity than larger organic-rich flocculated particle assemblages. In highly turbulent waters, the size distribution of particles favours these smaller particles with a higher mineral content. Thus, the suggestion is that mass-specific backscattering would be higher in turbulent waters with small mineral particles and lower in less turbulent water with larger organic flocculated particles.

Knowledge of the composition of particles is also important for prediction of suspended sediment concentration. Larger, flocculated particles were found to sink faster than smaller, singular particles (Dyer & Manning, 1999). Present measurements of the settling speed of particles are limited to those gathered using in-situ observation platforms or in the time-consuming use of settling velocity tubes, meaning that measurements are limited in both spatial and temporal resolution (Malarkey et al., 2013). However, settling velocity is not only important for sediment transport modelling, but also in the study of pollutant dispersion and in providing estimations of the sequestration of carbon in the water column (Bauer et al., 2013). Bowers (2003) predicted that spring-neap variability in the concentration of suspended sediments varies with settling speed but was unable to pursue this further due to the lack of sufficient observations.

## 1.1 Aims and objectives

This study aims to address the following questions:

1. How can observations of the influence of particle composition upon backscattering be integrated into future remote-sensing algorithms of suspended sediment concentration? (Chapter III)
    - Carry out field observations of suspended particle properties and the optical properties of the water column.
    - Analyse the influence of particle properties upon the particulate backscattering efficiency ($Q_{b_{b_p}}$) and mass-specific backscattering coefficient ($b^*_{b_p}$).

- Study the potential for improved representation of mass-specific backscattering in future remote-sensing algorithms for the suspended sediment concentration.

2. Can the remote-sensing archive be used to describe and predict the concentration of surface suspended sediment? (Chapter IV)

   - Analyse the temporal and spatial variability in the remotely-sensed suspended sediment concentration archive from MODIS Aqua between 2002 and 2015.

   - Expand the statistical modelling method used by Rivier et al. (2012) in the English Channel to the whole northwest European shelf.

3. How well can a simple turbulent energy based numerical model of suspended sediment concentration perform in comparison to the satellite archive of remotely-sensed surface suspended sediments? (Chapter V)

   - Produce a two-layer numerical resuspension model of the suspended sediment concentration using varied representation of the particle settling speed.

   - Compare the output from the numerical model to the MODIS Aqua archive of remotely-sensed suspended sediment.

   - Compare outputs of the model using static and seasonally-varying settling speed.

4. Can the settling speed of marine particles be quantified using remotely-sensed surface suspended sediment concentration from MODIS-Aqua? (Chapter VI)

   - From the remote-sensing archive, quantify the seasonal variability in spring-neap variation in the concentration of suspended sediments as proposed by Bowers (2003).

   - Explore whether this seasonal modulation may be used to estimate the settling speed over the shelf using remote-sensing observations of the suspended sediment concentration.

   - Compare these estimates of the settling speed to those of laboratory and field observations of particle settling.

## 1.2 Abstract

Mineral suspended solids are a strong source of backscattered light within coastal shelf seas. Backscattered light has a direct relationship to remotely-sensed reflectance, measured by satellites. For four decades, remote-sensing algorithms have been used to estimate the concentration of suspended particulate matter (SPM).

Present algorithms for SPM assume that the mass-specific backscattering coefficient ($b^*_{b_p}(667nm) = b_{b_p}(667nm)/SPM$) is constant. Chapter III aimed to explore how observations of the influence of particle compositon upon backscattering could be incorporated into remote-sensing algorithms to improve our representation of $b^*_{b_p}(667nm)$. Field observations showed that $b_{b_p} * (667nm)$ varies with the size, cross-sectional surface area and mineral content of particles, in addition to the total concentration of suspended solids. Observations showed that the increase in concentration related to an increase in the mineral content of the particles, presumed to be causing the relationship between concentration and $b^*_{b_p}(667nm)$. $b^*_{b_p}$ was shown to vary by a factor of 4, therefore using the latter relationship, iterative estimation of $b^*_{b_p}(667nm)$ suggested that it could be possible to reduce the assumption made in future algorithms for the remotely-sensed SPM, by a similar factor.

Using the ocean colour satellite archive of remotely-sensed SPM concentration from MODIS (Moderate Resolution Imaging Spectroradiometer) on the Aqua satellite, it is possible to produce statistical models based upon dominant forcings of tides, wind-driven waves and chlorophyll-a. Chlorophyll-a is used as an estimation of phytoplankton biomass, with increases in concentration expected to relate to increased particle size and thus increases in the particle settling speed ($w_s$) of suspended sediments. These have the potential to predict the concentration when atmospheric correction fails. Atmospheric correction failure is most commonly due to the presence of cloud (in addition to cloud shadowing, land, high concentrations of coccoliths or coastal adjacency), which lead to a lack of data in a given pixel (Ardanuy et al., 1991). Rivier et al. (2012) used average observed values of SPM concentration, a tidal coefficient, the significant wave height and chlorophyll-a concentration to predict the SPM concentration in the English Channel. Chapter IV aimed to improve upon Rivier et

al. (2012), looking at a wider subject area and improving representation of tides and $w_s$. Tidal inclusion was improved through the use of localised model predictions of tide for every pixel in comparison to a standardised single-location tidal coefficient based upon the tidal amplitude in Brest for the entire English Channel . This study expanded the region to the entire European shelf, included data from a global tidal model and used higher frequency wind speed observations to improve upon the results of Rivier et al. (2012). Furthermore, a crucial shortcoming of Rivier et al. (2012) is the use of single yearlong regression coefficients. The coefficients in this study were allowed to vary seasonally with a sinusoidal form, where the influence of forcings upon the subsequent concentrations varies seasonally. A sinusoidal coefficient was used upon the forcings to represent the effect of flocculation and the influence upon $w_s$. These improvements demonstrate a substantial improvement upon the framework of the present statistical model for suspended particulate matter concentration developed by Rivier et al. (2012).

Chapter V aimed to test the influence of $w_s$ upon SPM concentration and how well a simple model could be used to represent remotely-sensed observations of SPM. To examine the influence of $w_s$ upon the SPM concentration, a simple numerical turbulent kinetic energy (TKE) based resuspension model was used to predict the surface concentration on the northwest European shelf (Elliot & Clarke, 1991; Bowers, 2003). Using a seasonally-imposed $w_s$, the model was shown to perform well when compared to satellite observations. The model identified the importance of $w_s$ on the influence of the hydrodynamic forcings of the wind and tides.

Bowers (2003) predicted that spring-neap variation in SPM would vary seasonally due to changes in $w_s$. Chapter VI aimed to test this assumption using the remote-sensing archive and examine whether it was possible to quantify $w_s$ using the spring-neap variability. Spring-neap variation in the remotely-sensed SPM concentration was shown to be modulated seasonally. In the winter, the range of concentration observed was greater than in the summer. Following results from the numerical model, this variability was proposed to be due to seasonal changes in $w_s$. Quantifying this variation, the bulk $w_s$ was estimated through remote-sensing using a novel method. Remotely-sensed observations of the range of concentrations observed over the

spring-neap tidal cycle were related to the seasonal variability in $w_s$. Estimates of bulk $w_s$ were comparable in magnitude to field observations. $w_s$ was shown to peak in the summer, with some locations experiencing additional peaks in the spring and autumn, corresponding with localised blooms. This was proposed to be due to increased phytoplankton productivity, which leads to increases in EPS (extracellular polymeric substances), promoting flocculation and therefore increasing the speed of particle settling.

# Contents

**1 Thesis rationale** **5**

1.1 Aims and objectives . . . . . 6

1.2 Abstract . . . . . 8

**Contents** **11**

**List of Figures** **16**

**List of Tables** **28**

**I Literature Review** **40**

**2 Suspended Particulate Matter (SPM)** **40**

2.1 Measurements of suspended particulate matter . . . . . 45

2.2 Threshold of movement . . . . . 46

2.3 Forms of suspended sediment transport . . . . . 49

**3 Flocculation** **50**

3.1 Stokes Law . . . . . 52

3.2 Sediment Pollution . . . . . 53

3.3 Turbulence and flocculation . . . . . 53

**4 Particle settling** **54**

4.1 In-situ measurements of settling velocity . . . . . 55

4.2 Factors controlling particle settling . . . . . 56

**5 Turbulent activity** **58**

5.1 Tides . . . . . 58

5.2 Wind . . . . . 61

**6 Remote sensing of suspended sediments** **62**

6.1 Remote sensing . . . . . 62
6.2 Ocean colour . . . . . 62
6.3 MODIS . . . . . 66
6.4 Marine light . . . . . 70
6.5 The optical properties of water . . . . . 70
6.6 Backscattering, $b_b$ . . . . . 72
6.7 Mie Theory . . . . . 79
6.8 Ocean radiative transfer modelling . . . . . 79

**7 Statistical modelling of suspended sediment concentration 80**

**II Backscattering of light by marine particles 89**

**8 Introduction 89**

**9 Methods 90**

9.1 Fieldwork locations . . . . . 90
9.2 Sampling and processing . . . . . 97

**10 Results 104**

10.1 Backscattering of suspended solids . . . . . 104
10.2 Backscattering efficiency, $Q_{b_{b_p}} = b_{b_p}/CSA$ . . . . . 105
10.3 Mass-specific backscattering coefficient, $b_{b_p}*$ . . . . . 106
10.4 Median grain size, $D_{50}$ . . . . . 108

**11 Discussion 110**

11.1 Backscattering coefficient, $b_{b_p}$ . . . . . 110
11.2 Backscattering efficiency, $Q_{bb}$ . . . . . 110
11.3 Mass-specific backscattering coefficient, $b^*_{b_p}$ . . . . . 110
11.4 Mass-median particle size, $D_{50}$ . . . . . 111
11.5 Future developments . . . . . 112

11.6 Implications . . . . . 113
11.7 Remote-sensing algorithm iteration of $b^*_{b_p}$ . . . . . 113

**III Statistical analysis of remotely-sensed variability in suspended material concentration 117**

**12 Introduction 117**

**13 Methods 118**

13.1 OC5 Algorithm . . . . . 118
13.2 Usable remote-sensing observations . . . . . 125
13.3 Processing of remote-sensing observations . . . . . 128

**14 Results 135**

14.1 Suspended particulate matter in north-west Europe . . . . . 135
14.2 Spring-neap tidal variability in SPM . . . . . 138
14.3 Storm-events . . . . . 140
14.4 Chlorophyll-a in north-west Europe . . . . . 141
14.5 Model 1, Tides . . . . . 144
14.6 Model 2, Tides & Wind . . . . . 152
14.7 Model 3, Tides, Wind & Chlorophyll . . . . . 159

**15 Discussion 166**

15.1 Model 1, Tides . . . . . 166
15.2 Model 2, Tides and Wind . . . . . 166
15.3 Model 3, Tides, Wind and Chlorophyll . . . . . 167
15.4 Limitations . . . . . 167
15.5 Implications . . . . . 168

**IV Numerical model of suspended sediment concentration 173**

**16 Introduction 173**

**17 Methods 174**

17.1 Resuspension model . . . . . 174

17.2 Heating and stirring model . . . . . 178

17.3 Model inputs and run time . . . . . 184

17.4 Stratification . . . . . 185

17.5 How well does the model represent thermal stratification? . . . . . 187

17.6 Two layer resuspension model . . . . . 191

17.7 Model prediction, summer . . . . . 199

17.8 Model prediction, winter . . . . . 201

**18 Discussion 204**

**V Remote sensing of particle settling speed 208**

**19 Introduction 208**

**20 Methods 209**

**21 Results 213**

**22 Discussion 217**

22.1 Estimations of settling speed . . . . . 217

22.2 Limitations . . . . . 219

22.3 Semi-diurnal and spring-neap variability . . . . . 221

22.4 Do Chlorophyll-a or sea surface temperature (SST) relate directly to particle settling speed? . . . . . 224

22.5 Implications . . . . . 226

**VI Conclusions** **228**

**VII References** **232**

# List of Figures


1 The English Channel (La Manche) between England and France, taken during the Bay of Seine field campaign (January 2015). . . . . 39

2 Single particles, flocs and phytoplankton. Image represents a width of approximately $400\mu m$ by $300\mu m$, with the diatom on the left hand side of the image being approximately $100\mu m$ in diameter (Bowers, 2013). . . . . 41

3 The volume of particles measured at sizes between 0 and $500\mu m$ (Braithwaite et al., 2012; Graham et al., 2012; Bowers, 2013). . . . . 43

4 The cross-sectional area of particles measured at sizes between 0 and $500\mu m$ (Braithwaite et al., 2012; Graham et al., 2012; Bowers, 2013). . . . . 44

5 The common logarithm ($log_{10}$) of the number of particles per cubic metre measured at sizes between 0 and $500\mu m$ (Braithwaite et al., 2012; Graham et al., 2012; Bowers, 2013). . . . . 45

6 Particles flocculating in the presence of organic material (Kranck & Milligan, 1988). . . . . 55

7 Passover time of the MODIS-Aqua satellite over the north-west European shelf, note that times are in decimal hours UTC (Universal Time, Coordinated). . . 67

8 MODIS false colour swath image taken from EOSDIS WorldView for the 15th July 2014 (NASA EOSDIS, 2016). . . . . 68

9 Diagram representing the processes of absorption and scattering of light by a particle in the water column (Boss et al., 2004b). . . . . 70

10 The influence of the organic fraction of particles upon the mass-specific backscattering coefficient at 650nm (Neukermans et al., 2012). POC and PIC refer to the particle organic and inorganic contents of the suspended particles. The values of the x-axis can be considered to be the inverse of the mineral content used by Bowers et al. (2014), with high values representing highly organic particles and lower values representing highly mineral particles. Grey points are defined as case 1 and black points are defined as case 2. . . . . 77

11 The influence of the mineral content of particles (MSS/TSS) upon the backscattering efficiency ($Q_{b_{b_p}}$) at 665nm (Bowers et al., 2014). Curve displayed is $Q_{b_{b_p}} = 0.000087exp(6.9MSS/TSS)$. A represents the cross-sectional area (CSA). 78
12 $R^2$ coefficient of determination for Model 1, implemented by Rivier et al. (2012). Location 1 and 2 refer to time series a and b in figure 13. . . . . 81
13 Time series of predicted and observed SPM concentration for model 1 from Rivier et al., 2012. Locations a and b refer to locations 1 and 2 in figure 12. . 82
14 $R^2$ coefficient of determination for Model 2, implemented by Rivier et al. (2012). Location 1 and 2 refer to time series a and b in figure 15 respectively. 83
15 Time series of predicted and observed SPM concentration for model 2 from Rivier et al., 2012. Locations a and b refer to locations 1 and 2 in figure 14 respectively. . . . . 84
16 $R^2$ coefficient of determination for Model 3, implemented by Rivier et al. (2012). Location 1 and 2 refer to time series a and b in figure 17 respectively. 85
17 Time series of predicted and observed SPM concentration for model 3 from Rivier et al., 2012. Locations a and b refer to locations 1 and 2 in figure 16 respectively. . . . . 86
18 The explained variance of the four models described by Saulquin et al. (2015). HMM - the homogeneous non-autoregressive Markov model. HMM-AR - the homogeneous autoregressive Markov model. NHHMM - the non-homogeneous non-autoregressive Markov model. NHHMM-AR - the non-homogeneous autoregressive Markov model. dt represents the considered number of days prior to the prediction date which were used in the prediction. . . . . 87
19 Fieldwork locations on a map of the bathymetry of north-west Europe. . . . . 90
20 Map of the region surrounding the Menai Strait fieldwork location. . . . . 92
21 Map of the region surrounding the Bay of Biscay fieldwork location. . . . . 94
22 Map of the region surrounding the Seine Estuary fieldwork location. . . . . 96
23 A fractal floc made up of multiple aggregated particles, alongside the spherical assumption made by the LISST (Verney et al., 2011). . . . . 98

24 Schematic of a fixed-angle backscattering sensor, similar to that of the ECO-BB devices. This example represents a source and detector at a single wavelength of light (Boss et al., 2004b). . . . . 100

25 Variability in the backscattering coefficient at 650nm, with TSS, the concentration of total suspended solids, as observed at the field observation sites in the Menai Strait, the Gironde Estuary and the Seine Estuary over all campaigns. The correlation provided an $R^2$, coefficient of determination of 0.80. Following a t-Test, the relationship provided a p-value of $< 0.05$ (2.304E-21), inferring a significant relationship between the two variables. The error bars represent the range for observations of backscattering and of concentration of total suspended solids. . . . . 104

26 Variability in the backscattering efficiency, $Q_{b_{b_p}}$=$b_{b_p}$/CSA, with MSS/TSS, mineral content of sampled particulates, as observed at the field observation sites in the Menai Strait, the Gironde Estuary and the Seine Estuary over all campaigns. The correlation provided an $R^2$, coefficient of determination of 0.64. Following a t-Test, the relationship provided a p-value of $< 0.05$ (2.3388E-08), inferring a significant relationship between the two variables. The error bars represent the range of backscattering efficiency and of the mineral content. 105

27 Variability in the mass-specific backscattering coefficient, $b_{b_p}* = b_{b_p}/SPM$, with the concentration of total suspended solids, as observed at the field observation sites in the Menai Strait, the Gironde Estuary and the Seine Estuary over all campaigns. The correlation provided an $R^2$, coefficient of determination of 0.36. Following a t-Test, the relationship provided a p-value of $< 0.05$ (0.00625), inferring a significant relationship between the two variables. The error bars represent the range for observations of mass-specific backscattering and of concentration of total suspended solids. . . . . 106

28 Variability in the mass-specific backscattering coefficient, $b_{b_p}* = b_{b_p}/SPM$, with MSS/TSS, the mineral content of sampled particulates, as observed at the field observation sites in the Menai Strait, the Gironde Estuary and the Seine Estuary over all campaigns. The correlation provided an $R^2$, coefficient of determination of 0.38. Following a t-Test, the relationship provided a p-value of $< 0.05$ (5.1264E-54), inferring a significant relationship between the two variables. The error bars represent the range for observations of mass-specific backscattering and of mineral content. . . . . 107

29 Variability in the mass-specific backscattering coefficient,$b_{b_p}* = b_{b_p}/SPM$, with $D_{50}$, the mass median grain size in $\mu m$ as observed at the field observation sites in the Menai Strait, the Gironde Estuary and the Seine Estuary over all campaigns. The correlation provided an $R^2$, coefficient of determination of 0.43. Following a t-Test, the relationship provided a p-value of $< 0.05$ (1.6928-23), inferring a significant relationship between the two variables. The error bars represent the range for observations of mass-specific backscattering and mass-median particle diameter. . . . . 108

30 Variability in $D_{50}$, the mass median grain size in $\mu m$, with MSS/TSS, the mineral content of sampled particulates, as observed at the field observation sites in the Menai Strait, the Gironde Estuary and the Seine Estuary over all campaigns. The correlation provided an $R^2$, coefficient of determination of 0.59. Following a t-Test, the relationship provided a p-value of $< 0.05$ (2.4428E-23), inferring a significant relationship between the two variables. The error bars represent the range for observations of mass-median particle diameter and of mineral content. . . . . 109

31 Estimate of mass-specific backscattering, $b^*_{b_p}$, using iteration of equation inferred from field observations of the influence of the concentration of suspended material upon the $b^*_{b_p}$. The location is 51.95°N, -6.08°E, in the southern Irish Sea. The observations used come from remotely-sensed suspended particulate matter concentration derived from MODIS Aqua using the algorithm described in Gohin et al. (2005). . . . . 115

32 Cloudy MODIS image taken from EOSDIS WorldView for the 13th February 2013 (NASA EOSDIS, 2016). . . . . 122

33 Percentage of usable data observed in each month of the year taken from MODIS-Aqua images between 2002 and 2015. A low level of usable data can be termed to be a high rate of atmospheric correction failure. . . . . 126

34 Average suspended matter concentration and total percentage of usable data from remotely-sensed MODIS-Aqua images from between June 2002 and June 2015. . . . . 127

35 Suspended particulate matter concentration from MODIS Aqua at a resolution of $1km^2$ in the English Channel on the 30th January 2008. . . . . 128

36 Spatially-averaged suspended particulate matter concentration at a resolution of $10km^2$ from the source data at $1km^2$ from MODIS Aqua in the English Channel on the 30th January 2008. . . . . 129

37 Maximum tidal current speed from the TPXO 8.0 output of the north-west European shelf. . . . . 131

38 Maximum windspeed taken from a year of ECMWF model output of the north-west European shelf. . . . . 132

39 GEBCO bathymetry of the north-west European shelf. The scale is limited to 250m to accentuate shallower waters. Areas of the shelf in this region may exceed 2500m off the continental shelf. . . . . 133

40 Average suspended matter concentration from usable data observed in Winter, Spring, Summer and Autumn from MODIS-Aqua images between 2002 and 2015. . . . . 135

41 Remotely-sensed suspended particulate matter concentration time series from MODIS in 2012 at three locations: the Irish Sea, the English Channel and the North Sea, as shown in figure 46. . . . . 136

42 Remotely-sensed suspended matter concentrations on a neap and successive spring tide from MODIS-Aqua. The neap tide image was taken on the 2nd October 2015, with the spring tide image was taken on the 25th September 2015. 138

43 Amplification of remotely-sensed suspended matter concentrations on the spring tide over that observed on the neap tide by MODIS-Aqua. The neap tide values used were taken on the 2nd October 2015, with spring tide values taken on the 25th September 2015. Values off the land that are white signify points where data was unavailable for one or other of the two datasets. . . . . 139

44 Remotely-sensed suspended matter concentration following a storm event from MODIS-Aqua. The image was taken on the 9th March 2014. . . . . 140

45 Average Chlorophyll-a concentration from usable data observed in Winter, Spring, Summer and Autumn from MODIS-Aqua images between 2002 and 2015. . . . . 141

46 Location of observation points . . . . . 142

47 Remotely-sensed Chlorophyll-a concentration time series from MODIS in 2012 at three locations: the Irish Sea, the English Channel and the North Sea, as shown in figure 46. . . . . 143

48 Prediction of suspended sediment concentration using model 1 (tides) alongside remotely-sensed observations. Three locations are included to illustrate the model, one in the Irish Sea (53.6°$N$, 4°$W$, $R^2$=0.332, RMSE = 1.324$gm^{-3}$), the English Channel (50.0°$N$, 0°$W$, $R^2$=0.285, RMSE = 1.111$gm^{-3}$) and the North Sea (53.6°$N$, 3°$E$, $R^2$=0.306, RMSE = 1.621$gm^{-3}$). Locations plotted in Fig. 46. . . . . 146

49 The $R^2$ coefficient of determination between the model 1 prediction and remotely-sensed observations. . . . . 147

50 The root-mean squared error, RMSE, between the model 1 prediction and remotely-sensed observations. . . . . 148

51 The coefficient $a_1$ representing the amplitude of the sine curve fitted to the annual variation in the tidal current speed in a regression with the remotely-sensed observations. . . . . 149

52 The coefficient $a_2$ representing the phase difference of the sine curve fitted to the annual variation in the tidal current speed in a regression with the remotely-sensed observations. . . . . 150

53 The coefficient $a_3$ representing the additional component of the sine curve fitted to the tidal current speed in the regression with the remotely-sensed observations. 151

54 Prediction of suspended sediment concentration using model 2 (tides and wind) alongside remotely-sensed observations. Three locations are included to illustrate the model, one in the Irish Sea ($53.6°N$, $4°W$, $R^2$=0.373, RMSE = $1.121gm^{-3}$), the English Channel ($50.0°N$, $0°W$, $R^2$=0.327, RMSE = $1.012gm^{-3}$) and the North Sea ($53.6°N$, $3°E$, $R^2$=0.416, RMSE = $1.406gm^{-3}$). Locations plotted in Figure 46. . . . . 154

55 The $R^2$ coefficient of determination between the model 2 prediction and remotely-sensed observations. . . . . 155

56 The root-mean squared error, RMSE, between the model 2 prediction and remotely-sensed observations. . . . . 156

57 The coefficient $b_1$ representing the amplitude of the sine curve fitted to the wind speed in the regression with the remotely-sensed observations. . . . . 157

58 The coefficient $b_2$ representing the phase difference of the sine curve fitted to the wind speed in the regression with the remotely-sensed observations. . . . 158

59 Prediction of suspended sediment concentration using model 3 (tides, wind and Chlorophyll-a) alongside remotely-sensed observations. Three locations are included to illustrate the model, one in the Irish Sea ($53.6°N$, $4°W$, $R^2$=0.558, RMSE = $0.896gm^{-3}$), the English Channel ($50.0°N$, $0°W$, $R^2$=0.617, RMSE = $0.823gm^{-3}$) and the North Sea ($53.6°N$, $3°E$, $R^2$=0.667, RMSE = $0.821gm^{-3}$). Locations plotted in Figure 46. . . . . 161

60 The $R^2$ coefficient of determination between the model 3 prediction and remotely-sensed observations. . . . . 162

61 The root-mean squared error, RMSE, between the model 3 prediction and remotely-sensed observations. . . . . 163

62 The coefficient $c_1$ representing the amplitude of the sine curve fitted to the inverse of the Chlorophyll-a concentration in the regression with the remotely-sensed observations. . . . . 164

63 The coefficient $c_2$ representing the phase difference of the sine curve fitted to the inverse of the Chlorophyll-a concentration in the regression with the remotely-sensed observations. . . . . 165

64 The frequency of satellite data points on 1st April 2012 from MODIS-Aqua, MERIS and VIIRS, courtesy of Ifremer (ftp.ifremer.fr) at $1km^2$ resolution. A value of 3 in this case represents data at one pixel for all satellites, with 0 representing lack of coverage for that pixel on this day. . . . . 170

65 The maximum time difference in hours between first and last observed satellite data points on 1st April 2012 from MODIS-Aqua, MERIS and VIIRS, courtesy of Ifremer (ftp.ifremer.fr) at $1km^2$ resolution. A value of 0 in this case may either represent a lack of observations for that pixel or for the presence of only one data point. . . . . 171

66 Modelled and remotely-sensed observations of suspended sediment concentrations at three locations over the U.K. and Atlantic French region. The model is without thermal stratification and with a constant settling speed of $12mday^{-1}$ ($0.14mms^{-1}$). . . . . 176

67 The coefficient of determination, $R^2$ between the remotely-sensed observations of suspended sediment concentration and the modelled suspended sediment concentration without thermal stratification and with a static settling speed of $12mday^{-1}$ ($0.14mms^{-1}$). . . . . 177

68 The root-mean squared error, RMSE, between the remotely-sensed observations of suspended sediment concentration and the modelled suspended sediment concentration without thermal stratification and with a static settling speed of $12mday^{-1}$ ($0.14mms^{-1}$). . . . . 178

69 Plot showing the temperature modelled at the surface and bottom layers of the water column at three locations in the model region. Regions where the two temperatures differ represent periods of thermal stratification. The top plot features a profile from a location at $54°N$, $-4°E$, in the Irish Sea, near the Isle of Man. The middle plot features a profile from a location at $54°N$, $3°E$, in the North Sea. The bottom plot features a profile from a location at $50.2°N$, $0°E$, in the English Channel between Brighton (England) and Le Havre (France). . 186

70 The peak temperature difference between the surface and bottom layers of the water column as modelled using Elliot and Clarke (1991). . . . . 187

71 Regions expected to be stratified based upon the use of log10 over $h/u^3$, as defined in Simpson and Hunter (1974) and Pingree and Griffiths (1978). . . . 188

72 Point density comparison of $h/u^3$ method (as defined by Simpson and Hunter (1974) and Pingree and Griffiths (1978)) and the peak temperature difference modelled using Elliot and Clarke (1991). The density grid has the dimensions of $0.1°C$ and a value of $h/u^3$ of 1. Values which are shaded white, represent 0 points for that pixel. . . . . 190

73 Diagram describing the components of the resuspension model (Bowers, 2003). 192

74 Modelled and remotely-sensed observations of suspended sediment concentrations at three locations over the U.K. and Atlantic French region. The model is with stratification and with a constant settling speed of $12mday^{-1}$ ($0.14mms^{-1}$).194

75 The coefficient of determination, $R^2$, between the remotely-sensed observations of suspended sediment concentration and the modelled suspended sediment concentration with stratification and with a static settling speed of $12mday^{-1}$ ($0.14mms^{-1}$). . . . . 195

76 The root-mean squared error, RMSE, between the remotely-sensed observations of suspended sediment concentration and the modelled suspended sediment concentration with stratification and with a static settling speed of $12mday^{-1}$ ($0.14mms^{-1}$). . . . . 196

77 The sine curve representing settling speed over the year as used in the numerical model input. The settling speed is shown the vary between $7mday^{-1}$ ($0.08mms^{-1}$) in January and $17mday^{-1}$ ($0.2mms^{-1}$) in July. . . . . 197

78 Modelled and remotely-sensed observations of suspended sediment concentrations at three locations over the U.K. and Atlantic French region. The model is with stratification and with a seasonally-varying settling speed between $7mday^{-1}$ ($0.08mms^{-1}$) in January and $17mday^{-1}$ ($0.2mms^{-1}$) in July. . . . . 198

79 Modelled and remotely-sensed observations of suspended sediment concentrations averaged over the month of July over the U.K. and Atlantic French region. The model is with stratification and with a seasonally-varying settling speed between $7mday^{-1}$ ($0.08mms^{-1}$) in January and $17mday^{-1}$ ($0.2mms^{-1}$) in July. 199

80 Modelled and remotely-sensed observations of suspended sediment concentrations averaged over the month of January over the U.K. and Atlantic French region. The model is with stratification and with a seasonally-varying settling speed between $7mday^{-1}$ ($0.08mms^{-1}$) in January and $17mday^{-1}$ ($0.2mms^{-1}$) in July. . . . . 201

81 The coefficient of determination, $R^2$, between the remotely-sensed observations of suspended sediment concentration and the modelled suspended sediment concentration with stratification and with a seasonally-varying settling speed between $7mday^{-1}$ ($0.08mms^{-1}$) in January and $17mday^{-1}$ ($0.2mms^{-1}$) in July. 202

82 The root-mean squared error, RMSE, between the remotely-sensed observations of suspended sediment concentration and the modelled suspended sediment concentration with stratification and with a seasonally-varying settling speed between $7mday^{-1}$ ($0.08mms^{-1}$) in January and $17mday^{-1}$ ($0.2mms^{-1}$) in July. . . . . 203

83 MODIS remotely-sensed observations of suspended sediment south of the Isle of Man, $53.4 \circ N, -4 \circ E$. The dashed lines are used to represent the monthly minimum and maximum concentrations. This makes it possible to observe seasonal variability in the range of concentrations observed. . . . . 209

84 MODIS remotely-sensed observations of suspended sediment south of the Isle of Man, $53.65°N, -4.89°E$ between 2008 and 2010. The observations are plotted against the maximum daily tidal current speed relative to each observation at the same location, estimated using the output from TPXO 8.0 Atlas as described in the statistical model chapter. The variability from lowest maximum daily tidal current speed to highest maximum daily tidal current speed represents spring-neap variability. Two lines of best fit are plotted through the data points, one to represent points observed in January and another for points observed in July. The equations describing these two lines may be found in the legend. For each line, a t-Test produced p-values less than 0.05, suggesting that the dc/du values are significant (for January, p = 1.6439E-15; for July, p = 0.042965). . . . . 210

85 p-values produced by t-Test for the dc/du relationship in July over the northwest European shelf. Values less than 0.05 represent a significant relationship, with red pixels representing locations with p-values greater than or equal to 0.05, which are therefore deemed to not be significant. . . . . 213

86 Settling speed in January as calculated using equation 20.5. Map covers the region of the northwest European shelf. Settling speed calculated ranges from 0 to 20 $mday^{-1}$ ($0.25mms^{-1}$). . . . . 214

87 Settling speed in July as calculated using equation 20.5. Map covers the region of the northwest European shelf. Settling speed calculated ranges from 0 to 20 $mday^{-1}$ ($0.25mms^{-1}$). . . . . 215

88 Settling speed estimated for each month of the year at three locations: the Irish Sea, the English Channel and the North Sea. The locations of each point correspond to the red dot on the adjacent map. . . . . 216

89 Influence of reduced gravity (g') upon the settling speed ($w_s$) of marine particles.221

90 Proposed settling speed induced by the spring-neap tidal cycle. . . . . 222

91 Approximated settling speed variability over a semi-diurnal tidal cycle (Verney et al., 2011), excluding flood-ebb tidal asymmetry. . . . . 223

92 The estimated settling speed ($w_s$) alongside the sea surface temperature (SST) and Chlorophyll-a concentration at a location in the southern Irish Sea ($51.95°N, -6.08°E$).225

# List of Tables


1 Table of Units, a to f . . . . . 33

2 Table of Units, $f_w$ to $\rho_p$ . . . . . 34

3 Table of Units, $\rho_a$ to W . . . . . 35

4 Recent/present ocean colour satellites (with ocean colour wavebands) . . . . 65

5 Two water cases defined by Morel & Prieur (1977) . . . . . 69

6 Observed values of the mass-specific backscattering ($b_{b_p}*$) at 665nm from recent literature . . . . . 74

7 The three model forms described in Rivier et al. (2012). Suspended particulate matter (SPM) observations are from MODIS Aqua using the remote sensing algorithm defined by Gohin et al. (2005). $SPM_{clim}$ represents the climatology of SPM used as a baseline. $Tide_c$ represents the SHOM (Service Hydrographique et *Océanographique* de la Marine) tidal coefficient. Waves represents the wave speed, estimated using the WaveWatch3 numerical model. Chl represents the remotely-sensed Chlorophyll-a concentration. . . . . 86

8 Wavelengths measured by the WETLabs ECO-BB3 and ECO-BB9 devices (WETLabs, 2013; WETLabs, 2016). . . . . 99

9 Fieldwork summary from all sites. TSS, $gm^{-3}$. $b_{b_p}$, $m^{-1}$. $b_{b_p}*$, $m^2g^{-1}$. CSA, $m^{-1}$. $D_{50}$, $\mu m$. . . . . 103

10 The conversion values, from normalised water-leaving radiance to remote sensing reflectance (Gohin, 2013 - Personal communication) . . . . . 123

11 Statistical model formations used within the statistical modelling chapter. The table details all three models, $SPM_T$ (tide only), $SPM_{TW}$ (tides and wind) and $SPM_{TWC}$ (tides, wind and Chlorophyll-a). The inputs are as detailed above: the tidal current speeds are calculated from TPXO 8.0 Atlas solution; the wind speed from the ECWMF wind model and the suspended sediment and Chlorophyll-a concentrations were remotely-sensed using MODIS Aqua. The grid locations are represented by lon for longitude and lat for latitude. . 134

12 Table of constants for the heating and stirring model (Simpson & Bowers, 1984; Elliott & Clarke, 1991) . . . . . 184

# List of Equations


2.1 Drag force, F (Davis, 2012) . . . . . 46

2.2 Lift force, L (Davis, 2012) . . . . . 46

2.3 Immersed weight, W (Davis, 2012) . . . . . 46

2.4 Shields parameter, (Shields, 1936) . . . . . 47

3.1 Stokes Law (Thorpe, 2005) . . . . . 52

3.2 Reynolds number, Re . . . . . 52

3.3 Particle size limit using Reynolds number, $D_{max}$ . . . . . 53

3.4 Maximum floc diameter limited by the Kolmogorov microscale (Fugate & Friedrichs, 2003; Bowers & Binding, 2006). . . . . 54

4.1 Stokes law for single, spherical particles (Winterwerp, 2002) . . . . . 57

4.2 Stoke's Law for flocculated particles (Winterwerp, 2002) . . . . . 57

5.2 Equations of motion (Dushaw et al., 1997) . . . . . 60

5.3 Continuity equation (Dushaw et al., 1997) . . . . . 60

6.1 Reflectance ratio at a given wavelength, R($\lambda$) (Morel, 1973) . . . . . 68

6.2 Absorption of marine light, a . . . . . 71

6.3 Scattering of marine light, b (Kirk, 2011) . . . . . 72

6.4 Scattering of marine light, b . . . . . 72

6.5 Backscattering, $b_b$ (Kirk, 2011). . . . . 72

6.6 Forward scattering, $b_f$ (Kirk, 2011) . . . . . 72

6.7 Remotely-sensed reflectance, $R_{RS}$ (Gohin et al., 2005). . . . . 73

6.8 Backscattering of marine light ($b_b$) as a function of remotely-sensed reflectance ($R_{RS}$) (Gohin et al., 2005). . . . . 73

6.9 Backscattering ($b_b$) as a function of the volume scattering function ($\beta$) (Kirk, 2011) 73

6.10 Backscattering by suspended particles, $b_{b_p}$ . . . . . 73

11.1 Mass-specific backscattering, $b_{b_p}*$ iteration, step 1 . . . . . 114

11.2 Mass-specific backscattering, $b_{b_p}*$ iteration, step 2 . . . . . 114

13.1 Remotely-sensed reflectance, $R_{RS}$ (Austin, 1974; Preisendorfer, 1976; Gordon et al., 1975; 1988; Lee et al., 1994; Gohin et al., 2005) . . . . . 118
13.2 Backscattering coefficient, $b_b$ (Gohin et al., 2005) . . . . . 118
13.3 Absorption coefficient, a (Gohin et al., 2005) . . . . . 119
13.4 Assumed linear relationship of $R^*(\lambda)$ (Gohin et al., 2005) . . . . . 119
13.5 Algorithm for mineral suspended sediments using remotely-sensed reflectance from MODIS Aqua at 550nm and 650nm (Gohin et al., 2005; Rivier et al., 2012) 120
13.8 Calculating remote sensing reflectance from normalised water leaving radiance (Gohin - personal communication, 2013) . . . . . 123
17.1 Balance of resuspension and settling (Bowers, 2003) . . . . . 174
17.2 Change in suspended sediment concentration (Bowers, 2003) . . . . . 175
17.3 The rate of energy input by tides and wind, P (Bowers, 2003) . . . . . 175
17.4 Incoming short-wave radiation, $Q_S$ (Elliot & Clarke, 1991) . . . . . 180
17.5 Wind function, $f_W$ (Elliot & Clarke, 1991) . . . . . 180
17.6 Heat flux function of surface and dew point temperatures, $T_M$ (Elliot & Clarke, 1991) . . . . . 180
17.7 Thermal exchange coefficient, $\kappa$ (Elliot & Clarke, 1991) . . . . . 180
17.8 Change in the net flux of heat through the sea surface, $dQ_T/dt$ (Elliot & Clarke, 1991) . . . . . 181
17.9 Change in the potential energy anomaly, dE/dt (Elliot & Clarke, 1991) . . . . 181
17.10 Bulk water column temperature expression, $h\Delta T$ (Elliot & Clarke, 1991) . . . . 181
17.11 Mixed layer depth, h (Elliot & Clarke, 1991) . . . . . 182
17.12 Bottom temperature if the the water is fully-mixed, $T_S$ (Elliot & Clarke, 1991) 182
17.13 Bottom layer depth, $h_2$ (Elliot & Clarke, 1991) . . . . . 182
17.14 Surface layer temperature, $T_S$ (Elliot & Clarke, 1991) . . . . . 182
17.15 Change in the potential energy anomaly, dE/dt (Simpson & Bowers, 1984; Elliott & Clarke, 1991) . . . . . 183
17.16 Surface layer depth, $h_1$ (Elliot & Clarke, 1991) . . . . . 183
17.17 Bottom layer temperature, $T_B$ (Elliot & Clarke, 1991) . . . . . 183

17.18 Bottom layer temperature if the water is stratified, $T_B$ (Elliot & Clarke, 1991) 184
17.19 Elliot and Clarke (1991) peak temperature difference and $h/u^3$ (Simpson & Hunter, 1974). . . . . 189
17.20 Change in concentration $c_1$, in the upper layer of the water column (Bowers, 2003) 191
17.21 Change in concentration $c_2$, in the lower layer of the water column (Bowers, 2003) 191
17.22 The rate of energy input by tides, $P_T$ (adapted from Bowers, 2003) . . . . . 193
20.1 Steady-state suspended sediment concentration (Bowers, 2003) . . . . . 211
20.2 Steady-state suspended sediment concentration, with rate of energy input, P, expanded . . . . . 212
20.3 Change in concentration with change in daily maximum tidal current speed . . 212
20.4 Settling speed ($w_s$) as a function of dc/du . . . . . 212

Table 1: Table of Units, a to f

| Symbol | Description | Units |
|---|---|---|
| $a$ | absorption | $m^{-1}$ |
| $a_w$ | absorption by pure water | $m^{-1}$ |
| $a_{Chl}$ | absorption by Chlorophyll-a | $m^{-1}$ |
| $a_p$ | absorption by non-algal suspended solids | $m^{-1}$ |
| $a_{CDOM}$ | absorption by CDOM (coloured dissolved organic matter) | $m^{-1}$ |
| $a_p*$ | mass-specific absorption by non-algal suspended solids | $m^2g^{-1}$ |
| $\alpha$ | shape parameter | $dimensionless$ |
| $b$ | scattering | $m^{-1}$ |
| $b_p$ | scattering by suspended solids | $m^{-1}$ |
| $b_p*$ | mass-specific scattering by suspended solids | $m^2g^{-1}$ |
| $b_w$ | scattering by pure water | $m^{-1}$ |
| $b_b$ | backscattering | $m^{-1}$ |
| $b_f$ | forward scattering | $m^{-1}$ |
| $b_{b_p}$ | particulate backscattering | $m^{-1}$ |
| $b_{b_p}*$ | mass-specific particulate backscattering | $m^2g^{-1}$ |
| $b_{b_w}$ | backscattering by pure water | $m^{-1}$ |
| $b_{b_{Chl}}$ | backscattering by Chlorophyll-a | $m^{-1\}}$ |
| $\beta$ | shape parameter | $dimensionless$ |
| $\beta$ | volume scattering function | $m^{-1}sr^{-1}$ |
| $\beta_p$ | particulate volume scattering | $m^{-1}sr^{-1}$ |
| $c$ | suspended sediment concentration | $gm^{-3}$ |
| $C$ | function of solar zenith angle, angle of observation and surface roughness | $sr^{-1}$ |
| $C_P$ | specific heat capacity of water | $Jkg^{-1\circ}C^{-1}$ |
| $Chl$ | Chlorophyll-a concentration | $mgm^{-3}$ |
| $CSA$ | cross-sectional area of particles | $m^{-1}$ |
| $D$ | particle diameter | $\mu m$ or m |
| $D_{max}$ | maximum particle diameter | $\mu m$ |
| $D_{50}$ | mass-median particle diameter | $\mu m$ |
| $E$ | potential energy anomaly | $Jm^3$ |
| $E_u$ | Upwelling irradiance | $Wm^2nm^{-1}$ |
| $E_d$ | Downwelling irradiance | $Wm^2nm^{-1}$ |
| $\epsilon$ | efficiency of tidal mixing | $dimensionless$ |
| $\epsilon$ | rate of TKE dissipation per unit mass | $Wkg^{-1}$ |
| $\eta$ | surface displacement relative to sea level | $m$ |
| $\eta_e$ | equilibrium tidal response of the surface relative to mean sea level | $m$ |
| $f$ | Coriolis parameter | $^\circ s^{-1}$ |

Table 2: Table of Units, $f_w$ to $\rho_p$

| Symbol | Description | Units |
|---|---|---|
| $f_w$ | wind function used to calculate heat flux at ocean surface | $ms^{-1}$ |
| $F$ | Force | $N$ |
| $g$ | acceleration due to gravity | $ms^{-2}$ |
| $g'$ | reduced gravity, $g(\rho_s - \rho)/\rho$ | $ms^{-2}$ |
| $\gamma$ | efficiency of resuspension | $dimensionless$ |
| $H$ or $h$ | Total ocean depth or layer depth | $m$ |
| $k_b$ and $k_s$ | bottom and surface drag coefficients | $dimensionless$ |
| $K_d$ | diffuse attenuation coefficient | $m^{-1}$ |
| $L_t$ | top of atmosphere radiance | $Wm^{-2}sr^{-1}$ |
| $L_r$ | Rayleigh radiance | $Wm^{-2}sr^{-1}$ |
| $L_a$ | scattering by aerosols | $Wm^{-2}sr^{-1}$ |
| $L_{ra}$ | multiple interaction term between molecules and aerosols | $Wm^{-2}sr^{-1}$ |
| $L_{wc}$ | white cap radiance | $Wm^{-2}sr^{-1}$ |
| $L_g$ | specular reflection due to direct sunlight | $Wm^{-2}sr^{-1}$ |
| $L_wN$ | normalised water-leaving radiance | $Wm^{-2}sr^{-1}$ |
| $L_{path}$ | radiance path | $Wm^{-2}sr^{-1}$ |
| $\lambda$ | wavelength | $nm$ |
| $\lambda_r$ | reference wavelength | $nm$ |
| $MSS$ | mineral suspended solids concentration | $gm^{-3}$ |
| $TSS$ | total suspended solids concentration | $gm^{-3}$ |
| $MSS/TSS$ | mineral content | $dimensionless$ |
| $\mu$ | dynamic viscosity of water | $kgm^{-1}s^{-1}$ |
| $n_f$ | fractal dimension of floc | $dimensionless$ |
| $\nu$ | kinematic viscosity | $m^2s^{-1}$ |
| $P$ | rate of energy input by tides and wind | $kgm^{-3}s^{-1}$ |
| $Q_{b_b}$ | backscattering efficiency | $dimensionless$ |
| $Q_s$ | incoming short-wave radiation | $Wm^{-2}$ |
| $Q_T$ | net flux of heat through the sea surface | $Wm^{-2}$ |
| $r$ | parameterisation of drag | $dimensionless$ |
| $R_{RS}$ | remote sensing reflectance | $sr^{-1}$ |
| $R*$ | linear fit between $R_{RS}$ and IOPs | $dimensionless$ |
| $Re$ | Reynolds number | $dimensionless$ |
| $Re_p$ | particle Reynolds number | $dimensionless$ |
| $\rho$ | density of seawater | $kgm^{-3}$ |
| $\rho_w$ | density of pure water | $kgm^{-3}$ |
| $\rho_p$ | density of particle (solid) | $kgm^{-3}$ |

Table 3: Table of Units, $\rho_a$ to W

| Symbol | Description | Units |
|---|---|---|
| $\rho_a$ | density of air | $kgm^{-3}$ |
| $\Delta\rho$ | density difference, ($\rho_p$-$\rho$) | $kgm^{-3}$ |
| $S$ | exponential slope between $a_p*$ and $\lambda$ | $nm^{-1}$ |
| $SPM$ | suspended particulate matter concentration | $gm^{-3}$ |
| $SPM_T$ | model 1, SPM predicted using tides-only statistical model | $gm^{-3}$ |
| $SPM_{TW}$ | model 2, SPM predicted using tides and wind | $gm^{-3}$ |
| $SPM_{TWC}$ | model 3, SPM predicted using tides, wind and Chlorophyll-a | $gm^{-3}$ |
| $t$ | time | $minutes, hours, days$ |
| $t$ | diffuse atmospheric transmittance from the surface to the sensor | $dimensionless$ |
| $t_0$ | diffuse atmospheric transmittance from the sun to the surface | $dimensionless$ |
| $T$ | direct transmittance from surface to the sensor | $dimensionless$ |
| $T_M$ | function of surface and dew point temperatures | $^\circ C$ |
| $\Delta T$ | temperature difference, ($T_S$-$T_B$) | $^\circ C$ |
| $T_S$ | surface layer temperature | $^\circ C$ |
| $T_B$ | bottom layer temperature | $^\circ C$ |
| $T_D$ | dew point temperature | $^\circ C$ |
| $TSS$ | total suspended solids concentration | $gm^{-3}$ |
| $\theta$ | angle of scatterance | $^\circ$ |
| $\theta_{cr}$ | Shields critical parameter | $dimensionless$ |
| $\tau_{cr}$ | critical bed shear stress | $dimensionless$ |
| $u$ | orthogonal velocity component of tidal current speed | $ms^{-1}$ |
| $U$ | depth-averaged tidal current speed | $ms^{-1}$ |
| $v$ | orthogonal velocity component of tidal current speed | $ms^{-1}$ |
| $w_s$ | particle settling velocity | $mms^{-1}$ or $mday^{-1}$ |
| $W$ | wind speed | $ms^{-1}$ |

$\alpha$, $\beta$ and $\theta$ are also used to represent dimensionless coefficients in the Rivier et al. (2012) statistical model. In the later statistical modelling chapter, subscripted a, b and c are used for the same purpose.

## Acknowledgements

For this project, I am indebted to my supervisors:

- Prof. David Bowers of Bangor University, who always knows the right thing to say when you are confused or concerned and whose ability to explain scientific concepts rivals the late Prof. Richard Feynman.
- Dr. Francis Gohin of Ifremer, whose hospitality and advice helped me during my time in France. Without his expertise in satellite data analysis, this PhD would have been substantially diminished.
- Dr. Romaric Verney, also of Ifremer, who was dedicated to helping me during my PhD and without whom I would have unable to take part in either French field campaign.

The assistance given by supervisors is often understated, but they are the pillars upon which a Doctoral candidate builds their PhD and this would have been an impossible task without their continued support and their feedback of this manuscript.

I would like to thank the DSTL (Defence, Science and Technology Laboratory, U.K.) and the DGA (Direction Générale de l'Armement, France) for providing funding for this project. More specifically, I am thankful for the guidance and assistance during my PhD from my points of contact Dr. Timothy Clarke (DSTL) and Dr. Carole Nahum (DGA). The Lancaster House Treaties between the U.K. and France, part of the fruit of which is this PhD scheme, has shown a successful commitment to strengthening bonds between countries at a time when there are unfortunately those who wish to break those bonds.

The fieldwork chapter of this thesis would have been impossible without the cooperation and collaboration of many important people, I would like to thank:

- The team from the School of Ocean Sciences at Bangor, namely Gwynne Parry Jones and Ben Powell who got me out on the water in the RV Macoma and made sure I did not sink.

- The Universit*é* de Bordeaux and CNRS (Centre National de la Recherche Scientifique), including Dr. Virginie Lafon, Dr. Bertrand Lubac and Nicholas Ramé, the rest of the members of the RIVERCOLOR project and the crew of the RV Cotê de la Manche. You put up with my poor French and made me feel welcomed while working with you all.
- I would like to add extra thanks to my supervisor (Dr. Romaric Verney), who arranged my attendance of the SYNAPSES field campaign in the Seine Estuary (also aboard the RV Cotê de la Manche). I would also like to thank Matthias Jacquet, who was a great help in preparation for the cruise and while aboard the ship, whose technical assistance helped me when I found myself without a crucial nut for my underwater metal frame.

During my PhD, my girlfriend Danielle became my wife. Danielle has been a beacon of steadfast support throughout my PhD, experiencing with me the highs and lows. She has put up with my long periods away, times when I have been stressed and my lackadaisical attitude towards my natural circadian rhythm. I love you and I thank you for continuing to be positive even when I couldn't see the light at the end of the tunnel. To my brother and best man Thomas, who was always able to give me a unique perspective on what I was doing and who remained jealous when I was far away from home. To my mum and dad, who always showed that they were proud and who provided a place to live for me and Danielle while I finished my write up.

I have met too many friends during my PhD to name them all, but I would like to thank Diha, Martyn, Sophie, Alice, Holly, Suzie, Brian, Jingnan, Connor and Adam who made those completing PhDs feel less like it was work or a task and more like a family endeavour. I would also like to thank my friends John, Tom and Phil, who gave me the invaluable perspective of a PhD from outside of academia and were able to make me feel relaxed even when work was tough.

Completing a PhD is not just about the things you do to meet the criteria, but about building yourself up as a research-capable scientist. As part of my PhD, I have been able to travel around Europe to a multitude of conferences and exhibitions (in the U.K., France, Belgium

Austria), meeting some fantastic people whom I hope to remain friends with and collaborate with into the future. I would like to thank Ronan and Christine Loarer and Myriane Ruelen, who hosted me while I lived in France. During my time in the School of Ocean Sciences, I endeavoured to be a participating member of the department and am thankful for the staff for making me feel welcome. I am proud to have been part of what is now a very successful PhD skill-sharing group which will pass down the experience and knowledge to new PhD students into the future. I would also like to thank Prof. Tom Rippeth, the crews of the RRS James Clark Ross and RRS James Cook and the NERC-funded OSMOSIS, ACCACIA and TEA-COSI research groups, who gave me the opportunity to assist in research cruises outside of the scope of my PhD (in both the Arctic and Atlantic Oceans). When you are in the midst of project such as a PhD, it is easy to lose wider perspective, these colleagues were able to encourage, enthuse and excite me about my work and the possibilities of a future career in science.

Finally, I would like to thank my supervisory board; Dr. David Doxaran (external), Dr. Jaco Bass (internal) and Dr. Mattias Green (chair) for the time taken in reading the manuscript and giving me feedback regarding it. Answering the comments made in this manuscript and those expressed in the viva have undoubtedly made this a vastly superior thesis and for that I am forever grateful.

Figure 1: The English Channel (La Manche) between England and France, taken during the Bay of Seine field campaign (January 2015).

*"The best thing I know between France and England is the sea"*

- Jerrold, D.W.

## Part I

# Literature Review

## 2 Suspended Particulate Matter (SPM)

Material suspended within the water column is neither uniform in source nor in content (Fig. 2). Eisma (1993) defined suspended matter as material which may be retained upon a $0.5\mu m$ filter, with particles smaller than this considered to be dissolved (Eisma et al., 1980). Gordon (1970) observed particles below $0.2\mu m$, although particles at this size range are often difficult to quantify using conventional techniques (Gordon, 1970; Harris, 1977; Eisma, 1993). Suspended material is often a mixture of both organic and mineral material. Suspended material is made up of a large variety of different constituents, including bacteria, carbonates, clay minerals, silts and fine sands, diatoms, organic fragments and organic biofilms (Eisma, 1993). Organic suspended material ranges from phytoplankton to organic debris such as faecal pellets, whereas mineral suspended material is generally made up of quartz, feldspars and clay minerals which enter the water column through resuspension, erosion and through riverine discharge (Eisma, 1993). The ratio of these different constituents within a suspended particle assemblage varies widely both spatially and temporally. The composition of these constituents greatly influence the properties of a suspended assemblage, affecting the role and behaviour of suspended sediments within the marine environment. Variation in the properties of suspended sediments are most commonly observed through changes in the cohesivity of particle assemblages (known as flocs) and their fractal shape, which both strongly influence the overall density.

In addition to erosion and resuspension of bed sediments, the greatest influence upon the constituent formation of suspended material is through terrestrial outflows of riverine water, which transport not only vast amounts of sediment, but also terrestrial organic material, in addition to transporting fragments of marine organisms from the coastal zone. The role

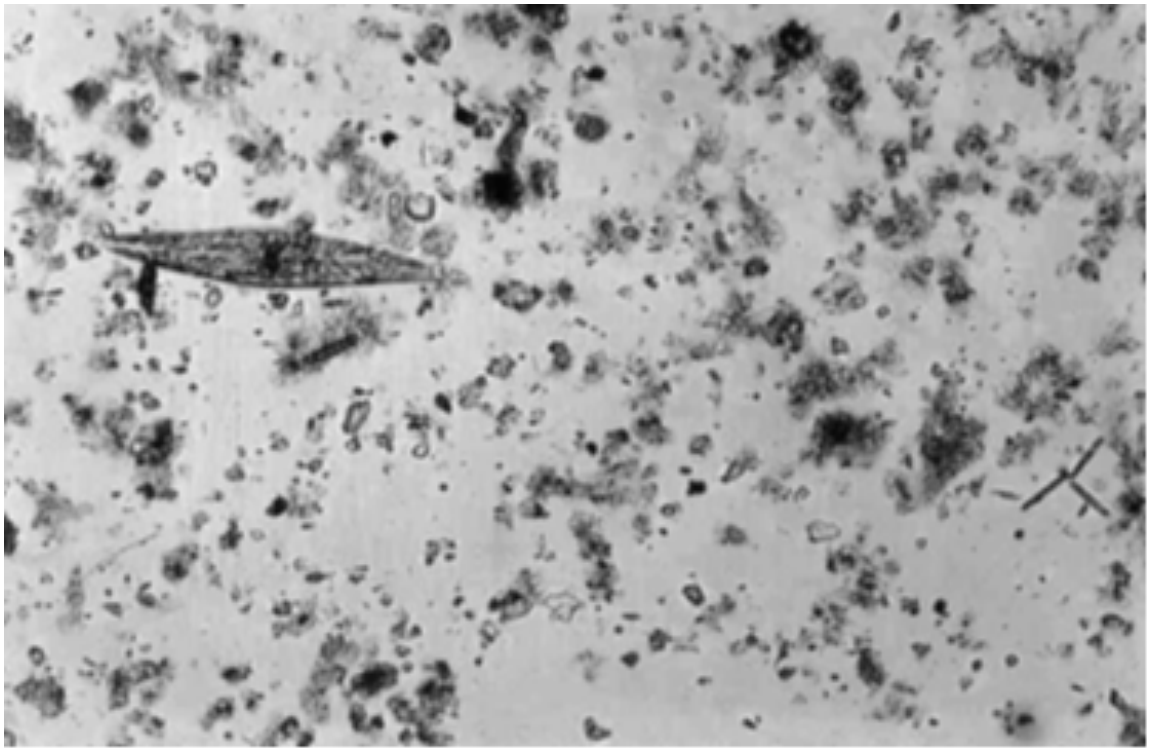

Figure 2: Single particles, flocs and phytoplankton. Image represents a width of approximately $400\mu m$ by $300\mu m$, with the diatom on the left hand side of the image being approximately $100\mu m$ in diameter (Bowers, 2013).

of the terrestrial-marine interface with regards to the transport of sediment often means that coastal regions are consistently supplied with suspended matter. In addition, fluxes of suspended matter are vastly influenced by not only the tidal- and wave-forcings of the ocean but also the variability in surges of riverine influx due to high rainfall.

Due to gravity, all suspended material with a density greater than the water surrounding it will eventually sink unless turbulent motions act to maintain the particles in suspension. In highly turbulent environments, particles with densities far greater than the density of water may be maintained in suspension (Khelifa & Hills, 2006; Curran et al., 2007), such as in regions of high tidal activity or in shelf-break regions.

The spatial and temporal variability of suspended matter is important for a variety of reasons; not least sediment transport, pollutant dispersal, monitoring of water quality and in the study of seabed light, which is important for photosynthetically active organisms such as algae. In the open-ocean, the study of mineral suspended material often comes latter to that of organic material as mineral particles are vastly outnumbered by the presence of zooplankton, phytoplankton and the resultant organic debris. In shallower shelf-sea regions, suspended material is often a mixture of organic and mineral matter. The size distribution, particulate mass and particle composition all have important roles in terms of the behaviour of suspended material (Hurd & Spencer, 1991; Eisma, 1993; Ellis et al., 2008). Singular particles are often considered near-spherical solid structures, however as particles aggregate in the form of flocs they often form voids which may result in densities less than their composite parts.

Similarly, suspended material can range from large numbers of small particles to far larger aggregated particle assemblages, referred to as flocs or marine snow. In the open ocean, particles are by and large mostly organic, made up of phytoplankton and organic detritus (Bowers et al., 2014). The mineral fraction of suspended sediment concentration is shown to increase with proximity to the coast due to the influx from rivers and the resuspension of sediments due to increased seabed turbulent dissipation (Bowers et al., 2014).

Bowers (2013) gives a good account of the nature of the size distribution of particles in water measured using the LISST-100 in the Irish Sea. The LISST-100 is used to measure the size

distribution of particles in water in 32 size classes, through laser diffraction (see methods section of the field observation chapter for further description) (Agrawal & Pottsmith, 2000). The measurements used for this example were taken within the Menai Strait, north Wales, processing the LISST output assuming that the particles are spherical (Braithwaite et al., 2012; Graham et al., 2012). Although not indicative of all conditions, they demonstrate the general variability observed and magnitudes associated in relation to the particle size distribution.

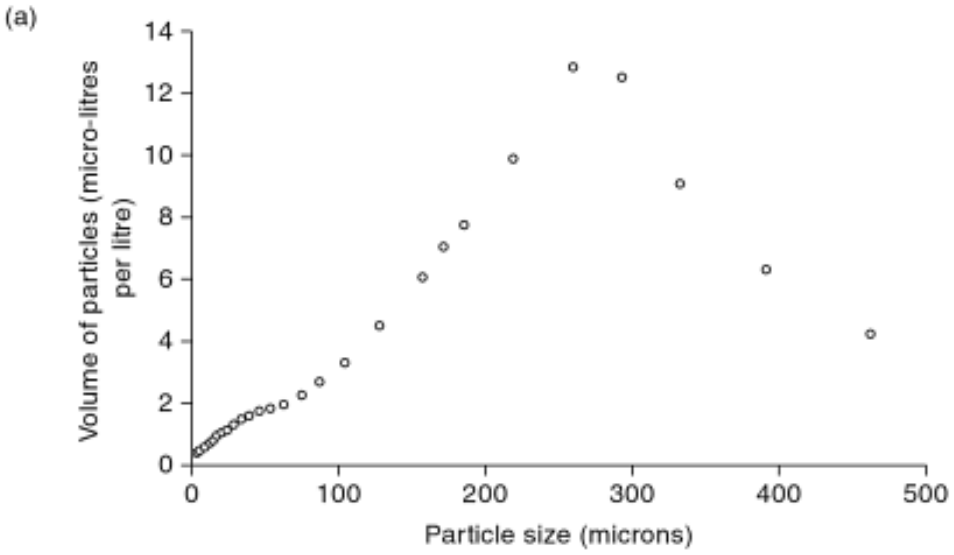


Figure 3: The volume of particles measured at sizes between 0 and 500$\mu m$ (Braithwaite et al., 2012; Graham et al., 2012; Bowers, 2013).

The size distribution of particle volume demonstrates that the largest proportion of the total particle volume is made up of particles between 200 and 400$\mu m$ (Fig. 3, Bowers, 2013).

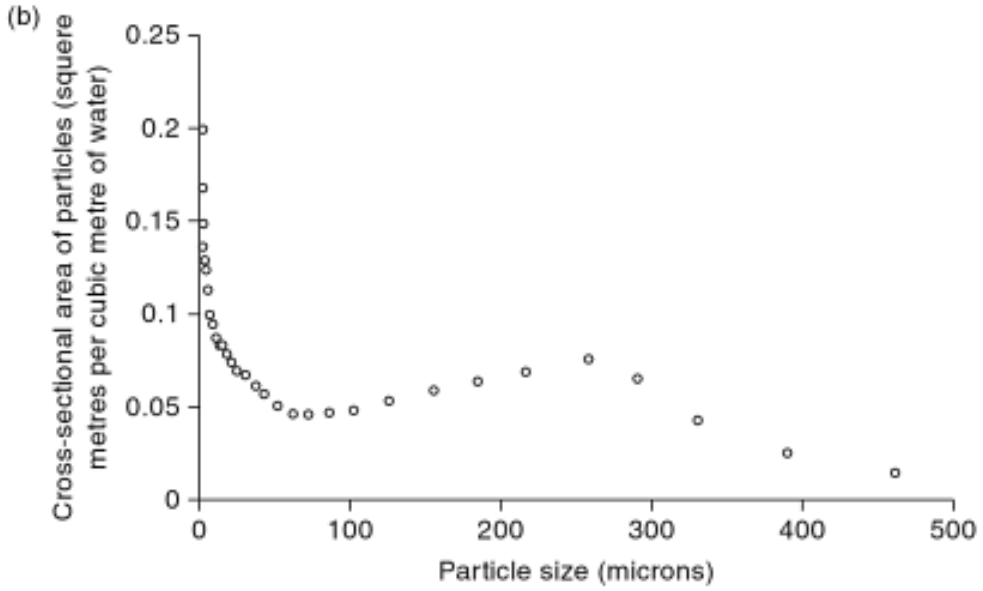


Figure 4: The cross-sectional area of particles measured at sizes between 0 and 500$\mu m$ (Braithwaite et al., 2012; Graham et al., 2012; Bowers, 2013).

In comparison to the importance of the larger particles in contribution to the total volume, the cross-sectional area of particles was found to be highest in the smallest particles observed. This demonstrates the significance of small particles for applications where the cross-sectional area is important, such as in remote sensing (Figure 4, Bowers, 2003; Bowers et al., 2014).

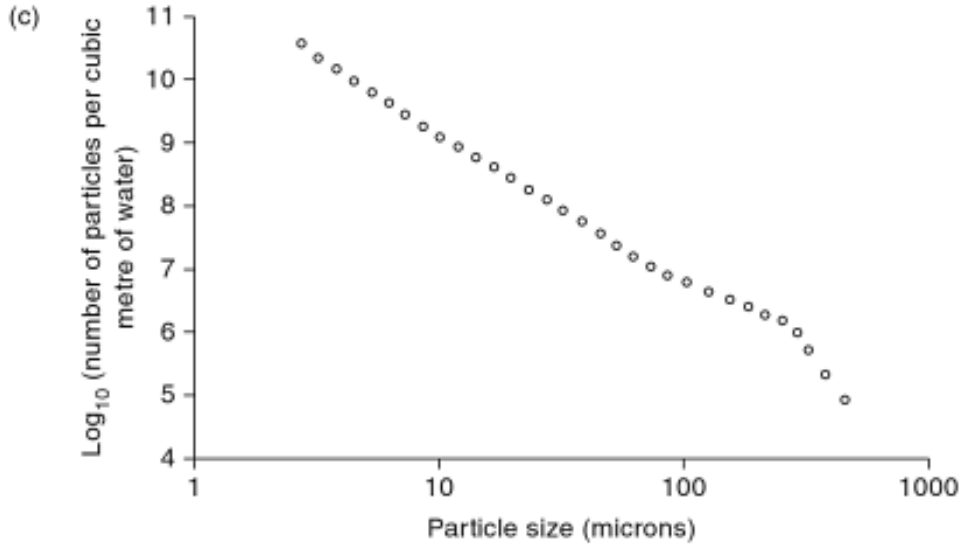


Figure 5: The common logarithm ($log_{10}$) of the number of particles per cubic metre measured at sizes between 0 and 500$\mu m$ (Braithwaite et al., 2012; Graham et al., 2012; Bowers, 2013).

Although they make up a smaller contribution to the total particle volume, the number of particles observed below 10$\mu m$ are $10^6$ times more prevalent than those observed above 300$\mu m$ (Fig. 5, Bowers, 2013).

## 2.1 Measurements of suspended particulate matter

The simplest and most direct method of measuring suspended matter concentration is through the gravimetry of water samples. Samples of water can be reliably taken at both the surface and also at depth using devices such as a Rosette sampler. The water is then filtering through a pre-weighed 47$mm$ glass-fibre filter (with a 0.7$\mu m$ pore size), with the amount of water used depending upon the turbidity, with preference for as much of the sample to be filtered as possible without overloading the filter. Once the filtering has been completed, it is necessary to dry the filter, normally in a drying over at 100°$C$ for approximately 12 hours. At this point, weighing the dried filters and removing the original weight will provide the total suspended solids load, which when divided by the volume of water filtered will provide the concentration. In order to find the mineral proportion of the suspended sediment load,

the filter must be placed in a furnace at $500°C$ for a further 3 hours, removing the organic material. Following the same process as with the total suspended solids concentration, it is possible to calculate the mineral suspended solids concentration (MSS). Utilising these water samples, acoustic and optical backscatter devices measure the signal profile through the water column, and then calibrate the signal with the water samples, providing the concentration of suspended sediments (Thorne et al., 1991; Boss & Pegau, 2001).

## 2.2 Threshold of movement

In order for suspension to occur within the marine environment, first the threshold of sediment movement must be surpassed. The threshold of movement depends upon the drag force (Eq. 2.1), the lift force (Eq. 2.2) and the immersed weight (Eq. 2.3) acting upon the sediment grains, all of which are dominated by the influence of the grain diameter.

*Drag force, F (Davis, 2012)*

$$F \propto \tau_0 D^2 \tag{2.1}$$

$\tau_0$ is the bed shear stress, $Nm^{-2}$

D is the particle diameter, m

*Lift force, L (Davis, 2012)*

$$L \propto \tau_0 D^2 \tag{2.2}$$

*Immersed weight, W (Davis, 2012)*

$$W \propto \Delta\rho g D^3 \tag{2.3}$$

$\Delta\rho$ is the density difference, ($\rho_s$-$\rho$), $kgm^{-3}$

$\rho_s$ is the particle density, $kgm^{-3}$

$\rho$ is the water density, $kgm^{-3}$

g is the acceleration due to gravity, $9.81ms^{-2}$

In an attempt to quantify the relationship of forces under which movement occurs, the Shield's formula was constructed, taking into account the fluid forces (Kramer, 1932; Kramer, 1935; Casey, 1935; Shields, 1936; Zanke, 2003). Shield's parameter ($\theta_{cr}$) represents the entrainment function (the ratio of shear forcings to gravity) of sediment grains within the water column (Reeve et al., 2004). Using Shield's equation (Eq. 2.4), it is possible to set the Shield's parameter to the level of entrainment categorised by sediment suspension and then to calculate the critical shear stress threshold ($\tau_{cr}$) required to result in sediment suspension.

*Shields parameter, $\theta_{cr}$ (Shields, 1936)*

$$\theta_{cr} = \frac{\tau_{cr}}{\Delta \rho g D} \tag{2.4}$$

$\theta_{cr}$ is the Shield's critical threshold
$\tau_{cr}$ is the critical bed shear stress, $Nm^{-2}$

When a body of water passes over the bed, a stress is generated relative to the bottom topography, known as the bed shear stress ($\tau_0$). Bed shear stress represents the effect of bottom topography on the interaction of the flowing water with the bed. A flat bed however, with little discontinuity would comparably have a far lower bed shear stress at the same current speed (van Rijn, 1984). Similarly, such a stress can be generated between two bodies of water, moving at different speeds or of different densities, forming internal waves between stratified layers (Stillinger et al., 1983). The process of the dissipation of this energy is referred to as turbulence, in the form of turbulent kinetic energy. In this way, turbulent activity may be increased by increasing either the fluid stresses or the bed shear stress. Fluid stresses can act between two stratified layers moving at different velocities to one another, causing friction which is then expressed as TKE. Similarly, bed shear stresses are caused when water moves along the seabed with TKE increasing with increased bed roughness. The main time-varying

fluid stress drivers of turbulence are tides and waves acting upon the entire ocean, with the topographical variation such as bedforms predominately impacting upon shallow regions.

## 2.3 Forms of suspended sediment transport

When the threshold of movement is met, sediment does not immediately enter suspension, the process is more gradual. In this vein, the stages of movement can be split into three main forms of sediment transport, which are fundamentally dependant on the particle's diameter and density:

(a) Bed load transport

This form of transport occurs when the lift force acting upon the grain surpasses that of the drag forces, but not to the extent to allow suspension. Bed load transport can be highly intermittent and sediment grains within this state are often observed to be rolling or saltating along the bed.

(b) Suspended load transport

When the lift force surpasses the drag forces further, it is possible for suspension of grains to occur. This form of transport is normally dependant upon tidal variation, with particles kept in suspension for several hours or more.

(c) Wash load transport

When suspension is maintained indefinitely, this is referred to as sheet flow transport. Here grains may often be maintained in suspension over an entire season or in some cases, for years.

# 3 Flocculation

In addition to the presence of singular grains, the predominance within suspended materials falls upon multiple grain assemblages, known as flocs. As previously described, particle assemblage composition varies greatly, the aggregation of constituents dictates the subsequent size, structure and density of the suspended floc, and the settling velocity of the assemblage, which controls whether it will settle or remain suspended (Gibbs, 1985; van Leussen, 1994; Verney et al., 2009).

Water-borne clay particles predominately have a negative electrical charge and as such are driven apart by the electrostatic repulsive force present (Sholkovitz, 1976; Eisma, 1986; Asmala et al., 2014). However, when positively-charged particles are present, the van der Waals force pulls these positive and negatively-charged particles to one another, creating weak particle aggregates. Due to water-filled gaps present between the particles that make up the flocs, the density is less than that of single particle of the same size. As would be expected, regions of high suspended matter concentration have a higher rate of collision between particles and therefore the likelihood of aggregation is greater than in an environment where there is a lower concentration and therefore fewer collisions (Dyer, 1986; Verney, 2009). The frequency of collisions is mainly driven by shear turbulence and differential settling (van Leussen, 1994).

In 1976, Sholkovitz described how the flocculation of particles varied within different proportions of fresh river water and sea water. This study described an increase in flocculation with increasing quantities of salt, suggesting that flocculation is salinity-dependant (Sholkovitz, 1976). It was suggested that increased salinity corresponded to an increase in the positively-charged sodium particles ($Na^{+2}$) required for flocculation (Sholkovitz, 1976). Despite the fact that at this point salinity was believed to strongly affect the flocculation of particles uniformly, it is now known to mostly affect clay particles and as such is a more dominant process in clay particle-rich regions (Thill et al., 2001). Due to the varied composition of aggregates, the effect of salinity on general flocculative processes is less dominant, especially in the case of large flocs, where size and density of the constituent particles are far greater influences (Verney, 2006).

Organic material which is found in suspension tends to be linked to the presence of suspended matter. Phytoplankton within the water column are positively-correlated with light availability due their dependance upon sunlight for photosynthesis. The food chain within the marine environment begins with phytoplankton, as such inhibitions to phytoplankton production effect the overall biological productivity of the ocean. As phytoplankton photosynthesise, they exude polysaccharides (referred to broadly as EPS - extracellular polymeric substances) into the water column which then stick to suspended matter. When particles flocculate within these polysaccharide-rich waters, the sugars strengthen the bonds between particles, allowing them to maintain far larger assemblages than would be possible otherwise. This is supported by a study by Chen and Eisma (1995), which showed that organic material increases within the water column greatly increased the likelihood of successful and maintained flocculation. Similarly, Lunau et al. (2006) showed that diatom blooms and bacteria encouraged the growth of flocs to larger sizes than would otherwise be expected, with a larger proportion of macroflocs being found during times of diatom blooms.

As described, different processes influence the flocculation of sediment particles to large assemblages, in terms of their size and their composition. The size of flocs are often designated into two distinct groups, microflocs (or microaggregates) and macroflocs (or macroaggregates). Microflocs are small (up to 100-160$\mu m$) and dense, with a subsequently high resistance to fragmentation by turbulent mixing (Manning & Dyer, 1999; Lafite, 2001). In comparison, macroflocs are larger assemblages (up to several mm), that are less dense and easily fragmented by turbulent mixing (Manning, 2004; Jarvis et al., 2005). This was demonstrated by Verney et al. (2009), who showed with experimental results from several studies, that the maximum floc size present within the water column correlated well with the Kolmogorov microscale boundary, a representation of the turbulent condition (Mikes et al., 2004; Verney, 2006; Winterwerp, 2006; Bowers et al., 2007).

### 3.1 Stokes Law

A floc may contain in excess of "$10^6$ individual particulates" (Manning et al., 2007), with floc density decreasing with growth (Koglin, 1977; Tambo & Watanabe 1979; Klimpel & Hogg, 1986; Manning et al., 2007). Despite the reduction in effective density with floc growth, their settling speed increases due to Stokes' Law (Dyer & Manning, 1999).

Due to the complex nature of flocs, their settling does not simply follow the format of Stokes Law (Kranenburg, 1994). Stokes Law describes the terminal settling velocity ($w_s$) of single spherical particles where the particle density is greater than that of water (Thorpe, 2005) (Eq. 3.1).

*Stokes Law (Thorpe, 2005)*

$$w_s = \frac{gD^2}{9\nu}\frac{\Delta\rho}{\rho} \tag{3.1}$$

$w_s$ is the terminal settling velocity, $ms^{-1}$ g is acceleration due to gravity ($= 9.81ms^{-2}$)
D is the particle diameter, m
$\nu$ is the kinematic viscosity, $m^2s^{-1}$
$\rho$ is the water density, $kgm^{-3}$
$\rho_p$ is the particle (or solid) density, $kgm^{-3}$
$\Delta\rho$ is defined as $\rho_p$-$\rho$

The consensus in literature is that Stokes Law may be used to describe the settling of particles up to a particle Reynolds number of 0.1 (McNown & Malaika, 1950). The particle Reynolds number (Eq. 3.2) describes the ratio of inertial to viscous forces acting upon the particle within the water column, a simple quantification of turbulent activity.

*Reynolds number*

$$Re = \frac{w_s D\rho_p}{\nu} = \frac{Inertial forces}{Viscous forces} \tag{3.2}$$

Below a particle Reynolds Number of 0.1, inertial terms within the Navier-Stokes equations may be neglected allowing for Stokes Law to be used. By rearranging the equation for the

Reynolds number, the particle size at which this limit is exceeded can be described by the following equation (Eq. 3.3):

*Particle size limit using Reynolds number, $D_{max}$*

$$D_{max} = \frac{\nu}{10 w_s \rho_p} \tag{3.3}$$

## 3.2 Sediment Pollution

The formation of flocculant masses involves the aggregation of matter within the water column which can often include pollutants (Ackroyd et al., 1986; Stewart & Thomson, 1997; Aldridge et al., 2003; Manning et al., 2007). These pollutants can be transported within flocs through the water column. Pollutants of this form can include bacteria, agricultural effluents and heavy metals. The potency of this form of pollutant dispersal means that flocculation within coastal regions, especially those close to regions of high anthropogenic activity are closely monitored (Uncles et al., 1998; James, 2002). In addition, modern waste treatment plants now go to great extents to reduce the impact of pollutant flocculation and the resultant dispersal of pollutants, through both chemical disaggregation and depuration, where waste is purged of pollutants (Di Natale et al., 2011).

## 3.3 Turbulence and flocculation

Several studies have identified turbulence as a limiting factor to the size of flocs (Fugate & Friedrichs, 2003; Bowers & Binding, 2006; Bowers et al., 2007). Although in the presence of high levels of EPS (extracellular polymeric substances), flocs may form large aggregations of many particles, this phenomenon is best observed in regions of weak turbulent shear (Eisma et al., 1991). In the presence of high levels of turbulent shear, flocs are prone to disaggregation (Winterwerp, 1998; Ellis et al., 2004). Winterwerp et al. (2006) described how particle size and settling velocity decreased with increased shear stress. Fugate and Friedrichs (2003)

described how the largest floc size within the water column is limited by the Kolmogorov microscale (Bowers & Binding, 2006):

*Maximum floc diameter, $D_{max}$, limited by the Kolmogorov microscale (Fugate & Friedrichs, 2003; Bowers & Binding, 2006)*

$$D_{max} = \left(\frac{\nu^3}{\epsilon}\right)^{1/4} \tag{3.4}$$

$\nu$ is the kinematic molecular viscosity, $m^2 s^{-1}$
$\epsilon$ is the rate of turbulent kinetic energy dissipation per unit mass, $W kg^{-1}$

# 4 Particle settling

Shelf-seas make up only "7% of the surface area of the ocean" (Bauer et al., 2013; Rippeth et al., 2014), but they are estimated to be responsible for "80% of organic carbon burial" (Bauer et al., 2013; Rippeth et al., 2014) in the oceans. The pathway through which carbon is transported from the ocean surface to bottom sediments is referred to as carbon sequestration (Herndl & Reinthaler, 2013).

A facilitating component of the sequestration from the upper ocean is through the aggregation and settling of marine particulates. When particles collide, they may aggregate to form larger assemblages, held together by weak Van der Waals forces (Hunter & Liss, 1979). These assemblages are extremely fragile and often break up when exposed to minimal turbulent activity (Alldredge et al., 1990). However, in the presence of organic polysaccharides such as those exuded from marine phytoplankton, particulate bonds may be strengthened, making them more resistant and allowing them to reach larger sizes and thus increasing their speed of settling (Fig. 6).

As they sink through the water column, flocculating particles attract both organic and inorganic marine detritus. These particles are referred to as flocs, or more colloquially as marine

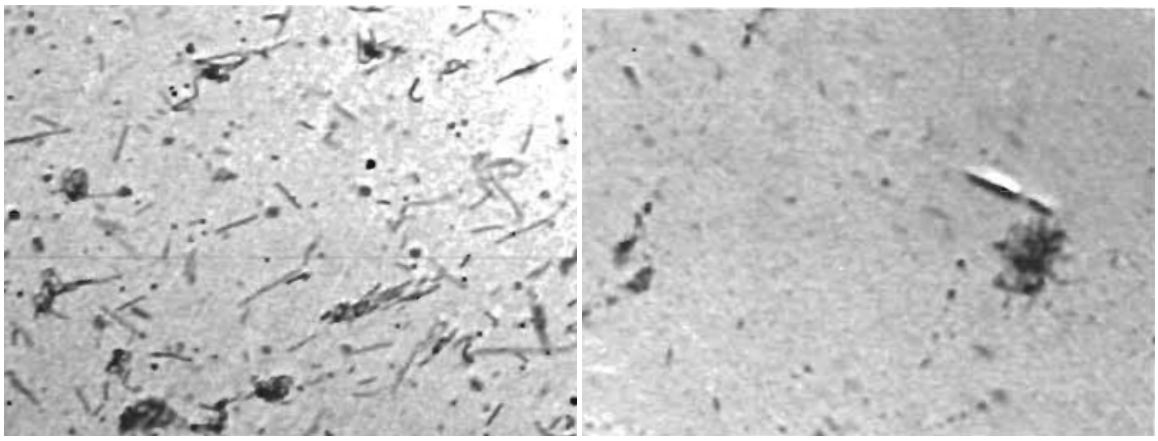

(a) Single particles and microflocs. (b) Microflocs and macroflocs.

Figure 6: Particles flocculating in the presence of organic material (Kranck & Milligan, 1988).

snow (Herndl & Reinthaler, 2013). The rate of floc settling can be seen as a controlling factor in the residence time of matter in the ocean surface, in addition to being a crucial parameter for models of sediment transport (Malarkey et al., 2013). To this endeavour, understanding the role of particle settling and flocculation impacts upon all aspects of the marine environment; including biological, chemical and geological processes.

As particles flocculate, their mass increases until they sink through the water column. The level to which particles continue to flocculate is controlled by the amount of organic material present. As the level of organic material varies from a low in the winter to a peak in the summer (Sambrotto, 2014), flocculation and the speed of particle settling is expected to vary on a seasonal cycle.

## 4.1 In-situ measurements of settling velocity

The rate of particle settling (or settling velocity) is most commonly directly quantified through the use of settling velocity tubes (SVTs) (Owen, 1976; Malarkey et al., 2013). In this method, water is stored within a tube, from which samples are removed at specific intervals. By comparing the concentrations of the removed samples it is then possible to estimate the speed at which the particles within suspension in the tube are settling. However, despite their wide use, this method has been questioned (Mantovanelli & Ridd, 2006), where suggestion is that

human error and the disturbance of in-situ samples may cause unaccountable errors within the subsequent results. Another suggestion has been to use plate samplers, measuring the immersed weight of material as it settles to the bottom of the settling tube (Mantonvelli & Ridd).

There have been several laboratory measurements of the settling of particles. Manning and Dyer (2002) examined the settling of particles of different sizes between $50\mu m$ and $800\mu m$. Manning and Dyer (2002) observed a particle of $50\mu m$ to settle at $0.15mms^{-1}$ (equivalent to $12mday^{-1}$), with a particle of $800\mu m$ settling at $2mms^{-1}$ (equivalent to $160mday^{-1}$), demonstrating the huge range of settling speeds. Manning et al. (2007) describes the use of the LabSFLOC system, which uses a 25Hz (25 times each second) floc camera, with a resolution of between $6.3\mu m$ and $20\mu m$ to image flocs as they settling. The LabSFLOC system allows semi-automatic processing of the digital images produced to calculate the floc diameter and the settling speed. Manning and Schoellhamer (2013) utilised the LabSFLOC system to observe settling velocities over a transect in San Francisco Bay. They observed floc sizes between $22\mu m$ and $639\mu m$ with settling velocities ranging between $0.04mms^{-1}$ (equivalent to $3.5mday^{-1}$ for the smallest flocs and $15.8mms^{-1}$ (equivalent to $1,365mday^{-1}$) for the largest flocs. Although Manning and Schoellhamer (2013) were able to further improve upon the understanding of settling velocity and floc size, upon the range shown in the laboratory (Manning and Dyer, 2002).

Unfortunately, Manning and Dyer (2002) did not look at particles below $50\mu m$, which often make up a large proportion of those present in the water column (Bowers, 2013).

## 4.2 Factors controlling particle settling

The simplest explanation of the main controlling factors of a particles settling speed comes in the form of Stokes Law (Winterwerp, 1998; Winterwerp, 2002). Stokes Law describes the unhindered settling of a single spherical particle, a simple idealised expression of an in-situ particle (Eq. 4.1):

*Stokes law for single, spherical particles (Winterwerp, 2002)*

$$w_s = \frac{(\rho_p - \rho_w) g D_p^2}{18\mu} \tag{4.1}$$

$\rho_p$ and $\rho_w$ represent the density of the solid (particle) and water respectively, $kgm^{-3}$

g represents acceleration due to gravity ($9.81ms^{-2}$)

$D_p$ represents the particle diameter, m

$\mu$ represents the dynamic viscosity of the water, $kgm^{-1}s^{-1}$

(Winterwerp, 2002)

However, particles within the ocean do not exist as single, spherical particles. As such, in the case of non-spherical clusters of particles as most commonly found, referred to as flocs, the settling speed is an inherently more complicated formulation (Eq. 4.2).

*Stokes Law for flocculated particles (Winterwerp, 2002)*

$$w_s = \frac{\alpha}{18\beta} \frac{(\rho_s - \rho_w) g}{\mu} D_p^{3-n_f} \frac{D^{n_f{}^-1}}{1 + 0.15 Re_p^0.687} \tag{4.2}$$

$\alpha$ and $\beta$ are dimensionless shape parameters

D is the floc size, m

$n_f$ is the fractal dimension of the floc (the three-dimensional complexity)

$Re_p$ is the particle Reynolds number

In practice, equation 4.2 is difficult to implement due to complexity of gathering detailed information regarding the structure of the concerned flocs and their constituent arrangements.

# 5 Turbulent activity

Turbulence is a stochastic process through which energy and momentum is transferred within the ocean. The presence of turbulence is observed throughout almost the entirety of the water column. Turbulence in the ocean occurs whereby kinetic energy produced mainly through tidal activity and waves are dissipated in the form of turbulent vortices. Although turbulence is visible as small-scale mixing within the water column, it can also be represented through far larger-scale mixing which occurs between water bodies. Turbulence is present in the form of eddies or vortices, often visible on the surface especially in areas of high turbulent activity. Such processes can be observed on both the small visible scale or as part of larger oceanic circulatory processes which may be visible from space.

Within a coastal shallow water environment such as within a shelf sea, the two main time-varying generators of turbulence are tides and storm- and wind-driven waves.

## 5.1 Tides

In the open-ocean, the effect of tides can often be small, however, in shallow tidal shelf seas, tides greatly influence the processes and dynamics of the region. The influence of tides in shelf seas is such that the dissipation of this energy can mix heat throughout the entire water column (Simpson, 1998).

Tides are produced by the centrifugal and gravitational forces between orbiting planetary bodies (Darwin, 1879). On Earth, the result of the gravitational pull of the moon is a bulging of water on the side closest to the moon. Due to inertia, the centrifugal force exerted results in a bulge on the side furthest from the moon. As the Earth rotates on its axis in orbit around the Sun (S2 tide, 12 hours), this causes a propagation of this bulge around the Earth, which is observed as a change in the local sea level, which results in two high tides in just over one Earth day. The delay is a result of movements of the moon. As the Moon moves 1/28th of the way round its own monthly orbit within the 24 hour period, the tides observed on earth are also delayed by 1/28th during 24 hours, observed as an additional 50 minutes to complete

two tidal cycles and referred to as the M2 (lunar semi-diurnal, 12 hours 25 minutes) tidal harmonic.

The synchronisation of the M2 and S2 variability is observed as spring and neap tidal variation, when the tidal range is at its highest and lowest ranges respectively. A spring tide occurs when the Moon is either between the Earth and the Sun or on the opposite side of the Earth from the Sun, here the tidal bulges are at their highest and therefore the tidal ranges are also at their highest. In contrast, a neap tide occurs when the Sun is at a right-angle to the Earth and the Moon, the tidal bulge is at its smallest and the tidal range is at its lowest. The Moon orbits the Earth approximately once every 28 days, thus spring-neap tidal cycles occur approximately every two weeks.

Understanding the phase and amplitude of tidal harmonics such as S2 and M2 allows us to predict precisely the variability of the tides using harmonic analysis. Although tidal forces act across the whole of the Earth's surface, in some areas the impact is greater than others (Dushaw et al., 1997). The tidal amplitude of a location is dependant upon the bathymetry of the ocean basin and the effect of the Coriolis force. In certain locations, the effect of these variables can cause a point of zero tidal amplitude, referred to as an amphidromic point.

**Tidal models**

Due to the harmonic nature of tides, predicting the tides at a specific location requires archived data from which to carry out harmonic analysis. Model systems such the TPXO (Topex-Poseidon) global tidal model use tide gauge observations and data from long-range acoustic transmissions as anchor points, between which the equations of motion and continuity are solved within two dimensions, to predict localised tidal variability (Dushaw et al., 1997) (Eq. 5.1; 5.2; 5.3).

*Equations of motion (Dushaw et al., 1997)*

$$\frac{\partial u}{\partial t} + u\frac{\partial u}{\partial x} v\frac{\partial u}{\partial y} - fv = -g\frac{\partial}{\partial x}(\eta + \eta e) - ru \tag{5.1}$$

$$\frac{\partial v}{\partial t} + u\frac{\partial v}{\partial x}v\frac{\partial v}{\partial y} - fu = -g\frac{\partial}{\partial y}(\eta + \eta e) - rv \tag{5.2}$$

Where u and v are the orthogonal components of the tidal current speed, $ms^{-1}$

g is acceleration due to gravity, $(= 9.81m^2s^{-1})$

f is the Coriolis parameter, $^{\circ}s^{-1}$

$\eta$ is the surface displacement relative to the mean sea level, m

$\eta_e$ is the equilibrium tidal response of the surface relative to the mean sea level, m

r is a parameterisation of drag

*Continuity equation (Dushaw et al., 1997)*

$$\frac{\partial \eta}{\partial t} + \frac{\partial}{\partial x}(Hu) + \frac{\partial}{\partial}(Hv) = 0 \tag{5.3}$$

Where H is the ocean depth

The propagation of tidal harmonics is highly dependant upon the localised topography, as such concentrated regional data is often unhelpful for global analysis. The impact of this is most apparent in the case of localised tidal harmonic resonance, such as that observed within the Bay of Fundy and the Bristol Channel (Lanzoni & Seminara, 2002). More recent versions of the TPXO global tidal model (TPXO 8.0, Figure 7) however use satellite time series to increase the resolution of tidal input data and such allows for continuously improved representation of tidal variability. Tidal currents are amplified on the shelf by local bathymetry. As such, in shallow waters, the current speed increases whereas in deeper waters such off the tidal shelf, the current speed is negligible.

## 5.2 Wind

Unlike tidal dissipation of energy, which can be modelled due to a well understood tidal cycle, wind is often more erratic and thus a less predictable processes, with a high degree of spatial variability (Green & Coco, 2014). There are two main impact regions in terms of wind-driven resuspension of particles, shallow water resuspension and deep water episodic resuspension (Bloesch, 1994). Wave resuspension which occurs in shallow waters occurs when the elliptical orbits of waves act in a horizontal motion upon the bottom sediments; if this force overcomes the bed friction and settling velocity, particles will be be suspended (Carper and Bachmann, 1984). Therefore, due to the elliptical orbits reducing in size exponentially with depth, shallow regions are more susceptible to resuspension than deeper regions (Green & Coco, 2014). Deeper, episodic resuspension also occurs due to wind-driven internal waves which act in stratified regions (Häkanson and Jansson, 1983).

# 6 Remote sensing of suspended sediments

## 6.1 Remote sensing

Satellite remote sensing or (sometimes referred to as Earth Observation) is the method of viewing the Earth using satellite imaging or high-resolution sensors. Ocean remote sensing utilises intensities in wavelengths from the near ultra-violet ( $300nm$) to the near infra-red ( $1000nm$) and up to $1m$ in the case of radar applications. The forms of data which can be extracted using satellites can usually be separated into four main distinctions:

1. Altimetry (topography)
2. Surface roughness
3. Temperature
4. Visible radiometry (colour)

From these four, many more can be subsequently deduced based upon the requirements of the research - from the levels of pollution within an urban region (Gupta et al., 2006) to harmful algal bloom monitoring (Kutser et al., 2006).

## 6.2 Ocean colour

Ocean colour imaging uses satellites to take high-resolution images of the Earth's surface. Ocean colour sensors record the spectral radiance ($Wm^{-2}m^{-1}sr^{-1}$), which is then normalised by the downwelling solar irradiance, to produce the remote sensing reflectance which is used in satellite algorithms ($R_{RS}$). This data is then analysed to extract the intensities within the visible range of wavelengths between 400nm and 700nm, with precise ranges dependant upon the sensor utilised. Satellite remote sensing is dependent upon the reflectance of sunlight in the ocean, therefore it is dependent upon sunlight penetration to identify oceanic properties. The penetration depth of sunlight is generally considered to be the point at which 90% of the sunlight at the surface is attenuated, Gordon and McLuney (1975) found that the mean

penetration depth for wavelengths between 500 and 600nm was approximately 20m and for wavelengths between 600 and 700nm this was approximately 2m.

There are three main forms of satellite algorithms:

1. *Empirical*

   Empirical algorithms use either single or multiple regressions to produce constants, which when multiplied by the remote sensing reflectance ($R_{RS}$) observed by the satellite at a specific wavelength ($\lambda$), will give the parameter (Topliss et al., 1989; Tassan, 1992; Binding et al., 2001; Lee et al., 2002; Werdell & Bailey, 2005; Campanelli et al., 2017). The positive of this method is that it is easy to apply as it does not rely upon understanding the relationship between remotely-sensed reflectance and the parameter. However it often favours certain conditions, so may not be applicable over a wide spatial area or throughout the year. Some empirical algorithms have therefore opted for look-up tables with spatially-varying constants and the use of multiple constants over a year (Gohin et al., 2002).

2. *Semi-analytical*

   In comparison, semi-analytical algorithms are composed of solutions to the radiative transfer equation (Lee et al., 2002). This method allows them to be implemented more broadly, to a wider spatial area, although is often more computationally-tasking to implement (Gohin et al., 2005; Nechad et al., 2010).

3. *Quasi-analytical*

   Quasi analytical algorithms are used to calculate the inherent optical properties (IOP) of the water column, absorption and backscattering (Lee et al., 2002; Le et al., 2009; Mitchell et al., 2014). This signal is then spectrally decomposed into contributions by different sources. Although they are computationally equivalent to empirical algorithms, they often rely upon empirical coefficients to relate IOPs to ocean parameters, such as Chlorophyll-a concentration (Mitchell et al., 2014)

There are a wide range of algorithms to process data from ocean colour satellites, including but not exclusive to the following:

- Absorption by yellow/gelbstoff substances (Werdell et al., 2013)
- Absorption due to phytoplankton, 443nm (Werdell et al., 2013)
- Aerosol optical thickness, 869nm (Levy et al., 2007)
- Calcite concentration (Balch et al., 2011)
- Chlorophyll-a concentration (Gohin et al., 2005; Hu et al., 2012)
- Diffuse attenuation coefficient (Werdell & Bailey, 2005)
- Fluorescence line height (Behrendfeld et al., 2009)
- Photosynthetically active radiation (PAR) (Harmel & Chami, 2016)
- Particulate organic carbon (POC) (Stramski et al., 2007, Evers-King et al., 2017))
- Particulate backscattering, 443nm (Werdell et al., 2013)
- Sea surface salinity (Font et al., 2010)
- Sea surface temperature (day and night)
- Suspended particulate matter (Gohin et al., 2005; 2011; Nechad et al., 2010)

Table 4 details the main recent/present satellites with ocean colour satellites and their respective wavebands.

Table 4: Recent/present ocean colour satellites (with ocean colour wavebands)

| Satellite | Start | End | Wavelengths, nm | Resolution, m | Swath width, km |
|---|---|---|---|---|---|
| SeaWiFS<br>(Sea-viewing Wide Field-of-View Sensor)<br>(Feldman, 2017) | 1997 | 2010 | 412, 443, 490, 510,<br>555, 670, 765, 865 | 1,100 | 2,801 |
| MODIS<br>(Moderate Resolution Imaging Spectroradiometer)<br>(Frazier, 2017) | Terra (1999)<br>Aqua (2002) | Still<br>active | 412, 443, 488, 531,<br>551, 667, 678, 748,<br>869 | 250,<br>500,<br>1,100 | 2,330 |
| MERIS<br>(Medium Resolution Imaging Spectroradiometer)<br>(Rast et al., 2010) | 2002 | 2012 | 412, 443, 490, 510,<br>560, 620, 665, 705,<br>754, 760, 775, 865,<br>890, 900 | 300,<br>1,200 | 1,150 |
| VIIRS<br>(Visible Infrared Imaging Radiometer Suite)<br>(Cao et al., 2013) | 2011 | Still<br>active | 411, 444, 486, 551,<br>672, 862 | 375,<br>700 | 3,060 |
| Sentinel-3<br>OLCI (Ocean and Land Colour Instrument) Sensor<br>(ESA, 2017) | 3A (2016)<br>3B (2017) | Still<br>active | 400, 412, 443, 510,<br>560, 620, 665, 674,<br>681, 709, 754, 765,<br>768, 779, 865 | 300,<br>1,200 | 1,270 |

## 6.3 MODIS

For this thesis, data from the MODIS (Moderate Resolution Imaging Spectroradiometer) instrument aboard the Aqua satellite was used, as such, processing methods described within the following chapters are centred around those relating to MODIS-Aqua.

The MODIS-Aqua instrument began service in 2002, following a multi-national NASA-led mission to improve the monitoring of ocean colour. The MODIS instrument has a resolution of $1km^2$, with a swath width of approximately 2,330km (NASA, 2016). The MODIS Aqua satellite orbits the Earth approximately once every 99 minutes, with its swath passing the same location either once or twice a day dependant upon the latitude and day length, with higher latitude regions generally being more frequently sampled. However, due to the difference between the satellites orbit and the Earth's rotation, the MODIS orbital track is completed every 16 days where the same location is once more directly under orbit, a sun-synchronous polar orbit (Figures 7 and 8). Data from MODIS-Aqua are supplied in the form of granules, which are 5 minute snapshots taken along the orbital track. Daily, the MODIS-Aqua instrument passes the North-West European shelf between 11am and 1pm UTC (Figure 7).

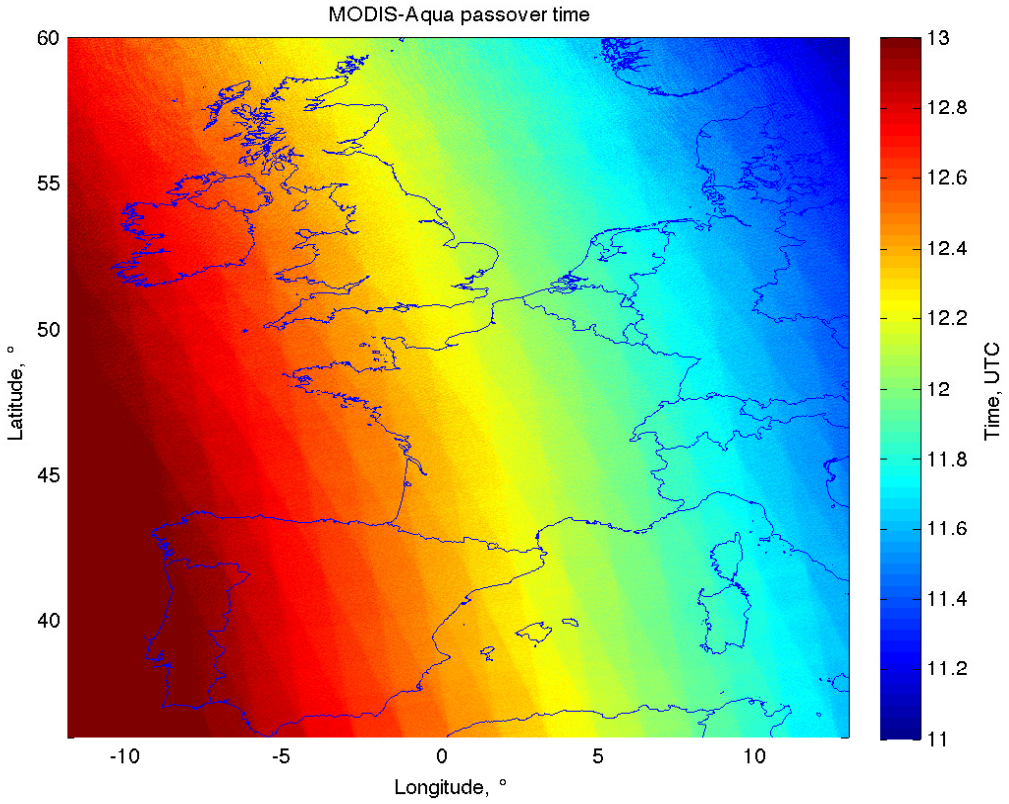


Figure 7: Passover time of the MODIS-Aqua satellite over the north-west European shelf, note that times are in decimal hours UTC (Universal Time, Coordinated).

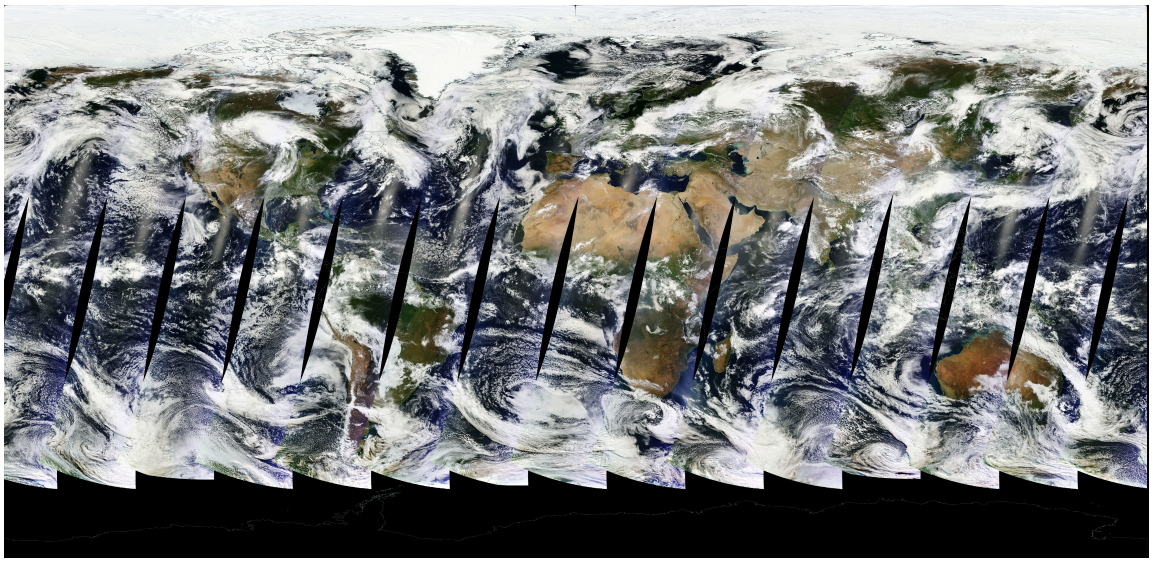

Figure 8: MODIS false colour swath image taken from EOSDIS WorldView for the 15th July 2014 (NASA EOSDIS, 2016).

The remote sensing of water properties can be described in three main steps:

1. Evaluate the effects of reflection at the air-sea interface including removing the effects of atmospheric attenuation and scattering which control the upwelling radiant flux. This provides the apparent optical properties (AOPs).

   *Reflectance ratio at a given wavelength, R(λ) (Morel, 1973)*

   $$R(\lambda) = E_u(\lambda)/E_d(\lambda) \tag{6.1}$$

   $\lambda$ is the respective wavelength of light, nm

   $E_u(\lambda)$ is the upwelling irradiance (the rate of radiant energy which is emitted upwards - away from the surface of the Earth) at a given wavelength, $\lambda$, $Wm^2nm^{-1}$

   $E_d(\lambda)$ is the downwelling irradiance (the rate of radiant energy which is emitted downwards - towards the surface of the Earth) at a given wavelength, $\lambda$, $Wm^2nm^{-1}$

2. Interpret the spectral composition of the reflectance to extract the waters inherent optical properties (IOPs: absorption, scattering and transmittance)

3. Define water properties using algorithms based upon calculated IOPs.

**Case 1 & Case 2 waters**

Morel and Prieur (1977) devised a simple scheme for describing the varying influence of the content of the oceans upon their optical properties. In this paper, water is classified into extreme cases (Table 5).

| Case | Dominated by |
|---|---|
| 1 | Phytoplankton |
| 2 | Inorganic particles |

Table 5: Two water cases defined by Morel & Prieur (1977)

Despite the evolution of algorithms for suspended materials, the case system defined by Morel and Prieur (1977) holds fast and is often used to define distinctions between algorithm formats. An example of this can be taken from the OC5 algorithm (Gohin et al., 2005; Gohin et al., 2011), which makes a distinction in the wavelengths used to calculate suspended load, with the green waveband used in case 1 waters and the red waveband used primarily in case 2 waters.

## 6.4 Marine light

Understanding the behaviour of light with different substances is crucial to our knowledge of the natural environment. In the ocean, absorption and scattering by suspended particles can greatly affect the level of light which eventually reaches the seabed.

The term light is usually used to describe radiation within the electromagnetic spectrum in the visible band (wavelengths between 400 and 700$\mu m$), which is both visible to the human eye and is the range within which plants may photosynthesise (Kirk, 2011). The propagation of light can be described in terms of quanta or photons, representing units of electromagnetic energy (Kirk, 2011). When reacting with a material, the propagating photon propagating can either be absorbed or scattered (Figure 9).

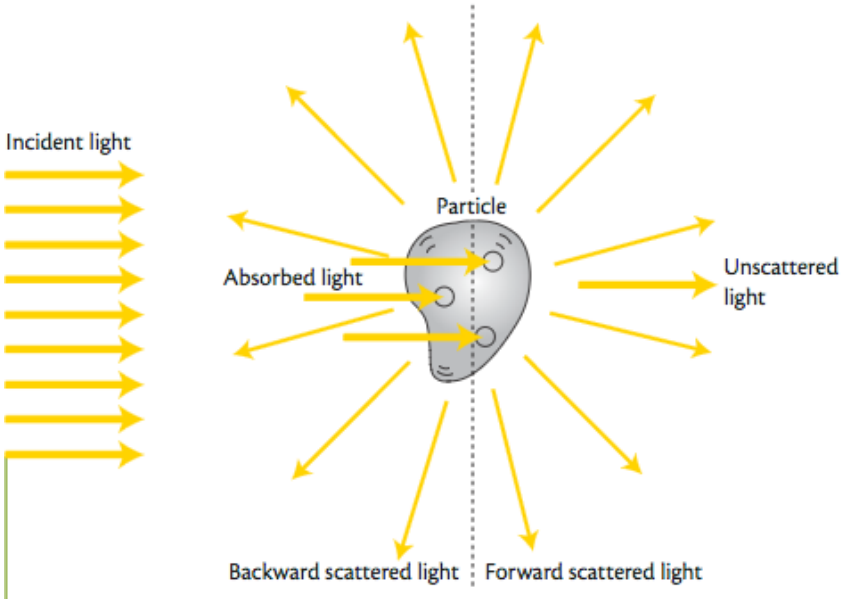


Figure 9: Diagram representing the processes of absorption and scattering of light by a particle in the water column (Boss et al., 2004b).

## 6.5 The optical properties of water

The optical properties of both pure water and seawater are well documented, with the effect of salt having a minimal impact upon the observed optical properties (Morel, 1974; Smith

and Baker, 1981; Pope and Fry, 1997; Bowers, 2013).

**Absorption, a**

Absorption occurs when potential energy from the photon is lost to a substance (Jonasz & Fournier, 2007). The total absorption in the water column is defined by absorption by water molecules, absorption by chlorophyll, absorption by mineral suspended solids and absorption by coloured dissolved organic matter (CDOM):

*Absorption of marine light, a*

$$a = a_w + a_{Chl} + a_p + a_{CDOM} \tag{6.2}$$

$a_w$ is the absorption by water, $m^{-1}$
$a_{Chl}$ is the absorption by Chlorophyll-a, $m^{-1}$
$a_p$ is the absorption by non-algal suspended solids, $m^{-1}$
$a_{CDOM}$ is the absorption by coloured dissolved organic matter (CDOM), $m^{-1}$

Different substances absorb light at different efficiencies. A way of measuring these efficiencies is the mass-specific absorption coefficient, $a_p*(= a_p/SPM)$, the absorption observed per unit of mass of suspended sediments (SPM).

**Scattering, b**

When light is scattered, the photon is absorbed and instantaneously re-emitted without losing energy, referred to as elastic scattering. The other, less common form of light scattering is Raman scattering, where the re-emitted photon has a different energy to the absorbed photon (Jonasz & Fournier, 2007). Scattering of light occurs through three main process: reflection, refraction and diffraction (Kirk, 2011; Bowers, 2013). To measure the efficiency of a substance to scatter light, the mass-specific scattering coefficient is often used, $b_p * (=$

$b_p/SPM, where b_p = b - b_w$).

*Scattering of marine light, b (Kirk, 2011)*

$$b = 2\pi \int_0^{\pi} \beta(\theta) \sin\theta d\theta \tag{6.3}$$

Where $\beta$ is the volume scattering function and $\theta$ is the angle of scatterance.
$b_w$ is scattering by pure water, $m^{-1}$.

Light which is scattered in water can be split into forward scattering ($b_f$, $m^{-1}$), scattering at an angle less than 90° and backward scattering (or backscattering, $b_b$, $m^{-1}$), scattering at an angle greater than 90°.

*Scattering of marine light, b*

$$b = b_b + b_f \tag{6.4}$$

By assuming that scattered light is azimuthally symmetric, $b_b$ and $b_f$ can be represented as the following function of the volume scattering function (Stramski et al., 2004).

*Backscattering, $b_b$ (Kirk, 2011)*

$$b_b = 2\pi \int_{\pi/2}^{\pi} \beta(\theta) \sin\theta d\theta \tag{6.5}$$

*Forward scattering, $b_f$ (Kirk, 2011)*

$$b_f = 2\pi \int_0^{\pi/2} \beta(\theta) \sin\theta d\theta \tag{6.6}$$

## 6.6 Backscattering, $b_b$

The backscattering coefficient ($b_b$), is the fraction of incident light scattered backward per unit distance travelled by the photons (Boss et al., 2004b). The use of backscattering in remote

sensing is prevalent due to the relationship between remotely-sensed reflectance ($R_{RS}(\lambda)$) and $b_b$. Light scattering has been shown to be the "first order determinant of reflectance" (Babin et al., 2003):

*Remotely-sensed reflectance, $R_{RS}$ (Gohin et al., 2005)*

$$R_{RS}(\lambda) = C\frac{b_b(\lambda)}{a(\lambda) + b_b(\lambda)} \tag{6.7}$$

*Backscattering of marine light ($b_b$) as a function of remotely-sensed reflectance ($R_{RS}$) (Gohin et al., 2005)*

$$b_b(\lambda) = \frac{R_{RS}(\lambda)a(\lambda)}{C - R_{RS}(\lambda)} \tag{6.8}$$

Where C is a function of the solar zenith angle, the angle of observation and the surface roughness (Gordon et al., 1975; Morel et al., 1995; Sydor & Arnone, 2002; Gohin et al., 2005), $sr^{-1}$

The volume scattering function ($\beta$, $m^{-1}sr^{-1}$) is the "radiant intensity in a given direction from a volume element (Kirk, 2011). It is possible to calculate $b_b$ using the volume scattering function measured at an angle of $\approx 120°$ (Kirk, 2011):

*Backscattering ($b_b$) as a function of the volume scattering function ($\beta$) (Kirk, 2011)*

$$b_b \approx 7\beta(120°) \tag{6.9}$$

The relationship between the backscattering coefficient and the concentration of suspended sediments is known as the mass-specific backscattering coefficient ($b_{b_p}* = b_{b_p}/SPM$).

*Backscattering by suspended particles, $b_{b_p}$*

$$b_{b_p} = b_b - b_{b_w} \tag{6.10}$$

In satellite remote sensing applications, $b_{b_p}*$ is generally assumed to be a constant (Gohin et

al., 2005), implying a linear relationship between the backscattering coefficient ($b_{b_p}$) and the concentration of suspended sediments (TSS). However, field measurements have shown this to be far from true. Table 2 outlines a series of values for $b_{b_p}*$ in the red waveband at 665nm calculated in recent publications. The lowest value for $b_{b_p}*$ was 0.0003 $m^{-2}g^{-1}$ by Bowers et al. (2014), with the largest value being 0.0137 $m^{-2}g^{-1}$ by Reynolds et al. (2016). Gohin et al. (2005) described a remote sensing algorithm for suspended sediment concentration where the assumed $b_{b_p}*$ is $0.0090m^{-2}g^{-1}$, potentially leading to an overestimation of a factor of approximately 30 in the minimum of Bowers et al. (2014) or an underestimation factor of approximately 0.66 in the maximum of Reynolds et al. (2016).

Table 6: Observed values of the mass-specific backscattering ($b_{b_p}*$) at 665nm from recent literature

| Journal | $b_{b_p}*^{665nm}, m^2g^{-1}$ |
|---|---|
| Maritorena et al., 2002 | 0.0041 |
| Carder et al., 2003 | 0.0086 |
| Babin et al., 2003 | 0.0058 |
| Lee et al., 2005 | 0.0096 |
| Gohin et al., 2005 | 0.0090 (OC5) |
| Bowers & Binding, 2006 | 0.0058 |
| Nechad et al., 2010 | 0.0068 |
| Neukermans et al., 2012 | 0.0050 (organic) & 0.0120 (mineral) |
| Bowers et al., 2014 | 0.0003 (organic) & 0.0058 (mineral) |
| Reynolds et al., 2016 | 0.0072 (organic), 0.0091 (mixed) & 0.0137 (mineral) |

**Backscattering by marine particles**

In shelf seas, which make up the majority of the European coastal region, most light is backscattered by a mixture of organic and mineral particles (Stramski et al., 2004; Bowers et al., 2014). As such, backscattering observed within the water column can be correlated with particulate properties; including particle abundance, size and particle composition (Boss et al., 2003). In practical terms, the relationship between reflectance at the surface and the backscattering coefficient is used in the form of remote sensing algorithms to describe properties not exclusive to the concentration of suspended sediments (Binding et al., 2005; Gohin et al., 2005; Doxaran et al., 2009).

Mineral particles are found to have a higher refractive index and therefore backscatter light more efficiently than organic particles (Twardowski et al., 2001; Stramski et al., 2004; Neukermans et al., 2012; Bowers et al., 2014). Twardowski et al. (2001) used Mie Theory to model the refractive index from in-situ measurements of scattering, attenuation and particle size in the Gulf of California. Twardowski et al. (2001) found low refractive indices in highly organic waters with high concentrations of Chlorophyll-a, with higher refractive indices in more mineral sediments. In waters which contain a mixture of organic and mineral particles, aggregates known as flocs are more commonly observed than single particles. Flocs have complex fractal structures which effect their optical properties (Flory et al., 2004). Variability in the fractal form in which aggregates are present in the water column exacerbates the existing variability due to refractive indices observed as a result of the organic content of the particles, thus impacting upon the way in which backscattering by flocs is observed. Boss et al. (2003) described the increase in mass-specific scattering ($b_p^*$) with increased refractive index. In highly mineral waters, the high refractive index increases the efficiency of particles to backscatter light, additionally particle collision is less likely to result in successful flocculation and thus particles generally have less of a fractal structure.

When considering single, spherical particles, Mie theory can be reasonably implemented. However, in the case of flocs, they are neither single nor spherical, as such treating them like this may be problematic. Bowers et al. (2014) described how the optical properties of a floc depend upon the floc size, the fractal form, floc density and the refractive index. Bowers et al. (2014) approximated these parameters in the form of the effective backscattering efficiency, ($Q_{bb} = b_{b_p}/CSA$), the observed backscattering coefficient as a proportion of the cross-sectional area of particles (CSA) per $m^3$, inferred by laser diffraction (Agrawal & Pottsmith, 2000). Flory et al. (2004) found that $Q_{bb}$ decreased after a phytoplankton bloom, when the water contained a high proportion of organic detritus. Similarly, Neukermans et al (2014) found an increase in $Q_{bb}$ relative to the presence of increasingly mineral-dominated particles, with size and density not found to have a significant effect upon $Q_{bb}$.

Flocculation alters the size distribution and abundance of particles which scatter light, leading

to a shift toward larger sizes and a reduction in the relative abundance (Alldredge & Jackson, 1995). Originally, there was no distinct understanding of the effective that flocculation had upon the optical properties of marine particles (Costello et al., 1995; Bunt et al., 1999; Hatcher et al., 2001). Despite this, it was identified that the fractal shape of flocs impacted upon both the reflection and refraction of light in the water column (Hatcher et al., 2001). Organic content has been understood to relate to floc formation and characteristics (Hatcher et al., 2001), effecting the availability of particles and the resistance of flocs to turbulent energy dissipation (Dyer & Manning, 1999). Additionally, enhanced absorption by organic particles was expected to reduce the relative backscattering observed by highly-organic flocculated particles (Meyer, 1979). Bowers and Binding (2006) described the potential indirect influence of turbulent kinetic energy (TKE) upon the mass-specific backscattering coefficient ($b^*_{b_p}$), through the influence upon flocculation. In high energy turbulent environments, large flocculated particles are likely to be broken up in smaller particles, increasing the cross-sectional surface area available to backscatter light and thus the mass-specific backscattering of the suspended particles (Bowers & Binding, 2006).

Neukermans et al. (2012) looked at the variability in backscattering of marine particles with respect to particle size, density and composition. In Neukermans et al. (2012), water samples were taken using Niskin bottles from just below the surface. The concentration of suspended solids within the samples was then determined gravimetrically as follows. Samples were filtered through pre-weighed $0.7\mu m$ glass-fibre filters (GFFs), then the filters were dried for at least 24 hours at $50°c$. Comparing the new weight to that of the pre-weighed filter it was then possible to determine the concentration of total suspended solids (TSS) within the sample. The dried filters were ashed at $450°c$ for 1 hour in order to remove organic material present and weighed once more to provide the concentration of mineral suspended solids (MSS). Optical measurements of particle size distribution were taken using the LISST particle sizer and also devices from the WetLabs ECO-BB9 to provide direct observations of backscattering at 650nm. This paper reported that the mass-specific backscattering coefficient, $b_{b_p}*$ at 650nm was well correlated with particle composition, with predominately mineral particles having coefficients up to three times that of particles with a higher organic content (Figure 10).

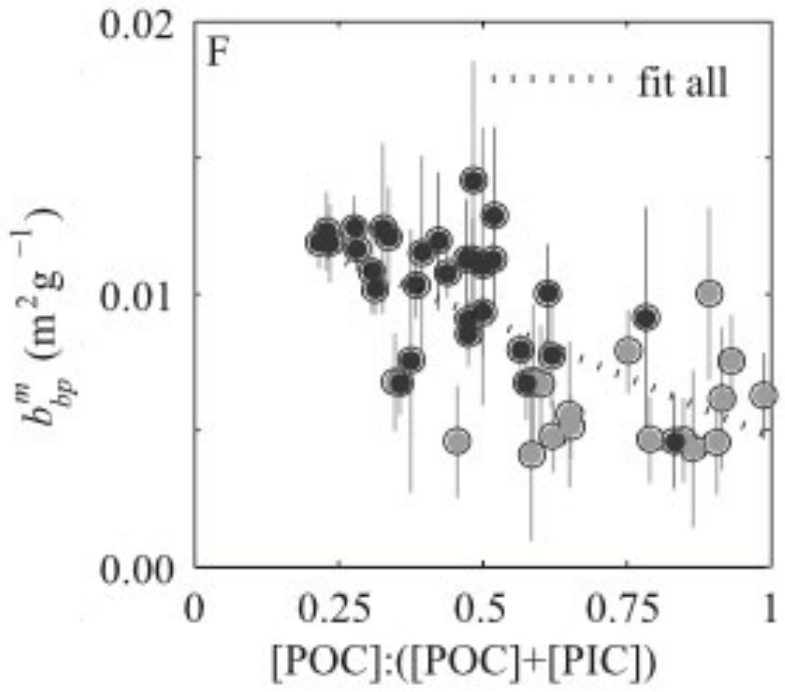


Figure 10: The influence of the organic fraction of particles upon the mass-specific backscattering coefficient at 650nm (Neukermans et al., 2012). POC and PIC refer to the particle organic and inorganic contents of the suspended particles. The values of the x-axis can be considered to be the inverse of the mineral content used by Bowers et al. (2014), with high values representing highly organic particles and lower values representing highly mineral particles. Grey points are defined as case 1 and black points are defined as case 2.

Although the presumption of Neukermans et al. (2012) was that $b_{b_p}*$ was directly influenced by particle size, only a weak relationship was found in this case, with this expected to be due to the influence of varying particle density on the efficiency of particles to backscatter light.

Bowers et al. (2014) followed on from this research by looking at the effect of particulate organic content upon particulate backscattering. Water samples were taken using a similar process to that of Neukermans et al. (2012), the main difference being that the GFFs were ashed at $500°c$ for 3 hours in order to remove organic material for the MSS measurement. In addition to using the LISST particle sizer, Bowers et al. (2014) used radiometer measurements alongside spectrophotometer measurements of absorption to infer the backscattering coefficient, in lack of a device which directly measured backscatter. Bowers et al. (2014) found that particles of high mineral content backscattered more effectively than those of higher or-

ganic content as observed by Neukermans et al. (2012). Bowers et al. (2014) showed that 62% of the variability in backscattering efficiency could be explained by the mineral to total suspended solids ratio (MSS/TSS) (Figure 11).

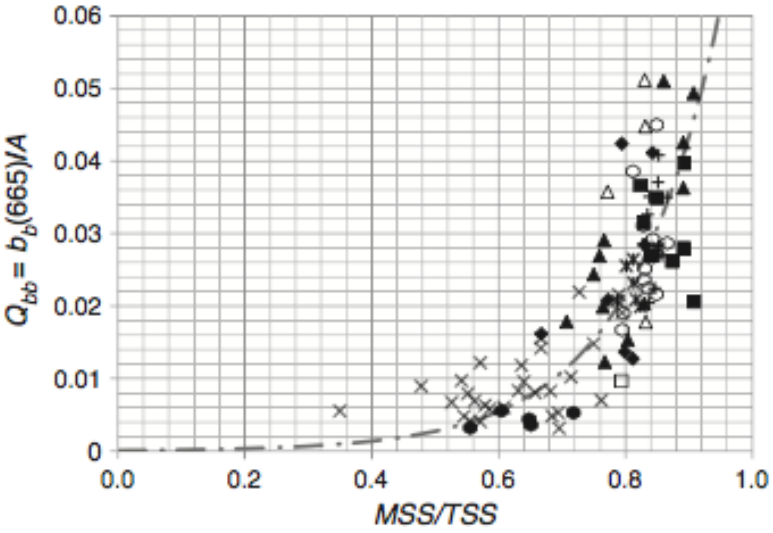


Figure 11: The influence of the mineral content of particles (MSS/TSS) upon the backscattering efficiency ($Q_{b_{bp}}$) at 665nm (Bowers et al., 2014). Curve displayed is $Q_{b_{bp}} = 0.000087exp(6.9MSS/TSS)$. A represents the cross-sectional area (CSA).

## 6.7 Mie Theory

Mie theory describes scattering of light by small, spherical particles, using Maxwell's electromagnetic theory (Mie, 1908; Hergert & Wreidt, 2012). The original intention of this method being to describe the change in colour of gold colloids with spherical diameter (Mie, 1908; Hergert & Wreidt, 2012). The first scattering diagrams were subsequently published in 1925 (Gans, 1925; Blumer, 1925). These first iterations of the Mie theory, discounted the effects of absorption and the presence of aggregated non-spherical particles.

The flaw of this many particulates in the water column have a more fractal than spherical structure. Aggregates multiply the light scattered by the composing particles (Okada, 2010). Okada (2010) reviewed methods for the simulation of light scattering of aggregates in an absorbing medium. Despite advances, Okada (2010) described how the computational complexity of non-spherical Mie theory simulations meant they were still unable to be implemented with accuracy on observed particles.

## 6.8 Ocean radiative transfer modelling

Radiative transfer theory describes the propagation of energy (light) in the ocean (Mobley, 2001; Mobley & Sundman, 2008). As light propagates through the ocean it is scattered and absorbed. Radiative transfer models describe the distribution of light as it propagates through a scattering and absorbing medium. One of the most commonly used radiative transfer models is Hydrolight. Hydrolight is a one-dimensional radiative transfer modelling suite, computing "radiant distributions and derived inherent optical properties for natural water bodies... as a function of depth, direction and wavelength" (Sequoia, 2017), by inputting the absorption and scattering parameters.

# 7 Statistical modelling of suspended sediment concentration

Statistical modelling is a valuable technique allowing not only the analysis of important factors controlling the variability of a parameter but also has the potential to be used as a method of prediction (Rivier et al., 2012; Saulquin et al., 2014; Gohin et al., 2015, Saulquin et al., 2015). When predicting tides, harmonic analysis is used to identify repeating cycles in tidal variability. Statistical models aim to fit this variability to explanatory forcings, not only to identify the dominant forcing in a particular area but also to enable prediction.

There have been two main statistical models of the suspended sediment concentration of note. Rivier et al. (2012) produced a statistical model of the concentration of suspended sediments using tides, waves and Chlorophyll-a in the English Channel (La Manche), whereas Saulquin et al. (2014) described a time-varying regression model which additionally includes river discharge in the region of the Gironde Estuary.

### Rivier et al., 2012

Rivier et al. (2012) described statistical models based upon the influence of tides (in the form of a tidal coefficient), waves and Chlorophyll-a upon a log transformation of the concentration of suspended matter (Table 7). The study used the large dataset from MODIS-Aqua (Moderate Resolution Imaging Spectroradiometer) and MERIS (Medium Resolution Imaging Spectroradiometer) applied with an Ifremer semi-analytical OC5 algorithm for a 3-year period within the English Channel, separating England and France. In order to boost the effectiveness of the model over the subject region, climatology values of SPM (averages over several years, in this case 2003 to 2009) for each day of the year were used as a baseline variability from which the secondary driver of variability was represented by the model parameters.

*Model 1 - Tides*

The first model (Fig. 12 and Fig. 13, Table 7) contained only the suspended material concentration climatology and the relative variability of the tidal range as described by the SHOM daily tidal coefficient divided by the maximum tidal coefficient. Values of $R^2$ from

regression with the remotely-sensed observations highlighted regions where the tide was a strong driver of the suspended sediment variability, in this case highlighting the central and eastern English Channel substantially. The tide-based model achieved $R^2$ values of between 0.15 and 0.25 in the central Irish Sea and central English Channel, with the $R^2$ reaching 0.4 in the Bristol Channel.

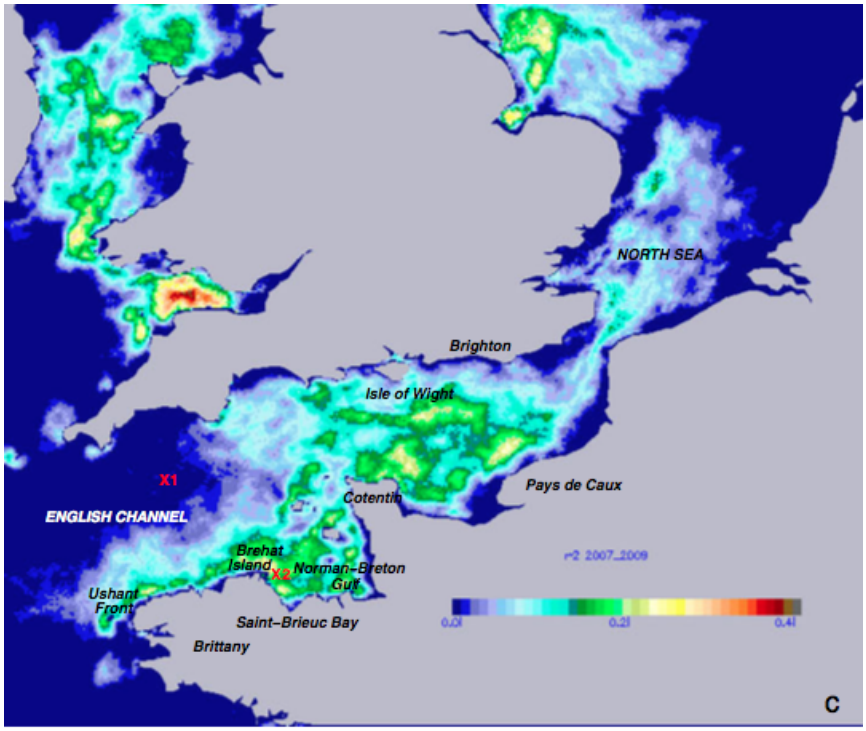


Figure 12: $R^2$ coefficient of determination for Model 1, implemented by Rivier et al. (2012). Location 1 and 2 refer to time series a and b in figure 13.

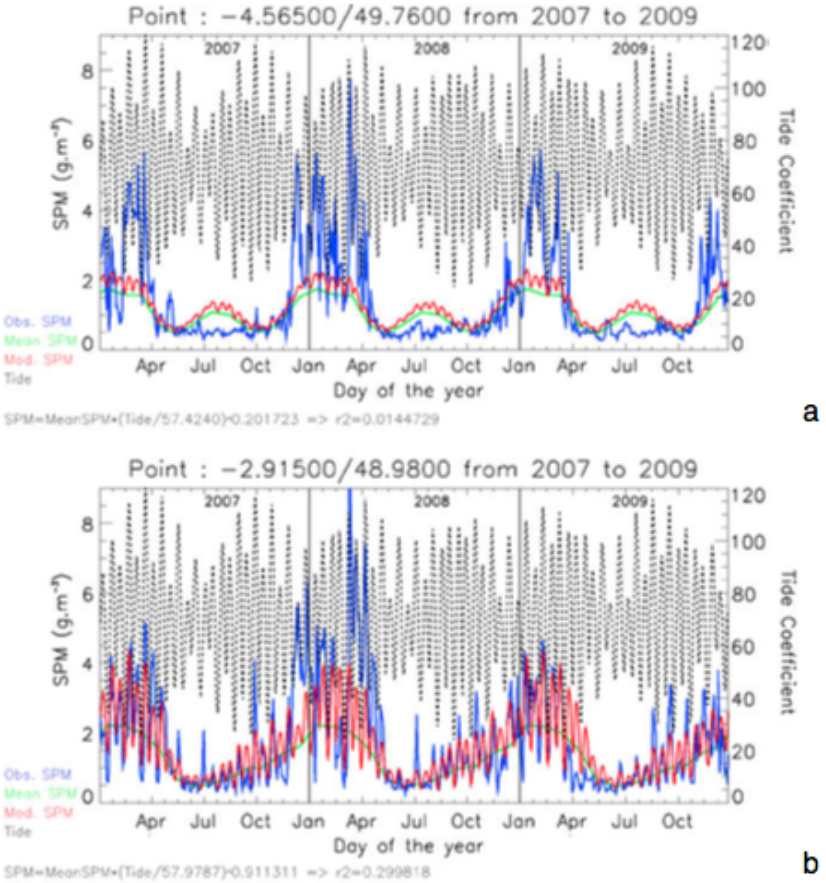


Figure 13: Time series of predicted and observed SPM concentration for model 1 from Rivier et al., 2012. Locations a and b refer to locations 1 and 2 in figure 12.

*Model 2 - Tides and Waves*

The second model (Fig. 14 and Fig. 15, Table 7) added the effect of waves as a multiplicative forcing. The performance of the model was most improved in the Western English Channel with the addition of waves, with an $R^2$ over 0.4, however due to the multiplicative nature, the model experienced reduced performance in the central English Channel, where waves were not as dominant as implied by the model format.

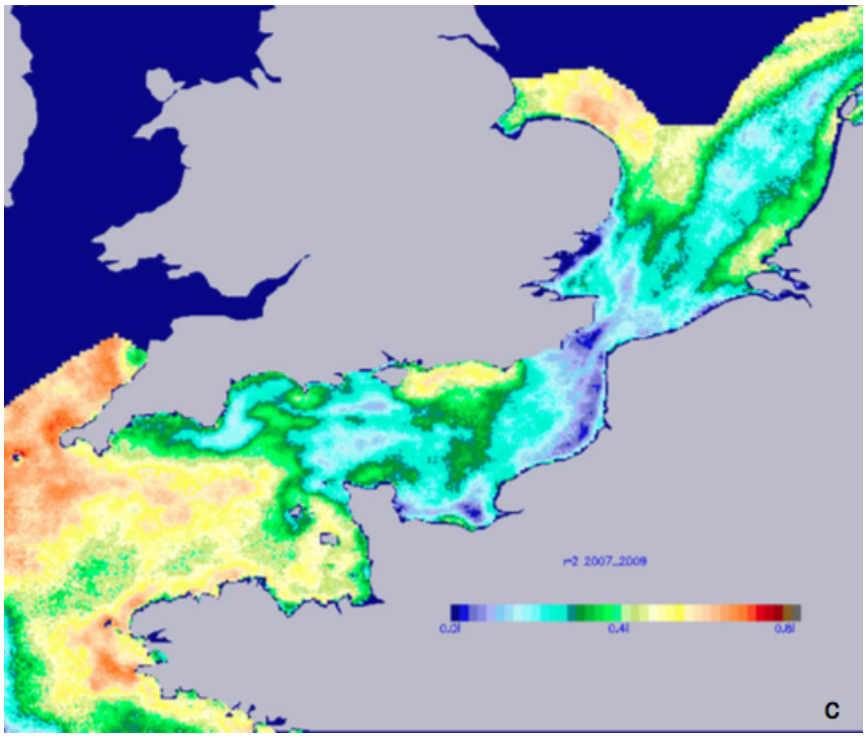


Figure 14: $R^2$ coefficient of determination for Model 2, implemented by Rivier et al. (2012). Location 1 and 2 refer to time series a and b in figure 15 respectively.

*Model 3 - Tides, Waves and Chlorophyll-a*

The third model (Fig. 16 and Fig. 17, Table 7) integrated the effect of Chlorophyll-a as a multiplicative factor. The intention of including Chlorophyll-a within the algorithm was to take account of flocculation processes, which are increased within organic-rich waters, represented in this case by high concentrations of Chlorophyll-a. The assumption is that the concentration of suspended particulate matter would be adversely affected by increases in the concentration of Chlorophyll-a. This model improved the representation of variability of the suspended sediment concentration signal further in the Western English Channel, with an $R^2$ of up to 0.7 in some locations surrounding the Scilly Isles and off the Western Brittany coast.

Rivier et al. (2012) used the SHOM tidal coefficient (SHOM, 2000) based upon the tidal variation in Brest, in place of localised representations of the tidal activity. Although this may not have a large influence over a small geographical area, it has the potential to limit the response of the model to tidal activity when moving between tidal regimes, where the local

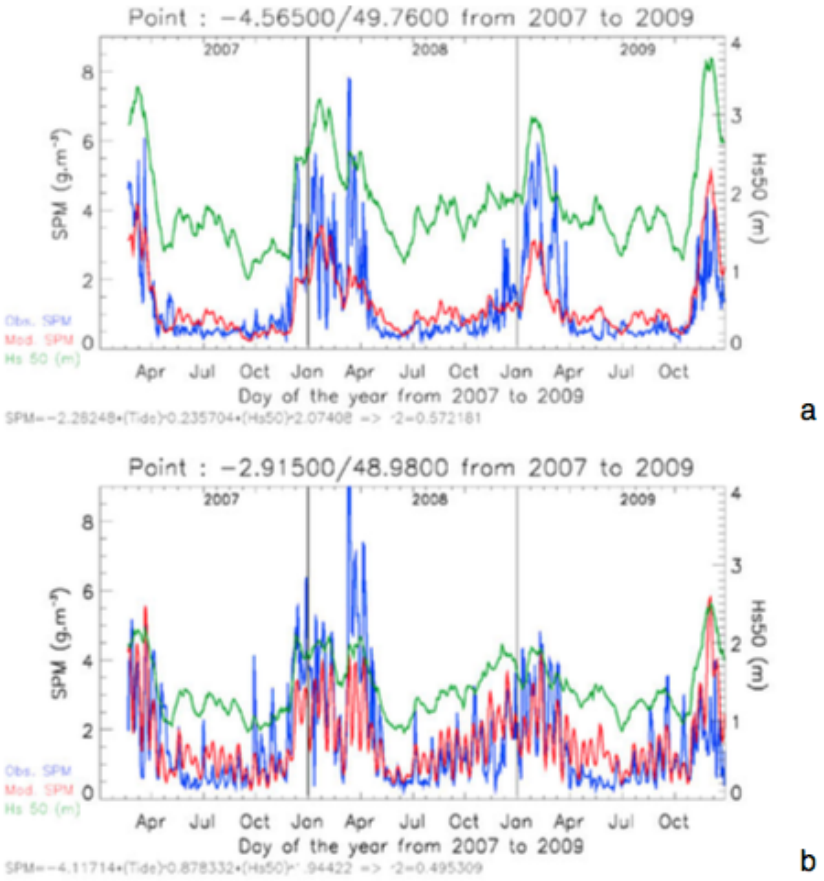


Figure 15: Time series of predicted and observed SPM concentration for model 2 from Rivier et al., 2012. Locations a and b refer to locations 1 and 2 in figure 14 respectively.

tidal dynamics may differ from that observed in Brest.

A flaw of the method used in Rivier et al. (2012) is that it assumes that all forcings have a multiplicative relationship in terms of representing the suspended sediment concentration. The issue of this is that if one forcing is low or high, this effect will increase the impact of the other forcing. The rationale for using a multiplicative form was to stabilise the high values resulting from the log transformation method utilised. With the addition of Chlorophyll-a, for the third model, the multiplicative form is less of an issue as the effect of flocculation can be seen as a modulating factor of the hydrodynamic resuspension of sediments represented by tide and wave activity. The limitation however of using Chlorophyll-a to represent flocculation is that although it may be a good estimate of biological activity and thus the

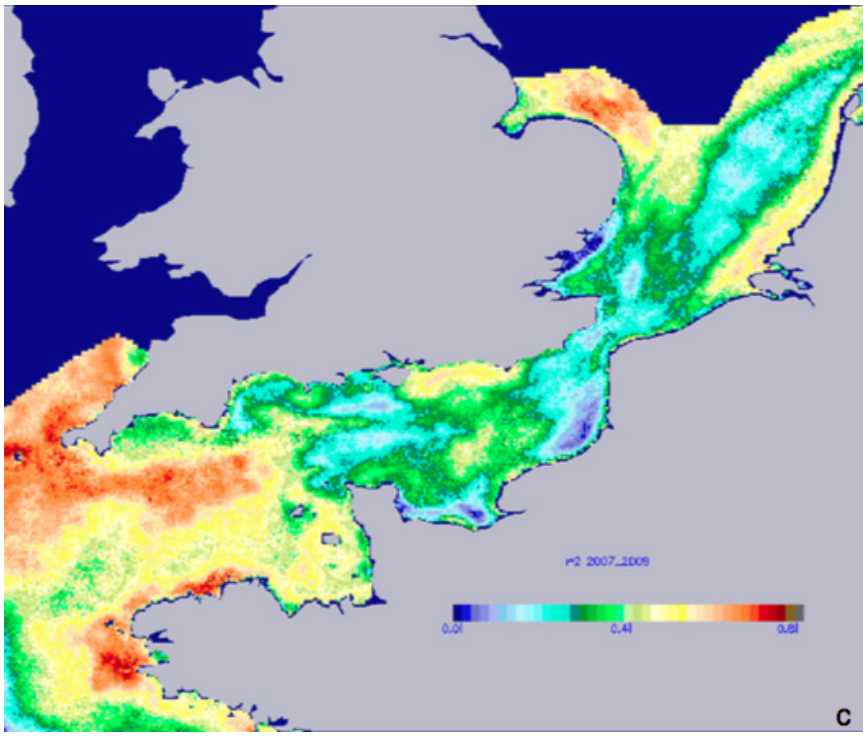


Figure 16: $R^2$ coefficient of determination for Model 3, implemented by Rivier et al. (2012). Location 1 and 2 refer to time series a and b in figure 17 respectively.

EPS (extracellular polymeric substances), which may make flocs more resistant to turbulent activity and thus grow larger, it does not take account of the influence of turbulent activity upon flocculated particles in the winter. Turbulent shearing has been shown to limit the size of flocs within the water column (Bowers et al., 2007). As flocculated particle assemblages break into smaller constituent particles, they take longer to settle, a phenomena not directly taken account of through the application of Chlorophyll-a. The first model as described in Rivier et al. (2012) relies very much upon the climatology data, making it limited in its use for prediction, with much of the seasonal variability imposed rather than being included by the representation of wind or Chlorophyll-a.

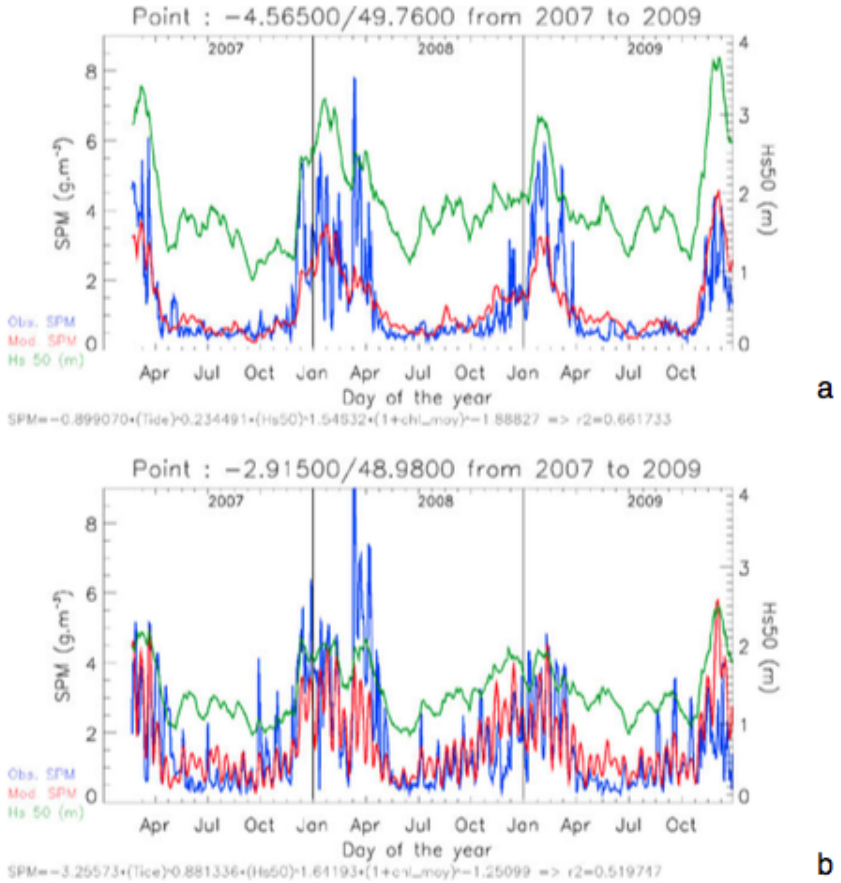


Figure 17: Time series of predicted and observed SPM concentration for model 3 from Rivier et al., 2012. Locations a and b refer to locations 1 and 2 in figure 16 respectively.

| Model | Formulation, SPM(day,lon,lat) = |
|---|---|
| 1 | $SPM_{clim}(day,lon,lat)(\frac{Tide_c(day)}{max(Tide_c)})^{\alpha(lon,lat)}$ |
| 2 | $a_0(x,y)[Tide(day)]^{\alpha(lon,lat)}[Waves(day,lon,lat)]^{\beta(lon,lat)}$ |
| 3 | $a_0(x,y)[Tide(day)]^{\alpha(lon,lat)}[Waves(day,lon,lat)]^{\beta(lon,lat)}[\frac{1}{1+Chl(day,lon,lat)}]^{\theta(lon,lat)}$ |

Table 7: The three model forms described in Rivier et al. (2012). Suspended particulate matter (SPM) observations are from MODIS Aqua using the remote sensing algorithm defined by Gohin et al. (2005). $SPM_{clim}$ represents the climatology of SPM used as a baseline. $Tide_c$ represents the SHOM (Service Hydrographique et *Océanographique* de la Marine) tidal coefficient. Waves represents the wave speed, estimated using the WaveWatch3 numerical model. Chl represents the remotely-sensed Chlorophyll-a concentration.

### Saulquin et al., 2015

Similar to the Rivier et al. (2012) statistical models, the intention of Saulquin et al. (2015) was to represent the time-varying geophysical processes which influence remotely-sensed suspended matter concentration. The analysis of Saulquin et al. (2015) concentrated upon the Gironde Estuary mouth, using wind and waves, tides and river discharge as explanatory forcings. Unlike the Rivier et al. (2012) approach, instead of using a modulating factor, the model was regressed seasonally, with the effects of flocculation through varying particle size referred to as a potential cause of the benefit of seasonal regression.

Saulquin et al. (2015) used the Markov switching multifractal (MSM) method (Calvet & Fisher, 2001; Calvet & Fisher, 2004) which was used to model volatility between regime changes. The necessary assumption of an MSM model is that the forecaster knows the primary forcing of the variability but does not know the direct correlation and thus represents the relationship between input and output in the form of a density-based prediction (Calvet & Fisher, 2001). Saulquin et al. (2015) used both homogenous (transition probability independent of time) and non-homogenous (time-varying transition probability) Markov forms, with and without autoregression (delayed or staggered impact of a forcing). Saulquin et al. (2015) showed that the inclusion of the observation from the previous day in the autoregressive model was able to improve the explanation of variance (from 80% to 93% in the non-homogenous models and from 73% to 93% in the homogenous models, Figure 18).

| dt (days) | EVAR for the 2010 validation dataset | | | |
|---|---|---|---|---|
| | HMM | HMM-AR | NHHMM | NHHMM-AR |
| 1 | 73 | 93 | 80 | 93 |
| 5 | 63 | 80 | 77 | 82 |
| 15 | 40 | 70 | 74 | 75 |

Figure 18: The explained variance of the four models described by Saulquin et al. (2015). HMM - the homogeneous non-autoregressive Markov model. HMM-AR - the homogeneous autoregressive Markov model. NHHMM - the non-homogeneous non-autoregressive Markov model. NHHMM-AR - the non-homogeneous autoregressive Markov model. dt represents the considered number of days prior to the prediction date which were used in the prediction.

Saulquin et al. (2015) noted the limitation of this form of prediction when without data for a sustained period. The best of the four models (non-homogenous and autoregressive), showed that moving from the use of data from the previous day to data from 15 days prior to the prediction caused a drop in the explained variance on the concentration of suspended matter from 73% to 40% (Figure 15).

# Part II

# Backscattering of light by marine particles

## 8 Introduction

Remote-sensing algorithms are used to estimate in-situ properties of the water column. This involves relating apparent optical properties (i.e. remote-sensing reflectance) to inherent optical properties (i.e. scattering). In-situ measurements of suspended particulate matter (SPM) show a strong correlation between the backscattering of light and SPM concentration (Gohin et al., 2005). The rate of increase in backscattering relative to SPM concentration is represented by the mass-specific backscattering coefficient, $b^*_{b_p}$. By assuming that the $b^*_{b_p}$ is constant allows us to use the relationship between backscattering and remote sensing reflectance, to directly infer the SPM concentration. However, this relationship has been shown to change under different regimes of varying particle properties as observed in field observations (Neukermans et al., 2012; Bowers et al., 2015) and is therefore not constant as often assumed.

This chapter will aim to answer the following question:
*Can observations of the influence of particle composition upon backscattering be integrated into future remote-sensing algorithms of suspended sediment concentration?*

In order to this, the following objectives will be carried out:

- Carry out field observations of suspended particle properties and the optical properties of the water column at three locations (two in France and one in the U.K.).
- Analyse the influence of particle properties upon the particulate backscattering efficiency ($Q_{b_{b_p}}$) and mass-specific backscattering coefficient ($b^*_{b_p}$).
- Study the potential for improved representation of mass-specific backscattering in future remote-sensing algorithms for the suspended sediment concentration.

# 9 Methods

## 9.1 Fieldwork locations

Three study sites are included in this chapter; the Menai Strait in northwest Wales, the Gironde Estuary on the west coast of France and the Seine Estuary on the northern coast of France near to the centre of the English Channel (Figure 19). The three locations all have their individual merits, with the Gironde and Seine Estuary datasets having the potential to identify a range of different turbidities. In addition, the advantage of the site in the Menai Strait is that due its local proximity it is possible to make comparable measurements on both a spring and neap tide.

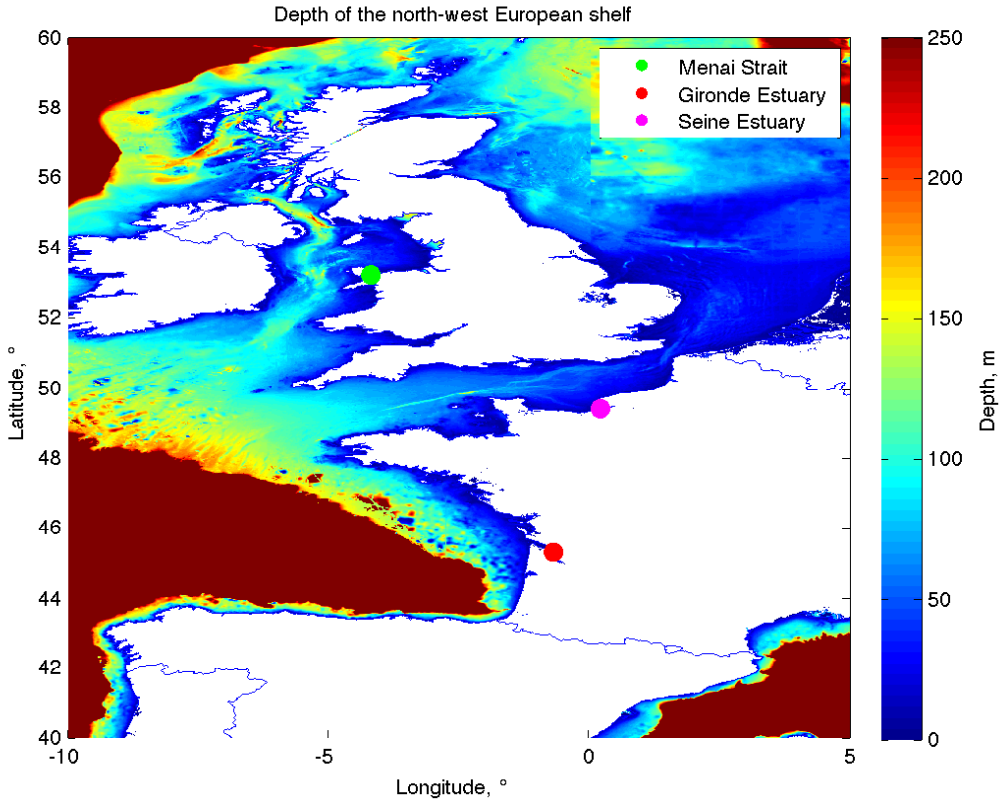


Figure 19: Fieldwork locations on a map of the bathymetry of north-west Europe.

**Menai Strait, Northwest Wales**

The Menai Strait sits on the Northwest coast of Wales, between the Isle of Anglesey and the mainland formed during the post-glacial period (Harvey, 1968) (Figure 20). The strait is orientated southwest to northwest and has a length of approximately 20 kilometres and a mean width of 800m down to 300m either end of the Swellies (Harvey, 1968). The depth of the strait varies between 22m in the Swellies to 1-2m at the shallowest points, with a mean depth of approximately 13m (Harvey, 1968; Bowers, 2003). The mean spring and neap tidal ranges at Menai Bridge have been observed to be 6.6m and 3.4m on a spring and neap tide respectively (Harvey, 1968). The flow has been shown to be dominate southwesterly along the strait, with a mean maximum tidal flow of $1.5ms^{-1}$ with a mean maximum tidal flow of $0.8ms^{-1}$ northeasterly along the strait (Harvey, 1968).

Fieldwork within the Menai Strait took the form of three days, two on a spring and neap tide in October 2013 and the third in August 2014. Measurements were taken from the Bangor University small research vessel, RV Macoma.

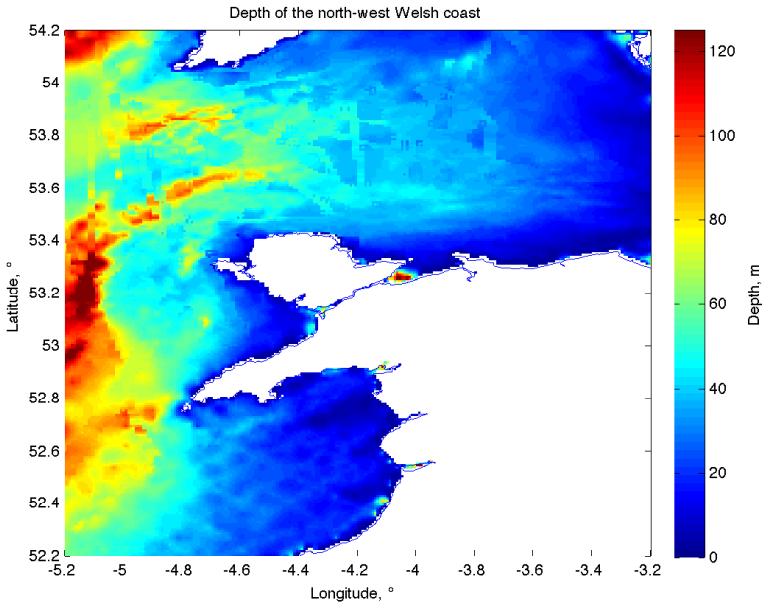


(a) Bathymetry of the North Wales region.

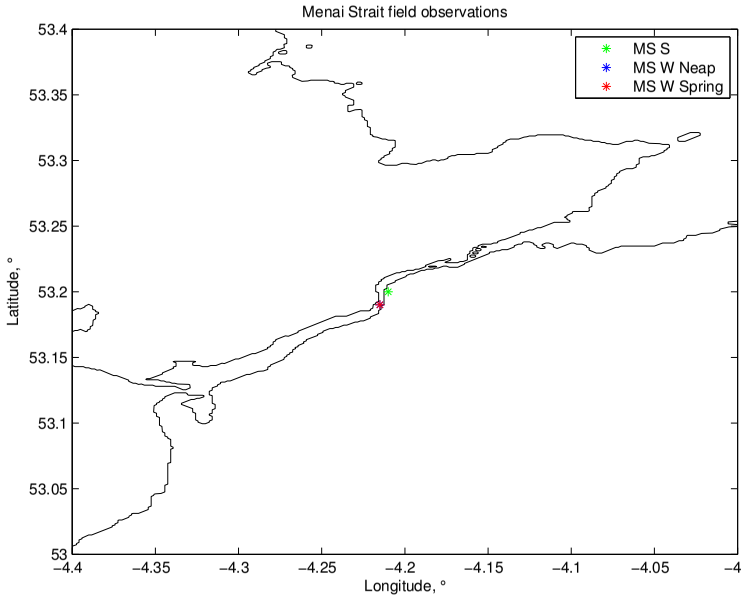


(b) Location of Menai Strait stations.

Figure 20: Map of the region surrounding the Menai Strait fieldwork location.

**Gironde Estuary, Bay of Biscay (Gulf de Gascoigne), Western France**

The Gironde Estuary sits on the western coast of France bordering the Atlantic Ocean (Figure 21). The Gironde Estuary is funnel-shaped, with a length of 180km and a surface area of $635km^2$ up to the junction with the Garonne and Dordogne rivers (Jalón-Rojas et al., 2015). The mean spring and neap tidal ranges at the mouth have been observed to be 5m and 2.5m on a spring and neap tide respectively (Bonneton et al., 2015).

Field observations within Gironde Estuary were taken in two two-week long sampling periods, the first in March 2014 and the second in July 2014. Measurements were taken from the CNRS research vessel, RV Côtes de la Manche.

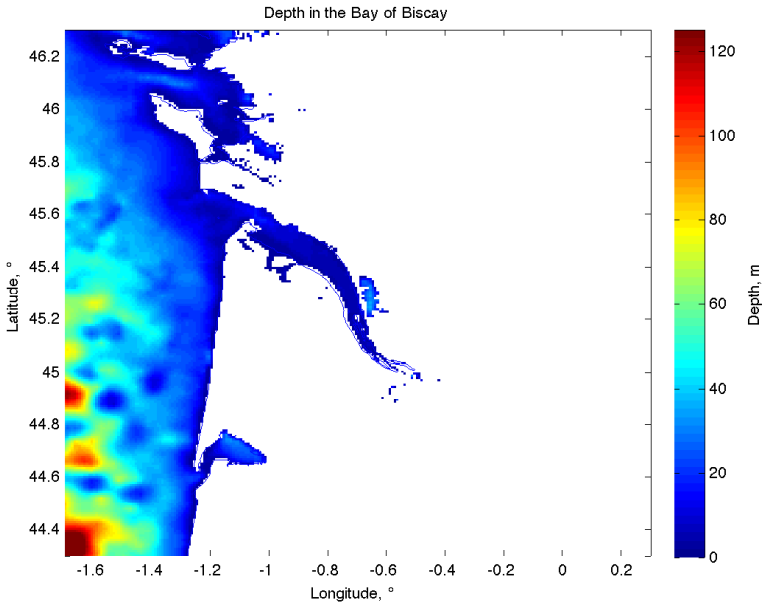


(a) Bathymetry of the Bay of Biscay region.

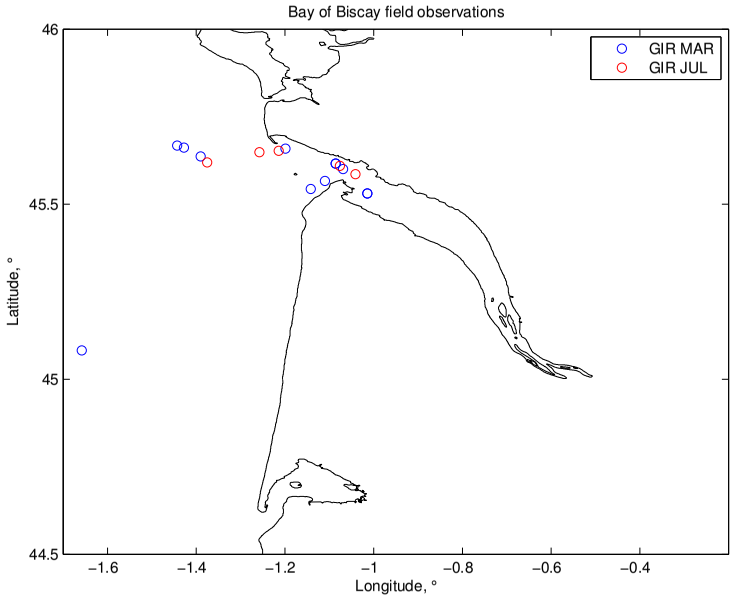


(b) Location of Bay of Biscay stations.

Figure 21: Map of the region surrounding the Bay of Biscay fieldwork location.

**Bay of Seine, English Channel (La Manche), France**

The Bay of Seine sits on the central northern coast of France, bordering the English Channel (Figure 22). The Seine river is approximately 160km long and dominated by the high-sediment load fluvial discharge through the Seine estuary, varying from $700m^3s^{-1}$ in the winter to $370m^3s^{-1}$ in the summer, amounting to 650,000 tonnes of sediments in 2004-2005 (Verney et al., 2009). The Seine catchment area has been estimated at $74,000km^2$, with over 40% of the French population and industry concentrated around its banks (Brenon & Le Hir, 1999). The mean spring and neap tidal ranges at the mouth of the estuary have been observed to be 8m and 3m on a spring and neap tide respectively (Verney et al., 2009).

Observations were made during a three week field campaign within the Bay of Seine during January 2015. These observations were also taken aboard the RV Côtes de la Manche.

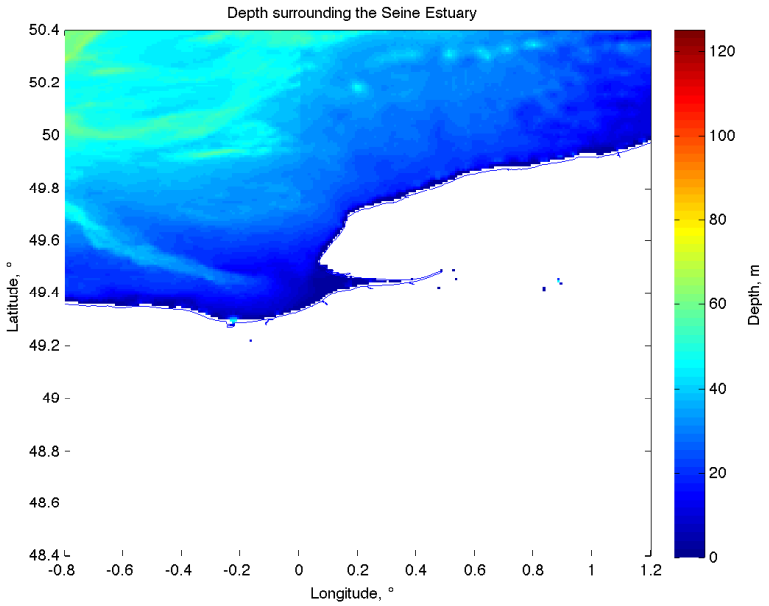


(a) Bathymetry of the Seine Estuary region.

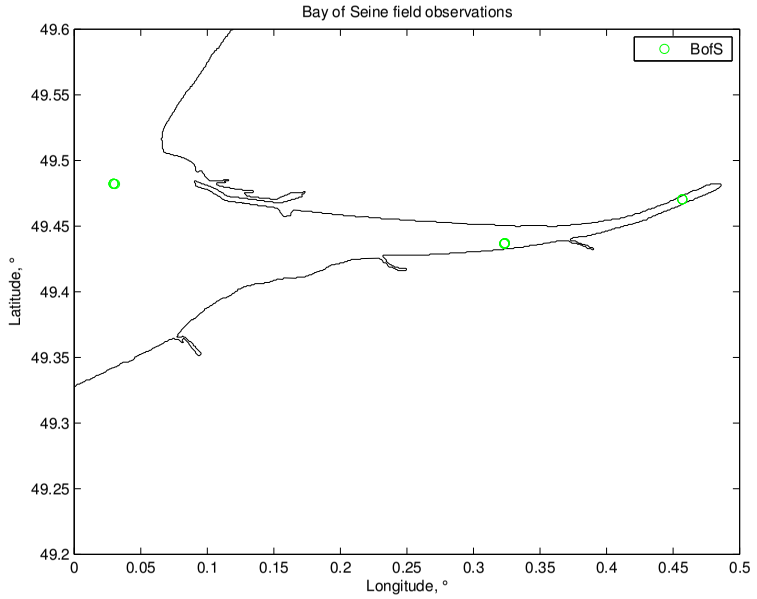


(b) Location of Seine Estuary stations.

Figure 22: Map of the region surrounding the Seine Estuary fieldwork location.

## 9.2 Sampling and processing

The maximum time between optical measurements and water sampling was always less than 10 minutes and for most of the stations less than 5 minutes.

### Water sampling

Water samples were taken regularly during the sampling periods at all sites, unless weather or ship movement interfered. Samples were filtered through pre-weighed and pre-combusted $47\mu m$ glass-fibre filters. Discretion was used in deciding the amount of water to be filtered, dependant upon time taken to filter in the case of heavily turbid sample sites. Filters were rinsed using at least 500ml of distilled water, to remove salt from the filter. All measurements were taken in triplicate form and then averaged. If one sample gave results a magnitude higher or lower than the other two, it was removed before averaging.

In order to calculate the total suspended solids (TSS) of the samples, the filters were dried in a drying oven for 12 hours at $100°C$. Following the drying process, the filters were weighed, with the difference between this mass and the pre-weighed filter mass representing the mass of TSS present. The mass was then divided by the volume of water filtered to provide the mass concentration.

Once the samples had been dried and weighed to calculate the TSS mass, the samples were placed in a furnace at $500°C$ for 3 hours, with the aim of removing organic material present on the filters. following this, the filters were weighed once more, with the remaining mass representing the MSS present in the filter. The mineral content proportion was then calculated by dividing MSS by TSS. The organic content proportion is 1-MSS/TSS.

### Sequoia LISST measurements of particle size and volume concentration

For each sampling set, a profile was carried out using the Sequoia LISST (Laser In Situ Scattering and Transmissometry) 100X type-C instrument. The LISST-100X measures the

volume scattering function (VSF), in the form of the intensity of scattering at 32 angles defined by concentric rings on the detector (Bale & Morris, 1987; Agrawal & Pottsmith, 2000; Agrawal & Traykowski, 2001). In order to produce the size distribution of the particles from the VSF, mathematical inversion is necessary, to find the multi-angle scattering required to produce the observation (Hirleman, 1987; Agrawal et al., 1991; Agrawal & Pottsmith, 2000). The scattered optical power from the LISST peaks at small angles for large particles and at larger angles for smaller particles (Agrawal & Pottsmith, 2000). From this, it is possible to calculate the volume concentration within each of the 32 sample size classes, logarithmically spaced between 2.5 and 500 $\mu m$. To increase the validity of the observations, daily background measurements were used to calibrate the field observations

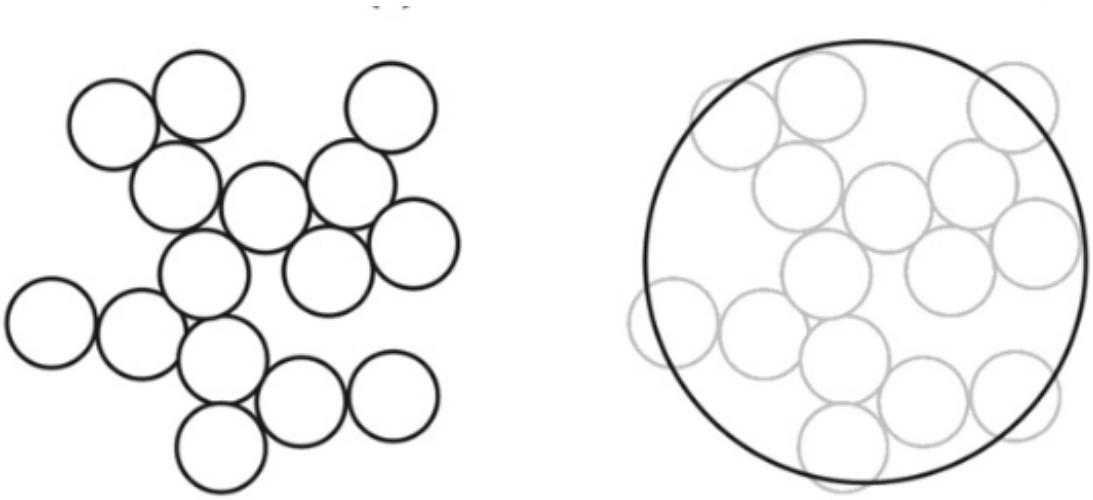

Figure 23: A fractal floc made up of multiple aggregated particles, alongside the spherical assumption made by the LISST (Verney et al., 2011).

The LISST assumes that particles are spherical when estimating the size distribution of a body of suspended sediments (Figure 23). When studying the size distribution in a natural environment, there has been some reservation as to the limitations of the LISST to accurately measure the size distribution in regions containing a high concentration of non-spherical particles (Agrawal & Pottsmith, 2000). In highly turbid environments, where the optical transmission is less than 30%, multi-scattering was proposed to occur which would overestimate

the size of flocculated particles, skewing the size distribution (Agrawal & Pottsmith, 2000). However, the study of Agrawal et al. (2008) found that natural particles of a non-spherical form only tended to cause a skew to one size class above the actual size, equating to an approximate 25% overestimation. From this, it was shown that particles that were "smooth, rounded but with random shape" (fractal) could generally be observed to behave as spheres (Agrawal et al., 2008). It is unlikely however that the impact of multi-scattering would effect results used in this study as devices such as the ECO-BB series would be similarly effected, causing saturation, therefore meaning that this data would not be included in analysis.

**WETLabs ECO-BB3 & ECO-BB9 observations**

The ECO-BB series devices directly measure the backscattering coefficient, $b_b$ (Figure 24). The ECO-BB3 and ECO-BB9 use three and nine emitters respectively to describe the backscattering at several wavelengths (Table 8). All optical devices, including the BB3/BB9 were deployed simultaneously alongside the LISST.

| Instrument | Wavelengths measured, nm |
|---|---|
| WetLabs ECO-BB3 | 470, 532, 650 |
| WetLabs ECO-BB9 | 412, 440, 488, 510, 532, 595, 650, 676, 715 |

Table 8: Wavelengths measured by the WETLabs ECO-BB3 and ECO-BB9 devices (WETLabs, 2013; WETLabs, 2016).

Measurements in the Menai Strait using the BB3 and LISST deployed both devices separately at corresponding times and held below the surface. Measurements made in France used a deployment frame containing both devices, with the frame held below the surface to compare to surface water samples. For the purpose of this study, the wavelength used for analysis is 650nm, due to its relationship with suspended sediment mass concentration and subsequent use in satellite algorithms (Gohin et al., 2005; Neukermans et al., 2012; Bowers et al., 2014). It is generally accepted that it is possible to measure the backscattering coefficient using measurements of scattered light between the angles of 100° and 150° (Oishi, 1990; Maffione & Dani, 1997; Boss & Pegau, 2001, Boss et al., 2004a). The ECO-BB series of backscatter

meters record the volume-scattering, $\beta$ ($m^{-1}sr^{-1}$), at the fixed angle of either 117° (BB3 (WETLabs, 2016)) or 124° (BB9, (WETLabs, 2013)) in the backward direction (Neukermans et al., 2012). The ECO-BB instruments emit light at the specified wavelengths and then detect how they are scattered backwards off particles in the water column (Figure 21).

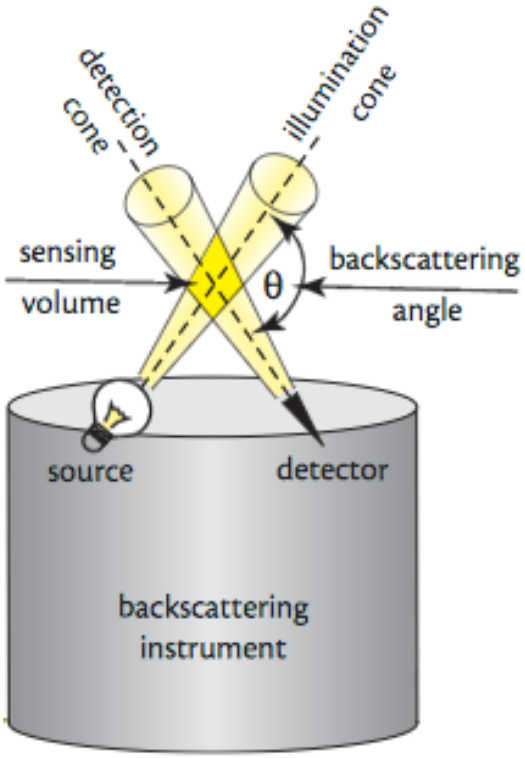


Figure 24: Schematic of a fixed-angle backscattering sensor, similar to that of the ECO-BB devices. This example represents a source and detector at a single wavelength of light (Boss et al., 2004b).

The data is then corrected for the effects of temperature and absorption, in addition to the influence of pure water irrespective of particulates (Neukermans et al., 2012; Zhang et al., 2009), to provide the particulate volume-scattering, $\beta_P$. By multiplying by $2\pi\chi$, where $\chi$ = 1.1, the $b_{bp}$ is calculated (Neukermans et al., 2012; Sullivan & Twardowski, 2009), with corrections for absorption and scattering as described in Sullivan et al. (2005). In the use as part of the project, the WetLabs ECO BB software was used to carry out the post-processing, automating the above calibration and correction. As the ECO-BB series were originally

developed to be used in open ocean regions with low scattering regimes, some concern has been raised as to the impact of saturation in highly scattering regions of high turbidity (such as the estuary catchment area) with lesser concerns of absorption and scattering loss and the influence of multi-scattering upon the measured signal (Doxaran et al., 2016). The result of the high sensitivity of the ECO-BB series therefore is that high turbidities are likely to oversaturate the signal, limiting the usable data under those conditions. It may be suggested that this would skew results towards lower turbidity in less scattering regimes, however this form of bias has not be observed in the literature.

Sullivan et al. (2013) also addresses the uncertainties relating to optical measurements of backscattering, noting the importance of calibration and regularly cleaning the sensors between profiles. All ECO-BB devices were calibrated before deployment reducing uncertainty from the baseline response, by standardising the dark offset. All sensors were also cleaned with filtered water used between profiles to remove organic and mineral detritus which may influence the signal. Sullivan et al. (2013) states that due to the multiplicative nature of the scaling factor, calibration of this is also important as per cent increases or decreases in the scaling factor would equate to relative increased in the recorded signal. Scaling factor has been shown to increase as a function of time, at a rate of approximately 3% a year for ECO-BB sensors.

**Sub-sampling**

During the field campaigns in the Gironde and Seine estuaries, due to the high turbidities observed, the signal from the ECO-BB devices was often saturation, preventing measruement of the backscattering coefficient at many of the survey stations. As described by Doxaran et al. (2016), in high turbidities multi-scattering can cause saturation of the signal. Observations included in this chapter are limited to those where water filtration for suspended sediment concentration were performed and where data from the LISST and ECO-BB devices were successfully retrieved. In both the Seine and Gironde estuaries, suspended sediment samples were observed to exceed 1,000 $gm^{-3}$.

**Cross-sectional area of particles, CSA,** $m^2/m^3 = m^{-1}$

Following the method detailed in Bowers et al. (2014), all particles measured in the 32 size classes by the LISST are assumed to be spherical. The cross-sectional area for a particle of each size class in then estimated and multiplied by the number of particles in each size class. When the summed areas for each size class are added to one another, this gives an estimation of the total cross-sectional area of particles. An additional assumption was made that for each size class, the particles all had a diameter equal to the mid-point particle size for that class.

**Backscattering Efficiency,** $Q_{b_b} = b_b/CSA$

The backscattering efficiency was used to represent the efficiency of particles to backscatter per unit of particle cross-sectional area. The backscattering coefficient at 650nm was used from the ECO-BB device for the study site, with the cross-sectional area calculated from the LISST volume concentrations in each size class as previously described.

Data from the fieldwork locations are summarised in table 9.

Table 9: Fieldwork summary from all sites. TSS, $gm^{-3}$. $b_{b_p}$, $m^{-1}$. $b_{b_p}*$, $m^2g^{-1}$. CSA, $m^{-1}$. $D_{50}$, $\mu m$.

| | TSS | $gm^{-3}$ | | $\frac{MSS}{TSS}$ | | | $b_{b_p}$ | $10^{-3}$ | $m^{-1}$ | $Q_{b_{b_p}}$ | $10^{-3}$ | | $b^*_{b_p}$ | $10^{-3}$ | $m^2g^{-1}$ | $CSA$ | $m^{-1}$ | | $D_{50}$ | | |
|---|---|---|---|---|---|---|---|---|---|---|---|---|---|---|---|---|---|---|---|---|---|
| Site | min | max | avg | min | max | avg | min | max | avg | min | max | avg | min | max | avg | min | max | avg | min | max | avg |
| MS W N | 20 | 31 | 27 | .61 | .80 | .73 | 30 | 58 | 44 | 12.3 | 27 | 20 | 1.0 | 2.6 | 1.7 | 1.5 | 3.6 | 2.2 | 68 | 165 | 123 |
| MS W S | 18 | 25 | 21 | .73 | .77 | .75 | 41 | 55 | 45 | 28.2 | 44 | 35 | 1.9 | 2.5 | 2.1 | 1.4 | 1.5 | 1.4 | 63 | 82 | 72 |
| MS S | 9 | 20 | 15 | .59 | .75 | .65 | 19 | 53 | 41 | 27.1 | 40 | 34 | 1.7 | 3.1 | 2.7 | .2 | .9 | .6 | 45 | 63 | 52 |
| G March | 11 | 64 | 42 | .59 | .79 | .67 | 27 | 82 | 80 | 8.7 | 32 | 14 | 1.5 | 2.5 | 1.8 | .8 | 11.7 | 6.9 | 53 | 210 | 127 |
| G July | 15 | 48 | 38 | .61 | .78 | .67 | 22 | 85 | 78 | 9.9 | 14 | 12 | 1.5 | 1.9 | 1.7 | 5.1 | 10.1 | 7.4 | 64 | 213 | 111 |
| B Of S | 23 | 70 | 51 | .73 | .87 | .82 | 33 | 107 | 68 | 7.9 | 61 | 54 | 1.4 | 4.1 | 3.1 | 1.5 | 8.3 | 5.6 | 47 | 104 | 61 |

MS W N and MS W S are Menai Strait field work during the winter on a neap and spring tide

MS S is the Menai Strait summer field work

G March is the Gironde Estuary field work in March 2014

G July is the Gironde Estuary field work in July 2014

B Of S is the Bay of Seine field work in January 2015

TSS is the concentration of total suspended solids, $gm^{-3}$

MSS/TSS is the ratio of mineral to total suspended solids

$b_{b_p}$ is the backscattering coefficient at 650nm, $m^{-1}$

$Q_{b_{b_p}}$ is the backscattering efficiency at 650nm

$b^*_{b_p}$ is the mass-specific backscattering at 650nm, $m^2g^{-1}$

CSA is the cross-sectional area of particles, $m^{-1}$ $D_{50}$ is the mass-median diameter, $\mu m$

# 10 Results

## 10.1 Backscattering of suspended solids

Figure 25 shows the backscattering coefficient ($b_{b_p}$) varying with the concentration of total suspended solids (TSS). It is notable that there is a a consistent positive gradient between the concentration and the backscattering coefficient, with a linear relationship providing a coefficient of determination defining that 80% of the variability may be explained.

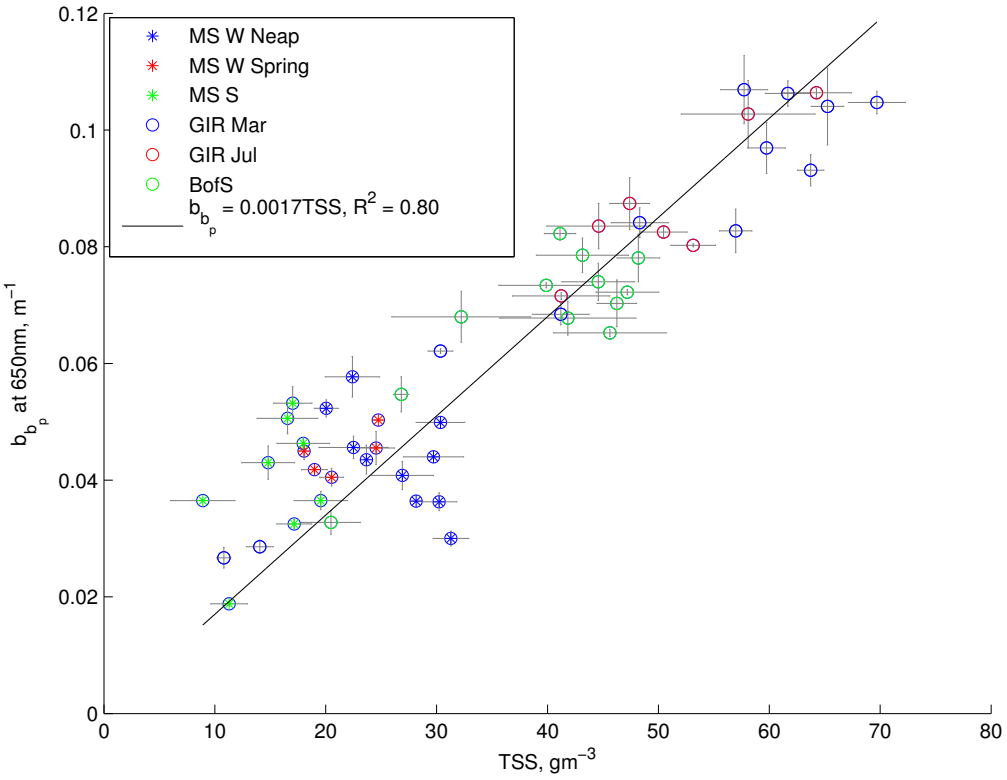


Figure 25: Variability in the backscattering coefficient at 650nm, with TSS, the concentration of total suspended solids, as observed at the field observation sites in the Menai Strait, the Gironde Estuary and the Seine Estuary over all campaigns. The correlation provided an $R^2$, coefficient of determination of 0.80. Following a t-Test, the relationship provided a p-value of $< 0.05$ (2.304E-21), inferring a significant relationship between the two variables. The error bars represent the range for observations of backscattering and of concentration of total suspended solids.

## 10.2 Backscattering efficiency, $Q_{b_{bp}} = b_{b_p}/CSA$

As detailed in Bowers et al. (2014), the backscattering efficiency is the backscattering coefficient per unit of cross-sectional area of particles. Figure 26 shows the variability in the backscattering efficiency with the mineral content of the particles. An exponential fit has been included through the data, which is able to represent 64% of the variability in this dataset.

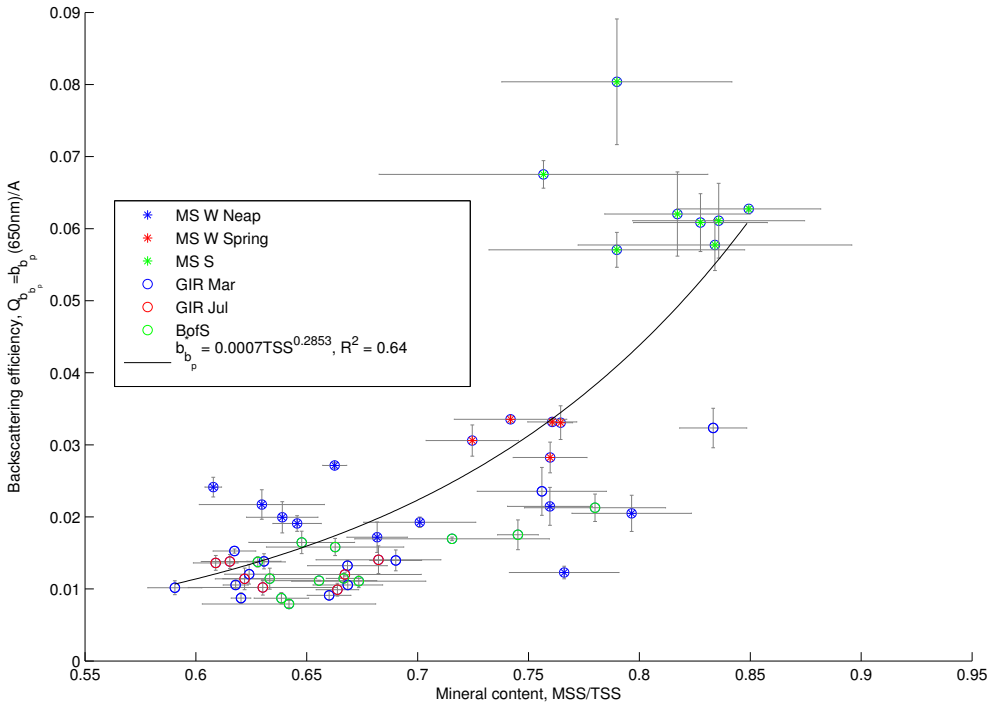


Figure 26: Variability in the backscattering efficiency, $Q_{b_{bp}}$=$b_{b_p}$/CSA, with MSS/TSS, mineral content of sampled particulates, as observed at the field observation sites in the Menai Strait, the Gironde Estuary and the Seine Estuary over all campaigns. The correlation provided an $R^2$, coefficient of determination of 0.64. Following a t-Test, the relationship provided a p-value of $< 0.05$ (2.3388E-08), inferring a significant relationship between the two variables. The error bars represent the range of backscattering efficiency and of the mineral content.

## 10.3 Mass-specific backscattering coefficient, $b_{b_p}*$

The mass-specific backscattering coefficient represents the relationship between the concentration of total suspended solids and the observed backscattering. As such, this is the most direct relationship to those in present remote-sensing algorithms. As stated previously, present remote-sensing algorithms assume $b^*_{b_p}$ to be constant. Figure 27 shows that there is a factor of 4 variability in the observed values for $b^*_{b_p}$. Using a logarithmic relationship, it was possible to represent 36% of the variability in $b^*_{b_p}$ using the concentration of total suspended solids alone.

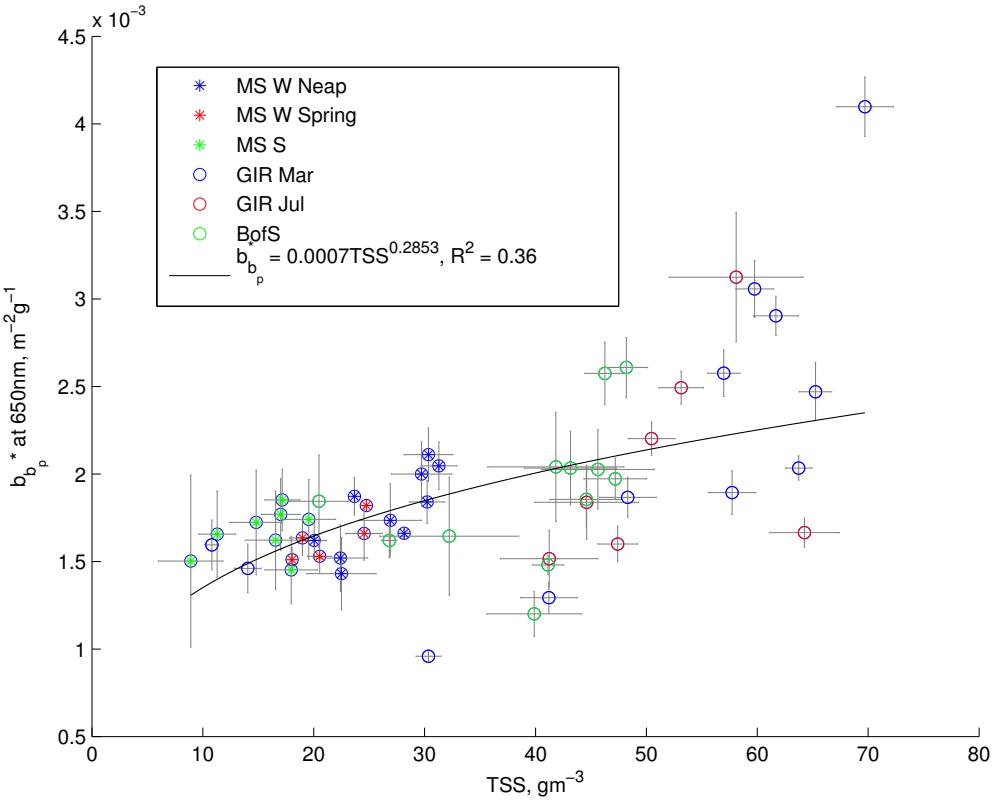


Figure 27: Variability in the mass-specific backscattering coefficient, $b_{b_p}* = b_{b_p}/SPM$, with the concentration of total suspended solids, as observed at the field observation sites in the Menai Strait, the Gironde Estuary and the Seine Estuary over all campaigns. The correlation provided an $R^2$, coefficient of determination of 0.36. Following a t-Test, the relationship provided a p-value of $< 0.05$ (0.00625), inferring a significant relationship between the two variables. The error bars represent the range for observations of mass-specific backscattering and of concentration of total suspended solids.

Figure 28 shows the influence of mineral content on the mass-specific backscattering coefficient ($b^*_{b_p}$). Although there is scatter in the observations there is a distinct increase in the observed $b_{b_p}*$ with the mineral content, from this it is possible to make a positive fit with an $R^2$ representing 38% of the observed variability.

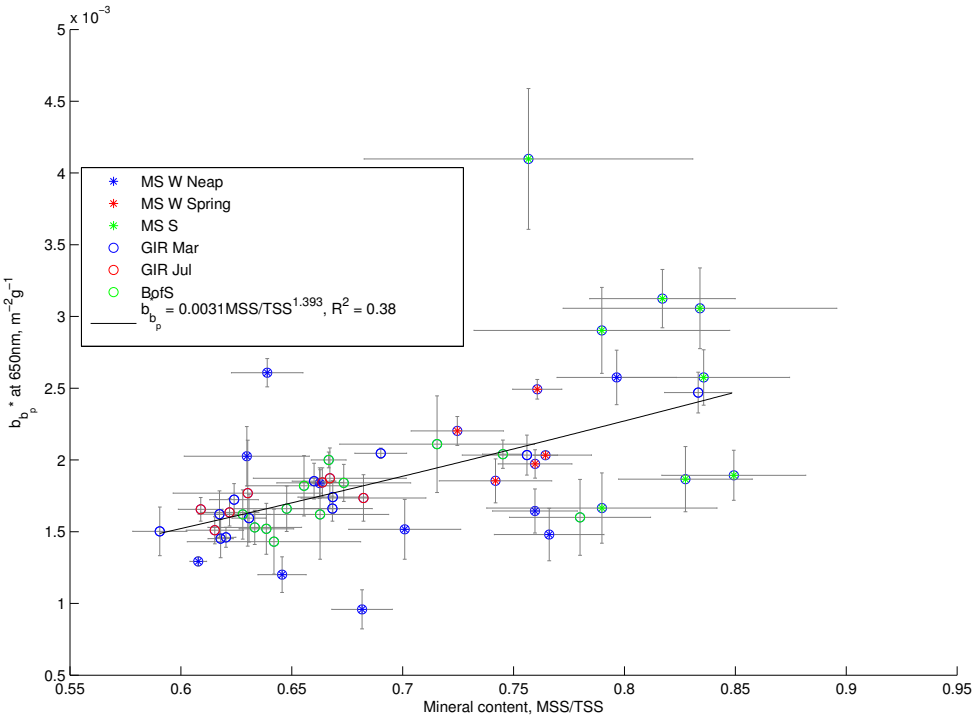


Figure 28: Variability in the mass-specific backscattering coefficient, $b_{b_p}* = b_{b_p}/SPM$, with MSS/TSS, the mineral content of sampled particulates, as observed at the field observation sites in the Menai Strait, the Gironde Estuary and the Seine Estuary over all campaigns. The correlation provided an $R^2$, coefficient of determination of 0.38. Following a t-Test, the relationship provided a p-value of $< 0.05$ (5.1264E-54), inferring a significant relationship between the two variables. The error bars represent the range for observations of mass-specific backscattering and of mineral content.

## 10.4 Median grain size, $D_{50}$

In order to approximate the influence of particle size upon the mass-specific backscattering coefficient, $D_{50}$, the median particle diameter is used. A negative power fit shows that as the median particle size gets larger, $b_{b_p}*$ reduces, representing 43% of the observed variability (Figure 29).

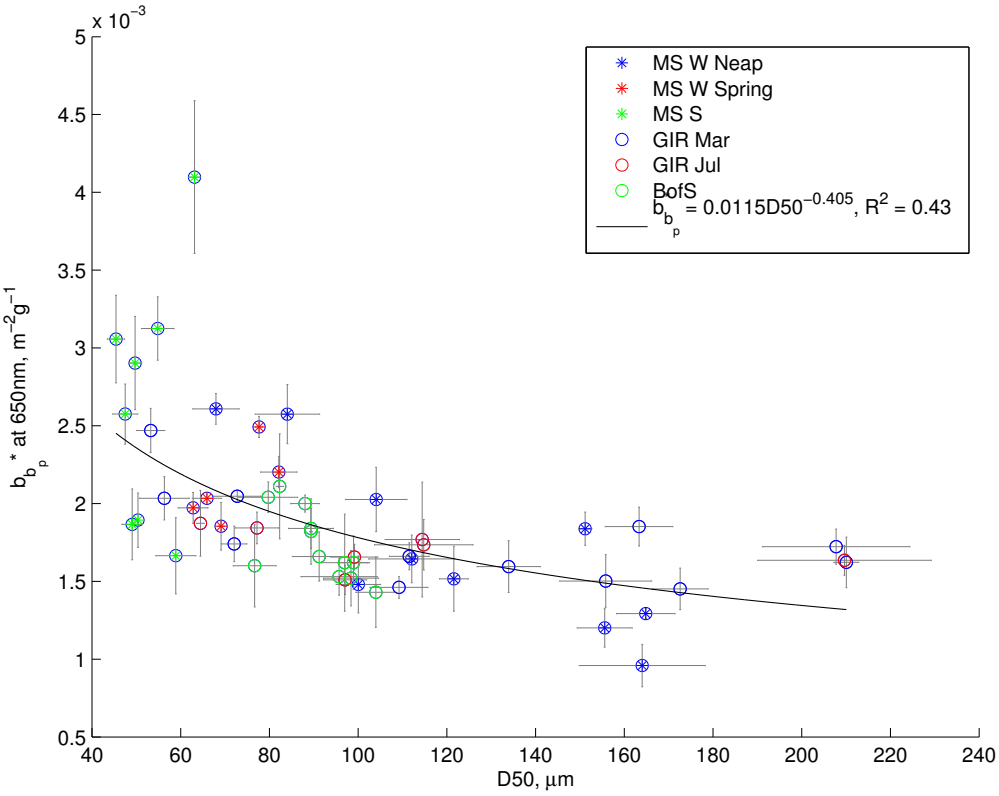


Figure 29: Variability in the mass-specific backscattering coefficient,$b_{b_p}* = b_{b_p}/SPM$, with $D_{50}$, the mass median grain size in $\mu m$ as observed at the field observation sites in the Menai Strait, the Gironde Estuary and the Seine Estuary over all campaigns. The correlation provided an $R^2$, coefficient of determination of 0.43. Following a t-Test, the relationship provided a p-value of $< 0.05$ (1.6928-23), inferring a significant relationship between the two variables. The error bars represent the range for observations of mass-specific backscattering and mass-median particle diameter.

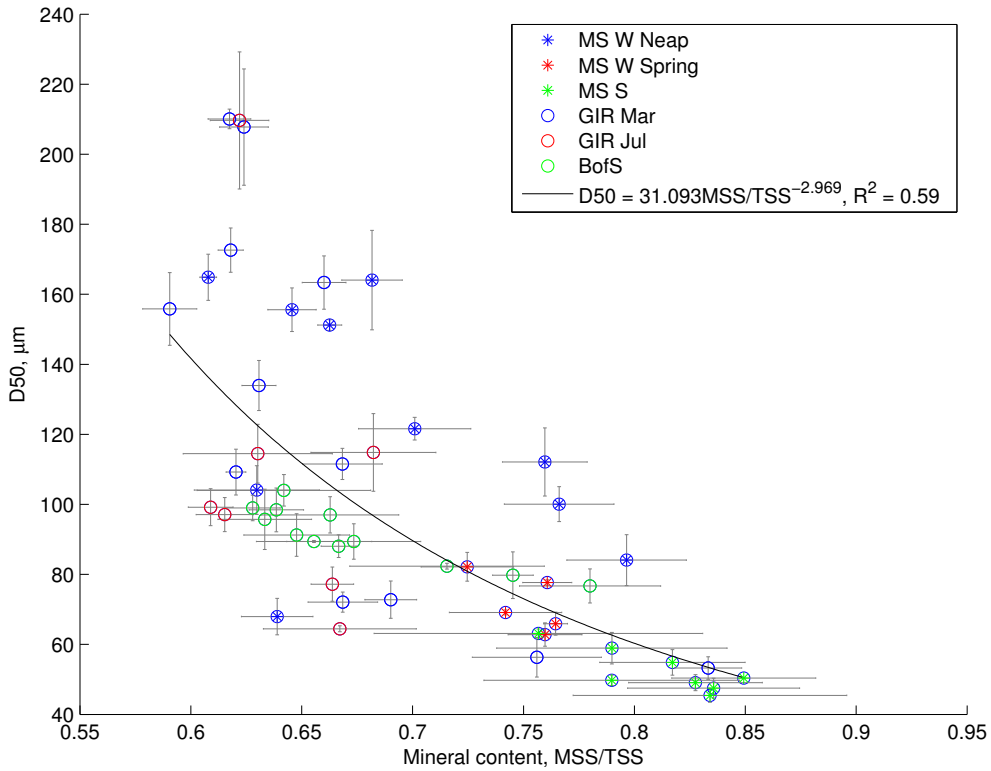


Figure 30: Variability in $D_{50}$, the mass median grain size in $\mu m$, with MSS/TSS, the mineral content of sampled particulates, as observed at the field observation sites in the Menai Strait, the Gironde Estuary and the Seine Estuary over all campaigns. The correlation provided an $R^2$, coefficient of determination of 0.59. Following a t-Test, the relationship provided a p-value of $< 0.05$ (2.4428E-23), inferring a significant relationship between the two variables. The error bars represent the range for observations of mass-median particle diameter and of mineral content.

The expectation is that as the organic proportion of the suspended material grows, that sustained flocculation increases and therefore the particle size. Figure 30 shows the median particle size varying with the mineral content, with a power fit providing an $R^2$ which represents 59% of the observed variability in the particle size.

# 11 Discussion

## 11.1 Backscattering coefficient, $b_{b_p}$

The concentration of total suspended solids shows a near linear relationship with the backscattering coefficient, $b_{b_p}$, with an $R^2$ of 0.80. Notably there was some scatter around the linear fit at the Menai Strait winter neap site, which from consulting the data table is expected to be due to low $b^*_{b_p}$ values observed at several of the sample points.

## 11.2 Backscattering efficiency, $Q_{bb}$

As also observed by Bowers et al. (2014), the mineral content was shown to influence the relationship between the particle surface area and the backscattering of light. The fit found by Bowers et al. (2014) was shown to represent most of the variability in this dataset although this studies fit was able to increase this representation from a $R^2$ of 0.58 to an $R^2$ of 0.64, an improvement upon the $R^2$ of 0.62 achieved in Bowers et al. (2014). As this improvement is minimal it may be proposed that this difference may be due to the method of inferring backscattering from radiometer readings used by Bowers as opposed to the direct observations of backscattering used throughout this study. Nevertheless, the similarity between the two fits suggest that the Bowers et al. (2014) method for inferring backscattering was indeed successful. The refractive index increases for highly mineral particles, the strong relationship between the mineral content and $Q_{b_{b_p}}$ would fit with the previous observation of backscattering increasing with the refractive index (Twardowski et al., 2001; Boss et al., 2004; Stramski et al., 2004, Bowers et al., 2014).

## 11.3 Mass-specific backscattering coefficient, $b^*_{b_p}$

A commonly used representation of the efficiency of a particle to backscatter light is the mass-specific backscattering coefficient, $b^*_{b_p}$, the relationship between the backscattering coefficient and the total suspended solid concentration. Over 36% of the variability in the mass-specific

backscattering coefficient was shown to be represented by the concentration of total suspended solids alone, showing that as the concentration grows the relative efficiency of the particulate mass to backscatter increases.

In addition, with a power fit this study was able to represent 38% of the variability observed in the mass-specific backscattering coefficient using the mineral content of the particles. This is a large improvement upon previous observed relationships, with Neukermans et al. (2012) representing only 18.5% of the variability using the comparable organic content and Bowers et al. (2014) representing 20% using the mineral content. A key note is that the value for $b^*_{b_p}$ is shown to vary from approximately 0.001 $m^2g^{-1}$ to 0.0041 $m^2g^{-1}$, emphasising the flawed notion that this can be assumed to remain constant as implemented in present remote-sensing algorithms.

It is expected that the observed relationship between the total suspended solids concentration and the $b^*_{b_p}$ is a secondary effect of the influence on the refractive index by the mineral content (Twardowski et al., 2001), as noticeable in Figure 36. Twardowski et al. (2001) describes how particles of an increased mineral content have a higher refractive index. In this analysis, the highest observed concentrations coincided with those that with a higher mineral content, thus influencing the observed relationship between total suspended solids concentration and mass-specific backscattering.

## 11.4 Mass-median particle size, $D_{50}$

The backscattering efficiency showed that the relationship between particle surface area and the backscattering coefficient is strongly dependant upon the mineral content of the particle. It is generally presumed that size of a particle does not directly control the mass-specific backscattering coefficient, $b_{b_p}*$, with no significant relationships observed in the literature (Neukermans et al., 2012). Nevertheless often particle size is related to the mineral content of a particle, with flocculated organic particles more likely to reach larger observed sizes. Using a negative power fit, it was possible to represent 43% of the observed variability in $b^*_{b_p}$ using the median particle size, $D_{50}$. However, when examined further, when observations of the

median particle size were compared to the mineral content, the negative power fit represented 59% of the observed variability and thus it is proposed that the observed relationship between the $D_{50}$ and $b^*_{b_p}$ is a secondary relationship controlled by the observed influence of mineral content on the mass-median particle size. Another consideration, as made by Agrawal et al. (2008), is that as a particle grows in size due to flocculation, the surface area available to scattering will diminish, resulting in a further reduced level of backscattering. In the samples observed in this study, smaller particles were found to be more mineral than larger particles, which tended to increased organic content. Further analysis would benefit from the inclusion of sample sites containing high levels of faecal matter, which present the characteristics of being both small and highly organic particles.

Neukermans et al. (2012) observes a higher range of values of mass-specific backscattering, $b_{b_p}*$ (0.02-0.02$m^2g^{-1}$), than in this study (0.001-0.042$m^2g^{-1}$). However, it must be noted that the observed values for Qbb in Neukermans et al. (2012) are higher also (0-0.12) in comparison to this study (0-0.08), suggesting that the backscattering per unit cross-sectional particulate area was higher at many of the Neukermans et la. (2012) locations than those covered in this study, which were spread internationally (the East Atlantic coastline, the Mediterranean Sea and South America. Bowers et al. (2014) surveyed similar locations to those used in this thesis chapter, observing a range of $b_{b_p}*$ similar to that of this study (0-0.005$m^2g^{-1}$) and a range of $Q_{b_b}$ less than that of this study (0-0.045). The suggestion therefore is that backscattering per unit mass and per unit cross-sectional area was higher in the study of Neukermans et al. (2012), but that the study of Bowers et al. (2014) showed a similar $b_{b_p}*$ range to this study and a lower range of $Q_{b_b}$, This study can be shown to fit between the ranges of data observed in Neukermans et al. (2012) and Bowers et al. (2014).

## 11.5 Future developments

As described in the methods section of this thesis, due to saturation of the optical devices in high turbidities, some data was excluded from this study. Future field observations could look to improve upon this issue, by implementing HydroScat type instruments which perform

under a higher threshold of turbidity (Doxaran et al., 2009).

Similarly, this study would benefit from the inclusion of Hydrolight radiative transfer modelling to reinforce the observations. This would allow further exploration of the variability in both mass-specific backscattering, $b_{b_p}*$ but also backscattering efficiency, $Q_{b_b}$.

## 11.6 Implications

The expectation from the literature is that mineral particles would be better at backscattering light as they have a higher refractive index. There is no substantiated reason to explain that smaller particles would be better at backscattering than larger particles. In the datasets included in this study, smaller particles are observed to be more mineral in content and as such the link between size and backscattering efficiency can be presumed to purely a secondary one.

For remote-sensing, it may be challenging to begin to include notions of the influence of particle size, surface area or mineral content upon the mass-specific backscattering coefficient without adding additional errors with the resulting assumptions. However, this study was able to find a relationship between the total suspended solids concentration and the mass-specific backscattering coefficient which could be used in an iterative approach to improve the represent remote-sensing algorithm and reduce the present shortcomings.

## 11.7 Remote-sensing algorithm iteration of $b^*_{b_p}$

Using the concentration of total suspended solids, it was possible to predict 36% of the variability in the mass-specific backscattering coefficient ($b^*_{b_p} = 0.0007SPM^{0.2853}$). Although this is not a strong relationship, it has potential to improve present remote sensing algorithms which assume a constant $b^*_{b_p}$ by adding this variability. In order to demonstrate the potential of such an inclusion a simple adaption of post-algorithm remotely-sensed suspended matter concentration was used to estimate seasonal variability in $b^*_{b_p}$.

$b^*_{b_p 0}$ is the constant mass-specific backscattering coefficient assumed by Gohin et al. (2005)

$(0.009m^2g^{-1})$.

$SPM_0$ is the present estimation of the concentration of suspended particulate matter from Gohin et al. (2005).

1. Using the remotely-sensed concentration from Gohin et al. (2005), it is possible to make a first estimate of $b^*_{b_p}1$, the new mass-specific backscattering coefficient.

   *Mass-specific backscattering, $b_{b_p}*$ iteration, step 1*

   $$b_{b_p}{}^*{}_1 = 0.0007(SPM_0)^{0.2853} \tag{11.1}$$

2. Dividing the original SPM concentration ($SPM_0$) by the original mass-specific backscattering coefficient ($b^*_{b_p}0$) provides the backscattering coefficient from Gohin et al. (2005). This can then be multiplied by the new estimation of the mass-specific backscattering coefficient ($b^*_{b_p}1$) to make a new estimate of the SPM concentration ($SPM_1$).

   *Mass-specific backscattering, $b_{b_p}*$ iteration, step 2*

   $$\frac{b_{b_p}{}^*{}_1 SPM_0}{b_{b_p}{}^*{}_0} = SPM_1 \tag{11.2}$$

3. Steps 1 and 2 must now be completed iteratively until the values for $b^*_{b_p}$ and SPM fall on the line ($b_{b_p}{}^*{}_1 = 0.0007(SPM_0)^{0.2853}$).

4. Using the new value for $b_{b_p}{}^*$, it is now possible to recalculate SPM using the Gohin et al. (2005) algorithm.

Implementing the above iterative sequence, it is possible to estimate $b^*_{b_p}$. Below is an example of a time series of $b^*_{b_p}$ using this approximation.

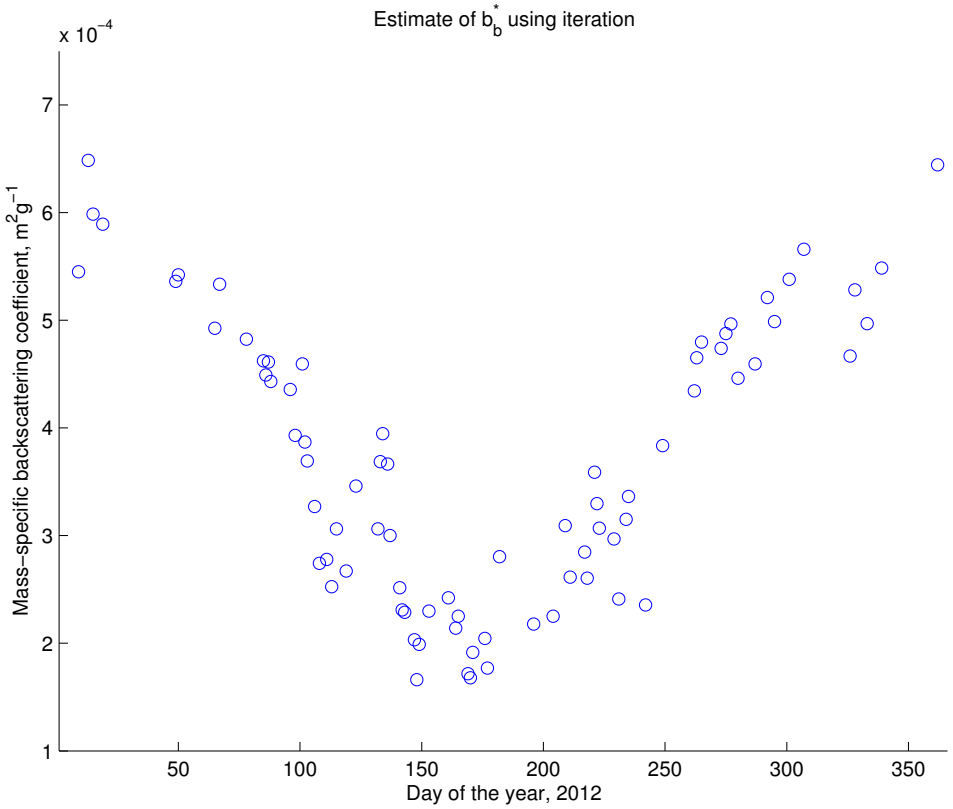


Figure 31: Estimate of mass-specific backscattering, $b^*_{b_p}$, using iteration of equation inferred from field observations of the influence of the concentration of suspended material upon the $b^*_{b_p}$. The location is 51.95°N, -6.08°E, in the southern Irish Sea. The observations used come from remotely-sensed suspended particulate matter concentration derived from MODIS Aqua using the algorithm described in Gohin et al. (2005).

Figure 31 shows a clear seasonal variation in the time series, with a higher $b^*_{b_p}$ in the winter and lower value in summer. Most likely, this is due to the mineral content of particles being higher in the winter, with particles being more organic in the summer, when the ocean is more biologically productive. The estimates of $b^*_{b_p}$ were significantly lower than the value of $0.009 m^2 g^{-1}$ used in Gohin et al. (2005). However, the example method described must be interpreted with the caveat that they were produced using the post-algorithm output used to estimate the backscattering coefficient. Future adaption would require iteration to involve full recalculation of the algorithm to better evaluate the possible applicability. Similarly, as noted earlier, the observations of Neukermans et al. (2012) showed a far larger range of values

of $b_{b_p}*$ than observed in this study, potentially limiting the fit used for this iterative example. Inclusion of a larger range of value of $b_{b_p}*$ would hopefully make the range developed using this method more feasible for application within future remote sensing algorithms.

# Part III

# Statistical analysis of remotely-sensed variability in suspended material concentration

## 12 Introduction

Using a remote sensing algorithm, it is possible to estimate the concentration of marine suspended materials from observations of ocean colour from earth-orbiting satellites. This method relies upon the relationship between remotely-sensed reflectance and backscattering of light in-situ, which is known to have an almost linear relationship with suspended matter concentration (Gohin et al., 2005; Bowers & Binding, 2006). The benefit of such a method of observation is great, due to its regular data sampling and large spatial coverage. A limitation however of taking observations from space is that atmospheric processes effect observations and in general observations only represent properties of the water column's surface. Rivier et al. (2012) and Saulquin et al. (2015) described the use of statistical models developed using the satellite archive as prediction tools when observations are unavailable.

This chapter will aim to answer the following question:
*Can the remote-sensing archive be used to describe and predict the concentration of surface suspended sediment?*

In order to do this, the following objectives will be carried out:

- Analyse the temporal and spatial variability in the remotely-sensed suspended sediment concentration archive from MODIS Aqua between 2002 and 2015.
- Expand and develop the statistical modelling method used by Rivier et al. (2012) in the English Channel to the whole northwest European shelf.

# 13 Methods

## 13.1 OC5 Algorithm

The OC5 algorithm uses and inverted semi-analytical model to derive SPM concentration from remote-sensing reflectance (and normalised water-leaving radiance). The following steps (Equations 13.1 to 13.5) were used in the OC5 algorithm to estimate the suspended matter concentration from remote sensing reflectance observed using the MODIS-Aqua instrument. The remote sensing reflectance at a given wavelength is a function of backscattering, $b_{b_p}$, and absorption, a, at this wavelength, modulated by C, a function of the solar zenith angle, the angle of observation and the surface roughness (Gordon et al., 1975; Morel et al., 1995; Sydor & Arnone, 2002; Gohin et al., 2005).

*Remotely-sensed reflectance, $R_{RS}$ (Austin, 1974; Preisendorfer, 1976; Gordon et al., 1975; 1988; Lee et al., 1994; Gohin et al., 2005)*

$$R_{RS}(\lambda) = C\frac{b_b(\lambda)}{a(\lambda) + b_b(\lambda)} \tag{13.1}$$

Backscattering in water can be split into three main components; backscattering by pure water, $b_{b_w}$, backscattering by Chlorophyll-a, $b_{b_{Chl}}$ and backscattering by non-algal particles, $b_{b_p}$. The relationship between backscattering of particles and the mineral concentration is represented as $b^*_{b_p}$ ($= b_{b_p}/SPM$, backscattering per unit mass of total suspended solids). For more information regarding the processes which control backscattering in water, see the introduction of this thesis and the chapter regarding field observations, where observations of backscattering by particles are discussed.

*Backscattering coefficient, $b_b$, $m^{-1}$ (Gohin et al., 2005)*

$$b_b(\lambda) = b_{b_w}(\lambda) + b_{b_{Chl}}(\lambda) + b^*_{b_p}(\lambda)SPM \tag{13.2}$$

Similarly, absorption in water is made up of absorption by pure water, $a_w$, absorption by

suspended solids, $a_{SPM}$, in addition to absorption by phytoplankton and endogenous yellow-substances, $a_{p+CDOM}$. The relationship between absorption and the concentration of suspended sediments is similarly represented by $a^*$ ($= a/SPM$, absorption per unit mass of total suspended solids). Absorption by exogenous yellow substances, $a_{CDOM}$ and the mass-specific absorption, $a^*$, are proposed to have an exponential slope with wavelength, S (Gohin et al., 2005). Babin et al. (2003b) proposed an S value of $0.0176nm^{-1}$ for the coastal water of Europe.

*Absorption coefficient, a, $m^{-1}$ (Gohin et al., 2005)*

$$a = a_w(\lambda) + a_{p+CDOM(Chl)}(\lambda) + a^*(\lambda)SPM + a_{CDOM}(\lambda_r)exp(-S[555 - \lambda_r]) \tag{13.3}$$

Both absorption and backscattering of pure water were well-documented in laboratory experiments (Morel et al., 2007). In the case of Gohin et al. (2005), $b^*_{b_p}$ and $a^*$ were assumed to be constant (Bowers et al., 2002; Babin et al., 2003). As discussed in the fieldwork chapter of this thesis, this assumption is flawed, with developments in field observations pursuing improved representation of variability in $b^*_{b_p}$ in future remote sensing algorithms (Bowers et al., 2014).

Equation 13.4 relates remote sensing reflectance from the satellite and reflectance.

*Assumed linear relationship of $R^*(\lambda)$ (Gohin et al., 2005)*

$$R^*(\lambda) = \alpha_0 + \alpha_1 R_{RS}(\lambda) \tag{13.4}$$

$\alpha_0$ and $\alpha_1$ represent regression coefficients between $R_{RS}$ and the optical properties controlling reflectance.

Using the shorthand of $R^*$ to describe the linear fit approach relating optical properties and remotely-sensed reflectance as defined in equation 13.4, equation 13.5 describes the overall equation for mineral suspended sediments from remotely sensed reflectance obtained from MODIS-Aqua.

*Algorithm for mineral suspended sediments using remotely-sensed reflectance from MODIS Aqua at 550nm and 650nm (Gohin et al., 2005; Rivier et al., 2012)*

$$SPM_{mineral} = \frac{R^*(\lambda)[a_w + a_{p+y}] - [b_{b_w} + b_{b_{Chl}}]}{b^*_{b_p} - a^* R^*(\lambda)} \tag{13.5}$$

In this chapter, the concentrations of suspended matter used were produced using an adapted version of the OC5 algorithm detailed in equations 13.1 to 13.5 (Gohin et al., 2005; Gohin et al., 2011). In order to improve the ability of the algorithm in highly turbid waters, a revision was made from the 2005 version of the OC5 algorithm, which relied upon remotely reflectance in the green waveband (550nm). Although the OC5 algorithm using the 550nm waveband performs well on the continental shelf, due to saturation it underestimates the concentration is more turbid coastal waters. In these more turbid waters, the red waveband (650nm) was shown to outperform the saturated green waveband (550nm) signal (Nechad et al., 2010). The updated algorithm therefore moves from the green waveband (550nm) to the red waveband (650nm) when the concentration is greater than $4gm^{-3}$ (Petus et al., 2010; Nechad et al., 2010; Gohin et al., 2011; Rivier et al., 2012). By switching from green to red in highly turbid waters, the saturating effect in the green waveband observed at high suspended loads is not present at higher concentration outputs of the algorithm.

Gohin et al. (2005) uses a linear relationship between in-situ values $\frac{b_b}{a+b_b}$ and $\frac{b_b}{a+b_b}$ inferred from remotely-sensed radiance. At low levels of remotely-sensed reflectance, there is sown to be a positive bias in this linear relationship, with higher levels of $\frac{b_b}{a+b_b}$ observed by the satellite than from in-situ observations due to limitations in the atmospheric correction. The result of this, is that at very low levels of remotely-sensed reflectance, there will be overestimation of the signal. In practical use, this will only be an issue when concentrating on SPM concentrations below $1gm^{-3}$ (Gohin et al., 2005; Gohin et al., 2011; Rivier et al., 2012).

Gohin et al. 2005 describes validation of the algorithm using the 550nm wavelength, from measurements within the Bay of Biscay. Extensive validation of the two-wavelength implementation of the Gohin et al. (2005) OC5 algorithm can be found in Gohin et al. (2011).

Gohin et al. (2011) showed successful performance of the algorithm at 26 in-situ observation stations across Europe (concentrating on sites in the Mediterranean Sea and the North Sea).

**Atmospheric correction**

Atmospheric correction is a key process within ocean colour remote sensing. Without correcting for the presence of the atmosphere, the atmospheric radiance adds to the ocean surface radiance within the visible spectrum (Austin, 1974). Additionally, atmospheric correction is used to exclude data due the presence of cloud cover which may obscure ocean surface observations (Figure 32). The main algorithm used with the MODIS and SeaWiFS (Sea-viewing Wide Field of View Sensor) instruments was developed by Gordon and Wang (1994), following the launch of the first MODIS satellite in 2002, this was then validated using in-situ observations (Wang et al., 2005; Zibordi et al., 2006; IOCCG, 2010).

*Top of atmosphere radiance,* $L_t, Wm^{-2}sr^{-1}$ *(IOCCG, 2010)*

$$L_t(\lambda) = L_r(\lambda) + L_a(\lambda) + L_{ra}(\lambda) + t(\lambda)L_{wc}(\lambda) + T(\lambda)L_g(\lambda) + t(\lambda)t_0(\lambda)cos\theta_0[L_w(\lambda)_N]$$

$L_r$ is the Rayleigh radiance, $Wm^{-2}sr^{-1}$

$L_a$ is the scattering by aerosols, $Wm^{-2}sr^{-1}$

$L_{ra}$ is the multiple interaction term between molecules and aerosols, $Wm^{-2}sr^{-1}$

$t_0$ and t are the diffuse transmittances of the atmosphere from the sun to the surface and the surface to the sensor respectively

$L_{wc}$ and $L_g$ are components of radiance due to whitecaps on the sea surface and specular reflection of direction sunlight, $Wm^{-2}sr^{-1}$

$L_{wN}$ is the normalised water-leaving radiance, $Wm^{-2}sr^{-1}$

T is the direct transmittance from the surface to the sensor

*Radiance path, $L_{path}$ (IOCCG, 2010)*

$$L_{path}(\lambda) = L_r(\lambda) + L_a(\lambda) + L_{ra}(\lambda)$$

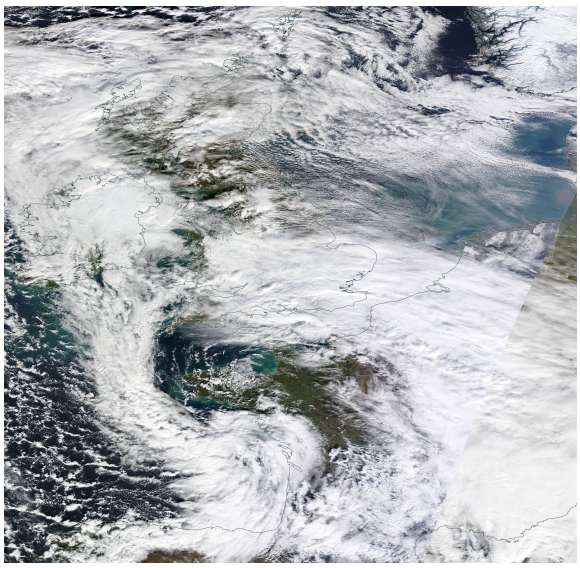

Figure 32: Cloudy MODIS image taken from EOSDIS WorldView for the 13th February 2013 (NASA EOSDIS, 2016).

The above equations display the constituent components of the radiance observed by the satellite. In order to output the normalised water leaving radiance, $L_w(\lambda)_N$, it is necessary to calculate the other components of the equation. The following steps are taken when carrying out the atmospheric correction upon a MODIS remotely-sensed image:

1. The Rayleigh radiance, $L_r(\lambda)$, is computed from lookup tables that are created using vector radiative transfer theory (which includes the effects of polarisation) (Wang, 2002; Wang, 2005; IOCCG, 2010);

2. The Whitecap radiance, $L_{wc}(\lambda)$, is then modelled from the wind speed at the sea surface (Moore et al., 2000).

3. The sun glint radiance observed at the top of the atmosphere, $T(\lambda)L_g(\lambda)$, can be in the most part removed from the observations. The remaining sun glint effects may be removed using a model of sea surface slope distribution as a basis (Cox & Munk, 1954; Wang & Bailey, 2001; IOCCG, 2010).

4. In the near infra-red, $L_w(\lambda)_N$ is minimal and is used to estimate the remaining atmospheric biases. $L_a(\lambda)$ and $L_{ra}(\lambda)$ can be extrapolated to visible wavebands using aerosol modelling techniques (IOCCG, 2010). Aerosol models account for the scattering effect upon $L_a(\lambda)$ and $L_{ra}(\lambda)$, which increases as the aerosol concentration increases (Shettle & Fenn, 1979).

5. $t_0(\lambda)$ and $t(\lambda)$ are estimated using Yang & Gordon (1997), to then calculate the $L_w(\lambda)_N$ within the visible wavelengths.

From this, the spectra of $L_W(\lambda)_N$ is used as to calculate optical products. From the water-leaving radiance, a linear relationship is used to calculate the remote sensing reflectance at the sea surface (using Equation 13.8 and the values for $\alpha$ in Table 10).

*Calculating remote sensing reflectance from normalised water leaving radiance ($Wm^{-2}sr^{-1}$) (Gohin - personal communication, 2013)*

$$R_{RS}(\lambda) = L_W(\lambda)_N/\alpha(\lambda) \tag{13.8}$$

Table 10: The conversion values, from normalised water-leaving radiance to remote sensing reflectance (Gohin, 2013 - Personal communication)

| Wavelength, $\lambda$, nm | $\alpha$ |
|---|---|
| 412 | 171.182 |
| 443 | 188.754 |
| 488 | 194.178 |
| 531 | 184.944 |
| 551 | 189.998 |
| 667 | 152.439 |

It has been proposed that due to assumptions which are made in the atmospheric correction of MODIS data, unintentional error may be added to the remote-sensing algorithm of Gohin

et al. (2005) (Aznay & Santer, 2009; Rivier et al., 2012).

## 13.2 Usable remote-sensing observations

Unfortunately, in some circumstance atmospheric correction is still unable to provide usable observations of the Ocean's surface, referred to as atmospheric correction failure. This is prevalent in the presence of clouds (Figure 32) or in the case of coastal adjacency. The following monthly figures (Figures 33 and 34) demonstrate the percentage of daily images which provided usable data points.

Two main features can be identified from the following figures detailing the percentage of usable data provided from MODIS:

- There is a latitudinal variability in the percentage of usable data, with locations with more southerly latitudes providing a higher percentage of usable data than those further north. In the northern North Sea, the percentage of usable data varies between 5% and 25%, whereas in the Mediterranean Sea, the percentage of usable data varies between 25% and 65%.
- The percentage of usable data varies between the winter and the summer, with lower levels of usable data in the winter and higher levels in the summer. At one location in the Irish Sea, only 7% of data was usable in January, whereas the same location provided 38% of usable data in July.

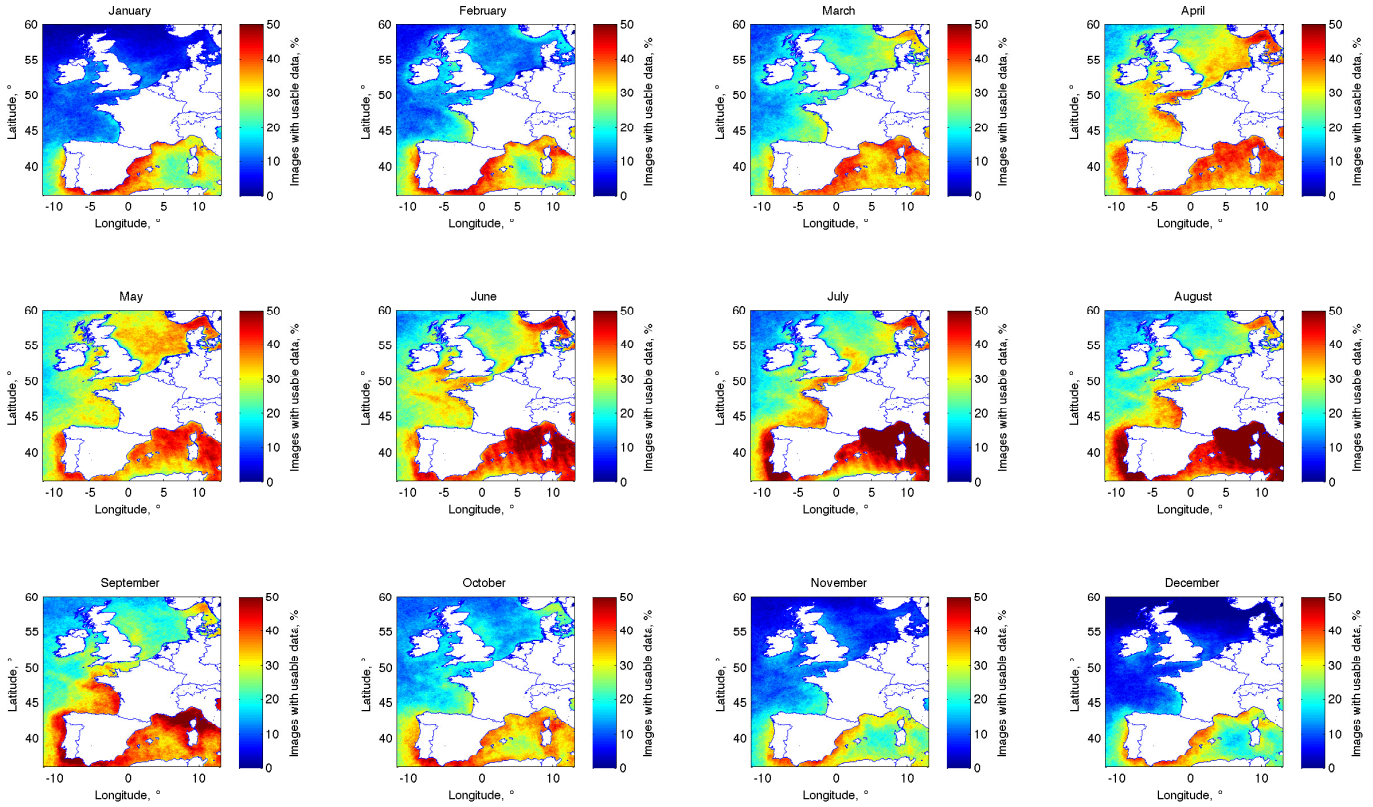


Figure 33: Percentage of usable data observed in each month of the year taken from MODIS-Aqua images between 2002 and 2015. A low level of usable data can be termed to be a high rate of atmospheric correction failure.

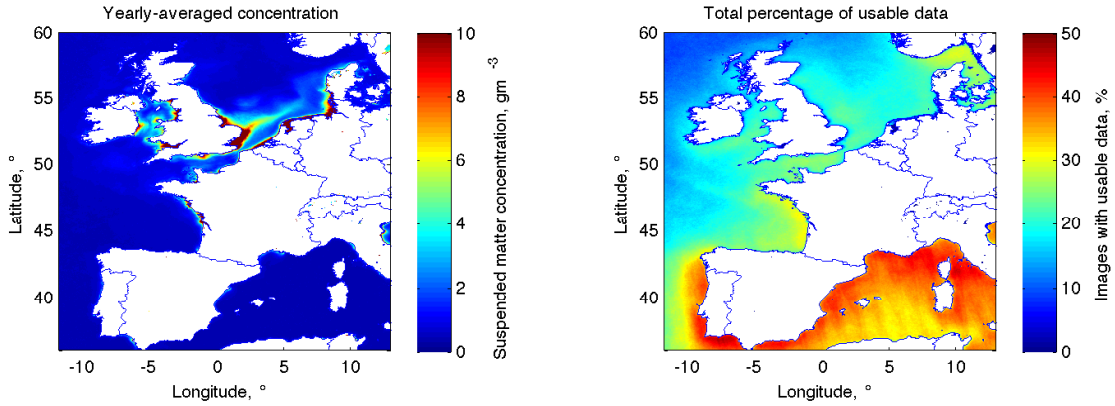


Figure 34: Average suspended matter concentration and total percentage of usable data from remotely-sensed MODIS-Aqua images from between June 2002 and June 2015.

## 13.3 Processing of remote-sensing observations

Remote-sensing data of the Chlorophyll-a and suspended particle matter (SPM) concentrations observed by the MODIS Aqua satellite were obtained through the Ifremer public FTP (file transfer protocol):

*ftp://ftp.ifremer.fr/ifremer/cersat/products/gridded/ocean-color/atlantic/modis/*

The data were then extracted from the daily NetCDF4 source files and stored in the form of yearly datasets. Each file included observations at a resolution of $1km^2$ for each pixel, from a longitude of $-12°E$ to $12.99°E$ and a latitude of $36°N$ to $60°N$ (1667km longitudinally by 2401km latitudinally). Figure 35 shows a section of the total dataset, the English Channel, at the full resolution of $1km^2$.

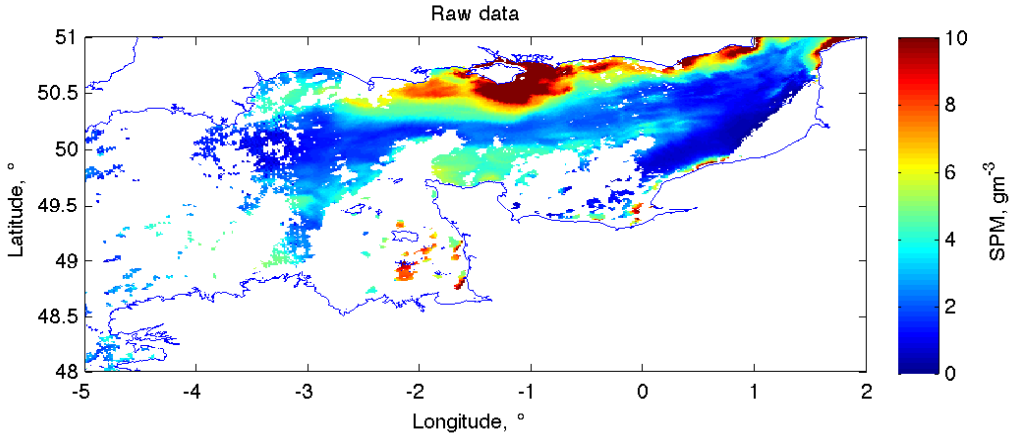


Figure 35: Suspended particulate matter concentration from MODIS Aqua at a resolution of $1km^2$ in the English Channel on the 30th January 2008.

In order to reduce the impact of low data availability due to atmospheric correction failure upon the statistical analysis, the daily images were averaged spatially into $10km^2$ grids, excluding NaN values (not a number, due to atmospheric correction failure or land) into a grid of 166 by 240 pixels. Figure 36 demonstrates the spatial averaging effect upon the full resolution dataset present in Figure 35.

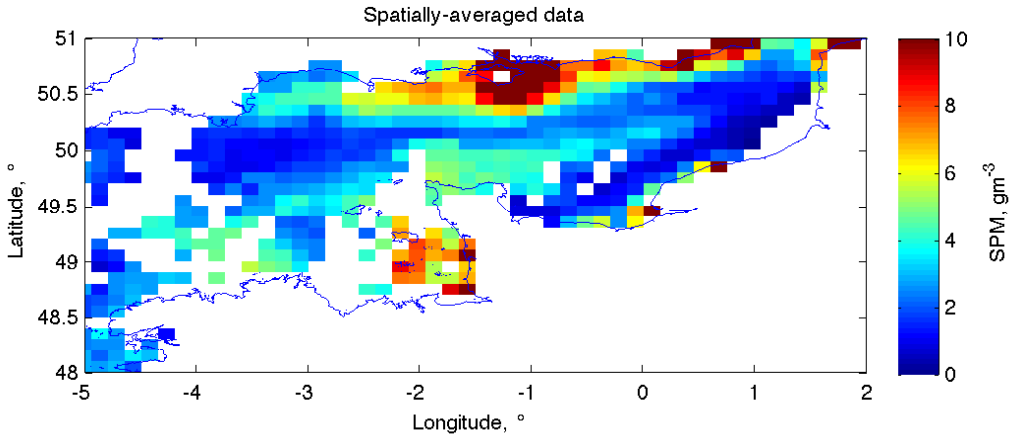


Figure 36: Spatially-averaged suspended particulate matter concentration at a resolution of $10km^2$ from the source data at $1km^2$ from MODIS Aqua in the English Channel on the 30th January 2008.

### Statistical model construction

The main purpose of producing statistical models of suspended matter concentrations, such as those detailed in Table 11, is to better understand the role that sediment transport forcings have upon remotely-sensed surface suspended sediment concentrations and how they may vary spatially and temporally. In addition, comparing outputs of these models to observations suggest how well variation in observed suspended matter concentration can be explained through the use of minimal input parameters. This has implications not only for understanding local and regional dynamics but also has potential to provide simple prediction methods.

The main hydrodynamic factors controlling the resuspension of sediments at a predictable scale are tides (both semi-diurnal and spring-neap) and wind-driven waves. Tides act from the bed to stir up loose bed sediments and are efficient in shallow regions with high tidal current speeds. Whereas, wind-generated waves at the ocean surface drive mixing through the water column, reducing in vigour with increasing depth. driven suspension acts from the air-sea interface downwards. The effect of wind upon resuspension is most apparent in areas of either low tidal activity or areas where the tide alone is unable to bring sediment to the surface, such as in deeper water.

Whereas hydrodynamic forcings act to resuspend sediment, flocculation of particles into larger aggregates acts to increase the settling speed of suspended particles, hampering the impact of hydrodynamic forcings. The most effective form of flocculation of particles occurs in the presence of organic-derived polysaccharides such as those excreted by marine organisms. To represent the presence of this organic material within the statistical models, Chlorophyll-a concentrations are used as a proxy. Bathymetry is an important factor, with hydrodynamic influence on resuspension of sediments diminishing with depth. For the purpose of these statistical models, because the coefficients vary spatially and with the bathymetry, they take into account the influence of depth.

*Tides*

In order to represent the spring-neap variability of the tides, the maximum daily tidal current

speed in metres per second ($ms^{-1}$) is used, calculated from the tidal phases and amplitudes from the latest iteration of the global TPXO 8.0 Atlas solution (Egbert et al., 1994; Egbert & Erofeeva, 2004; Egbert et al., 2010; Ray et al., 2010). This was chosen as an alternative to the spatially centralised SHOM Brest tidal coefficient favoured by Rivier et al., 2012 (SHOM, 2000), in order to better represent spatial variability in tidal activity. The values were calculated for each day and each latitude and longitude grid location of the shelf region. The model output was interpolated from the 1/30th degree output of TPXO to $10km^2$ for the statistical model, with the maximum tidal current speed for each day calculated (Figure 37).

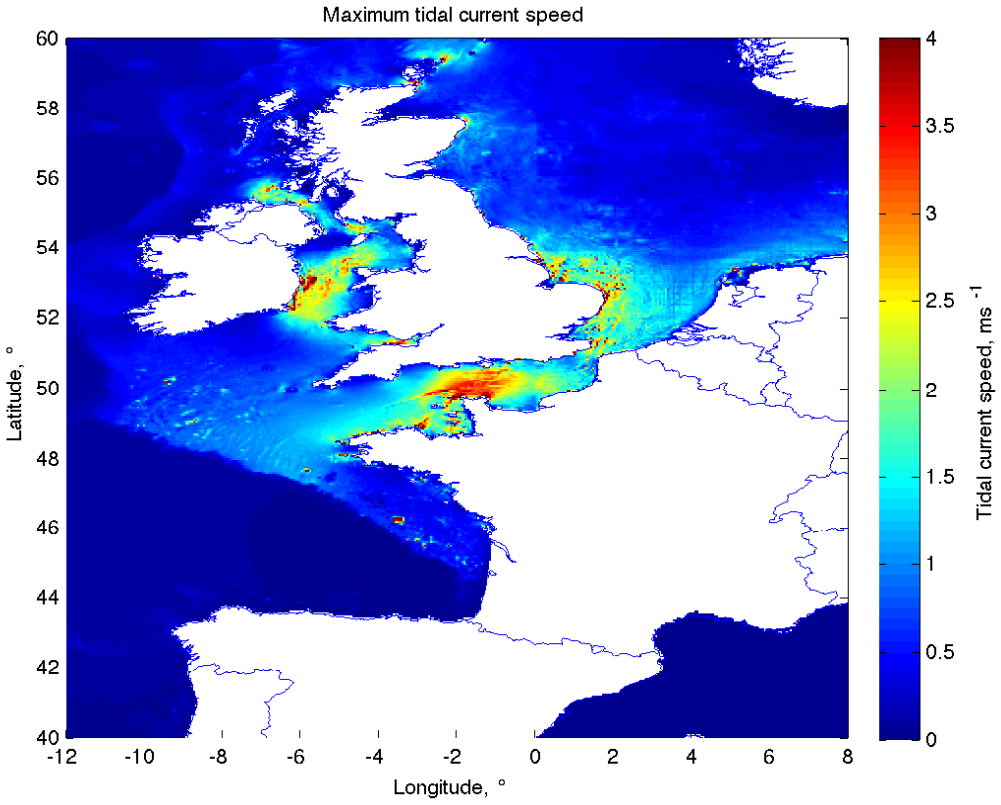


Figure 37: Maximum tidal current speed from the TPXO 8.0 output of the north-west European shelf.

*Wind*

The wind speed used as an input is taken from the ECMWF (European Centre for Medium-term Weather Forecasts) wind model output (Figure 38). The wind speed at the ocean surface is measured in metres per second ($ms^{-1}$), calculated from the U and V orthogonal velocity components using the Pythagorean theorem. The output was interpolated from the $25km^2$ grid to $10km^2$ and 10 days to 1 day for the statistical model. Wind speed was chosen instead of the significant wave height as with Rivier et al. (2012), to take account of the varied influence of the wind speed on the ocean surface as used in the numerical model designed by Bowers (2003).

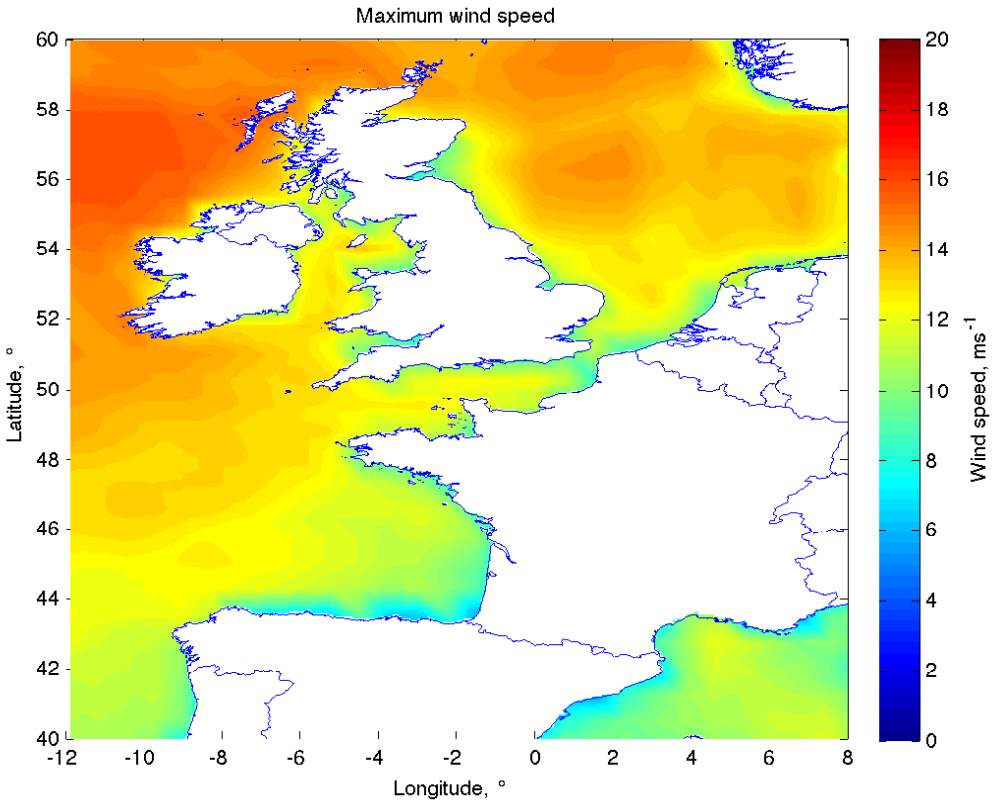


Figure 38: Maximum windspeed taken from a year of ECMWF model output of the north-west European shelf.

*Bathymetry*

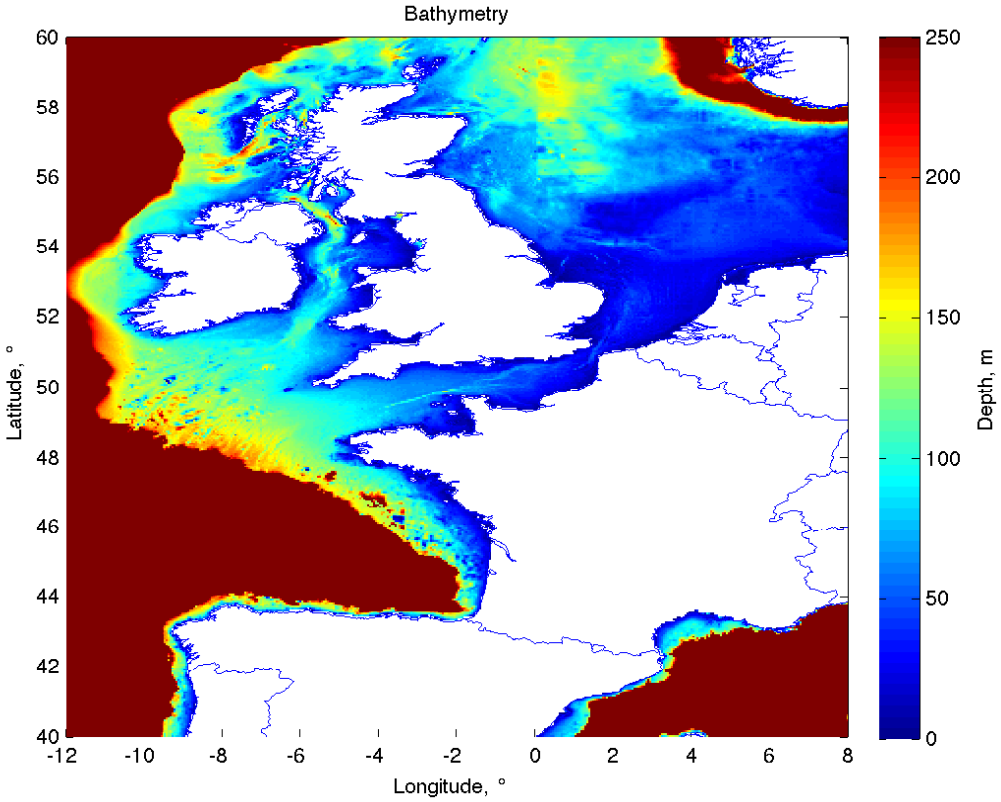


Figure 39: GEBCO bathymetry of the north-west European shelf. The scale is limited to 250m to accentuate shallower waters. Areas of the shelf in this region may exceed 2500m off the continental shelf.

The bathymetry of the northwest European shelf is shown to have a steep drop along the shelf break west of France and Ireland (Figure 39). The Irish Sea is observed to have a channel between the Scotland-Northern Ireland entrance and the Republic of Ireland-England entrance, which is approximately 150m deep. Elsewhere in the Irish Sea, the North Sea and the English Channel, the depth is shown to vary between 0 and 100m.

*Suspended sediment and Chlorophyll-a concentrations*

Suspended sediment and Chlorophyll-a concentrations were obtained from the Ifremer publicly-available database of remote sensing observations. The suspended sediment and Chlorophyll-a concentrations were calculated from remote sensing reflectance from MODIS Aqua (Gohin et

al., 2005; Gohin et al., 2011; Hu et al., 2012). In order to include concentrations for each day, the observations were averaged over 10x10 sets of $1km^2$ resolution observations (Fig. 35; 36), in order to reduce the impact of atmospheric correction failure upon the input data to the model. Figures 33 and 34 show the percentage of days where atmospheric correction was successful over the shelf region, both in each month of the year and over the entire MODIS Aqua period for this study from 2002 to 2015.

| Model | Formulation, SPM(day,lon,lat) = |
|---|---|
| 1 | $SPM_T = (a_1(lon,lat)sin(\frac{2\pi(day-a_2(lon,lat))}{365}) + a_3(x,y)) * Tide(day,x,y)$ |
| 2 | $SPM_{TW} = (b_1(lon,lat)sin(\frac{2\pi(day-b_2(lon,lat))}{365}) * Wind(day,x,y)) + SPM_T$ |
| 3 | $SPM_{TWC} = (c_1(lon,lat)sin(\frac{2\pi(day-c_2(lon,lat))}{365}) * (\frac{1}{Chl(day,lon,lat)})) * SPM_{TW}$ |

Table 11: Statistical model formations used within the statistical modelling chapter. The table details all three models, $SPM_T$ (tide only), $SPM_{TW}$ (tides and wind) and $SPM_{TWC}$ (tides, wind and Chlorophyll-a). The inputs are as detailed above: the tidal current speeds are calculated from TPXO 8.0 Atlas solution; the wind speed from the ECWMF wind model and the suspended sediment and Chlorophyll-a concentrations were remotely-sensed using MODIS Aqua. The grid locations are represented by lon for longitude and lat for latitude.

A key factor in the resuspension of sediments is the settling speed of particles, which increases as particles flocculate. Particles are expected to flocculate most in the spring and summer months, when photosynthetic activity generally peaks, causing high particle settling speeds. In contrast, in the winter when photosynthetic activity is often lower, flocculation is less efficient and thus the settling speed of particles would be expected to be at its lowest. To take account of this seasonal variation in flocculation, the production of the model involves a least-squares regression to fit a sine curve coefficient upon the forcings of the wind, the tides and Chlorophyll-a. The model assumes that the coefficients will vary sinusoidally, although the amplitude and phase are allowed to vary for the regression aiming to take account of regions with little seasonal variability represented by a sine curve. Rivier et al. (2012) depended solely upon Chlorophyll-a to derive the influence of flocculation, with the inclusion of Chlorophyll-a in this model aiming to build upon the imposed sinusoidal variability.

# 14 Results

## 14.1 Suspended particulate matter in north-west Europe

Figure 40 shows the average of all remotely-sensed concentrations of suspended matter within each season, observed within the period of June 2002 and May 2015. Figure 41 shows the remotely-sensed concentrations of suspended matter at three locations (one in the Irish Sea, one in the English Channel and one in the North Sea).

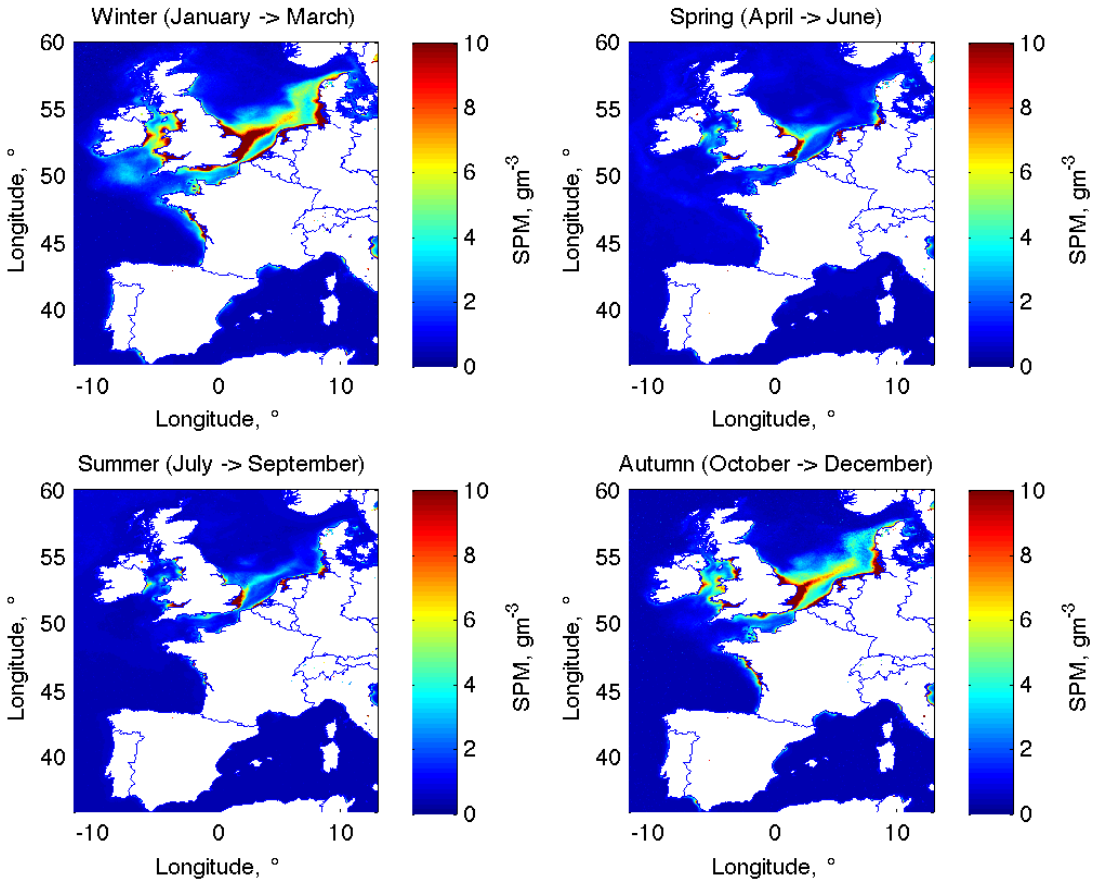


Figure 40: Average suspended matter concentration from usable data observed in Winter, Spring, Summer and Autumn from MODIS-Aqua images between 2002 and 2015.

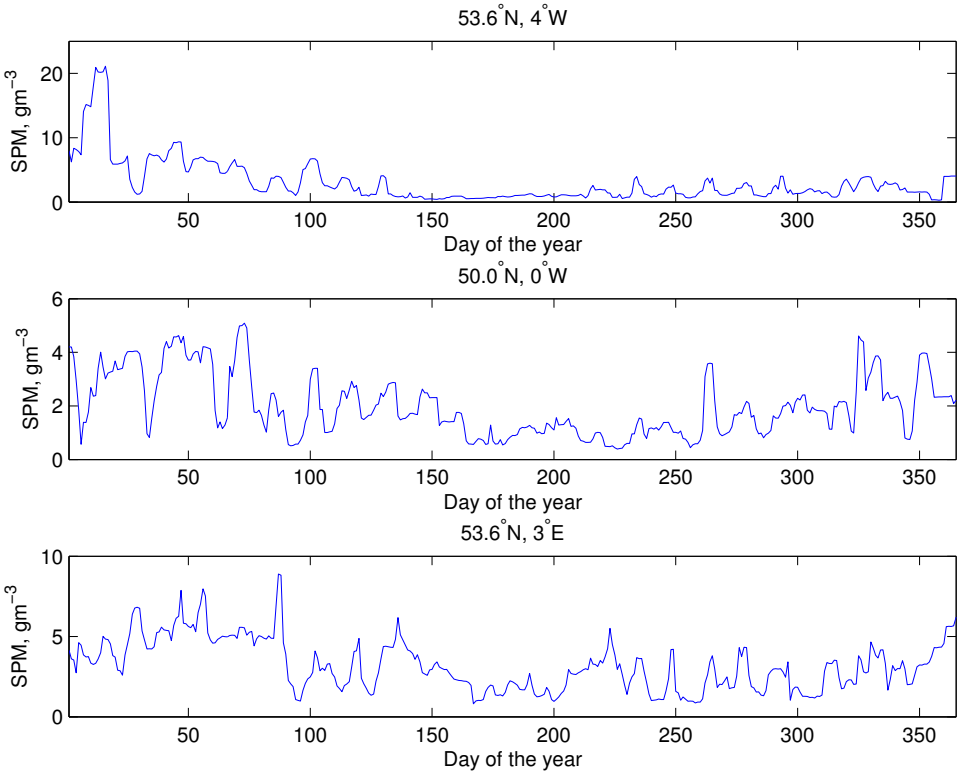


Figure 41: Remotely-sensed suspended particulate matter concentration time series from MODIS in 2012 at three locations: the Irish Sea, the English Channel and the North Sea, as shown in figure 46.

### Spatial variability

The concentration of suspended particulate matter is shown to be highest along the Irish Sea coastline and in the southern North Sea, surrounding the East Anglian coastal region, with a large plume of suspended material. A high concentration of SPM is also observed around the coast of the Isle of Wight in the north central English Channel. In the figure for the spring-averaged concentration, there is a noticeably higher concentration on the shelf which is believed to be due to the presence of coccolithophores and is not non-algal (Balch et al., 2005). Coccolithophores peak in concentration when the water is less turbid, the level of turbulent activity drops and their is a high level of biological productivity, peaks in coccolithophores therefore most commonly coincide with the spring bloom and the summer months.

### Temporal variability

The concentration of suspended material is observed to vary from the highest concentration in the winter, where wind and wave activity are at their greatest to the summer where the concentration of suspended material is at its lowest. This effect is exacerbated by the seasonal variability in the settling speed of particles due to increased flocculation in the summer, resulting in an even lower concentration at this time than would otherwise be expected if only accounting for variability in wind and wave activity.

## 14.2 Spring-neap tidal variability in SPM

The sum of the M2 and S2 tidal harmonics leads to tidal range variability at a cycle of approximately 14 days. Within this cycle, the period of the largest tidal range is referred to as the spring tide, the period of the smallest tidal range referred to as the neap tide. During a spring tide, a larger volume of water must be moved between the ebb and flood and as such the tidal current speeds are greater. The result is a variation in the maximum current speed observed in approximately 14 day cycles, with resuspension rates peaking following the spring tide and therefore also the concentration of suspended material (Figure 42).

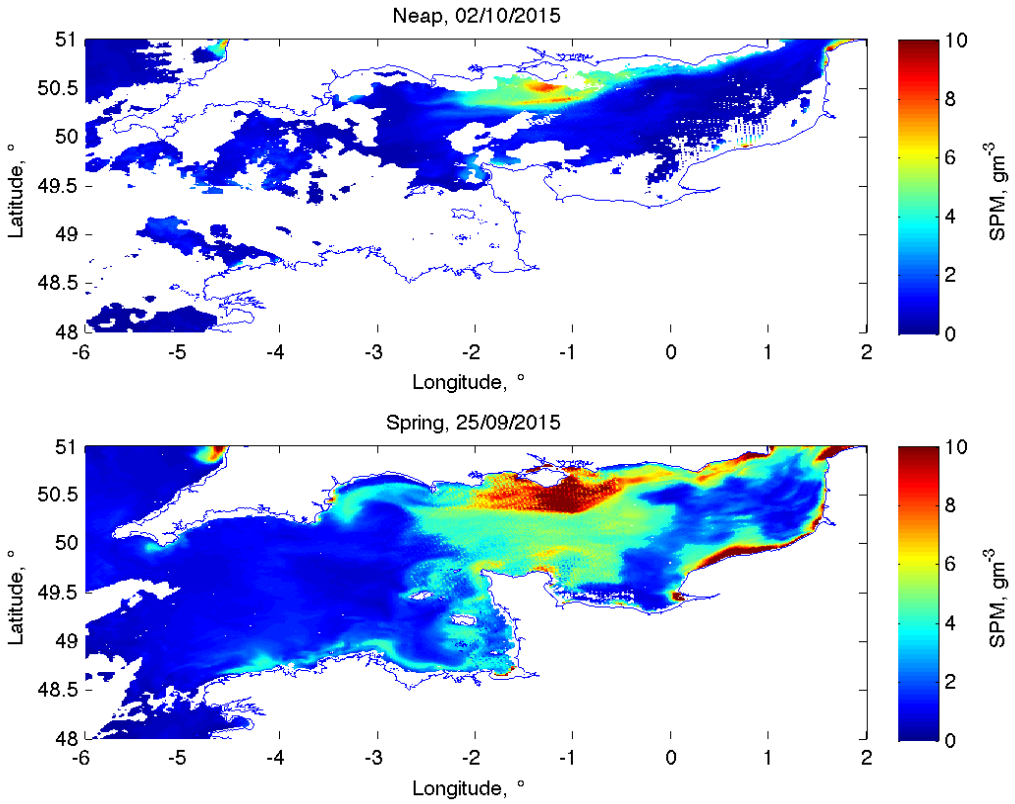


Figure 42: Remotely-sensed suspended matter concentrations on a neap and successive spring tide from MODIS-Aqua. The neap tide image was taken on the 2nd October 2015, with the spring tide image was taken on the 25th September 2015.

Figure 43 demonstrates the amplification of the concentration of suspended particulate matter

on a spring tide over that observed on a neap tide. The area surrounding the North coast of France and the central English Channel are shown to observed concentrations on the spring tide up to 5 times that observed on the neap tide.

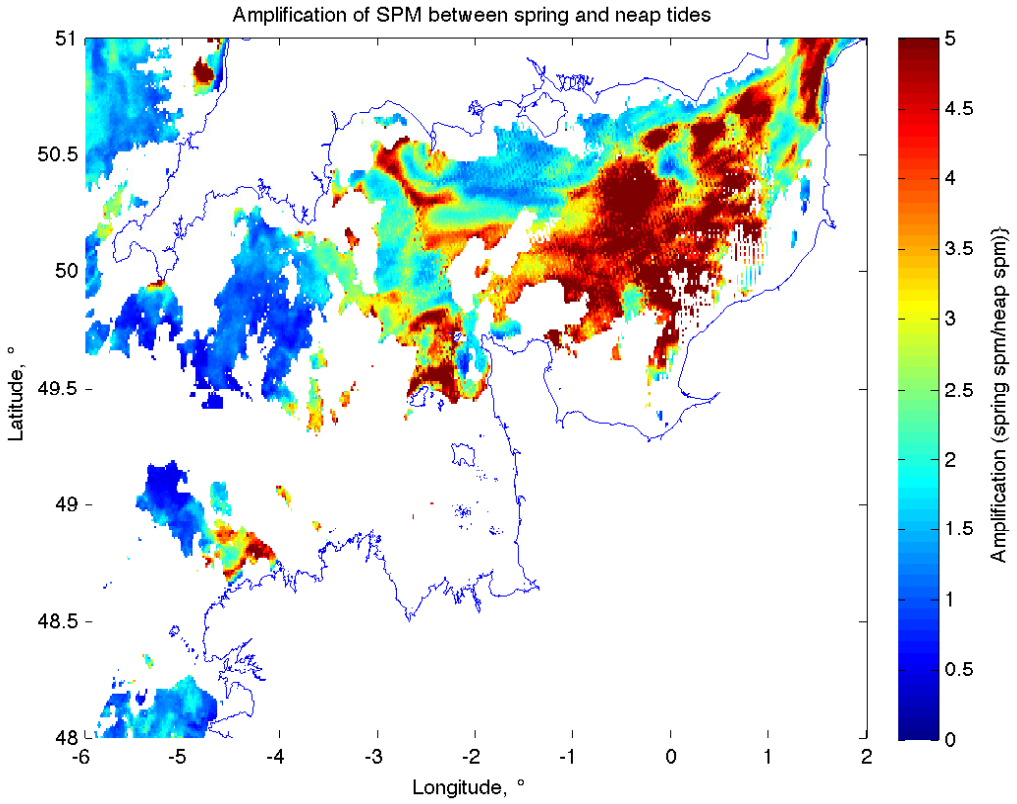


Figure 43: Amplification of remotely-sensed suspended matter concentrations on the spring tide over that observed on the neap tide by MODIS-Aqua. The neap tide values used were taken on the 2nd October 2015, with spring tide values taken on the 25th September 2015. Values off the land that are white signify points where data was unavailable for one or other of the two datasets.

## 14.3 Storm-events

During storms, large wind-driven waves drive a large increase in the resuspension rate. As storms are most prevalent in the winter, when also the settling speed is lower (Bowers, 2003; Ellis et al., 2008), sediment resuspended by storms at this time of the year is liking to remain in suspension for several days to weeks following the initial event.

The winter period of 2013 to 2014 was hailed as the stormiest winter on record by meteorological agencies in both the U.K. and Ireland (Matthews et al., 2014). The effect of this extreme winter was detailed in Gohin et al. (2015), associated to this thesis.

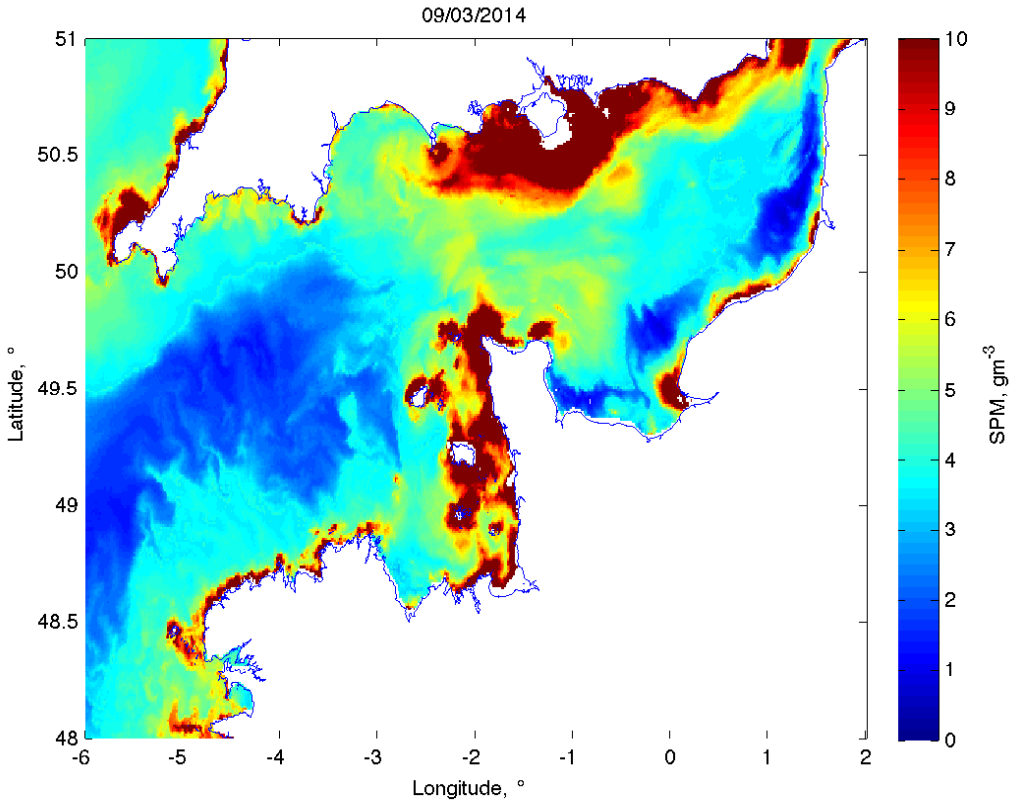


Figure 44: Remotely-sensed suspended matter concentration following a storm event from MODIS-Aqua. The image was taken on the 9th March 2014.

Figure 44 shows large areas of turbidity, notably around the Isle of Wight and the area of Cherbourg. The central English Channel (especially towards the western mouth) are shown

to observed far lower concentrations than the two adjacent coastlines.

## 14.4 Chlorophyll-a in north-west Europe

Chlorophyll-a concentration can be used as a representation of the phytoplankton productivity in the ocean. The Chlorophyll-a data for this thesis was processed using the NASA algorithm described by Hu et al. (2012).

Figure 45 shows the average of all remotely-sensed concentrations of Chlorophyll-a within each season, observed between the period of June 2002 and May 2015.

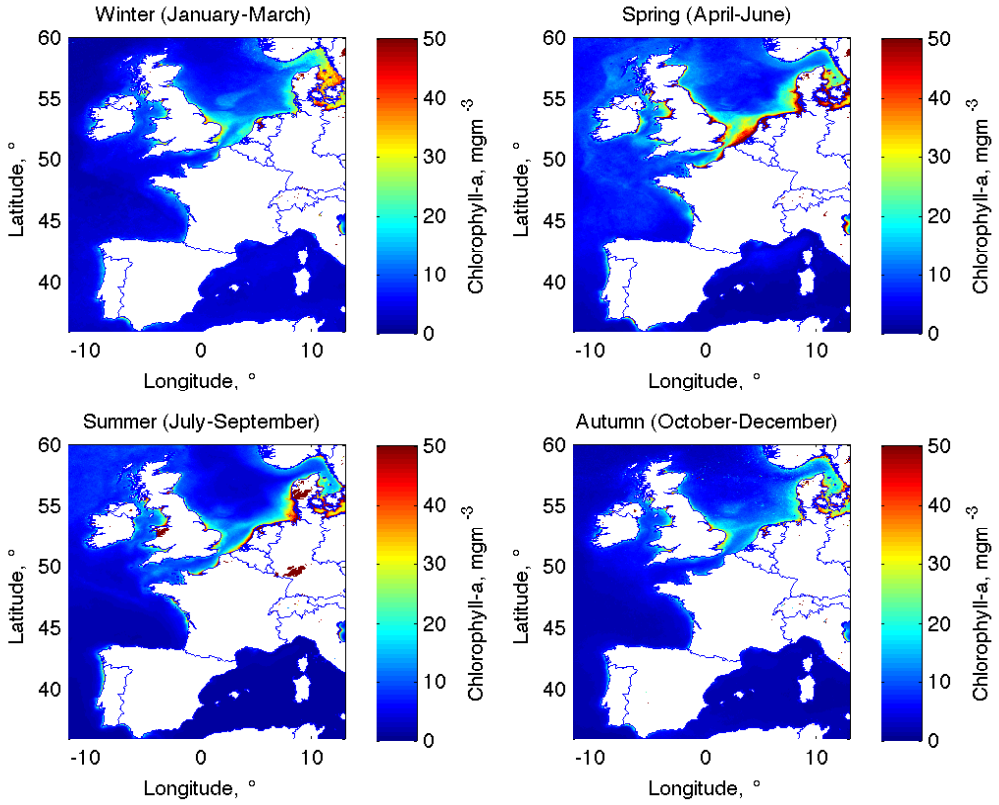


Figure 45: Average Chlorophyll-a concentration from usable data observed in Winter, Spring, Summer and Autumn from MODIS-Aqua images between 2002 and 2015.

### Temporal variability

Chlorophyll-a concentration is shown to peak in the spring period (between April and June) (Figure 45), coinciding with the spring phytoplankton bloom. Similarly, notable mainly in the Spring and Summer, there is blooming along the shelf break (off the west coast of Ireland), which causes increased concentrations of Chlorophyll-a.

### Spatial variability

The locations with the highest concentration of Chlorophyll-a are generally observed to be shallower coastal areas (such as in Liverpool Bay). In the Spring period, the concentration is shown to peak further from the coastline in the southern North Sea.

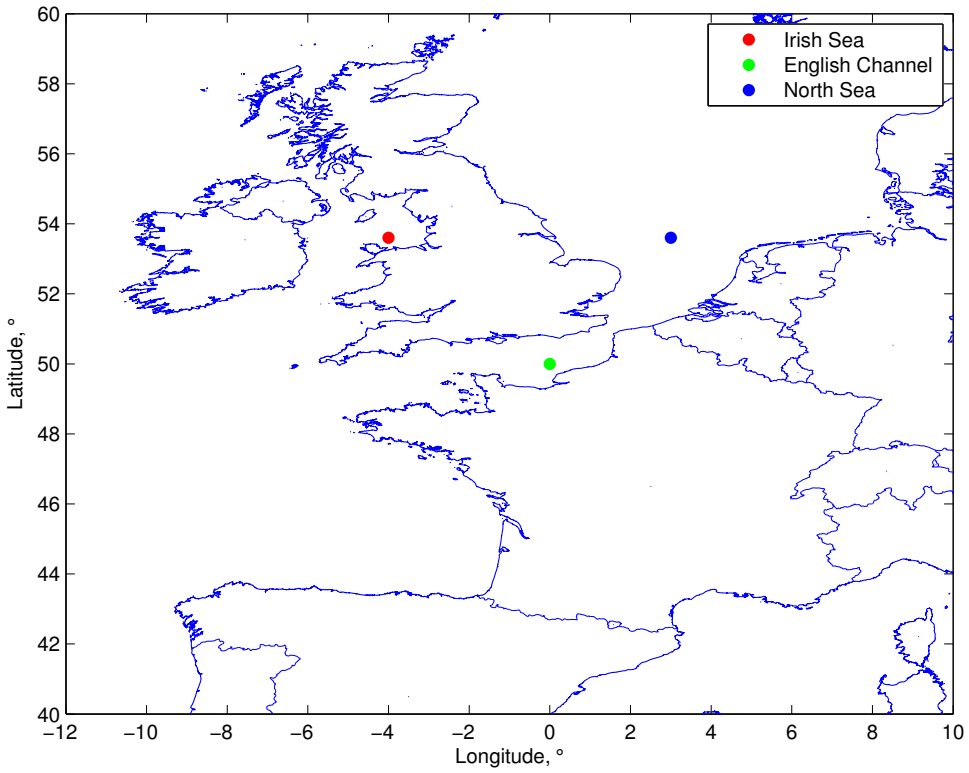


Figure 46: Location of observation points

Figure 47 shows a time series of Chlorophyll-a concentration observed in 2012 at three locations (see figure 46).

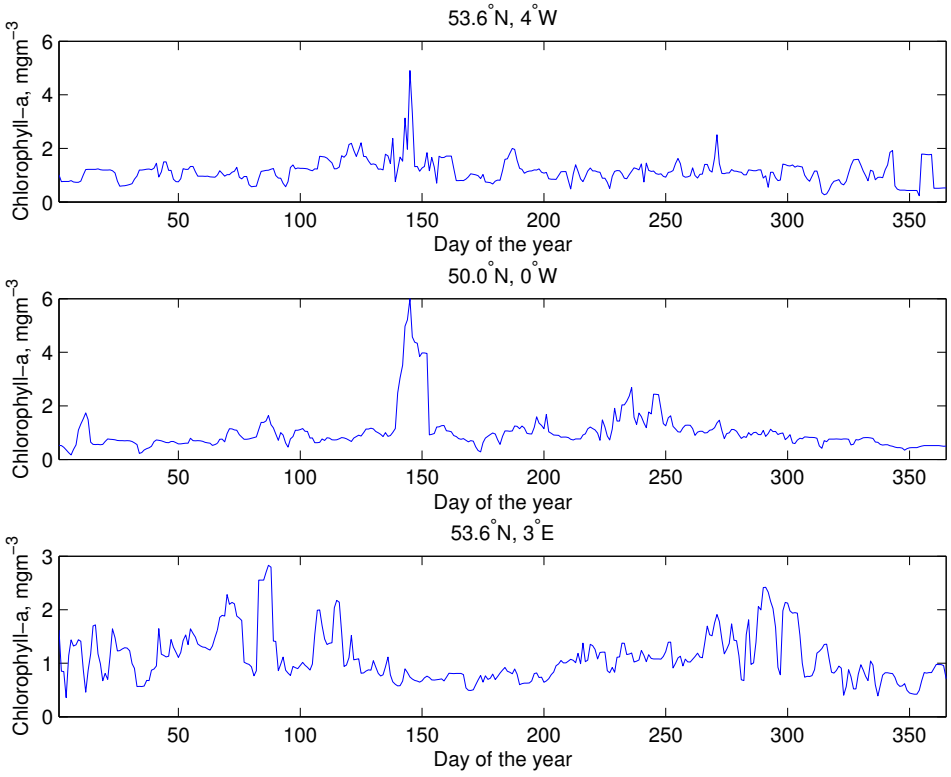


Figure 47: Remotely-sensed Chlorophyll-a concentration time series from MODIS in 2012 at three locations: the Irish Sea, the English Channel and the North Sea, as shown in figure 46.

All three locations show peaks in the spring period, with secondary peaks later in the year (coinciding with the autumn bloom). Despite similar temporal variability, the spring peaks are separated by almost two months (day 90 - day 150) between the Irish Sea location ($53.6°N$, $4°W$) and the North Sea location ($53.6°N$, $3°E$). Additionally the Irish Sea location and English Channel location ($50°N$, $0°W$) have a seasonal range twice that of the North Sea location (0-6$mgm^{-3}$ in comparison to 0-3$mgm^{-3}$).

## 14.5 Model 1, Tides

$SPM_T = (a_1(lon, lat)sin(\frac{2\pi(day - a_2(lon,lat))}{365}) + a_3(x, y)) * Tide(day, x, y)$

*Irish Sea (*$53.6°N$, $4°W$*)*

The top time series in Figure 48 shows the output of model 1 alongside the remotely-sensed observations for the location in the Irish Sea (red point in Figure 46). The seasonal variability in the concentration is predicted well by model 1, with peaks in the concentration during the winter months and troughs in the summer when the concentration drops, with the highest $R^2$ of the three locations, 0.332. The main secondary feature of the variability is the spring-neap tidal variation, which is represented in model 1. The model does not represent the irregular peaks in concentration, especially during the winter months (January-March 2010) and also as illustrated in summer peaks (July 2010; 2011; 2012), leading to an RMSE of $1.324gm^{-3}$ (10% of the highest observed concentration at this location).

*English Channel (*$50.0°N$, $0°W$*)*

The middle time series in Figure 48 shows the output of model 1 alongside the remotely-sensed observations for the location in the English Channel (green point in Figure 46). Although the features described for the Irish Sea location are also visible in the English Channel, model 1 does not represent the spring-neap variability in concentration to the same degree, with under-prediction in the concentration range in the winter months. This location has the lowest $R^2$ value of the three described, at 0.285. The model does not represent the irregular peaks in concentration observed in the winter months, above the existing seasonal and spring-neap variability, leading to an RMSE of $1.111gm^{-3}$ (13% of the highest observed concentration at this location). In 2010 and 2011, the model is shown to overestimate the concentration during the summer months, maintaining spring-neap variability which is minimal in the remotely-sensed observations.

*North Sea (*$53.6°N$,$3°E$*)*

he bottom time series in Figure 48 shows the output o model 2 alongside the remotely-sensed observations for the location in the North Sea (blue point in Figure 46). The model predicts the seasonal variability in the range of values observed during spring-neap cycles in the North Sea demonstrated by the $R^2$ value of 0.306, however the model predicts a clear spring-neap variability, which is not necessarily as clear in the observations. In comparison to the Irish Sea and English Channel locations, there is a higher level of variability around the model prediction in the observations, with an RMSE of $1.621gm^{-3}$ (12.5$ of the highest observed concentration at this location).

Overall, model 1 is shown to represent the spring-neap tidal variation well at all three locations, matching with the remotely-sensed observations. The model also clearly represents the seasonal variation in the spring-neap concentration range, with a larger range of concentrations in the winter than at the summer at the three locations. The model is shown to underperform in representation of surges in concentration, relating to storms (such as that in the March 2010), where the observations exceed the model prediction. This can also be seen in further erratic peaks (such as those in the summer of 2012), where there are multiple peaks in the concentration which are not represented by the model.

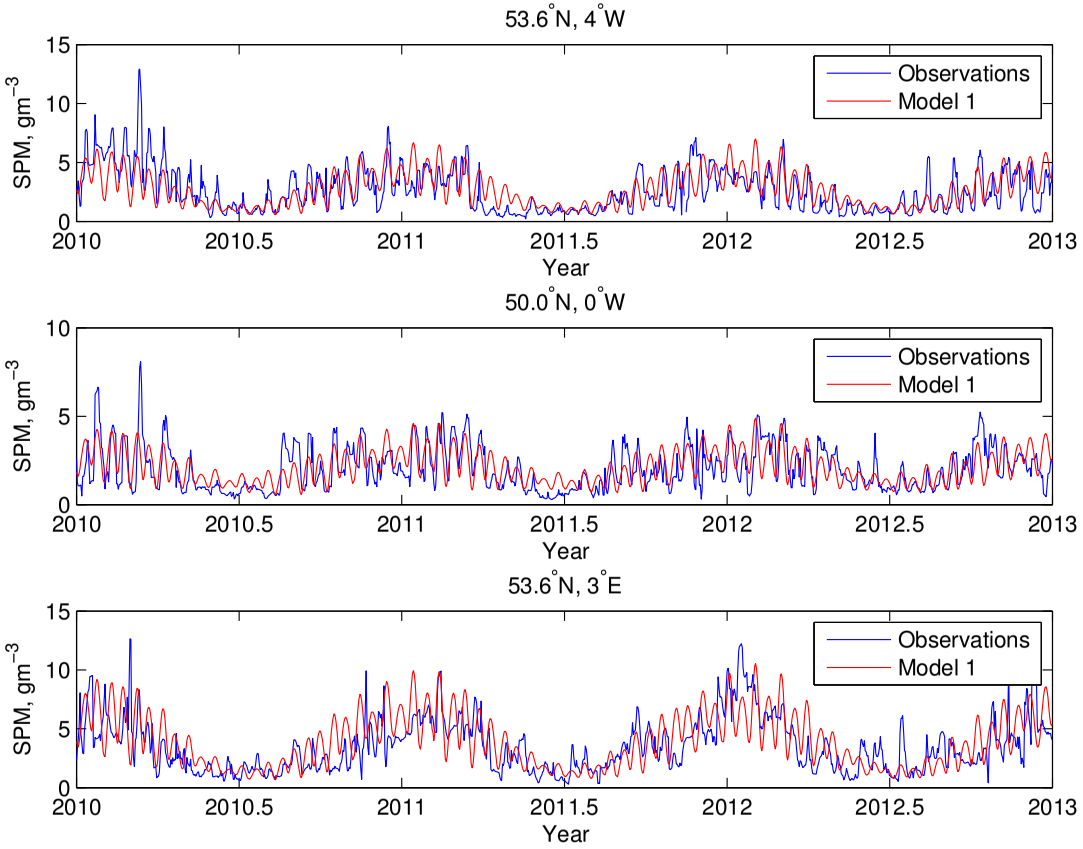


Figure 48: Prediction of suspended sediment concentration using model 1 (tides) alongside remotely-sensed observations. Three locations are included to illustrate the model, one in the Irish Sea ($53.6°N$, $4°W$, $R^2$=0.332, RMSE = $1.324gm^{-3}$), the English Channel ($50.0°N$, $0°W$, $R^2$=0.285, RMSE = $1.111gm^{-3}$) and the North Sea ($53.6°N$, $3°E$, $R^2$=0.306, RMSE = $1.621gm^{-3}$). Locations plotted in Fig. 46.

Figure 49 shows the values of $R^2$ between the statistical prediction from model 1 and the remotely-sensed observations. Over the shelf region, the model is shown to predict over 45% of the variability with $R^2$ values as high as 0.6 in the central Irish Sea and on the East coast of England.

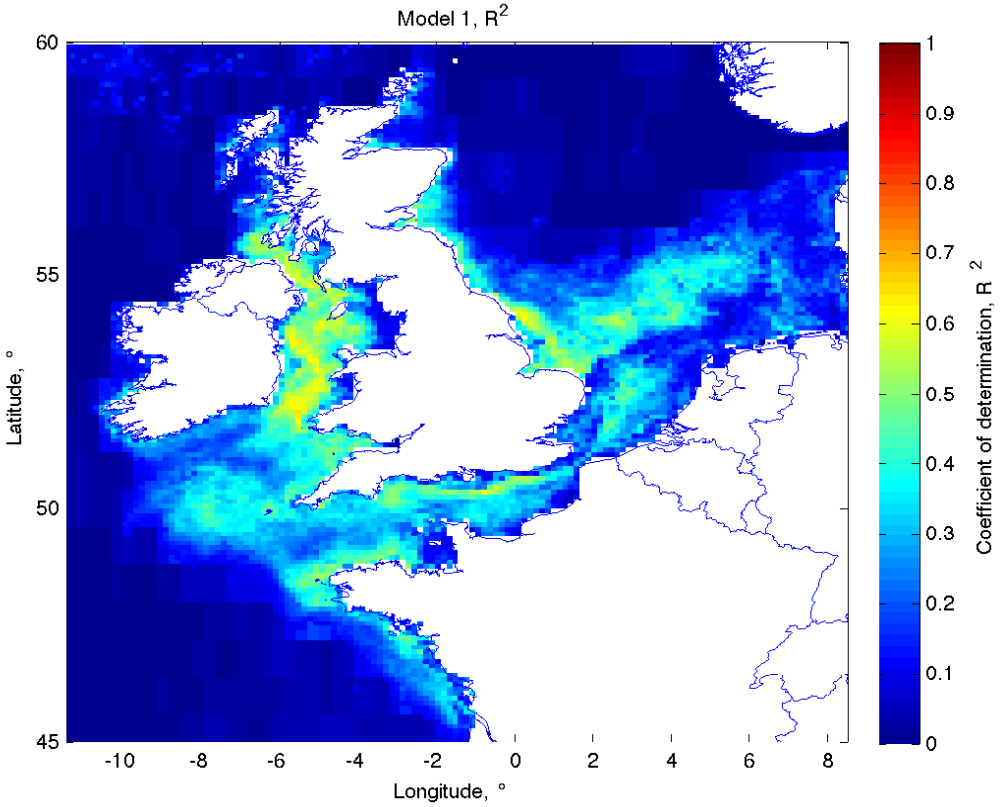


Figure 49: The $R^2$ coefficient of determination between the model 1 prediction and remotely-sensed observations.

Figure 50 shows the root-mean squared error from the statistical model based upon tides. The root-mean squared error of the prediction from model roughly follows the observed concentration, with high error in the coastal regions of the Eastern Irish Sea and off the East Anglian coast.

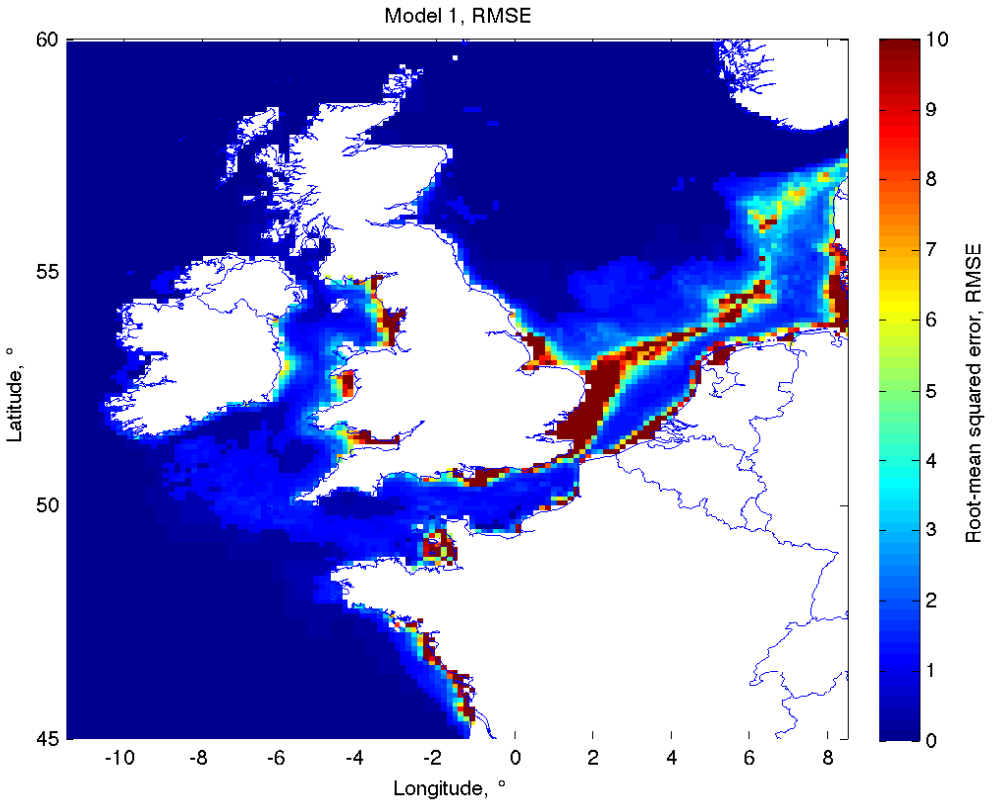


Figure 50: The root-mean squared error, RMSE, between the model 1 prediction and remotely-sensed observations.

The coefficient $a_1$ describes the amplitude of the sine curve fitted to the annual variation in the tidal current speed in a regression with the remotely-sensed observations (Figure 51). High amplitudes are observed in areas with high concentrations, including the Irish Sea and the East Anglian coast. Additionally, high values for $a_1$ are observed off the Shelf, north of Spain and in the Western North Sea.

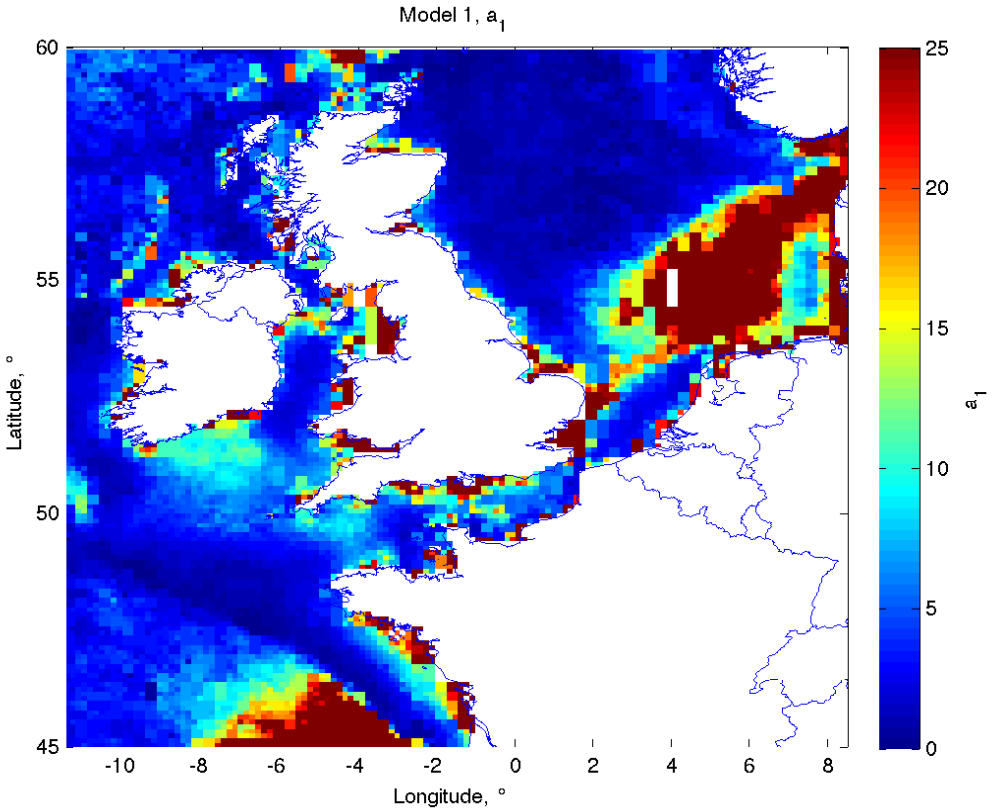


Figure 51: The coefficient $a_1$ representing the amplitude of the sine curve fitted to the annual variation in the tidal current speed in a regression with the remotely-sensed observations.

The coefficient $a_2$ represents the phase of the sine curve fitted to the annual variation in the tidal current speed in a regression with the remotely-sensed observations (Figure 52). The correlated phase difference is shown the be predominately between 80 and 120 days. Values off the shelf are shown to be significantly less, at 20 to 40 days.

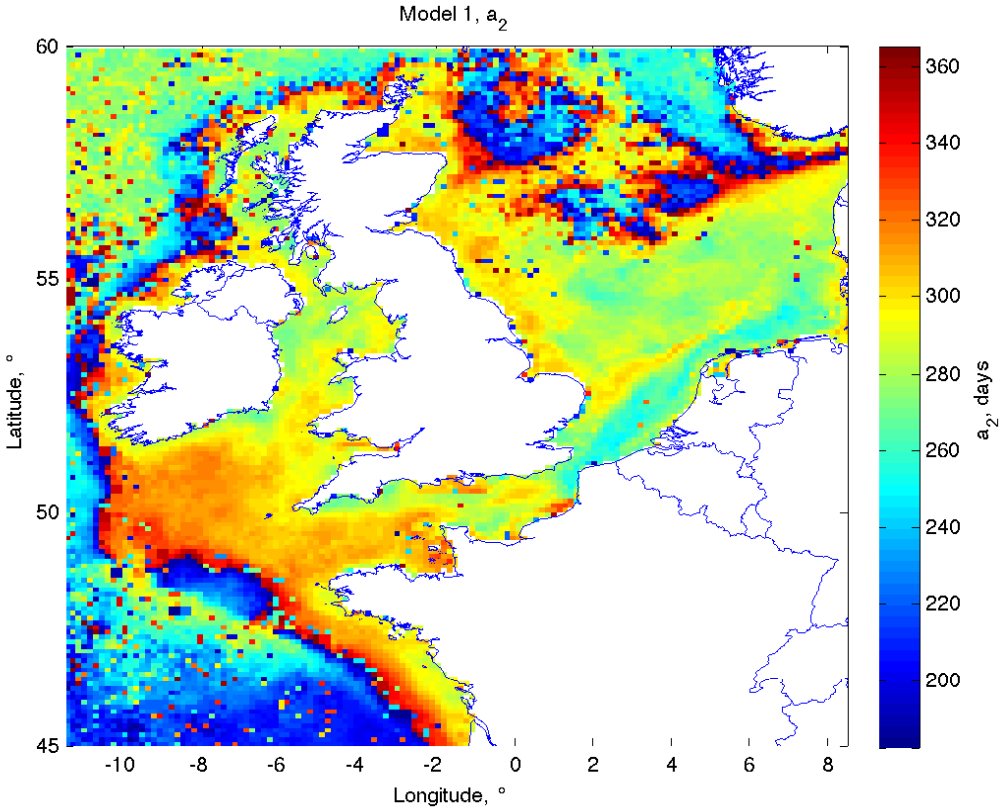


Figure 52: The coefficient $a_2$ representing the phase difference of the sine curve fitted to the annual variation in the tidal current speed in a regression with the remotely-sensed observations.

The coefficient $a_3$ represents the additional component of the sine curve fitted to the tidal current speed in the regression with the remotely-sensed observations, with values ranging between 0 and 30 on the shelf (Figure 53). Values off the shelf are shown to far exceed those on the shelf, where there is a tidal current speed less than $0.25ms^{-1}$ and the depth exceeds 1000m.

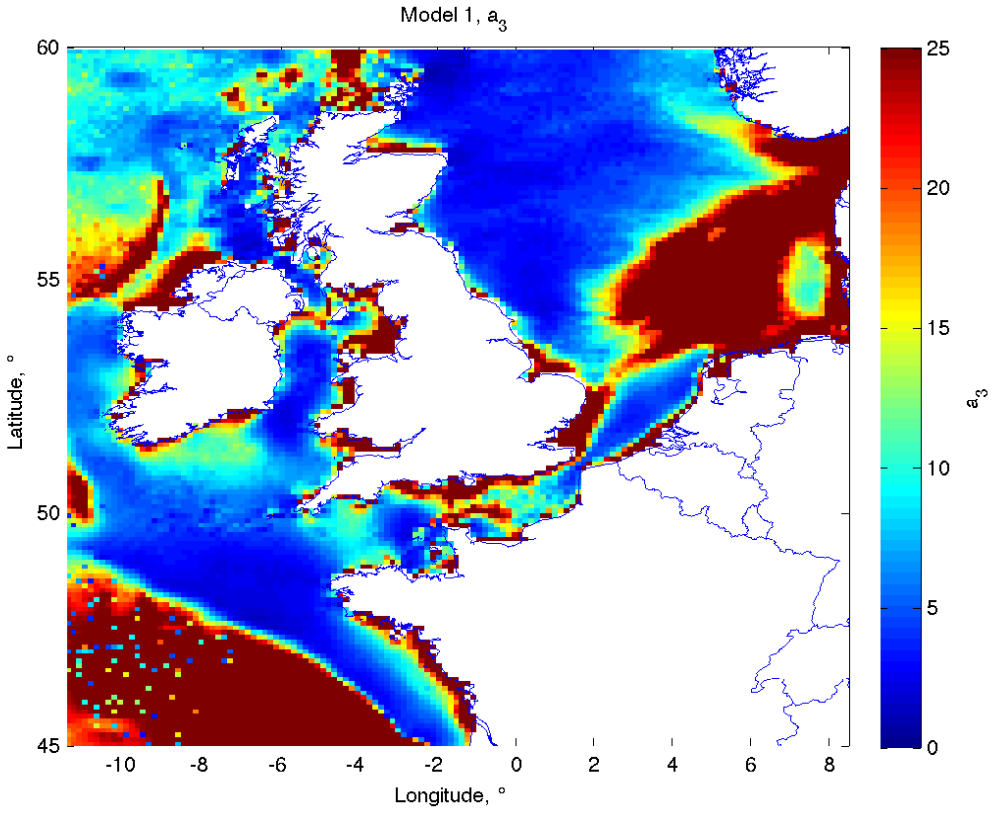


Figure 53: The coefficient $a_3$ representing the additional component of the sine curve fitted to the tidal current speed in the regression with the remotely-sensed observations.

## 14.6 Model 2, Tides & Wind

$$SPM_{TW} = (b_1(lon, lat)sin(\frac{2\pi(day - b_2(lon,lat))}{365}) * Wind(day, x, y)) + SPM_T$$

*Irish Sea (*$53.6°N$, $4°W$*)*

The top time series in Figure 54 shows the output of model 2 alongside the remotely-sensed observations for the location in the Irish Sea (red point in Figure 46). The inclusion of wind within model 2 adds to the representation of peaks in both the winter and the summer. Additionally, there is a reduction in the overestimation of SPM concentration in the summer in comparison to model 1, due to the generally reduced wind speed during the summer months. The inclusion of wind speed adds up to $0.5gm^{-3}$ to the winter concentration prediction and lowers the winter prediction by $0.6gm^{-3}$, bringing the model closer in line with the remotely-sensed observations. Model 2 shows a modest increase in $R^2$ from 0.332 in model 1, to 0.373 in model 2, with a reduction in the RMSE from $1.324gm^{-3}$ in model 1 to $1.121gm^{-3}$ in model 2, most likely associated with the improved winter-summer variability.

*English Channel (*$50.0°N$, $0°W$*)*

The middle time series in Figure 54 shows the output of model 1 alongside the remotely-sensed observations for the location in the English Channel (green point in Figure 46). At this location, there is only minor improvement in the performance of the model, with an $R^2$ of 0.327 over 0.285 in model 1 and a small reduction in the RMSE from $1.111gm^{-3}$ to $1.012gm^{-3}$.

*North Sea (*$53.6°N$,$3°E$*)*

The bottom time series in Figure 54 shows the output of model 2 alongside the remotely-sensed observations for the location in the North Sea (blue point in Figure 46). This location shows the best improvement in model performance of the three locations described with the inclusion of wind. There is a reduction in the summer concentration by up to $0.8gm^{-3}$ in line with the remotely-sensed concentration. Similarly, the addition of wind speed increases the winter concentration prediction by $0.8gm^{-3}$. This can be shown to represent the increased seasonality of the model with the inclusion of wind speed. The $R^2$ at the North Sea location

is shown to increase from 0.306 in model 1, to 0.416 in model 2, with a reduction in the RMSE from 1.621$gm^{-3}$ to 1.406$gm^{-3}$.

The improvement with the inclusion of the wind speed is shown to vary spatially, with locations such as the Irish Sea and North Sea showing improved representation of the seasonal variability in the SPM concentration. In contrast, only minimal improvement from model 1 is shown in the English Channel.

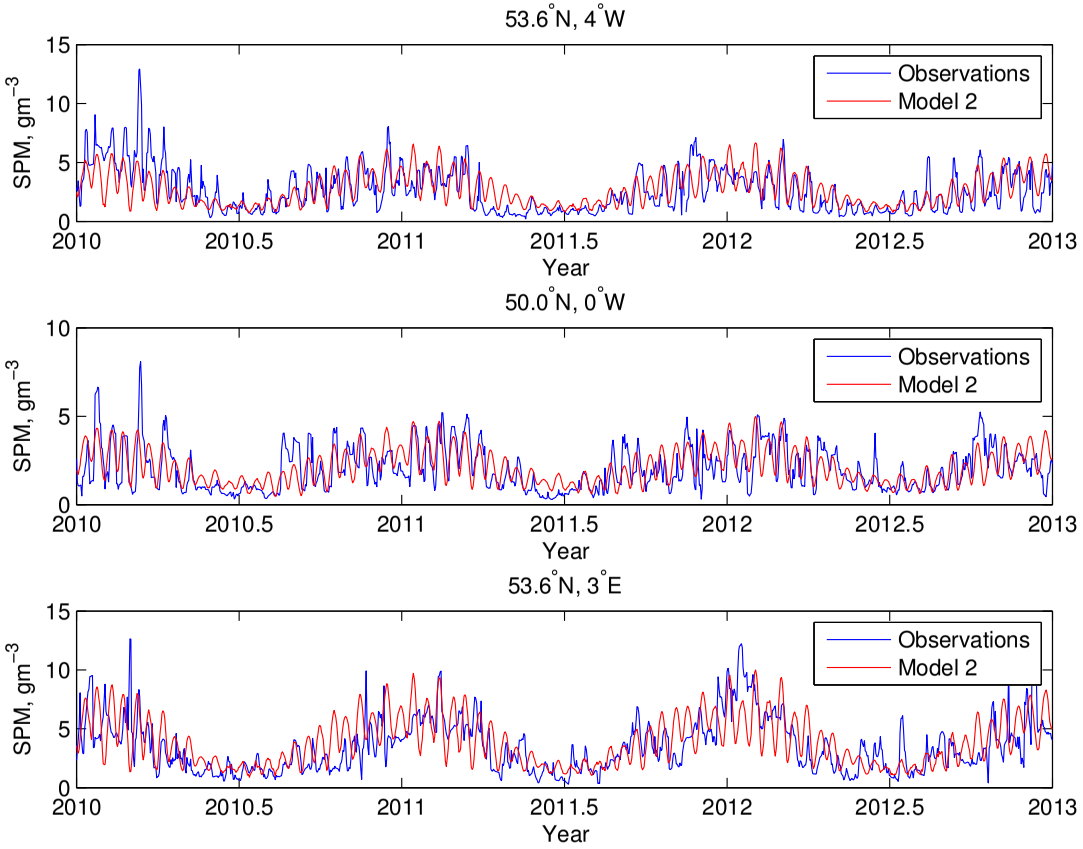


Figure 54: Prediction of suspended sediment concentration using model 2 (tides and wind) alongside remotely-sensed observations. Three locations are included to illustrate the model, one in the Irish Sea ($53.6°N$, $4°W$, $R^2$=0.373, RMSE = $1.121gm^{-3}$), the English Channel ($50.0°N$, $0°W$, $R^2$=0.327, RMSE = $1.012gm^{-3}$) and the North Sea ($53.6°N$, $3°E$, $R^2$=0.416, RMSE = $1.406gm^{-3}$). Locations plotted in Figure 46.

Figure 55 shows the values of $R^2$ between the statistical prediction from model 2 and the remotely-sensed observations.

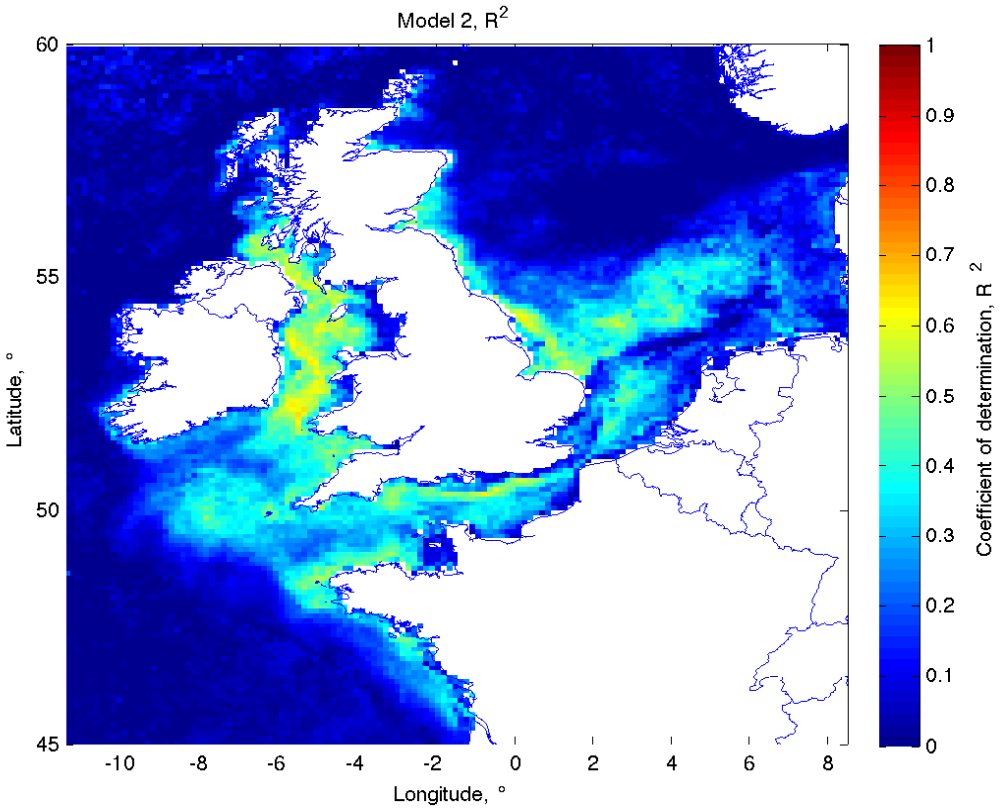


Figure 55: The $R^2$ coefficient of determination between the model 2 prediction and remotely-sensed observations.

Model 2 shows a slight decrease in the coastal error described by RMSE, although this represents less than a 3% decrease in coastal regions (Figure 56).

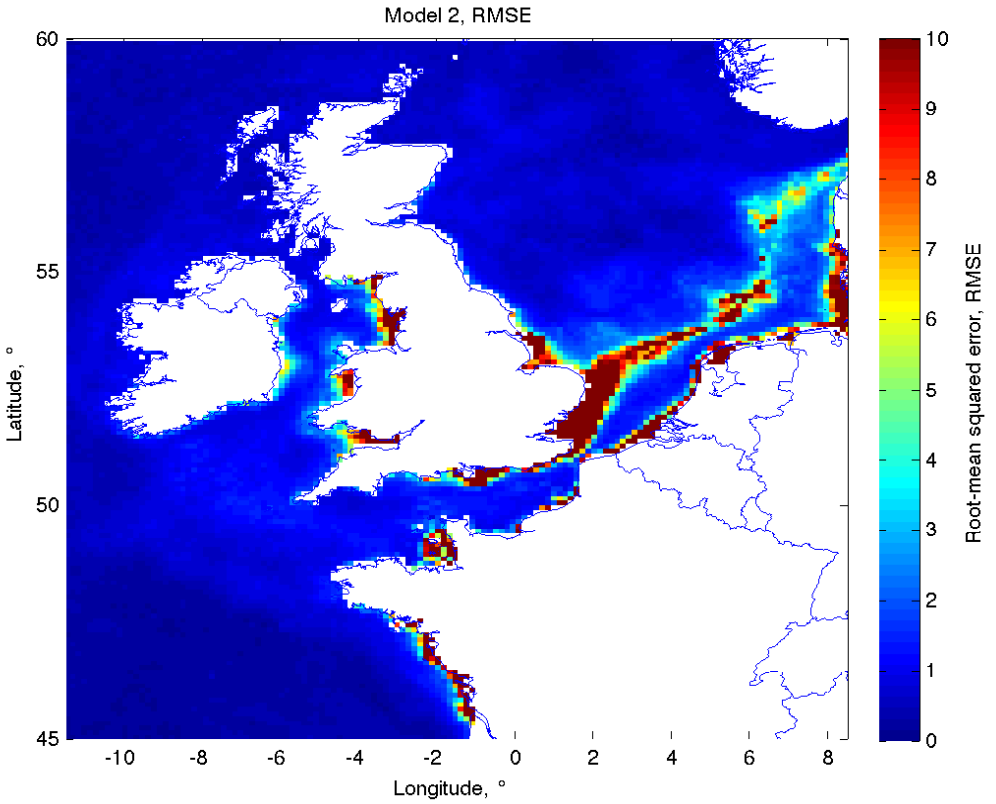


Figure 56: The root-mean squared error, RMSE, between the model 2 prediction and remotely-sensed observations.

The coefficient $b_1$ describes the amplitude of the sine curve fitted to wind speed in the regression with the remotely-sensed observations (Figure 57). In addition to high amplitudes in coastal regions associated with high concentrations (the Irish Sea and southern North Sea), the amplitude is shown to be high on the shelf break region of the Celtic Sea and southern Irish Sea, off the coast of Cornwall.

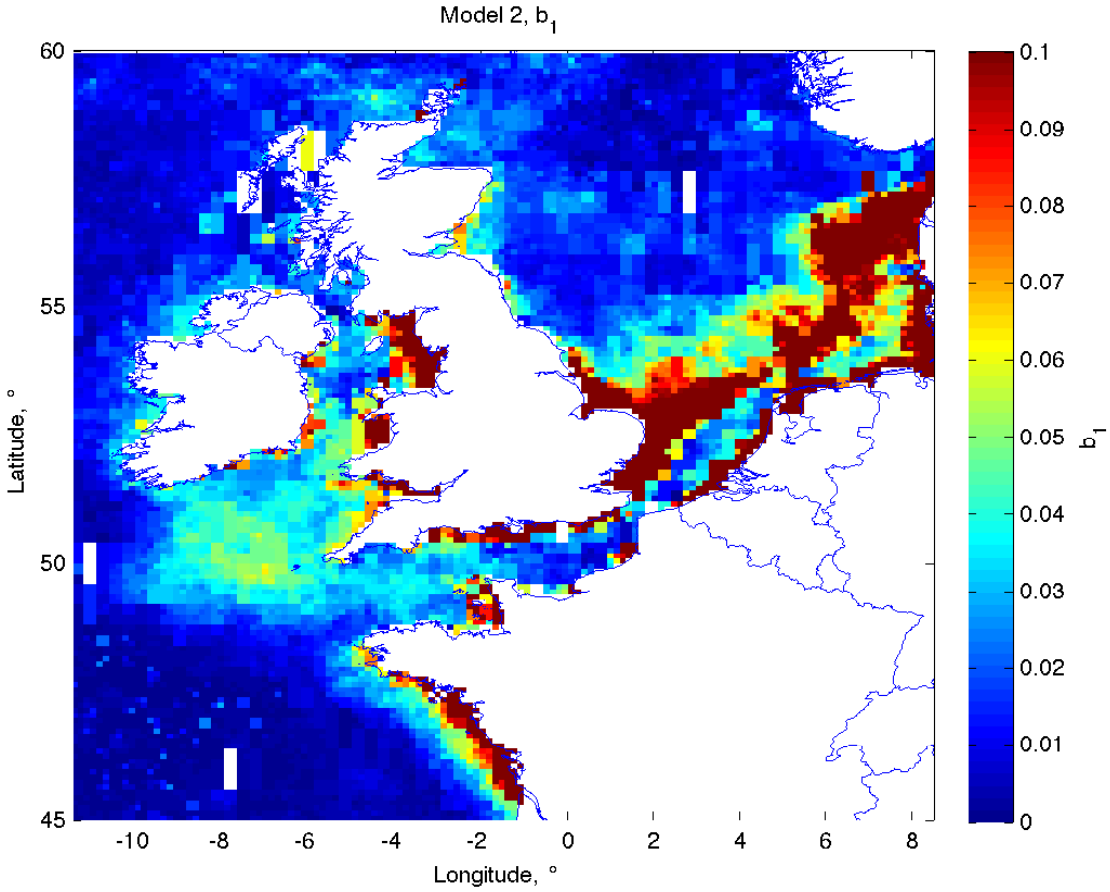


Figure 57: The coefficient $b_1$ representing the amplitude of the sine curve fitted to the wind speed in the regression with the remotely-sensed observations.

The coefficient $b_2$ describes the phase difference of the sine curve fitted to the wind speed in the regression with the remotely-sensed observations (Figure 58). The phase difference is shown to be between 140 and 180 days in the Irish Sea and Celtic Sea, with a phase difference of 100 to 120 days in the North Sea region. The phase difference from the regression is highly variable off the shelf due to the difficulty in regression in a region with a concentration below $1gm^{-3}$.

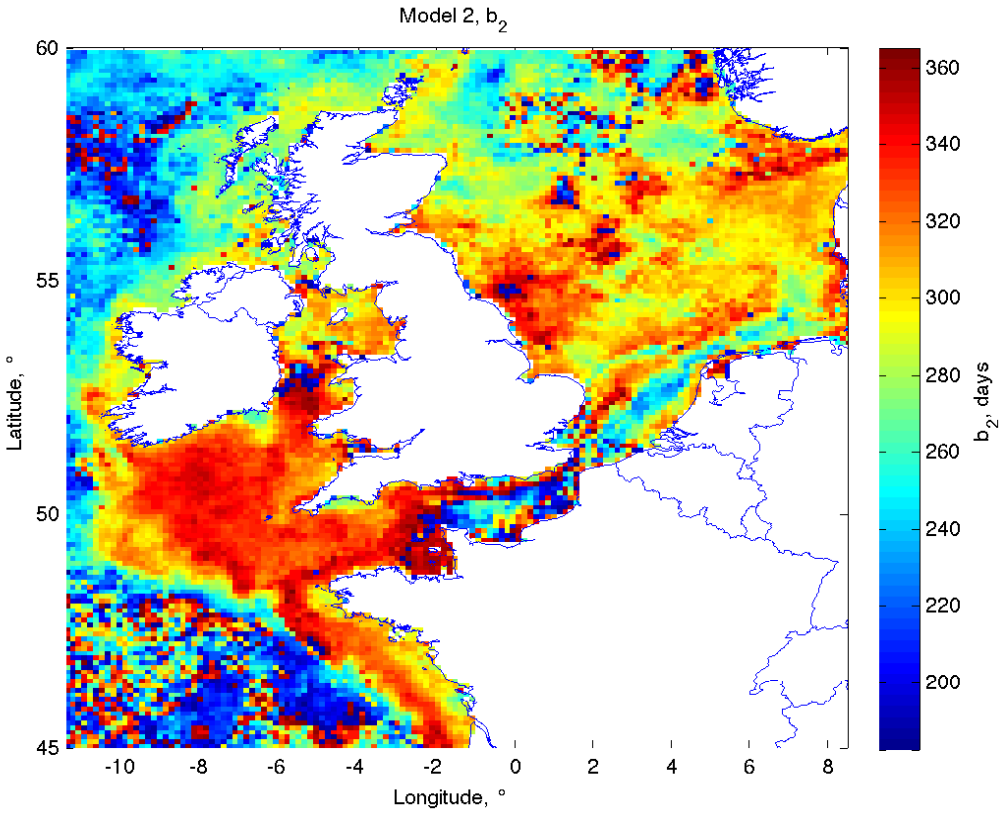


Figure 58: The coefficient $b_2$ representing the phase difference of the sine curve fitted to the wind speed in the regression with the remotely-sensed observations.

## 14.7 Model 3, Tides, Wind & Chlorophyll

$$SPM_{TWC} = (c_1(lon, lat)sin(\frac{2\pi(day - c_2(lon,lat))}{365}) * (\frac{1}{Chlor(day,lon,lat)})) * SPM_{TW}$$

*Irish Sea (*$53.6°N$, $4°W$*)*

The top time series in Figure 59 shows the output of model 3 alongside the remotely-sensed observations for the location in the Irish Sea (red point in Figure 46). The inclusion of Chlorophyll-a into model 3 increases further the seasonality in spring-neap tidal cycle of SPM concentration, with a lower range in the summer and a larger range in the winter. The model shows improved representation of higher concentration peaks (up to $6gm^{-3}$ than model 2), however this leads to overestimation for the spring and summer period (April-September) in the Irish Sea location. The model $R^2$ at this location increases from 0.373 in model 2, to 0.558 in model 3, with a reduction in the RMSE from $1.121gm^{-3}$ in model 2 to $0.896gm^{-3}$ in model 3.

*English Channel (*$50.0°N$, $0°W$*)*

The middle time series in Figure 59 shows the output of model 3 alongside the remotely-sensed observations for the location in the English Channel (green point in Figure 46). Similarly to the Irish Sea location, model 3 shows improved representation of the timing of the peaks in concentration, however the model under-predicts the actual concentration peak in the winter and slightly overestimates in the summer. Due to the increased representation of peak timing in this model, the $R^2$ in this location increases to 0.617 from 0.416 in model 2. Due to the over-prediction of this model, there is only a modest decrease in the RMSE, from $1.012^{-3}$ to $0.823gm^{-3}$.

*North Sea (*$53.6°N$,$3°E$*)*

The bottom time series in Figure 59 shows the output of model 3 alongside the remotely-sensed observations for the location in the North Sea (green point in Figure 46). The inclusion of Chlorophyll-a improves the seasonality in the concentration further, with the minimum and maximum values closely aligned between observation and prediction in both timing and intensity. Despite this, there is only minimal representation of the spring-neap variation

observed through remote-sensing. Model 3 improves on the $R^2$ in model 2, from 0.416 to 0.667, with a reduction in the RMSE from $1.406gm^{-3}$ to $0.821gm^{-3}$

The inclusion of Chlorophyll-a in model 3 is shown to improve the prediction at all three locations, however in the case of the Irish Sea location, this leads to over-prediction for the spring and summer. In contrast, the English Channel location prediction shows that the model under-predicts the concentration in the winter and slightly over-predicts the concentration in the summer.

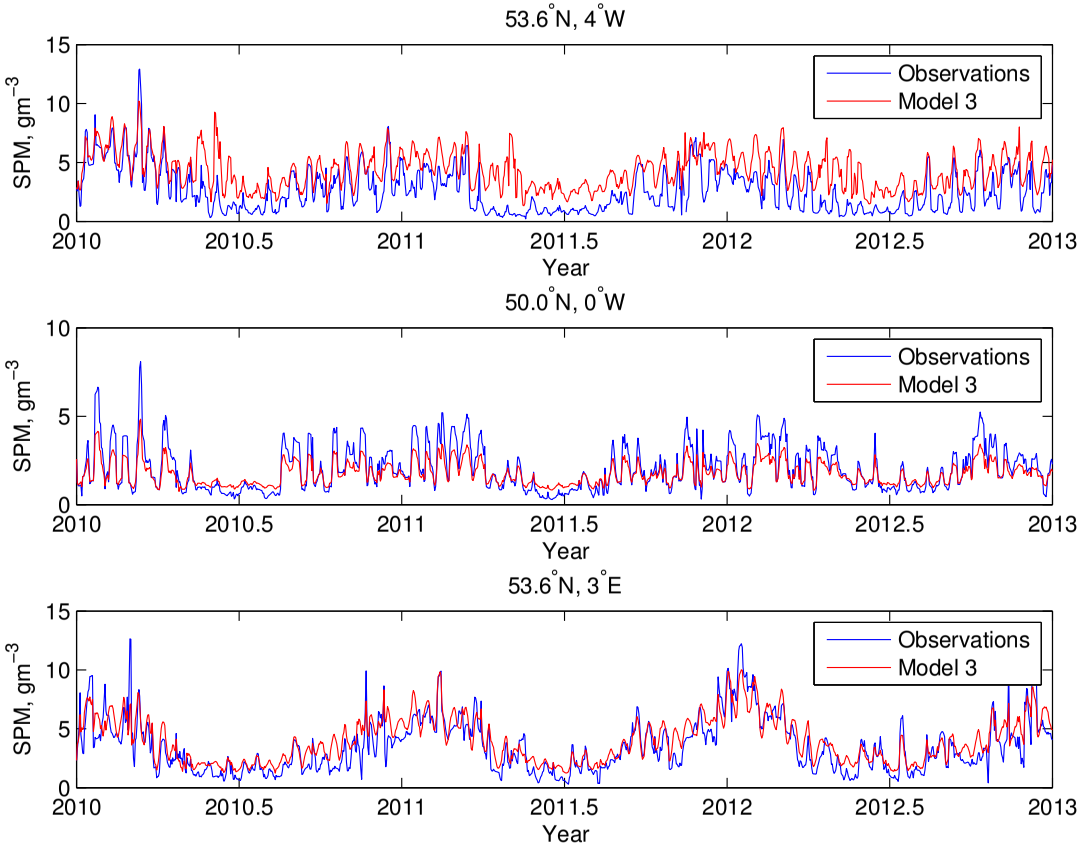


Figure 59: Prediction of suspended sediment concentration using model 3 (tides, wind and Chlorophyll-a) alongside remotely-sensed observations. Three locations are included to illustrate the model, one in the Irish Sea ($53.6°N$, $4°W$, $R^2$=0.558, RMSE = $0.896gm^{-3}$), the English Channel ($50.0°N$, $0°W$, $R^2$=0.617, RMSE = $0.823gm^{-3}$) and the North Sea ($53.6°N$, $3°E$, $R^2$=0.667, RMSE = $0.821gm^{-3}$). Locations plotted in Figure 46.

Figure 60 shows the prediction $R^2$ of the suspended sediment concentration using model 3. Model 3 improves the prediction $R^2$ within stratifying regions including the central Irish Sea and the English Channel.

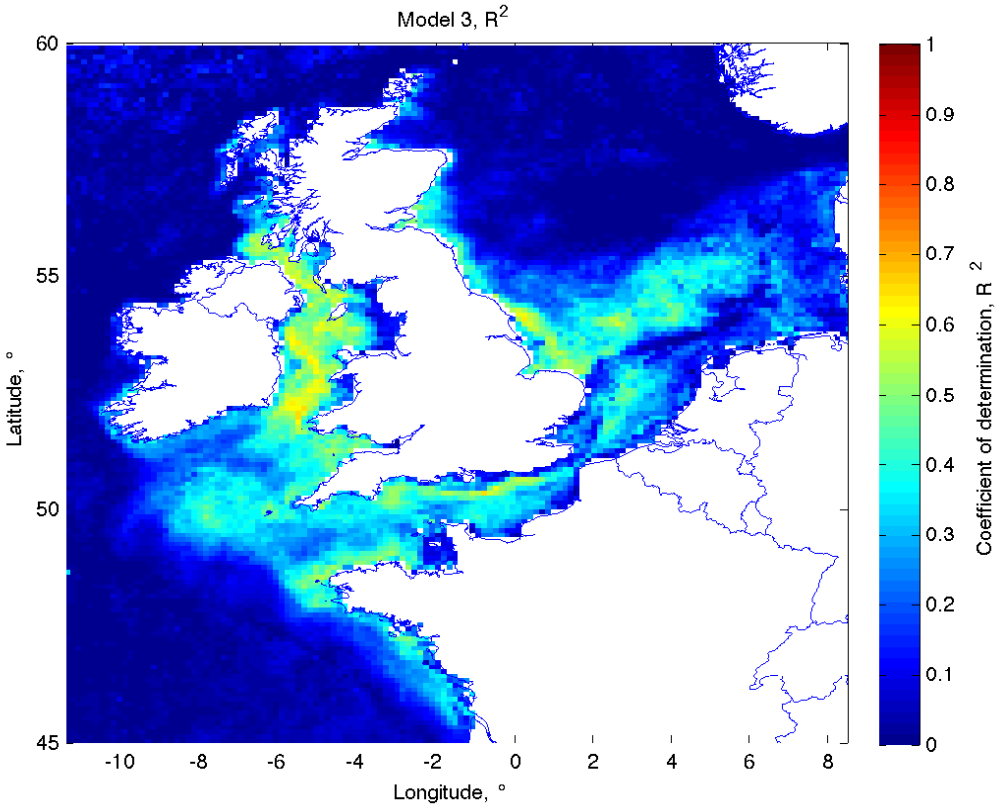


Figure 60: The $R^2$ coefficient of determination between the model 3 prediction and remotely-sensed observations.

Model 3 shows a further reduction in the RMSE, concentrated in the stratifying regions of the Irish Sea (Figure 61). In regions with no stratification, there is little improvement in the error as compared to model 2.

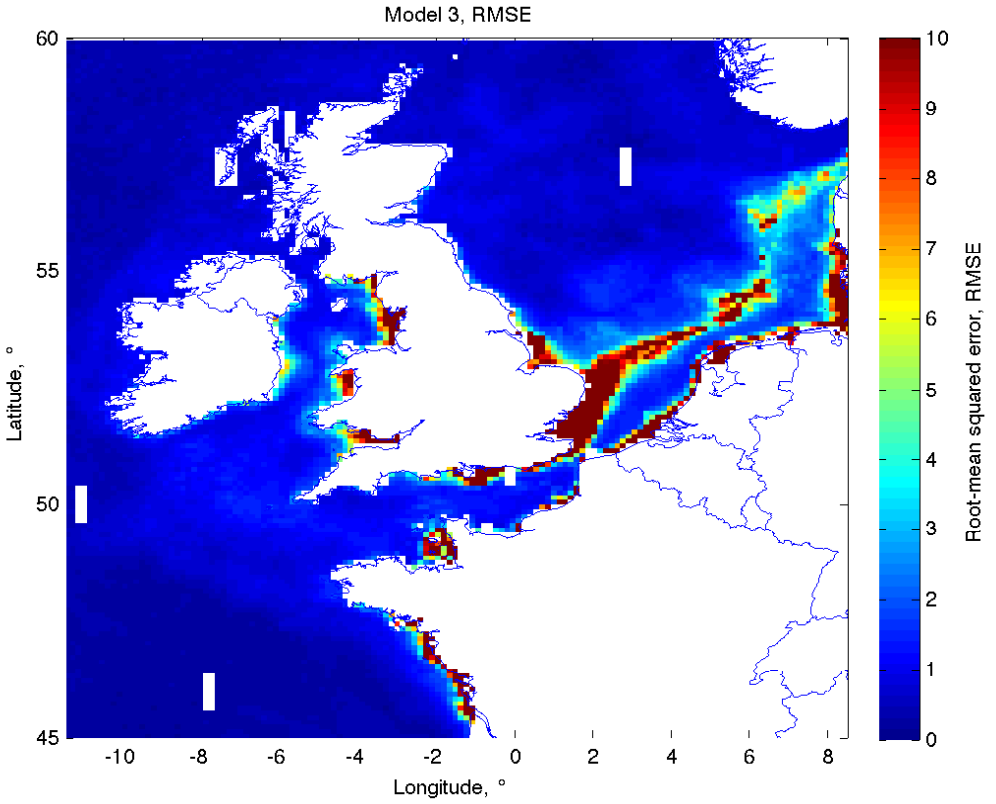


Figure 61: The root-mean squared error, RMSE, between the model 3 prediction and remotely-sensed observations.

The coefficient $c_1$ describes the amplitude of the sine curve fitted to inverse of the Chlorophyll-a concentration in the regression with the remotely-sensed observations (Figure 62). The high amplitudes in coastal regions are associated with high concentrations (the Irish Sea and southern North Sea) as in the previous two sine curves. The amplitude is shown to be raised along the shelf break, within the Irish Sea and North of Scotland.

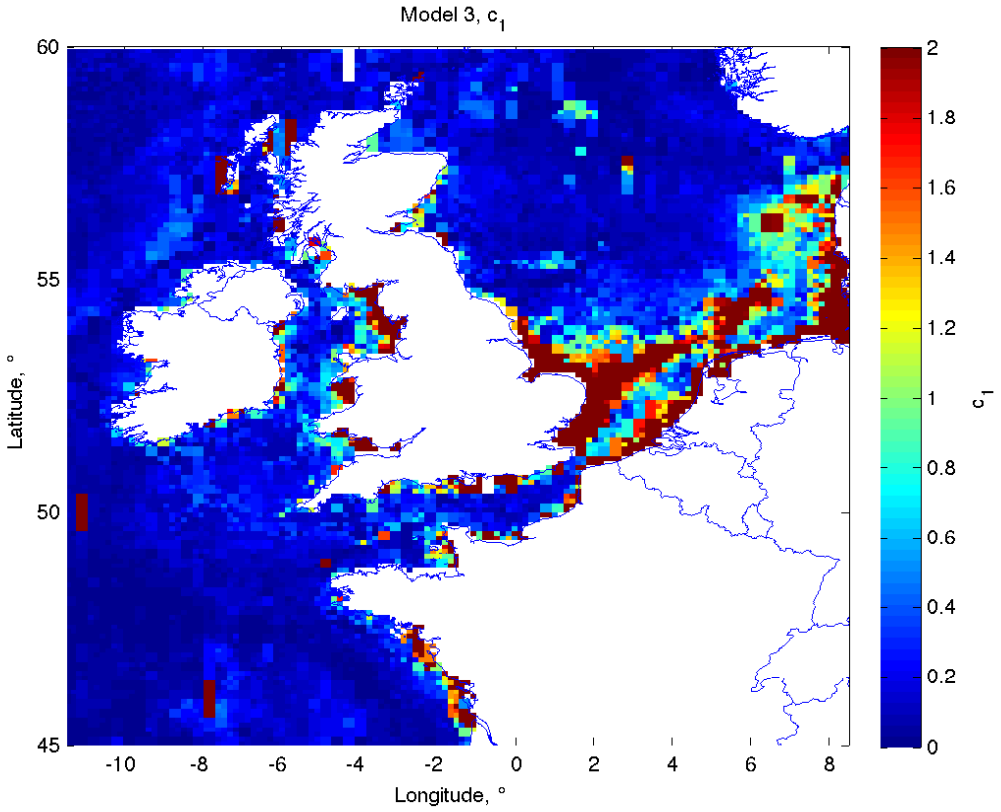


Figure 62: The coefficient $c_1$ representing the amplitude of the sine curve fitted to the inverse of the Chlorophyll-a concentration in the regression with the remotely-sensed observations.

The coefficient $c_2$ describes the phase difference of the sine curve fitted to the inverse of the Chlorophyll-a concentration in the regression with the remotely-sensed observations (Figure 63). There is a lot of noise in the phase difference, however there are broader patterns in the main areas of the region. The phase difference is shown to be erratic along the shelf due to the low concentrations in these regions. In the Celtic Sea and southern Irish Sea, the phase difference is shown to be between 310 and 330 days, and lower at 290 to 310 days in the northern Irish Sea and the southern North Sea. The phase difference in the northern North Sea is shown to be between 320 and 340 days. The phase difference drops to between 210 and 250 days in the eastern English Channel.

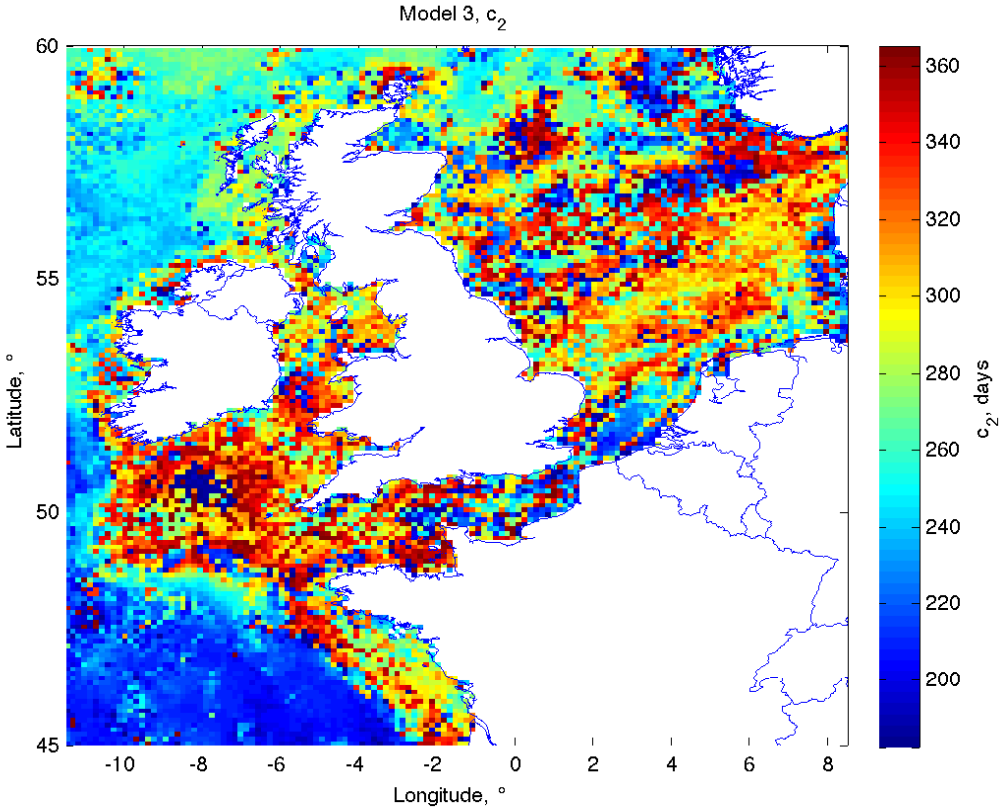


Figure 63: The coefficient $c_2$ representing the phase difference of the sine curve fitted to the inverse of the Chlorophyll-a concentration in the regression with the remotely-sensed observations.

# 15 Discussion

The purpose of this chapter was to test a statistical model using tides, wind and Chlorophyll-a to predict the concentration of suspended material on the U.K. and Atlantic French shelf. In addition to expanding the method described by Rivier et al. (2012), the model pertained in this chapter aims to improve upon the performance and broad applicability in the shelf sea region.

## 15.1 Model 1, Tides

Using tides alone, with a coefficient seasonal sine curve, the model is shown to predict both the seasonal variabiltiy in the observed concentration and also the spring-neap tidal cycle in the concentration. The model was shown to predict between 30 and 65% of the variability in the concentration. This shows a large improvement upon the predictability of Rivier et al. (2012). The model shows increased performance in the central English Channel over Rivier et al. (2012), in addition to a significant improvement ($R^2$ greater than 0.45 in comparison to less than 0.05) in the western English Channel and Celtic Sea.

## 15.2 Model 2, Tides and Wind

There is a slight improvement in the prediction with the inclusion of wind in the model prediction. In comparison to the model of Rivier et al. (2012), the increase in performance is not as substantial as much of the seasonal variability is accounted for in the sine curve seasonal coefficient used in the tidal model. The model 2 improvement is shown to vary spatially, with some locations showing more improvement than others. The English Channel location shows very little improvement with the inclusion of wind in the model. However, the two other locations show increased representation of the seasonal difference between winter and summer on the SPM concentration (higher in the winter, lower in the summer).

## 15.3 Model 3, Tides, Wind and Chlorophyll

The inclusion of Chlorophyll-a in the statistical model has the effect of increasing the representation of stratification in the model. When the concentration of Chlorophyll-a is high in the summer, the concentration of suspended sediment in the model drops steeply. Model 3 shows that the inclusion of Chlorophyll-a in a multiplicative form improves the timing of drops in the concentration (coinciding with periods of high biological activity). However, inclusion of Chlorophyll-a in this form leads the model to over-predict in the summer (Irish Sea, Figure 66) and under-predict in the winter (English Channel, Figure 66).

All three models are shown to underestimate the concentration in the first winter (2010), which shows a large peak in the remotely-sensed concentration of SPM. The wind speed is higher than normal for the winter at this point, but not at a level proportional to the peak in concentration. It is likely that this is due to prolonged wind-driven wave activity, which has maintained suspension and allowed increasing amounts of bed sediment to be suspended leading up to period covered by the time series.

## 15.4 Limitations

- The model format assumes that the process of settling speed and flocculation of particles may be represented by a sinusoidal curve with only one peak and trough. Although this has its benefits in terms of use as a prediction tool, it may limit its accuracy. As flocculation is influenced by biological activity, in certain areas it is likely there will be more than one peak (i.e. spring and autumn blooms).
- The depth of each grid location is not taken account of directly as a parameter in the statistical model formulation. As the statistical coefficients are set for each location independently, their variability will therefore be influenced by depth, with any influence of shallow or deep waters taken account of by the coefficient itself, without the need for depth as a separate parameter. It would be expected that depth would act to reduce the coefficients, due to decreased depth-averaged turbulent activity in deeper regions.

- As the model considers each location independently for statistical analysis, the process of tidal or wind-driven advection is discounted in the model. This could improve the representation of plume regions where suspended sediments may be advected in the surface layer of the water column.
- This statistical model format does not take account of delayed or prolonged impact of the hydrodynamical forcings, such as following storm activity or large spring tides, which may sustain the suspended sediment concentration following the original peak.
- In the present form, the model is unable to directly take account of stratification. Future use could include the numerical models of stratification to represent this (Simpson & Bowers, 1984; Elliott & Clarke, 1991; Elliott et al., 1991).
- Spatial-averaging of the remote-sensing data was necessary for statistical analysis in regions with poor atmospheric correction due to clouds or land adjacency. In some areas, this potentially could either dampen or exacerbate the variability. Future application could modulate the use of spatial-averaging dependant upon the success rate of atmospheric correction.

## 15.5 Implications

The final model described in this chapter is shown to predict over 70% of the observed variability in the majority of the shelf region of northwest Europe. This shows not only that improvements can be made upon the method described in Rivier et al. (2012), but that the method can also be applied over a far broader area. Much of this improvement may decided by the sine curve seasonal coefficients used, which appear to take account of the influence of flocculation upon variation in the settling speed over the shelf. The model assumes a sine curve in this respect which is potentially an oversimplification as the reality is likely to be one of multiple peaks at certain locations, accounting for the presence of spring and autumnal blooms.

The method described by Saulquin et al. (2015) states that over 80% of the variability in the

suspended matter concentration in the Gironde may be accounted for. The model described in this chapter is shown to produce comparable levels of performance over a significantly larger spatial area, without the inclusion of river discharge data. Despite this, as the spatial resolution of Saulquin et al. (2015) is finer, it would be expected that inclusion of river discharge would be beneficial to future model performance. Much of the data used in this chapter is easily accessible, allowing this method to be used in new shelf seas regions with little difficulty.

There are several proposed improvements to future iterations of this model format:

- Inclusion of temporally-averaged wind, to account for sustained impact of wind events such as storm activity. This could come in the form of a density-based prediction similar to that of Saulquin et al. (2014) and Gohin et al. (2015), using several representations of wind which are averaged over 3, 5, 10, 25, and 50 days, with diminishing influence.

- River discharge as described in Saulquin et al. (2014) is an important factor influencing the concentration of surface suspended sediments in coastal regions. The exclusion of river discharge in the statistical model is likely to be the cause of larger values of RMSE around major rivers. To include river discharge may be more challenging than Saulquin et al. (2014) to expand over a larger area as in this chapter. Using the main regional rivers of northwest Europe may however be useful as an alternative to inclusion of each coastal river/estuary, for both calculation and data accessibility purposes.

- If remote-sensing data of increased temporal resolution were available, it may be possible to include high frequency tidal variability within the statistical format. In addition to MODIS-Aqua used for this study, utilising data from MODIS-Terra, MERIS and VIIRS could allow increased frequency of images, with up to 4 images for each day.

  The following is a preliminary assessment of the potential of using MODIS-Aqua, MERIS and VIIRS to expand the data frequency for this form of analysis:

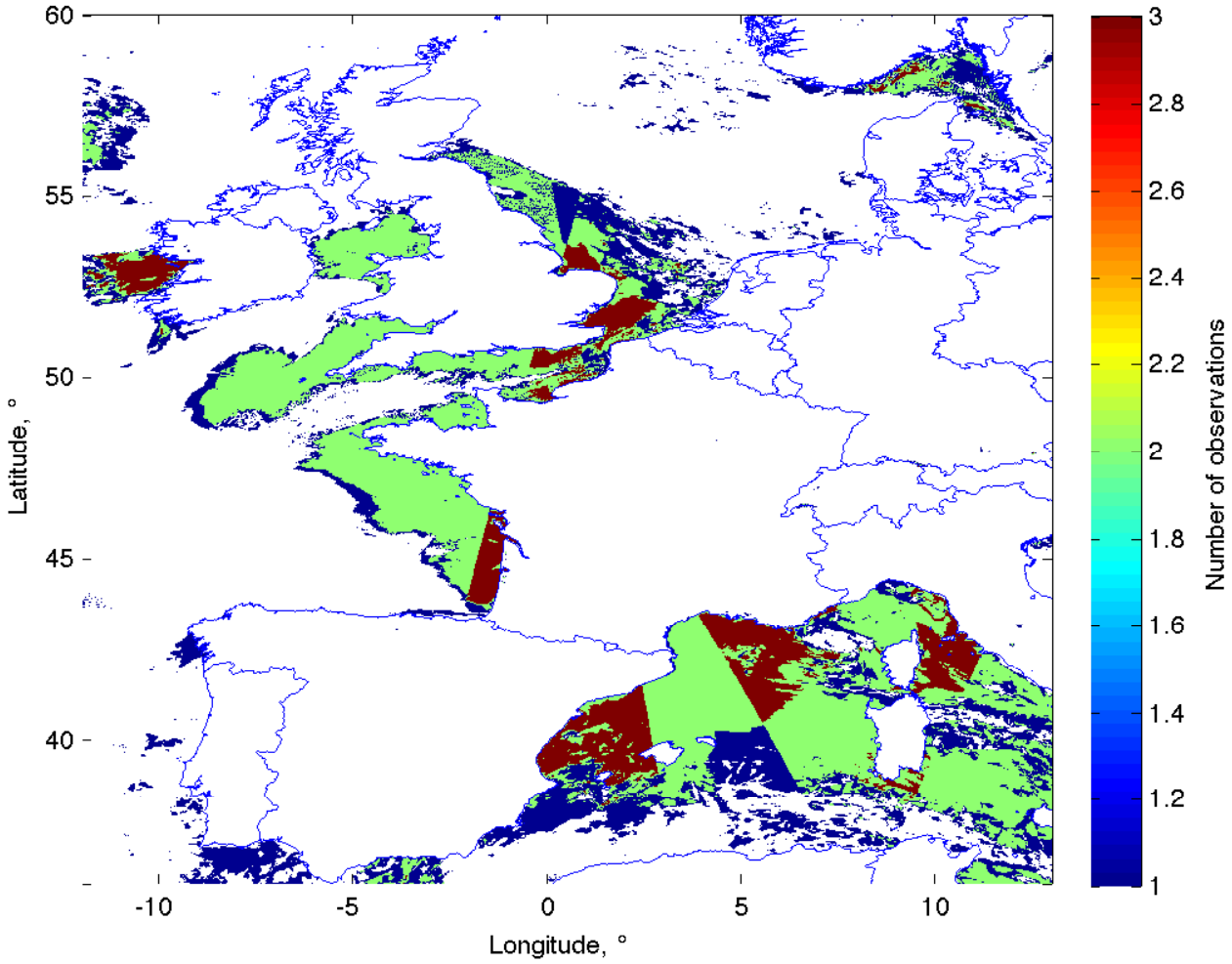


Figure 64: The frequency of satellite data points on 1st April 2012 from MODIS-Aqua, MERIS and VIIRS, courtesy of Ifremer (ftp.ifremer.fr) at $1km^2$ resolution. A value of 3 in this case represents data at one pixel for all satellites, with 0 representing lack of coverage for that pixel on this day.

Figure 64 shows that in pixels where there is data on this day, the frequency of daily data points is often at least two (51.44% of pixels). 34.48% of pixels observed only one data point, with only 14.08% pixels providing data from MODIS-Aqua, MERIS and VIIRS on this day.

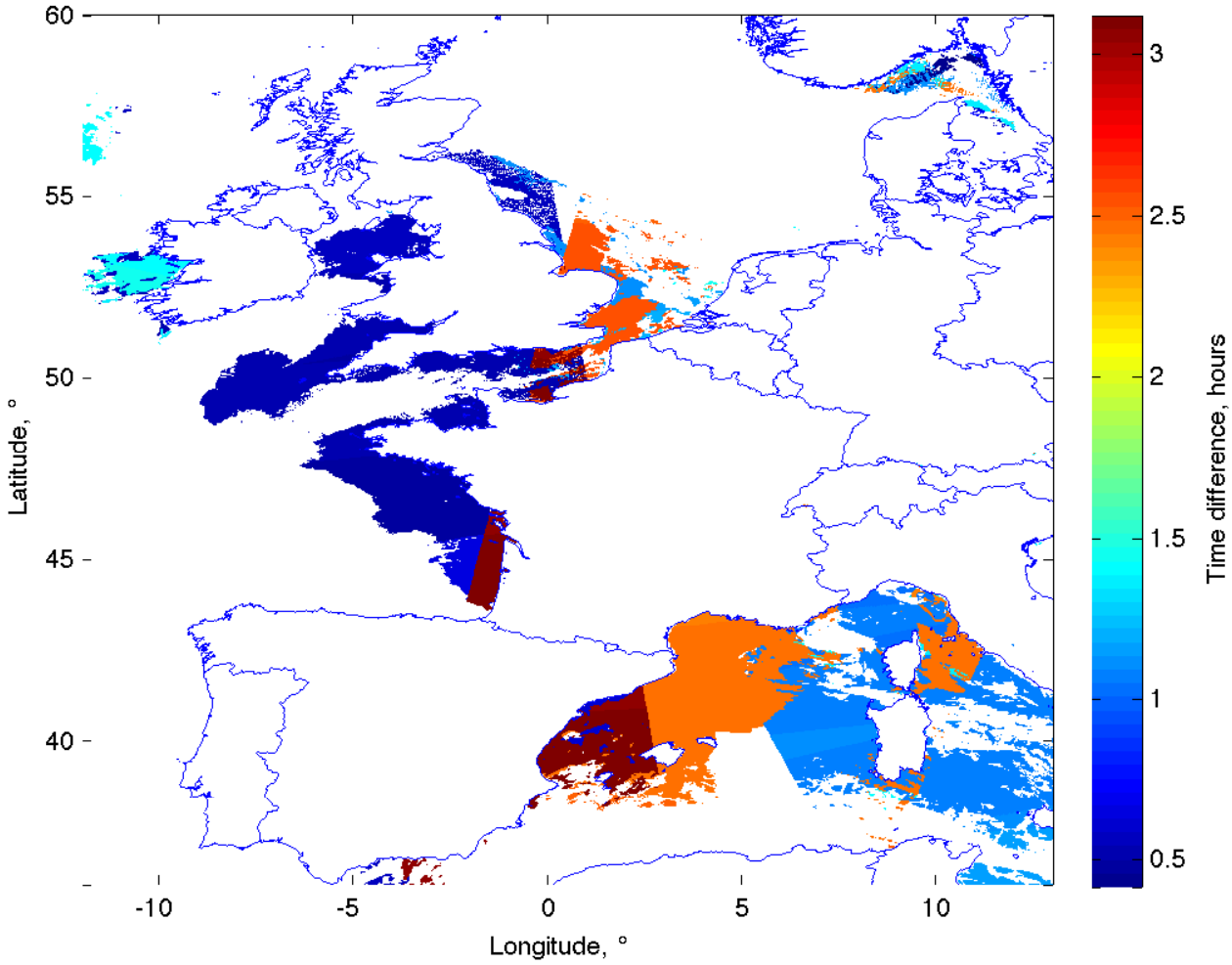


Figure 65: The maximum time difference in hours between first and last observed satellite data points on 1st April 2012 from MODIS-Aqua, MERIS and VIIRS, courtesy of Ifremer (ftp.ifremer.fr) at $1km^2$ resolution. A value of 0 in this case may either represent a lack of observations for that pixel or for the presence of only one data point.

Figure 65 suggests that the application of increasing the frequency of data points used in analysis to at least two is feasible. However, two points in a very short time period (less than 1 hour), may do little to increase representation of variability within a day, especially if both points fell during the slack tide for example. Figure 68 shows the maximum time difference between pixels with two or more data points on the 1st April 2012. Further analysis shows that 32.33% of locations with two or more data points,

had observations with a timeframe of less than one hour separating them. Between one and two hours time difference, this increased to 33.12%. Between a timeframe of two and three hours separation, the coverage dropped to 25.26%, with only 9.29% having a separation of up to four hours. This is promising for further analysis as the majority (67.67%) of pixels with a frequency of two or more daily observations across the three satellites had maximum time separations of between 1 and 4 hours.

The inclusion of MODIS-Terra data would would hope to expand this coverage further, providing the potential for semi-diurnal analysis.

Expansion into analysis of future data could involve the use of data from the geostationary satellite SEVIRI (Spinning Enhance Visible and Infrared Imager), which provides a repeat cycle of coverage of 15 minutes of Europe (Neukermans et al., 2012b; Ody et al., 2016). Neukermans et al. (2012b) describes the potential use of SEVIRI data in mapping turbidity, to analysis diurnal variability.

- Direct implementation of stratification in the statistical model output could be progressed using a numerical model such as that described by Elliott & Clarke (1991).

# Part IV

# Numerical model of suspended sediment concentration

## 16 Introduction

Water clarity or turbidity is highly variable within the shelf sea environment, impacting upon both human interaction with the coastal ocean (i.e. fisheries), coastal engineering and the success of benthic driven food webs. Also important are the secondary processes relating to resuspension of sediments, namely pollutant dispersion and carbon sequestration. The ability to successfully model the concentration of suspended sediment in the water column to complement satellite remotely-sensed observations of the oceans surface when atmospheric correction fails, leads to more effective management of the marine environment. This chapter describes a simple method of numerically modelling suspended sediment concentration, relative to the main drivers of variability in the concentration of suspended sediments - wind, tides and settling speed.

This chapter will aim to answer the following question:
*How well can a simple turbulent energy based numerical model of suspended sediment concentration perform in comparison to the satellite archive of remotely-sensed surface suspended sediments?*

In order to do this, the following objectives will be carried out

- Produce a two-layer numerical resuspension model of the suspended sediment concentration using varied representation of the particle settling speed.
- Compare the output from the numerical model to the MODIS Aqua archive of remotely-sensed suspended sediment.

# 17 Methods

## 17.1 Resuspension model

In order to maintain sediment in suspension energy must be inputted into the water column. Without the presence of this energy, sediment will soon settle. In the presence of this input of energy, the lift and drag forces generated may exceed the resisting forces of the settling particles, allowing particles to become suspended. Within the water column, this energy comes through the forcing of wind-generated waves (W) and tides (U). The rate at which sediment sinks through the water column, ($w_s$), is modulated by the hydrodynamic forces. Bowers (2003) described the balance between resuspension and settling speed, neglecting advection and assuming a fully-mixed water column, in the form of the following equation:

*Balance of the resuspension and settling of suspended sediments (Bowers, 2003)*

$$\frac{P}{g^{'}h^2} = \frac{w_s c}{h} \tag{17.1}$$

P is the rate of energy input by tides and wind (Equation 10.3), $kgm^{-3}s^{-1}$
$g^{'}$ is the reduced gravity of sediment in suspension, $ms^{-2}$
h is the water depth, m
$w_s$ is the particulate settling speed $ms^{-1}$
c is the suspended sediment concentration, $kgm^{-3}$

Equation 17.1 describes the scenario at which the forces driving resuspension (on the left-hand side of the equation) are balanced by the forces driving the settling of particles (on the right-hand side). When the two sides equal one another, as in Equation 17.1, the concentration remains static. Following on from this, Bowers (2003) derived the rate of change in concentration as the level at which the resuspending forces exceed the settling forces:

*Change in suspended sediment concentration (Bowers, 2003)*

$$\frac{dc}{dt} = \frac{2P}{g'h^2} - \frac{2w_s c}{h} \tag{17.2}$$

The rate of energy input (P) from tides and wind-generated waves are expressed in the following form:

*The rate of energy input by tides and wind, P (Bowers, 2003)*

$$P = \gamma(\underbrace{\frac{4}{3\pi}k_b\rho_w U^3}_{\text{Tides}} + \underbrace{k_s\rho_a W^3}_{\text{Wind}}) \tag{17.3}$$

$k_b$ and $k_s$ are the bottom and surface drag coefficients

$\rho_w$ and $\rho_a$ are the densities of water and air, $kgm^{-3}$

U is the depth-averaged tidal current speed, $ms^{-1}$

W is the wind speed, $ms^{-1}$

$\gamma$ is the efficiency of resuspension

For the purpose of this model, it is assumed that the supply of sediment at the bed is infinite. In reality, the supply is limited by the thickness of suspendable sediments on the bed and eventually the presence of unsuspendable sediments and bedrock. However, when using realistic setup parameters, this eventuality is unlikely to be achieved.

In order to explain the resuspension model used in this chapter, figure 66 shows the predicted variability in suspended particulate matter at three locations over the U.K. and Atlantic French region. Theses examples describe the performance of the resuspension model to predict the concentration of suspended material with a static settling speed ($w_s$) of $12mday^{-1}$ ($0.14mms^{-1}$) for the year.

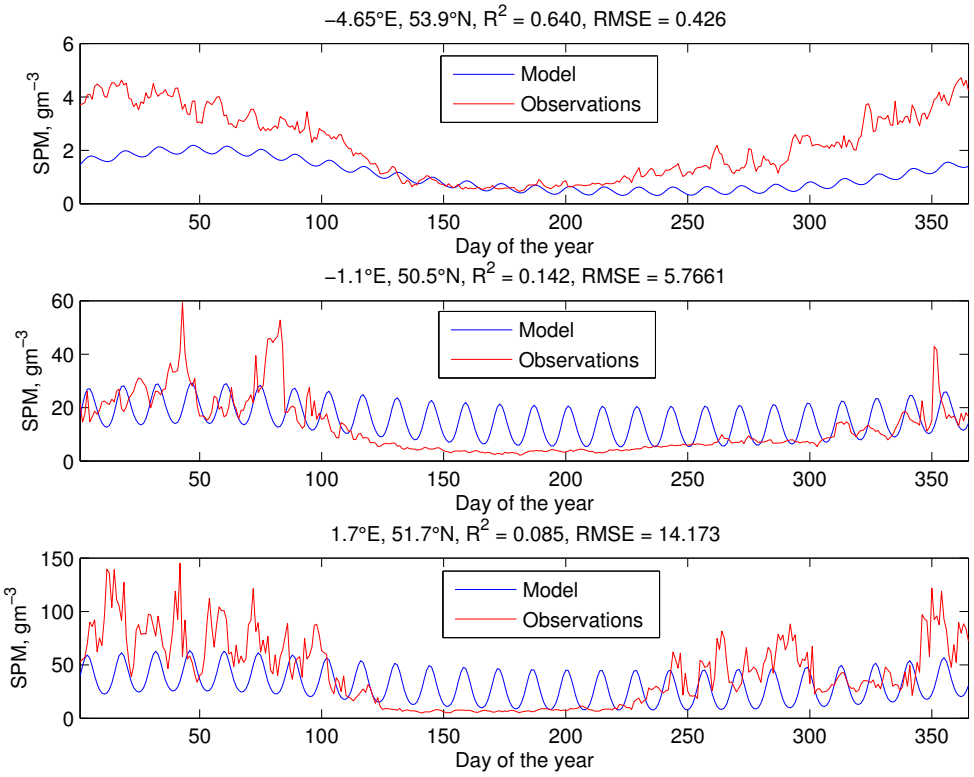


Figure 66: Modelled and remotely-sensed observations of suspended sediment concentrations at three locations over the U.K. and Atlantic French region. The model is without thermal stratification and with a constant settling speed of $12mday^{-1}$ ($0.14mms^{-1}$).

Figure 66 shows that the model performs well in estimating the magnitude of the observation site, however, there is minimal seasonal variability predicted by the models in comparison to that of the remotely-sensed observations. Similarly, the lack of a stratifying water column is clearly noted in the summer months at all three locations.

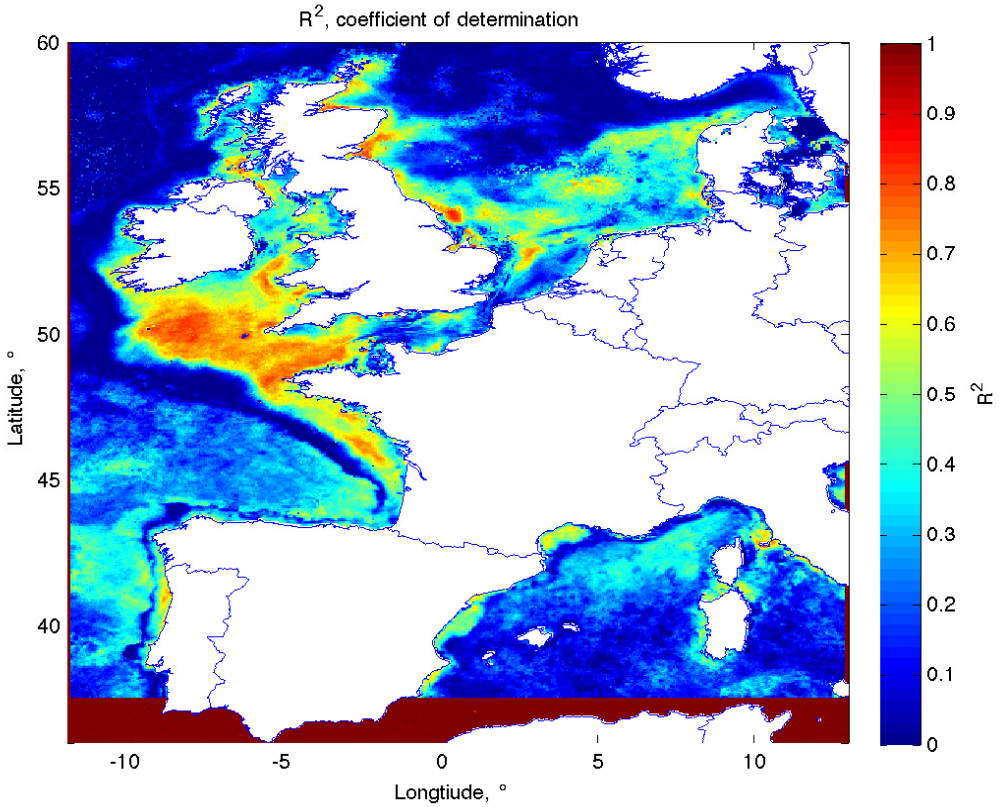


Figure 67: The coefficient of determination, $R^2$ between the remotely-sensed observations of suspended sediment concentration and the modelled suspended sediment concentration without thermal stratification and with a static settling speed of $12mday^{-1}$ ($0.14mms^{-1}$).

Figure 67 shows the $R^2$ value describing the proportion of the remotely-sensed observations that are explained by the numerical model using a static settling speed ($w_s$). Although the southern Irish Sea and Celtic Seas have high calculated $R^2$ values in the order of 0.55 to 0.75, the English Channel and the North Sea show more irregular model performance. It is noted that regions off the Atlantic Shelf and the Mediterranean Sea provide high values for $R^2$, however this is expected to be due to the relatively low seasonal variability and low concentrations observed in both the model and in remotely-sensed observations in these regions.

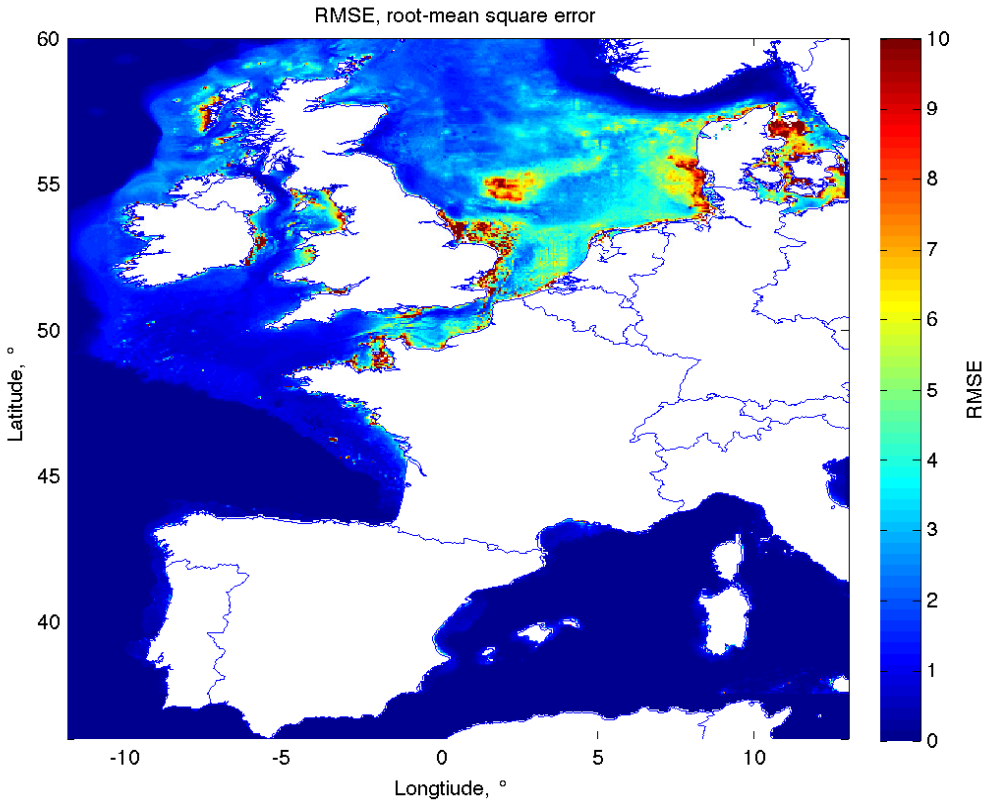


Figure 68: The root-mean squared error, RMSE, between the remotely-sensed observations of suspended sediment concentration and the modelled suspended sediment concentration without thermal stratification and with a static settling speed of $12mday^{-1}$ ($0.14mms^{-1}$).

Figure 68 shows the values of root-mean squared error (RMSE) between the observations and the numerical model when using a static settling speed. The values observed range between more than $6gm^{-3}$ in the North Sea to generally less than $3gm^{-3}$ in the central Irish Sea.

## 17.2 Heating and stirring model

A key process within the dynamics of the ocean and especially shallow temperate shelf seas, is seasonal stratification. It is generally observed that surface heating increases in the summer and decreases in the winter. Likewise, the observed wind speed is at its highest in the winter and at its lowest in the summer. The result of this is that

surface heating heading into the summer months is not mixed thoroughly throughout the water column due to decreased turbulent kinetic energy (TKE). The result of this is a warm layer of mixed water at the surface, sitting above a cooler unmixed layer. This phenomenon is referred to as thermal stratification, forming a temperature denoted thermocline. As surface heating decreases and the wind speed increases towards the winter months, this causes the thermocline to be broken down and the water column to be fully mixed.

The ability of the water column to stratify can be termed to be in part controlled by the depth, with deeper waters requiring a higher level of turbulent kinetic energy in order to be mixed throughout. Similarly, regions with a high level of turbulent kinetic energy, in areas of high tidal activity for example, remain mixed at deeper depths than areas with lesser turbulent kinetic energy. As defined in Simpson & Bowers (1979), the presence of waters which stratify seasonally could be identified using the value of $h/u^3$ (Simpson & Hunter, 1974; Pingree & Griffiths, 1978; van Leeuwen et al., 2015), the depth over the cube of the maximum tidal current amplitude, which the limit being greater than 55 to maintain stratification.

The approach of using tidal activity to term stratification is a helpful one, in as much as the tides are easily predicted through harmonic analysis. However, Simpson et al. (1978) proposed to include wind-driven mixing in the calculation, as described in Simpson & Bowers (1981). From this, Simpson & Bowers (1984) developed a simple model of heating and stirring with two vertical layers, to be implemented over shelf-sea regions.

Elliot & Clarke (1991) improved upon the model described in Simpson & Bowers (1984) by using an alternative parameterisation of the flux of heat between the surface of the ocean and the air. This two-layer thermal model describes seasonal stratification within the northwest European shelf seas using the effects of surface heating, wind mixing and stirring due to tides. The model was able to reproduce the seasonal temperature structure as observed by XBT observations, to an agreement of better than 1°C (Elliot et al., 1991). XBT (expendable bathythermograph) sensors are free-falling thermistor

probes, attached to a boat with a self-detaching signal cable. The northern North Sea however had a less accurate representation of thermal stratification as the vertical thermal structure here is near linear with depth, so using a two-layer form is a poor representation of this (Elliot & Clarke, 1991).

The model equations are:

*Incoming short-wave radiation, $Q_S$ (Elliot & Clarke, 1991)*

$$Q_S = 117 + 103cos(\frac{2\pi}{365}(day - 171)) \tag{17.4}$$

$Q_S$ is the incoming short-wave radiation, $Wm^{-2}$

*Wind function, $f_W$ (Elliot & Clarke, 1991)*

$$f_W = 11.2 + 2.5W \tag{17.5}$$

$f_W$ is the wind function used in the calculation of the heat flux at the ocean surface, $ms^{-1}$, with W being the wind speed, $ms^{-1}$

*Heat flux function of surface and dew point temperatures, $T_M$ (Elliot & Clarke, 1991)*

$$T_M = 0.5(T_S + T_D) \tag{17.6}$$

$T_M$ is used in calculation of the heat flux, $°C$

$T_S$ is the temperature of the surface layer, $°C$

$T_D$ is the dew point temperature (provided by the MetOffice), $°C$

*Thermal exchange coefficient, $\kappa$ (Elliot & Clarke, 1991)*

$$\kappa = 4.5 + 0.05T_S + f_W(0.35 + 0.0015T_M + 0.0012{T_M}^2 + 0.47) \tag{17.7}$$

$\kappa$ is the thermal exchange coefficient

*Change in the net flux of heat through the sea surface, $dQ_T/dt$ (Elliot & Clarke, 1991)*

$$\frac{dQ_T}{dt} = Q_S + \kappa(T_D - T_S) \tag{17.8}$$

$Q_T$ is the net flux of heat through the sea surface (positive = in, negative = out), $Wm^{-2}$

Equation 17.9 defines the first change in the potential energy anomaly, E, a function of the wind speed, W.

*Change in the potential energy anomaly, dE/dt (Elliot & Clarke, 1991)*

$$\frac{dE}{dt} = \frac{-agQ_T d}{2C_P} + \delta C_d \rho_a W^3 \tag{17.9}$$

E is the potential energy anomaly, $Jm^{-3}$ (Bowers, 1984)

g is acceleration due to gravity, (=$9.81ms^{-2}$)

$C_P$ is the specific heat capacity of water, $Jkg^{-1}{}^{\circ}C^{-1}$

$\rho_a$ is density of air, $kgm^{-3}$

W is the wind speed, $ms^{-1}$

*Bulk water column temperature expression, $h\Delta T$ (Elliot & Clarke, 1991)*

$$h\Delta T = \frac{Q_T}{C_P \rho} - dT_B \tag{17.10}$$

h is the depth of the mixed layer, m

$\Delta T$ is the difference in temperature between the surface and bottom layers ($T_S$-$T_B$), $^{\circ}C$

$\rho$ is the water density, $kgm^{-3}$

$T_B$ is the bottom layer temperature, $^{\circ}C$

*Mixed layer depth, h (Elliot & Clarke, 1991)*

$$h = d + \frac{2E}{\rho g \alpha h \Delta T} \tag{17.11}$$

$\alpha$ is the coefficient of the thermal expansion of water

If the mixed layer depth (h) is equal to the total depth (d):

*Bottom temperature if the the water is fully-mixed, $T_S$ (Elliot & Clarke, 1991)*

$$T_S = \frac{Q_T}{C_P \rho d} \tag{17.12}$$

The bottom temperature ($T_B$) is assumed to therefore be equal to the surface depth ($T_S$).

If the mixed layer depth (h, m) is less than the total water column depth (d, m), then the surface layer depth ($h_1$) is equal to the mixed layer depth (h).

*Bottom layer depth, $h_2$ (Elliot & Clarke, 1991)*

$$h_2 = d - h \tag{17.13}$$

$h_2$ is the bottom layer depth, m

*Surface layer temperature, $T_S$ (Elliot & Clarke, 1991)*

$$T_S = T_B + \frac{h \Delta T}{h_1} \tag{17.14}$$

The second change to the potential energy anomaly, E, is a function of the tidal current speed, U (Eq. 17.15)

*Change in the potential energy anomaly, dE/dt (Simpson & Bowers, 1984; Elliott &*

*Clarke, 1991)*

$$\frac{dE}{dt} = \epsilon k_b \rho U^3 \frac{4}{3\pi} \tag{17.15}$$

$\epsilon$ is the efficiency of tidal mixing

$k_b$ is the bottom drag coefficient

U is the tidal current speed, $ms^{-1}$

If the potential energy anomaly, E, is greater than 0, the value is returned to 0 in order to calculate the surface layer depth. The result of this being that if the potential energy anomaly (E) is 0, the surface layer depth must also be 0 (Eq. 17.16)

*Surface layer depth, $h_1$ (Elliot & Clarke, 1991)*

$$h_1 = \frac{2E}{\rho g \alpha (T_S - T_B)(h_1 - d)} \tag{17.16}$$

$\alpha$ is the coefficient of thermal expansion of seawater

If the surface layer depth ($h_1$) is equal to 0m, the bottom temperature is calculated using the following equation:

*Bottom layer temperature, $T_B$ (Elliot & Clarke, 1991)*

$$T_B = \frac{Q}{C_P \rho d} \tag{17.17}$$

If the surface layer depth ($h_1$) is equal to 0m, the water column is fully mixed and thus the surface and bottom temperatures are assumed to be equal ($T_S$=$T_B$).

If the surface layer depth ($h_1$) is greater than 0m, the bottom temperature is calculated using the following equation:

*Bottom layer temperature if the water is stratified, $T_B$ (Elliot & Clarke, 1991)*

$$T_B = T_S - \frac{T_S - T_B}{h_1 - d} \tag{17.18}$$

There are several assumptions necessary to run this model, which are detailed within Table 12.

Table 12: Table of constants for the heating and stirring model (Simpson & Bowers, 1984; Elliott & Clarke, 1991)

| Variable | Value |
|---|---|
| Specific heat capacity of water, $C_P$ | 3,900Jkg$^{-1}{}^{\circ}C^{-1}$ |
| Drag coefficient, $C_D$ | 0.0013 |
| Acceleration due to gravity, g | 9.81m$^2s^{-1}\}$ |
| $k_b$ | 0.0025 |
| $\delta$ | 0.00006 |
| $k_s$ | 0.0012 |
| Density of water, $\rho$ | 1025 kgm$^{-3}$ |
| Density of air, $\rho_a$ | 1kgm$^{-3}$ |
| Coefficient of the thermal expansion of seawater, $\alpha$ | 0.00021 |

## 17.3 Model inputs and run time

As with the statistical modelling chapter, the bathymetry came from GEBCO, the tidal current speed from TPXO 8.0 Atlas and the wind speed from the ECMWF wind model. For the stratification model, it was necessary to provide the dew point temperature, which was obtained through the MetOffice DataPoint service over the entire shelf region. In order to allow the model to reach a steady state based on the starting temperature ($8°C$) and suspended sediment concentration ($5gm^{-3}$) assumptions, each model was run for a minimum of 30 years using a climatology of the input parameters. Although the suspended sediment concentration observed by satellite could be used instead of the assumption, the change in runtime would be minimal. When variation was repeated each year, the model was assumed to be stable, allowing for interpretation of the results using the final input data.

## 17.4 Stratification

Figure 69 shows the temperature predicted in the surface and bottom layers of the water column at three points over the model region. Although all three observe seasonal summer stratification, there is only minimal spring-neap tidal stratification observed in first and third locations, with the second location presenting more persistent stratification over approximately 60 days.

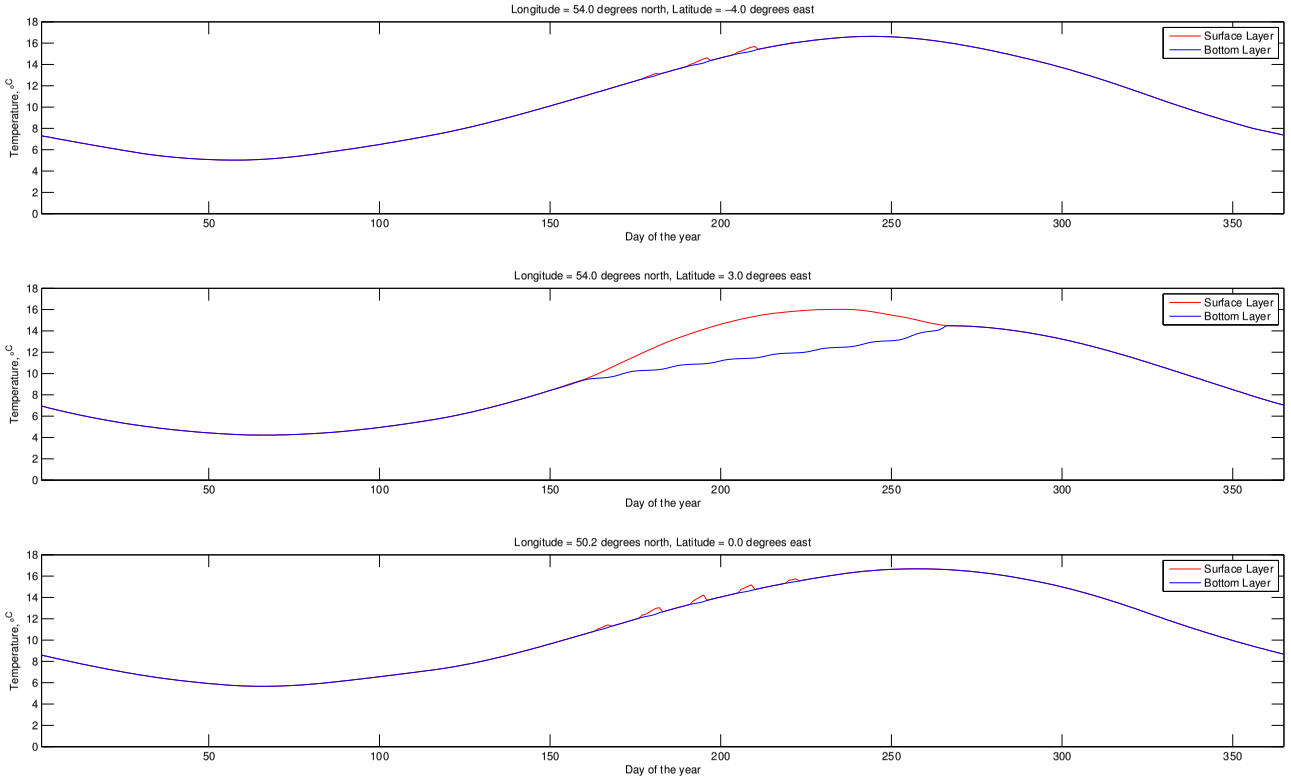


Figure 69: Plot showing the temperature modelled at the surface and bottom layers of the water column at three locations in the model region. Regions where the two temperatures differ represent periods of thermal stratification. The top plot features a profile from a location at $54°N$, $-4°E$, in the Irish Sea, near the Isle of Man. The middle plot features a profile from a location at $54°N$, $3°E$, in the North Sea. The bottom plot features a profile from a location at $50.2°N$, $0°E$, in the English Channel between Brighton (England) and Le Havre (France).

## 17.5 How well does the model represent thermal stratification?

To compare the performance of the model to the $\frac{h}{u^3}$ contour method defined in figure 71, figure 70 displays the peak temperature difference between bottom and surface as defined by the model. Few locations are shown to not stratify in the peak of summer, however many locations have only a minimal temperature difference between surface and bottom. Areas that are West of the shelf break along the Irish and Western French coast are shown to observed significant peak temperature differences between the layers of $6°C$. Similarly, the Northern half of the North Sea, along the coast of Norway is predicted to show a temperature difference in excess of $8°C$.

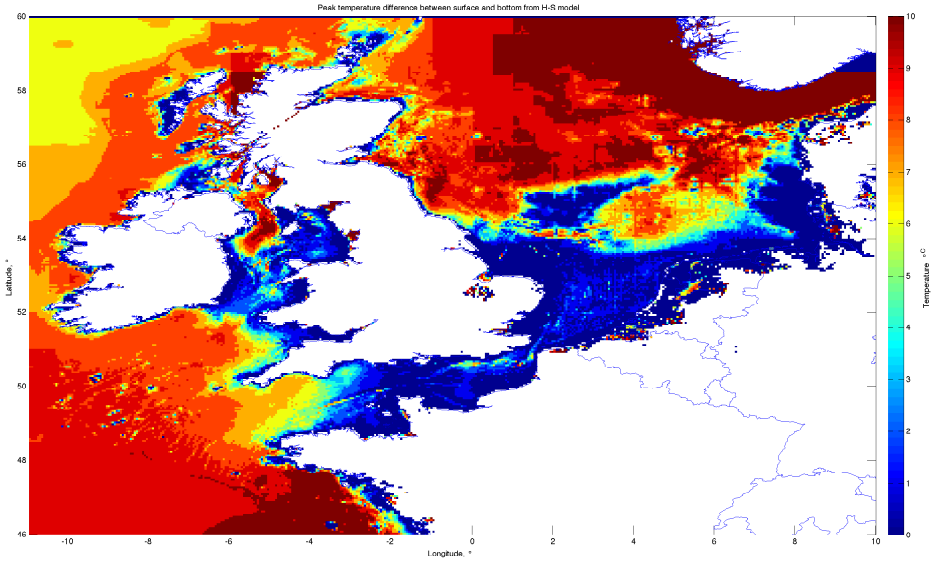


Figure 70: The peak temperature difference between the surface and bottom layers of the water column as modelled using Elliot and Clarke (1991).

Generally, the model output of peak temperature difference is shown to relate favourably to the stratifying regions as dictated by the $h/u^3$ parameterisation. Both the model and the parameterisation identify the southern North Sea, the English Channel and the central Irish Sea as areas which would be expected to stratify in the summer.

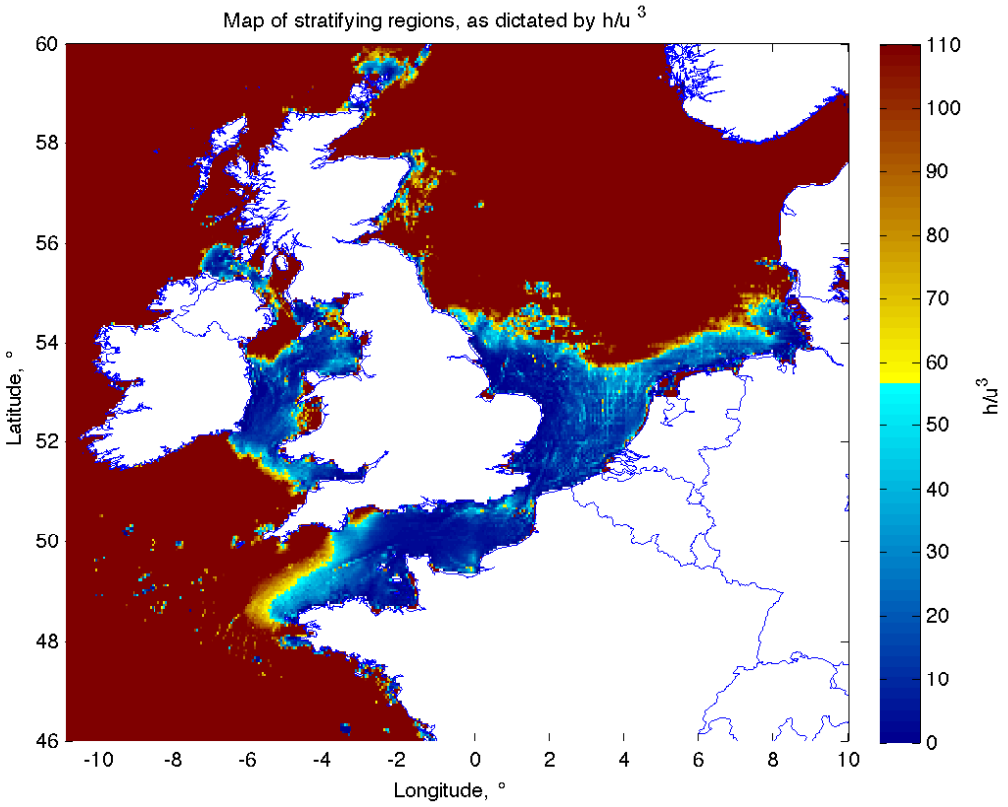


Figure 71: Regions expected to be stratified based upon the use of log10 over $h/u^3$, as defined in Simpson and Hunter (1974) and Pingree and Griffiths (1978).

In order to compare the performance of the Simpson and Hunter (1974) and Elliot and Clarke (1991) methods, a point density scatter plot (Figure 72) is able to distinguish the relationship. This method is implemented in comparison to a standard scatter to illustrate the density variability when working over a 6,004,901 pixel grid. The plot shows a positive correlation, with the highest temperature differences corresponding to the highest values for $h/u^3$. The plot produces an S-curve, with the the highest densities of points found in areas with a peak temperature difference less than $2°C$ and areas with a temperature difference over $7°C$.

The relationship between peak temperature difference calculated from Elliot and Clarke (1991) and the $h/u^3$ values from Simpson and Hunter (1974), can be represented by the following expression, with an $R^2$ of 0.775 and an RMSE of 17.9.

*Elliot and Clarke (1991) peak temperature difference and $h/u^3$ (Simpson & Hunter, 1974).*

$$h/u^3 = 0.79\Delta T^2 + 5.5\Delta T + 40 \tag{17.19}$$

h is the water depth, m

u is the tidal current speed, $ms^{-1}$

$\Delta T$ is the difference between surface and bottom temperature, $°C$

The $R^2$ value along with qualitative assessment, suggest that the Elliot and Clarke (1991) model can be used as a good approximation of stratification in the two-layer model for resuspension.

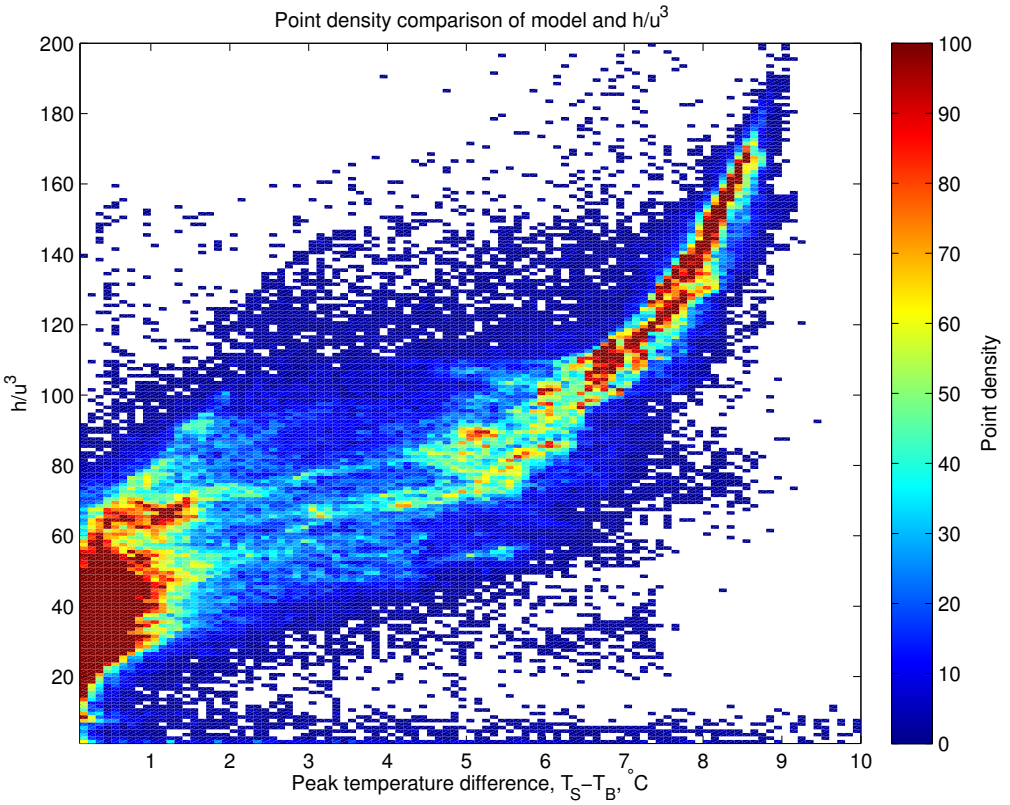


Figure 72: Point density comparison of $h/u^3$ method (as defined by Simpson and Hunter (1974) and Pingree and Griffiths (1978)) and the peak temperature difference modelled using Elliot and Clarke (1991). The density grid has the dimensions of $0.1°C$ and a value of $h/u^3$ of 1. Values which are shaded white, represent 0 points for that pixel.

## 17.6 Two layer resuspension model

In temperate waters such as those of the north-western European shelf which are of concern in this chapter, thermal stratification is often observed in the summer. In the summer, the rate of solar input is at the highest, corresponding with reduced wind stirring. The process of stratification will be described further within the next section of this chapter, regarding the heating and stirring model used to dictate when stratification occurs.

When modelling the resuspension of sediment under these conditions, it is necessary to adapt the one layer model formulation (Equation 17.2) to take account of the two layers. When water is stratified, resuspension at the bed is driven by the effect of the tides, with the wind effect from the surface not having a direct effect upon bed resuspension, this is taken into account by the alternate use of $P_T$ to denote tidal input of energy, excluding the effect of the wind, with P representing both the input of the wind and tides.

Between the top and bottom layers, entrainment occurs, resulting in parcels of water being interchanged between the two layers. The rate of entrainment between the surface and bottom layers is driven by both the tide and wind, resulting in an indirect influence of wind upon the sediment concentration in the bottom layer when the water is stratified.

*Change in concentration $c_1$, in the upper layer of the water column (Bowers, 2003)*

$$\frac{dc_1}{dt} = \frac{U_{ew}}{h_1}(c_2 - c_1) - \frac{w_s c_1}{h_1} \tag{17.20}$$

*Change in concentration $c_2$, in the lower layer of the water column (Bowers, 2003)*

$$\frac{dc_2}{dt} = \frac{2P_T}{g' h^2} + \frac{U_{et}}{h_2}(c_2 - c_1) + \frac{w_s c_1}{h_2} - \frac{2w_s c_2}{h_2} \tag{17.21}$$

$c_1$ and $c_2$ denote the surface and bottom suspended sediment concentrations, $kgm^{-3}$

$U_{ew}$ is entrainment due to wind-driven waves, $m^3 s^{-1}$

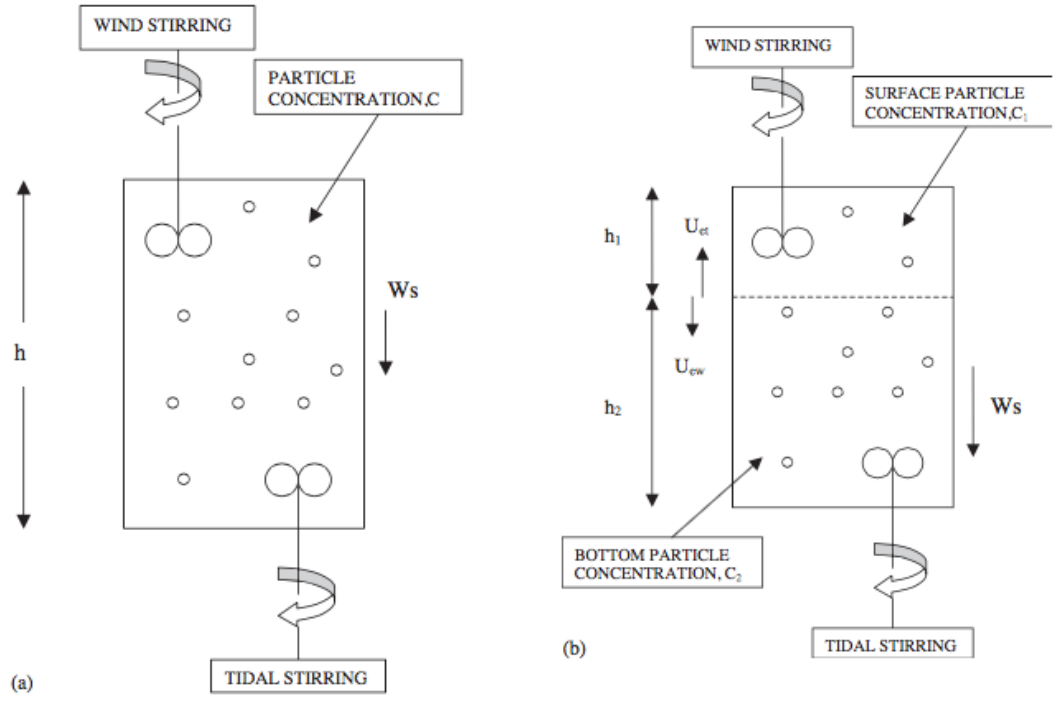


(a) One vertical layer, not thermally stratified.

(b) Two vertical layers, thermally stratified.

Figure 73: Diagram describing the components of the resuspension model (Bowers, 2003).

$U_{et}$ is entrainment due to tides, $m^3 s^{-1}$

$h_1$ and $h_2$ are the thickness of the surface and bottom layers, h = $h_1$ + $h_2$, m

*The rate of energy input by tides, $P_T$ (adapted from Bowers, 2003)*

$$P_T = \gamma \frac{4}{3\pi} k_b \rho_w U^3 \tag{17.22}$$

$\gamma$ is the efficiency of resuspension

$k_b$ is the bottom drag coefficient

$\rho_w$ is the density of water, $kgm^{-3}$

U is the tidal current speed, $ms^{-1}$

The above equations (Eq. 17.20-17.22) show the rate of change in the concentration of sediment in the upper layer ($c_1$) and the lower layer ($c_2$). When the water initially becomes stratified, the concentration is at first considered equal in both layers (diagram (b), Figure 73). Similarly, when stratification breaks down and the water returns to a one-layer formation, the concentration is first assumed to be a mixture of the two stratified layers (diagram (a), Figure 73).

**Static settling speed**

Figure 74 displays the model prediction of suspended material concentration with a seasonally-stratifying water column and a static settling speed ($12mday^{-1}$, $0.14mms^{-1}$). As there is no variation in the settling speed used from the non-stratifying model run, the main difference between the two runs occurs during the intermittent stratification during spring-neap cycles between day 150 and day 200 in the first example in figure 74. Here the model is shown to stratify on the neap tides during this period.

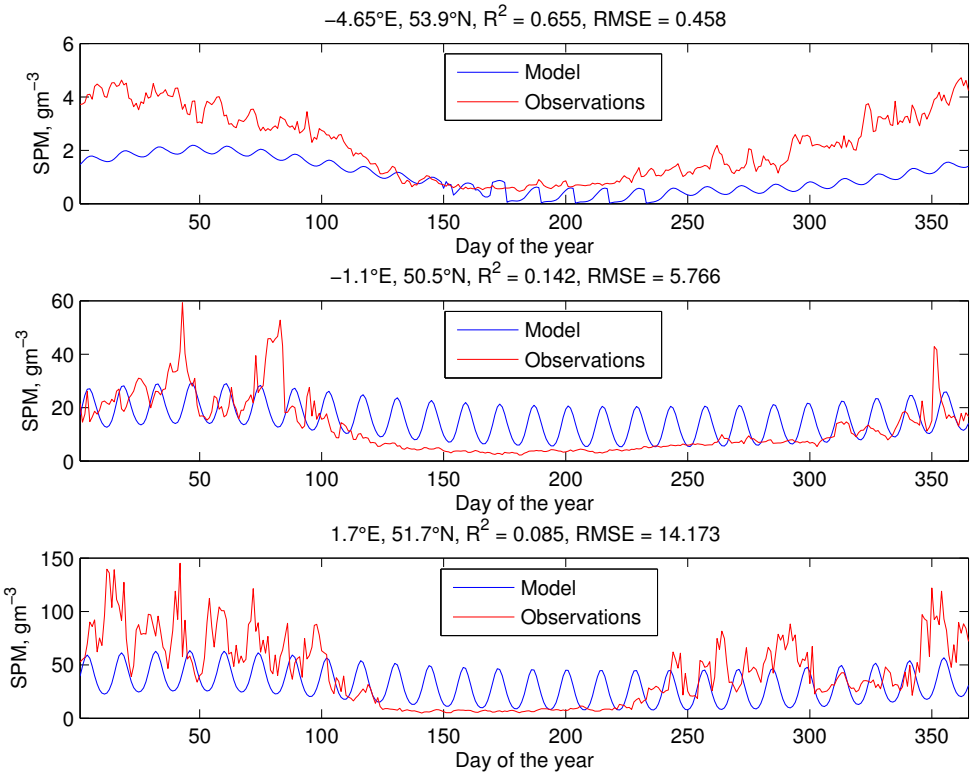


Figure 74: Modelled and remotely-sensed observations of suspended sediment concentrations at three locations over the U.K. and Atlantic French region. The model is with stratification and with a constant settling speed of $12mday^{-1}$ ($0.14mms^{-1}$).

In the latter half of the year, the model shows a great disparity between the observed and predicted concentrations. This is evidenced by an increase in concentration observed that is almost twice that which is predicted.

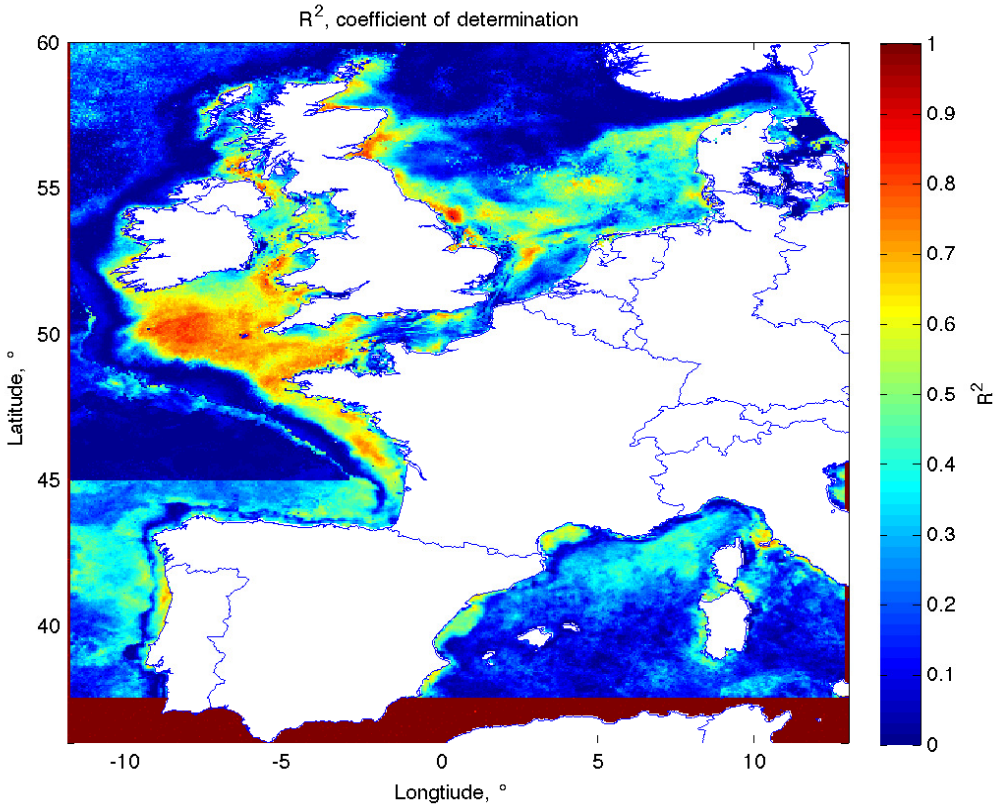


Figure 75: The coefficient of determination, $R^2$, between the remotely-sensed observations of suspended sediment concentration and the modelled suspended sediment concentration with stratification and with a static settling speed of $12mday^{-1}$ ($0.14mms^{-1}$).

With a static settling speed, figure 75 shows that the coefficient of determination, $R^2$ reaches between 0.5 and 0.6 in the Celtic Seas and southern Irish Sea. In the English Channel, the $R^2$ lowers to below 0.3 in the region between the Isle of Wight and Cherbourg.

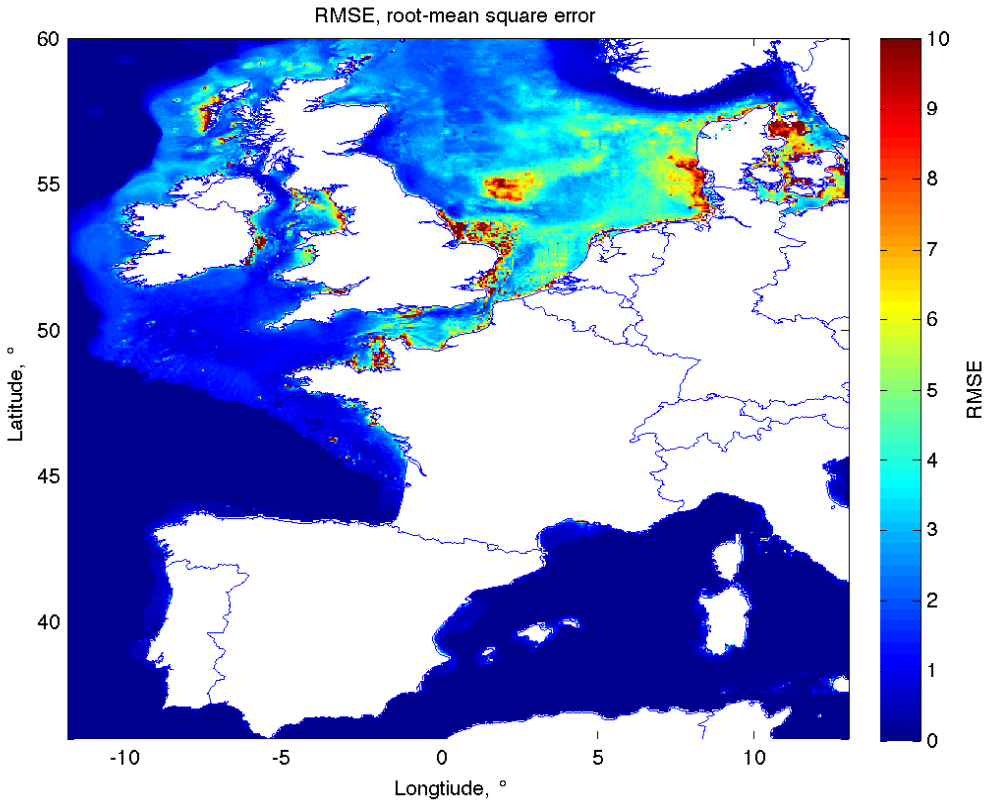


Figure 76: The root-mean squared error, RMSE, between the remotely-sensed observations of suspended sediment concentration and the modelled suspended sediment concentration with stratification and with a static settling speed of $12 m day^{-1}$ ($0.14 mm s^{-1}$).

Figure 76 shows the root-mean squared error, to be at its highest in areas corresponding to high concentrations, in the Western Irish Sea and the southern North Sea. A high RMSE is also observed in the central Irish Sea, corresponding to the low $R^2$ calculated.

**Seasonally-varying settling speed**

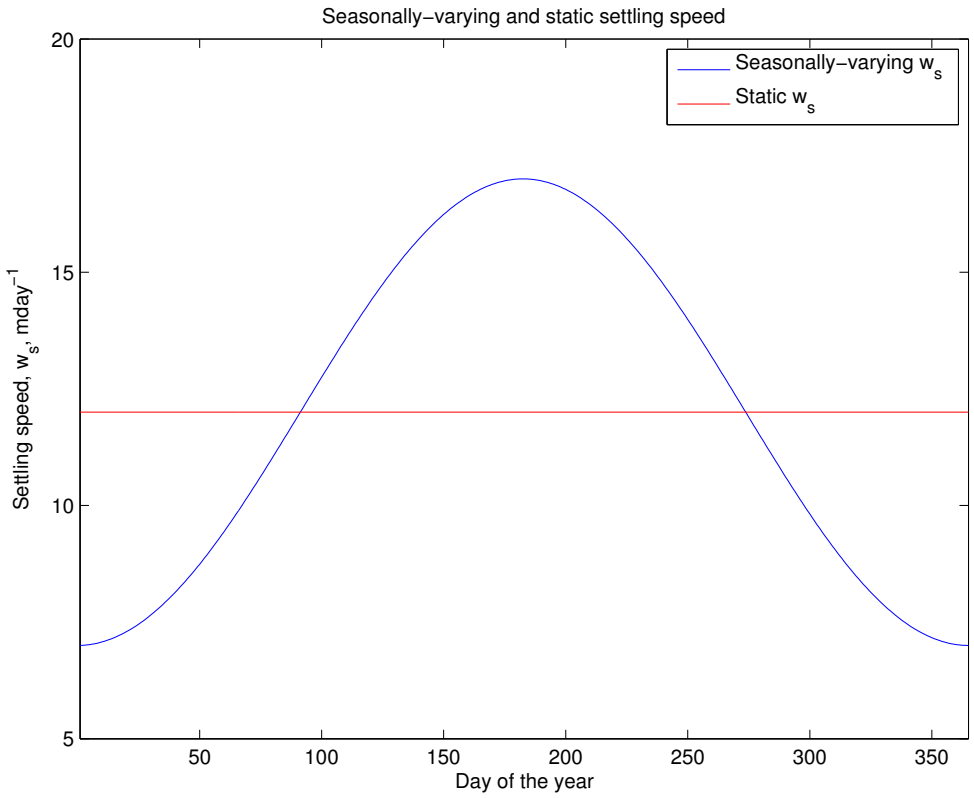


Figure 77: The sine curve representing settling speed over the year as used in the numerical model input. The settling speed is shown the vary between $7mday^{-1}$ ($0.08mms^{-1}$) in January and $17mday^{-1}$ ($0.2mms^{-1}$) in July.

Figure 78 displays the model prediction of suspended material concentration with both a seasonally-stratifying water column and also a seasonally-variable settling speed (represented by a sine curve, varying between $7mday^{-1}$ ($0.08mms^{-1}$) on the 1st of January to $17mday^{-1}$ ($0.2mms^{-1}$) on the 1st of July, Fig. 77).

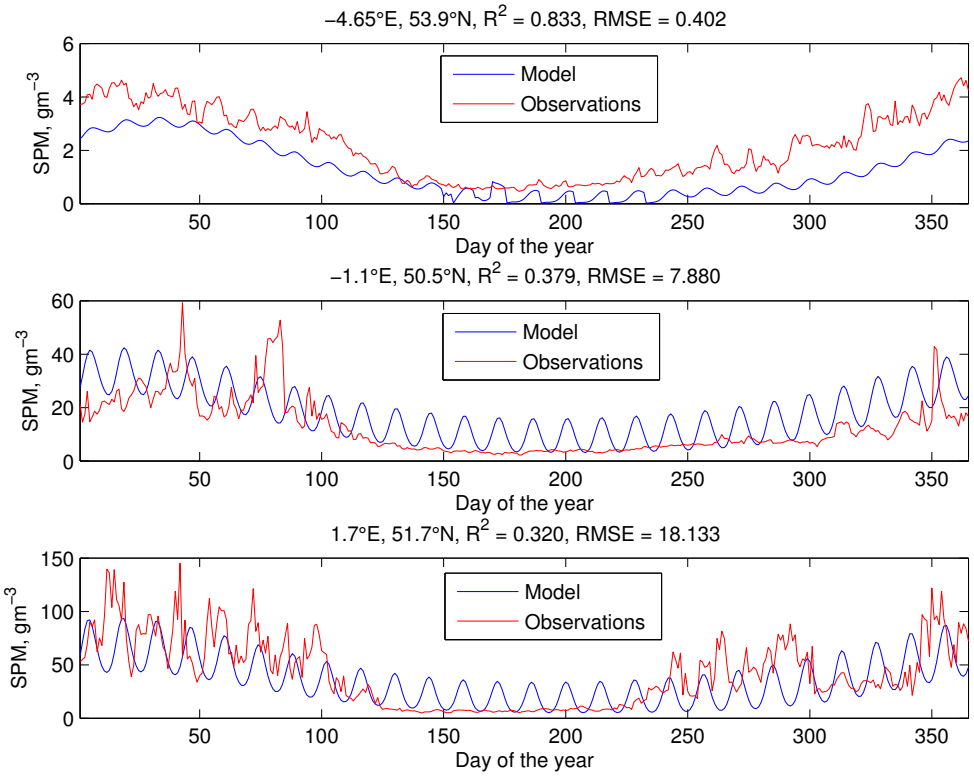


Figure 78: Modelled and remotely-sensed observations of suspended sediment concentrations at three locations over the U.K. and Atlantic French region. The model is with stratification and with a seasonally-varying settling speed between $7mday^{-1}$ ($0.08mms^{-1}$) in January and $17mday^{-1}$ ($0.2mms^{-1}$) in July.

Improving upon the static settling speed prediction, with a seasonal settling speed, the model is better able to match the rate of increase in remotely-sensed concentration observed, although the increase is still not as pronounced as in the observations.

To demonstrate the ability of the final model to predict the suspended sediment, the following two figures (Fig. 79; 80) display the prediction of the suspended sediment concentration in the summer and the winter alongside that of the remotely-sensed observations.

## 17.7 Model prediction, summer

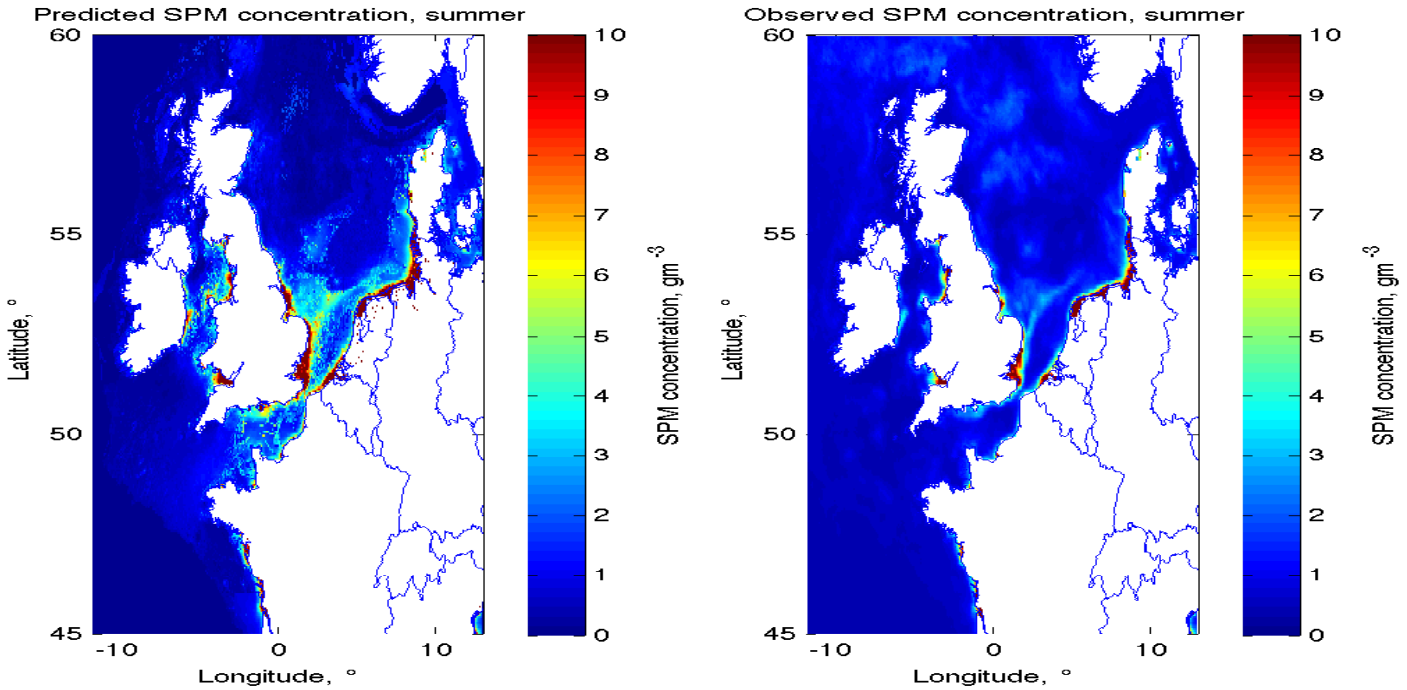


Figure 79: Modelled and remotely-sensed observations of suspended sediment concentrations averaged over the month of July over the U.K. and Atlantic French region. The model is with stratification and with a seasonally-varying settling speed between $7mday^{-1}$ ($0.08mms^{-1}$) in January and $17mday^{-1}$ ($0.2mms^{-1}$) in July.

The summer prediction is shown to reproduce the main regions of high concentration, namely those in the Bristol Channel, the Thames Mouth and the Irish Sea, however the model over predicts the concentration. In addition the model predicts a far higher concentration of the East coast of England than observed.

## 17.8 Model prediction, winter

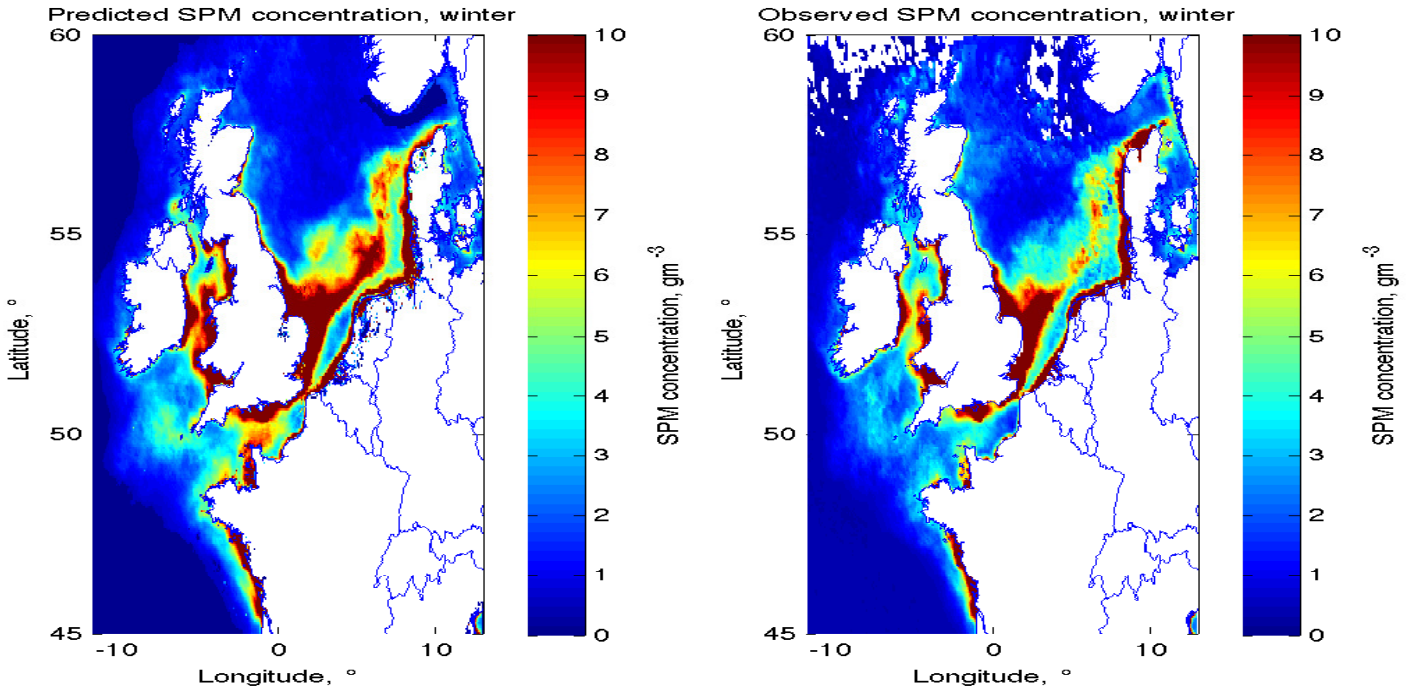


Figure 80: Modelled and remotely-sensed observations of suspended sediment concentrations averaged over the month of January over the U.K. and Atlantic French region. The model is with stratification and with a seasonally-varying settling speed between $7mday^{-1}$ ($0.08mms^{-1}$) in January and $17mday^{-1}$ ($0.2mms^{-1}$) in July.

Similarly to the summer prediction, the model over predicts the concentration of suspended material in the winter. In the winter, this is most notable off the coast of Cherbourg on the French side of the English Channel and also near to the Scilly Isles.

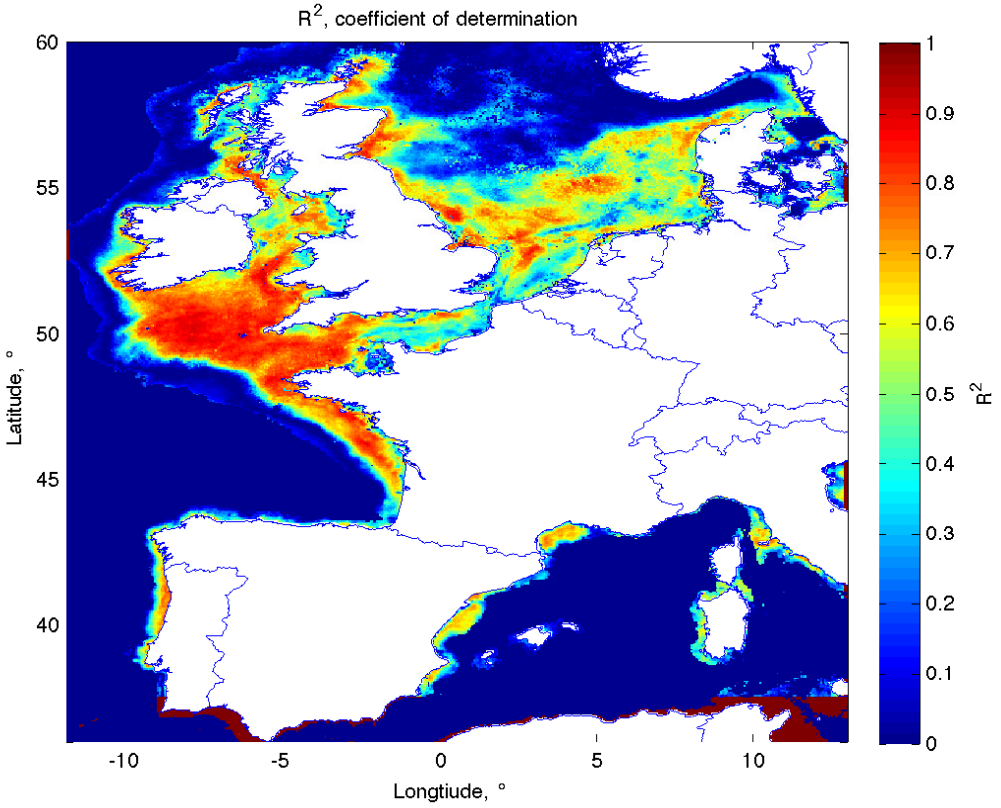


Figure 81: The coefficient of determination, $R^2$, between the remotely-sensed observations of suspended sediment concentration and the modelled suspended sediment concentration with stratification and with a seasonally-varying settling speed between $7mday^{-1}$ ($0.08mms^{-1}$) in January and $17mday^{-1}$ ($0.2mms^{-1}$) in July.

The $R^2$ value calculated is over 0.1 greater than with a static settling speed (Fig. 81). This is especially apparent in the central English Channel and the southern Irish Sea where the $R^2$ exceeds 0.8 off the coast of Cornwall.

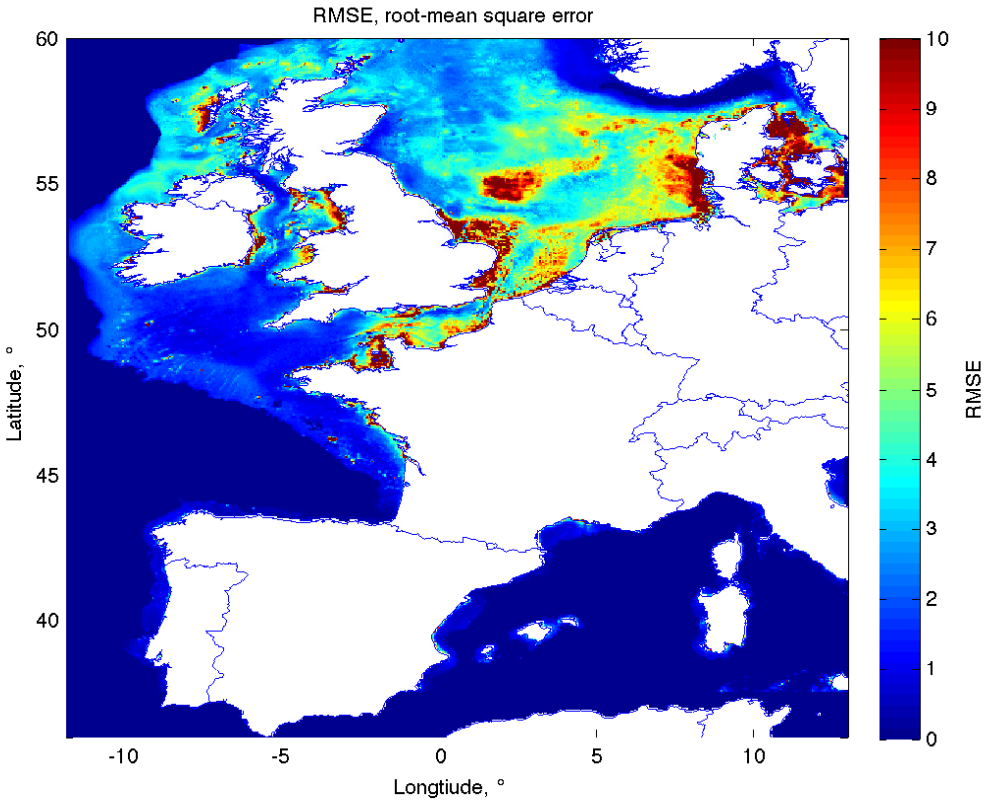


Figure 82: The root-mean squared error, RMSE, between the remotely-sensed observations of suspended sediment concentration and the modelled suspended sediment concentration with stratification and with a seasonally-varying settling speed between $7mday^{-1}$ ($0.08mms^{-1}$) in January and $17mday^{-1}$ ($0.2mms^{-1}$) in July.

As with the static settling speed model, the regions of high turbidity correspond to those of high RMSE (Fig. 82). The central English Channel observes RMSE levels in excess of $7gm^{-3}$ of the northern French coastline.

# 18 Discussion

### Settling speed

When using a static settling speed, the model was unable to represent the seasonal variability in the spring-neap variation of the suspended concentration as described by Bowers (2003) and discussed in the chapter considering particle settling speed of this thesis. As suggested by Bowers (2003), with the inclusion of seasonally varying settling speed into the model (higher in the summer and lower in the winter), a seasonal variation was observed in the spring-neap variation of the suspended matter concentration akin to that of the observations. The inclusion of a seasonally-varying settling speed is in the form of a sine curve. The presumption of this format is that the settling speed will be highest in the summer as organically-derived polysaccharides will be at their peak at this period, leading to a higher rate of successful flocculation. There are several caveats that could also affect the rate of flocculation and subsequent settling speed:

- In several locations, spring and autumnal blooms may also be observed in phytoplankton populations. The resulting exuded EPS (extracellular polymeric substances) released during these periods of high biological activity may also be linked to periods of increased flocculation and settling. As these occurrences are spatially variable, the broad approach as described for this model may not coherently account for the timing and duration described by a singular mid-summer peak in settling speed.
- Similarly, the amplitude of variability in the settling speed in the numerical model is assumed to be constant over the spatial area. For the same reasons as addressed in the previous point, certain areas are likely to observe larger variability in the settling speed than others.

**Spatial comparison**

- The model represents the remotely-sensed observations with $R^2$ values between 0.6 and 0.8 within the Irish and Celtic Seas. The model is less able to predict the concentration in the shallow regions north of Liverpool Bay and in the Western Irish Sea, with an $R^2$ of 0.4.
- In the English Channel, the model is able to predict the variability with an $R^2$ of $\approx 0.7$ in the western English Channel, lowering to an $R^2$ of 0.4 in the Eastern English channel (East of Cherbourg).
- The model is able to predict the concentration of SPM in the North Sea, south of $55°N$, with an $R^2$ of 0.65 in the region of the East Anglian plume. However in the northern North Sea, the model is only able to account for less of the observed variability with an $R^2$ of 0.4, discounting the shallow waters along the Eastern Scottish coast, where the $R^2$ is greater at between 0.6 and 0.75.
- The model was able to represent the temporal variability with an $R^2$ value of over 0.45 within much of the Irish Sea and the East Anglian plume.

**Temporal differences**

The numerical model with both stratification and a seasonally-varying settling speed produces values of $R^2$ over 0.8 at several locations (including the first example in figure 78) when compared with the remotely-sensed observations. Comparisons with the static settling speed run of the model show an improvement in the representation of seasonal variability in the spring-neap range of observed suspended sediment concentrations. The settling speed was shown to influence the range of observations occurring over a spring-neap cycle, with reduced winter settling speed leading to an increased range in SPM concentrations. The third location in figure 50 shows that the range of settling speeds used in the model are less than those necessary to match the observation, with spring-neap variability almost twice that of the model in the winter months.

All three examples in figure 50, appear to stratify seasonally, with the observed concentration dropping over the summer months with little observed spring-neap variability. Although the stratification is represented in the first example, the model runs for the second and third locations do not appear to stratify to the same extent as observed during this period. Ideally the numerical model would stratify in all three locations, however this is something which could be addressed in a future iteration.

**Implications**

This model demonstrates that a simple turbulent kinetic energy-based model can be used to represent between 50 and 90% of the observed variability in the remotely-sensed suspended matter concentration at the surface. However the model does not include the role of river discharge which greatly influences the concentrations of SPM in close proximity to large estuaries. Similarily, the model does not represent stratification as consistently as observed through remote-sensing. Even with improved representation of stratification and seasonal variability (with temporally and spatially varying settling speed), the model would be limited to its two-layer form for complicated coastal environment. This suggests that although it is useful when in comparison to remote sensing observations and comparing the influence of broader hydrodynamics parameters, for more detailed analysis it may be more favourable to use more computationally-developed hydrodynamic models such as those described by Guillou et al. (2016).

With this in mind, there are several potential improvements which could improve the numerical prediction of suspended materials:

- Estimations of river discharge in coastal regions, as with Saulquin et al. (2015). This may be especially important in regions dominated by the influx of riverine sediments such as in the Gironde and Seine estuaries.
- Further vertical layers in the water column, to describe varied vertical settling and flocculation (Ellis et al., 2008).

- A native hydrodynamic model, specialised to shelf sea dynamics.
- Different forms of particles, more representative of the size distributions and composition observed in the field.
- Better representation of the bed, including variable bed shear stresses and varied erodibility.

# Part V

# Remote sensing of particle settling speed

## 19 Introduction

As remotely-sensed observations of suspended sediments at the surface are limited by the settling speed of these particulates, it may be possible to use the observed presence of particles to infer information regarding their settling. The rate at which tides and wind resuspend sediment through near bottom turbulence can be quantified within physical models (Bowers, 2003; Ellis et al., 2008; Rivier et al., 2012).

Bowers (2003) predicted that the range of suspended sediment concentrations observed over a spring-neap cycle would be greater in the winter and lesser in the summer due to increased settling speed in the summer. Unfortunately, Bowers (2003) did not have the range of satellite observation to test this.

This chapter will aim to answer the following question:
*Can the settling speed of marine particles be quantified using remotely-sensed surface suspended sediment concentration from MODIS-Aqua?*

In order to do this, the following objectives will be carried out:

- From the remote-sensing archive, quantify the seasonal variability in spring-neap variation in the concentration of suspended sediments as proposed by Bowers (2003).
- Explore whether this seasonal modulation may be used to estimate the settling speed over the shelf using remote-sensing observation of the suspended sediment concentration.
- Compare these estimates of the settling speed to those of laboratory and field observations of particle settling.

# 20 Methods

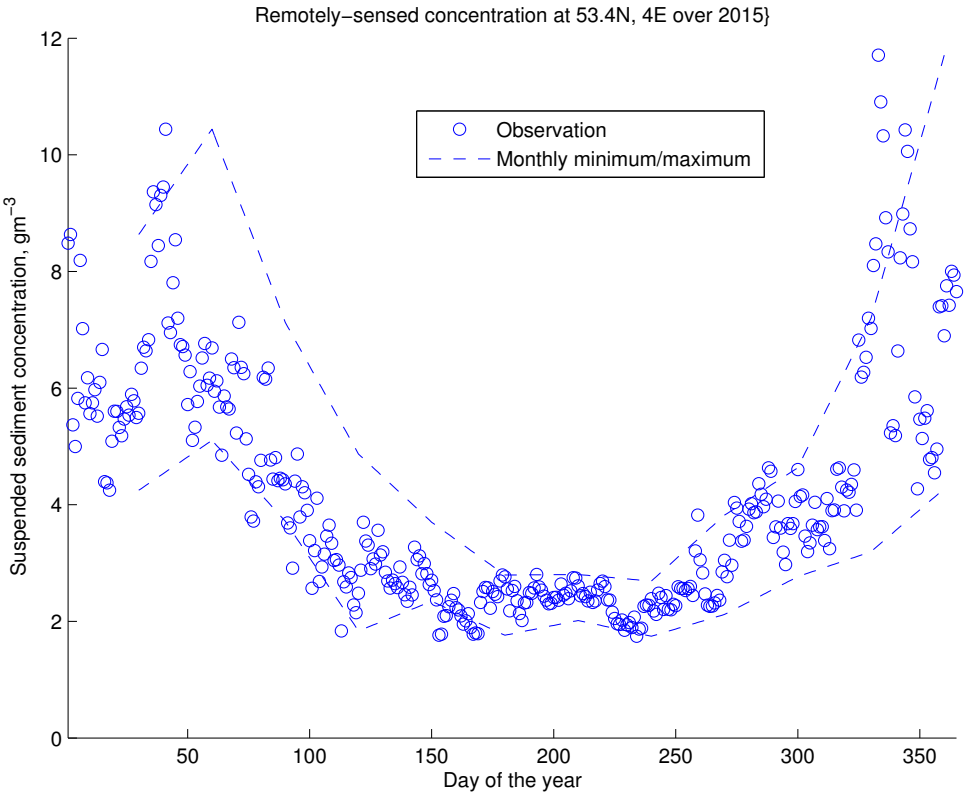


Figure 83: MODIS remotely-sensed observations of suspended sediment south of the Isle of Man, $53.4 \circ N, -4 \circ E$. The dashed lines are used to represent the monthly minimum and maximum concentrations. This makes it possible to observe seasonal variability in the range of concentrations observed.

As can be seen in Figure 83, the highest range of concentrations observed occur in the winter months, between November (day 290) and February (day 60), as predicted by Bowers (2003). Bowers (2003) proposed that this is due to the range of concentration observed over a spring-neap tidal cycle being larger in the winter than in the summer.

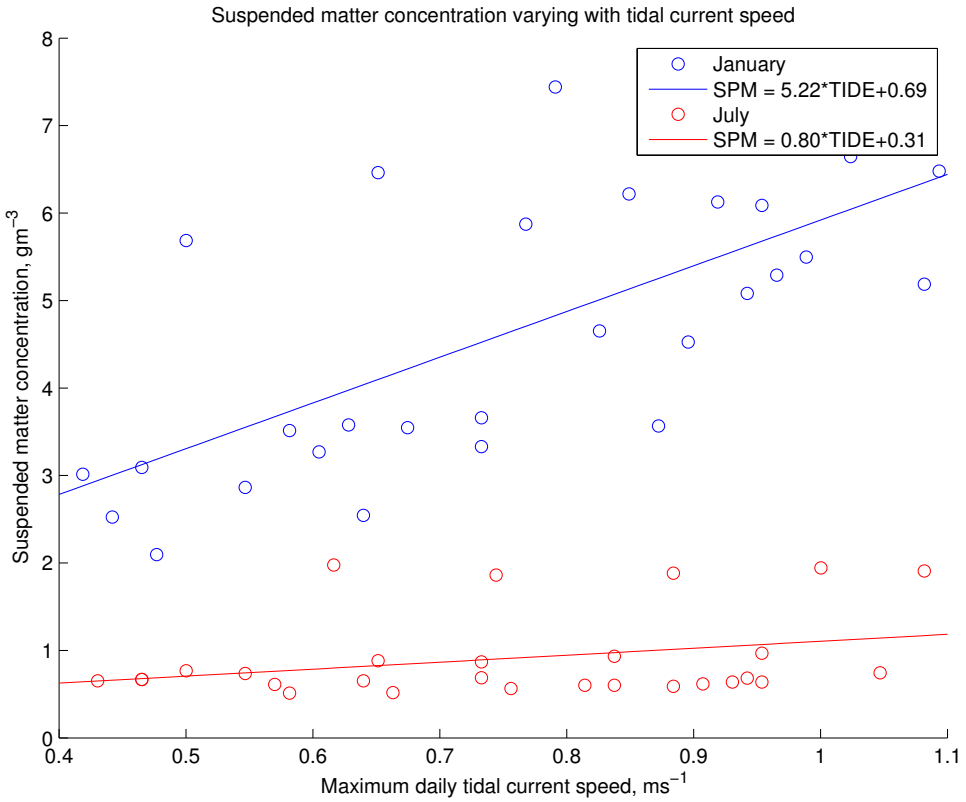


Figure 84: MODIS remotely-sensed observations of suspended sediment south of the Isle of Man, $53.65°N, -4.89°E$ between 2008 and 2010. The observations are plotted against the maximum daily tidal current speed relative to each observation at the same location, estimated using the output from TPXO 8.0 Atlas as described in the statistical model chapter. The variability from lowest maximum daily tidal current speed to highest maximum daily tidal current speed represents spring-neap variability. Two lines of best fit are plotted through the data points, one to represent points observed in January and another for points observed in July. The equations describing these two lines may be found in the legend. For each line, a t-Test produced p-values less than 0.05, suggesting that the dc/du values are significant (for January, p = 1.6439E-15; for July, p = 0.042965).

The range of concentrations observed over a spring-neap cycle can be described by the slope of the suspended sediment concentration, c, with the tidal current speed, u. Figure 84 displays the variability in the suspended matter concentration with the maximum daily tidal current speed. The slope of these lines can be expressed simply as dc/du. In the example above the value for dc/du in the winter is over 6 times larger than that in the summer, describing a larger range of suspended sediment concentrations observed over a spring-neap tidal cycle in

the winter than the summer.

In Bowers (2003), the equations for a simple turbulent energy-based numerical model are used to predict the concentration of suspended sediment over the year using information about the tides, wind-driven waves and an estimation of the particle settling speed. Part of this equation defines the change of concentration over time as a function of the tidal current speed. By rearranging these equations, it is possible to estimate the particle settling speed as a function of dc/du, the change in the concentration over a spring-neap cycle over the change in the maximum daily current speed observed.

Equation 20.1 describes the forces which act to suspend or settle material in the ocean, The left term representing the turbulent kinetic energy dampened by the water depth the force is acting over. The right term represents the settling of suspended material acting over the depth of the water column. When dc/dt is 0, the steady state concentration can be described by equation 20.1.

*Steady-state suspended sediment concentration (Bowers, 2003)*

$$c = \frac{P}{g' h w_s} \tag{20.1}$$

c is the suspended sediment concentration, $kgm^{-3}$
P is the rate of energy input from the tides and wind, $kgm^{-3}s^{-1}$
g' is reduced gravity, $ms^{-2}$
h is the water depth, m
$w_s$ is the particle settling speed, $ms^{-1}$

Equation 17.3 describes the rate of energy input from winds and tides, P. By inputting equation 17.3 into equation 20.1 (equation 20.2) and then differentiating equation in terms of the current speed, u, it is possible to rearrange the term in terms of dc/du and $w_s$ (equations 20.3 and 20.4).

*Steady-state suspended sediment concentration, with rate of energy input, P, expanded*

$$c = \frac{\gamma(\frac{4}{3\pi}k_b\rho_w u^3 + k_s\rho_a w^3)}{g'hw_s} \tag{20.2}$$

$\gamma$ is the efficiency of resuspension

$k_b$ and $k_s$ are the bottom and surface drag coefficients

$\rho_w$ is the water density, $kgm^{-3}$

u is the tidal current speed, $ms^{-1}$

w is the wind speed, $ms^{-1}$

*Change in concentration with change in daily maximum tidal current speed*

$$\frac{dc}{du} = \frac{\gamma\frac{4}{\pi}k_b\rho_w u^2}{g'hw_s} \tag{20.3}$$

By using the MODIS suspended sediment observations as the concentration (c) and the tidal model output approach detailed in the numerical model in the previous chapter, it is possible to calculate dc/du for each month of the year. By rearranging equation 20.4 it is then possible to use dc/du to estimate the settling speed ($w_s$) for each month of the year.

*Settling speed ($w_s$) as a function of dc/du*

$$w_s = \frac{\gamma\frac{4}{\pi}k_b\rho_w u^2}{g'h\frac{dc}{du}} \tag{20.4}$$

# 21 Results

Using equation 20.4 it is then possible to estimate the particle settling speed from the slope between suspended material concentration and tidal current speed, dc/du.

A t-Test was carried out for each pixel, in each monthly period. The relationship identified by the dc/du values in January were shown to produce values almost entirely throughout under the p = 0.05 threshold. Figure 85 displays the p-values for July, where there are several small regions where the dc/du relationships are not significant.

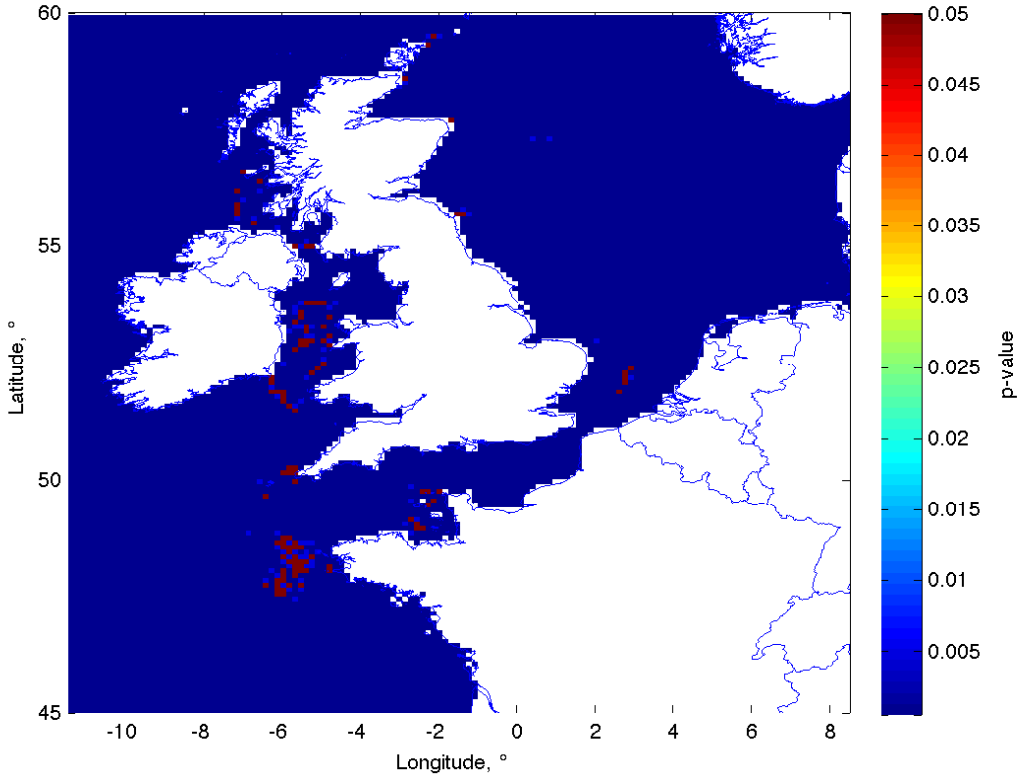


Figure 85: p-values produced by t-Test for the dc/du relationship in July over the northwest European shelf. Values less than 0.05 represent a significant relationship, with red pixels representing locations with p-values greater than or equal to 0.05, which are therefore deemed to not be significant.

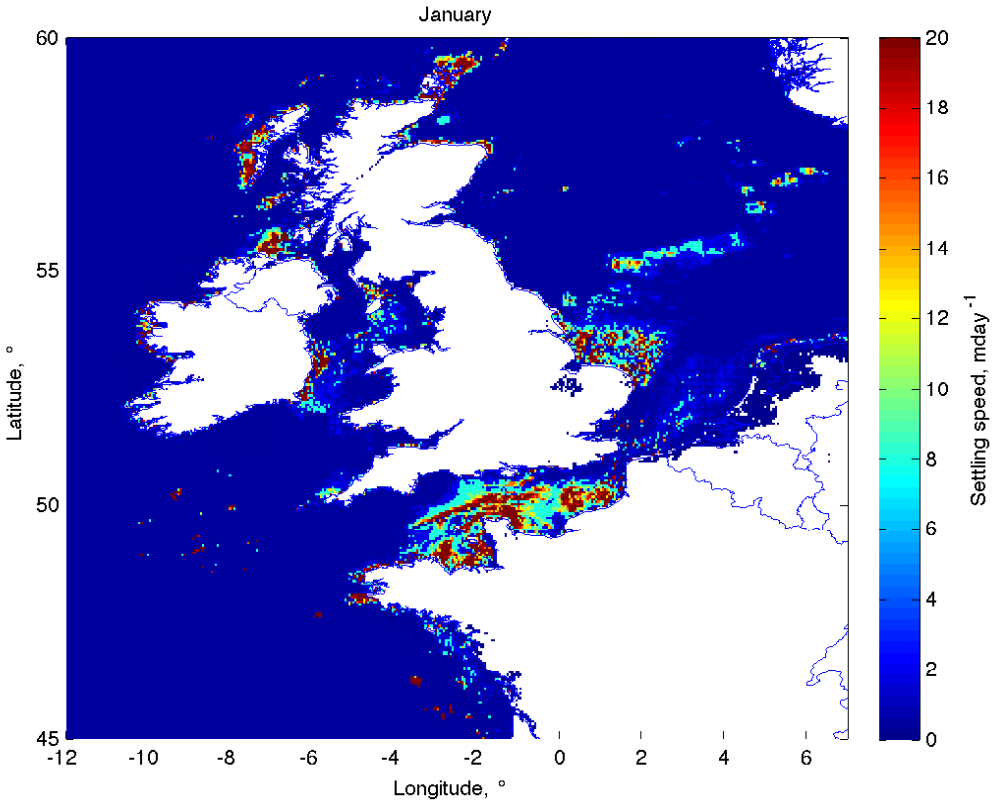


Figure 86: Settling speed in January as calculated using equation 20.5. Map covers the region of the northwest European shelf. Settling speed calculated ranges from 0 to 20 $mday^{-1}$ ($0.25mms^{-1}$).

Figure 86 displays the estimated settling speed for the month of January. A high settling speed is observed within the English Channel, in addition to off the Southeast coast of Ireland and the Norfolk coast.

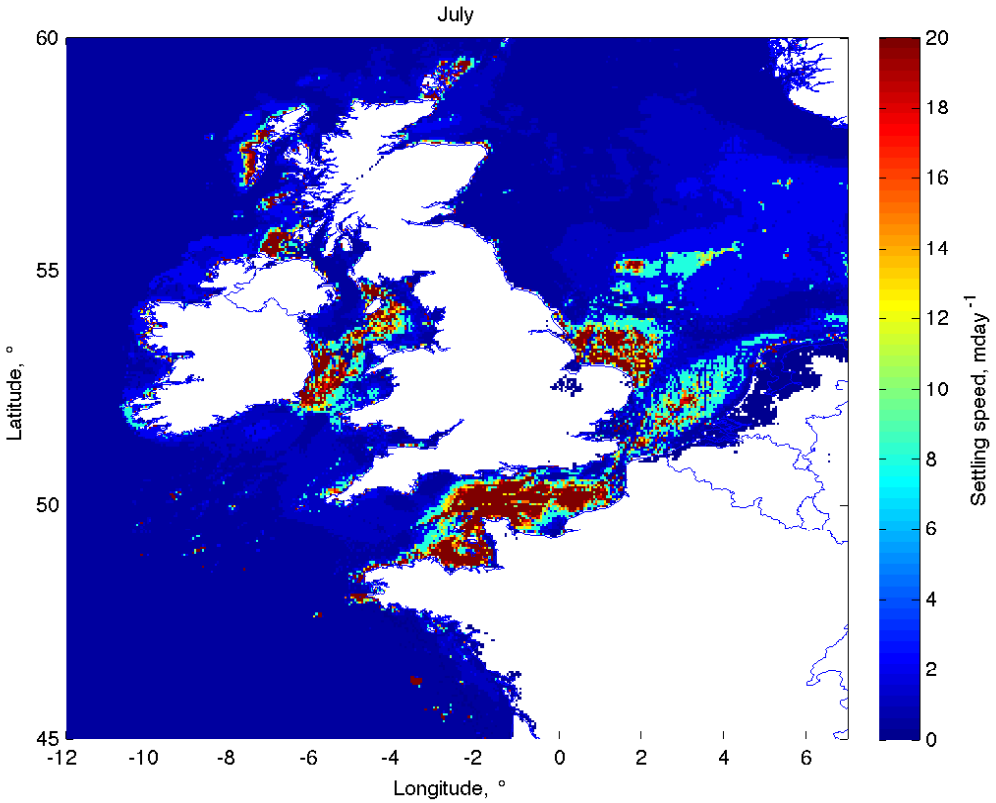


Figure 87: Settling speed in July as calculated using equation 20.5. Map covers the region of the northwest European shelf. Settling speed calculated ranges from 0 to 20 $mday^{-1}$ ($0.25mms^{-1}$).

The July settling speed shows not only an increase in settling speed in the regions highlighted in the winter, but also an expansion into Liverpool Bay and north of the Belgian coast (Figure 87).

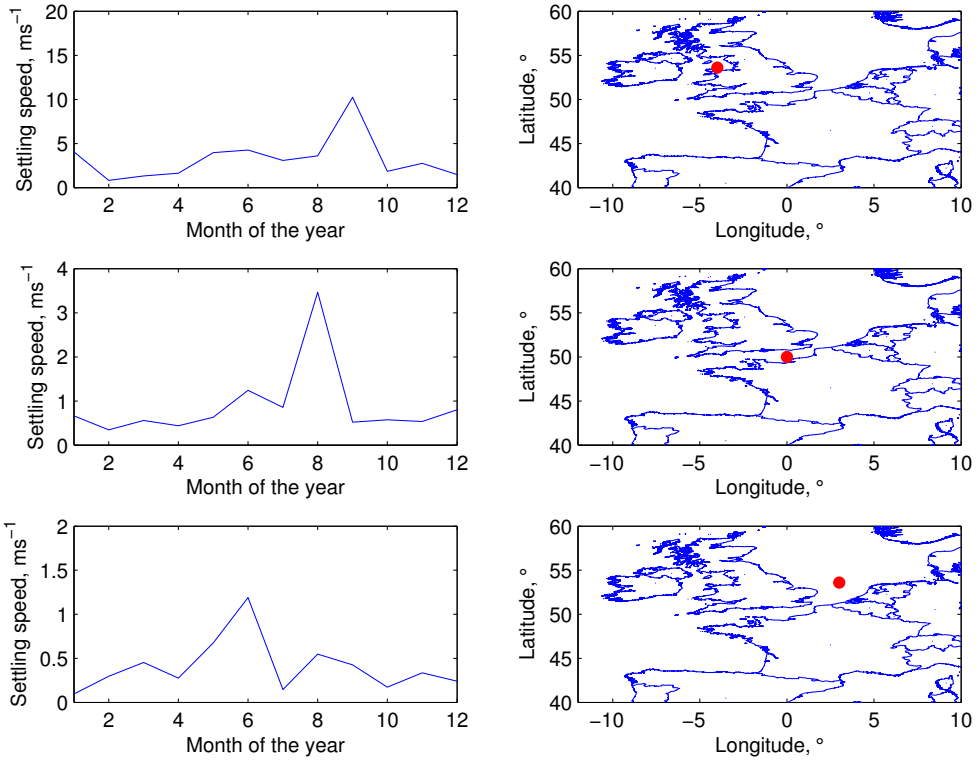


Figure 88: Settling speed estimated for each month of the year at three locations: the Irish Sea, the English Channel and the North Sea. The locations of each point correspond to the red dot on the adjacent map.

In order to look at the month-by-month variation in the estimated settling speed, three locations have been used (Figure 88). All three locations show a peak in settling speed within the summer months however the duration of the peak varies from the pronounced peak observed in August in the English Channel location, to the less pronounced peak at the Irish Sea location. There is also large variability between the three points in the magnitude of settling speeds estimated, with the range being $1mday^{-1}$ and $11mday^{-1}$ in the Irish Sea, to between $0.2mday^{-1}$ and $1.2mday^{-1}$ in the North Sea.

# 22 Discussion

In Bowers (2003), a simple numerical model of resuspension detailed seasonal modulation of the spring-neap variability in the suspended sediment concentration, describing the potential link to the particle settling speed. Using the remotely-sensed observations of the suspended sediment concentration, it was possible to estimate the bulk settling speed. The bulk settling speed represents the net settling of the body of suspended material in contrast to referring to the settling of a specific particle of a given size.

## 22.1 Estimations of settling speed

From the remotely-sensed observations of suspended material concentration and the daily maximum tidal current speed from the model, it was possible to calculate values for dc/du for each spring-neap tidal cycle. From this, by implementing Equation 20.4 derived from the simple turbulent kinetic energy-based resuspension model described by Bowers (2003), it was possible to estimate the particulate settling speed from the observed values of dc/du.

From the maps of settling speed in January and July, there are several things to note:

- The settling speed is observed to be higher in July than January.
- Areas such as the central Irish Sea, the English Channel and the East Anglian coast all experience high levels of settling speed.

From the single point estimations of settling speed, there are several things to note:

- At all locations, there was an observed seasonal variation in the settling speed.
- Generally, the settling speed was at its lowest in the winter months.
- There was variability in the timing of the peak of the settling speed, with some locations peaking in the spring and some in the summer, with the North Sea location observing a peak before and after the summer.

The estimations of settling speed were found to be in excess of $20 m day^{-1}$ at several locations

over the shelf region. Studies such as those by Manning and Dyer (2002) and Soulsby et al. (2013) would suggest that this settling speed corresponds to a particle diameter of approximately $75\mu m$. In field observations, this size would be considered relatively small but it is expected that the settling speed calculated in the above chapter represents the variability in settling speed upon the bulk of the suspended material. In this case, it is appropriate to define the bulk settling speed as the overall settling speed which is representative for a body of suspended material.

This study has provided overview of the spatial and temporal variability of the settling of marine particles using the novel method relating to the dc/du term. So far, there is no large scale estimation of settling speed variability of this nature in the literature, with observations limited to laboratory investigations and deployments of settling velocity tubes (Dyer & Manning, 1999; Soulsby et al., 2013).

As predicted by Bowers (2003) a seasonal variability in the settling speed was observed. It is expected that this seasonal change is due to the variation in particle properties. At times when there is assumed to be low level of EPS (extracellular polymeric substances) in the water (during the winter) and a high level of turbulent shear, the settling speed is shown to be at its lowest (Verney et al., 2011; Safak et al., 2013; Soulsby et al., 2013). In periods where the level of EPS is expected to increase (during the summer or within a bloom period) and the level of turbulent shear is less (within the middle of the year), the settling speed is shown to be higher.

At present, there is no data to validate the remotely-sensed settling speeds provided, however further work could involve the integration of settling speed observations through metadata analysis at different locations at multiple points in the year as a form of validation, including studies such as Verney et al. (2011). However, due to the fine spatial resolution of such survey data for validation often occurring in the coastal zone, it would most likely be necessary to use higher resolution remote sensing data for validation.

## 22.2 Limitations

One noted caveat of this method of estimation regards the requirement of a high enough concentration to provide reasonable regression in order to calculate the value of dc/du necessary for the calculation. Areas with low concentration ($< 1gm^{-3}$) are unlikely to provide reasonable estimates of the settling speed and therefore subsequent estimates on these grounds must be treated with caution.

Within the results chapter, it was shown that it is possible to estimate the settling speed of particles within the water column using remotely-sensed observations of the suspended particulate matter concentration to monitor the response of the concentration to the local maximum tidal current speed. By monitoring the rate of decrease or increase in the concentration with change in the relative tidal current speed, the expression dc/du may be estimated. Using a formulation derived from the model formulae of Bowers (2003), this can be directly related to the particle settling speed using assumptions derived from peer-reviewed literature. In spite of the potential issues that may arise from using assumptions in the case, it can be proposed that overestimation or underestimation of these assumptions would have little consequence on overarching settling speed dynamics observed. To this vein, these assumptions may act to dampen the clear response described acting to overestimate the winter settling speed and underestimate the summer settling speed, further increasing the seasonal variability. The key assumptions used in this calculation can be described as follows:

**Efficiency of sediment resuspension, $\gamma$**

The value for the efficiency of sediment resuspension represents the fraction of turbulent kinetic energy (TKE) required to maintain sediment in suspension. The value used in Bowers (2003) was estimated using observations over the year from 10-day averages from gravimetric measurements of total suspended sediment concentration within the Menai Strait, Anglesey.

**Bottom drag coefficient,** $k_b$

The bottom drag coefficient is also assumed to be constant in the formulation. In reality, variation would be expected dependent upon the variation in seafloor roughness. It can be proposed that in the winter, the seafloor would be rougher due to increased wave-driven winter erosion, therefore increasing the drag coefficient (Howarth, 1998; Werner et al., 2003; Safak, 2016). If this variation was observed, it would act to increase the estimated settling speed in the winter and likewise decrease the settling speed in the summer. As this would act against the observation variability, it could be seen to dampen the settling speed, overestimating in the winter and underestimating in the summer.

**Reduced gravity,** $g^{'} = g\frac{\rho_s - \rho}{\rho}$

- The acceleration due to gravity is uniformly cited a $9.81ms^2$ on Earth so this is used in this formulation.
- The density of water, $\rho$ can be assumed to be between $1000kgm^{-}3$ for fresh water and $1050kgm^{-3}$ for water of high salinity, averaging at $1025kgm^{-3}$ as a default water density.
- In the case of the solid density of particles in the water, $\rho_s$, the formulation assumes that this is $1500kgm^{-3}$, 57% of the solid density of quartz ($2650kgm^{-3}$) leading to a reduced gravity, $g^{'}$ of $5m^2s^{-1}$. As this is most contentious assumption in this formulation, two scenarios may be assumed, in the winter as particles are smaller, more mineral and more dense the solid density could increase to $1600kgm^{-3}$ and in the summer where particles are bigger, more organic and less dense, the solid density could decrease to $1400kgm^{-3}$ (estimates from Dyer & Manning, 1999). These two values would lead to a $g^{'}$ of $5.5m^2s^{-1}$ in the winter and $3.5m^2s^{-1}$ in the summer, therefore acting to increase the winter settling speed by a factor of 1.1 and depress the summer settling speed by a factor of 0.7. The below figure shows the settling speed using the present formation and that with an approximated seasonally-varying reduced gravity, clearly

showing overestimation in the winter and underestimation in the summer.

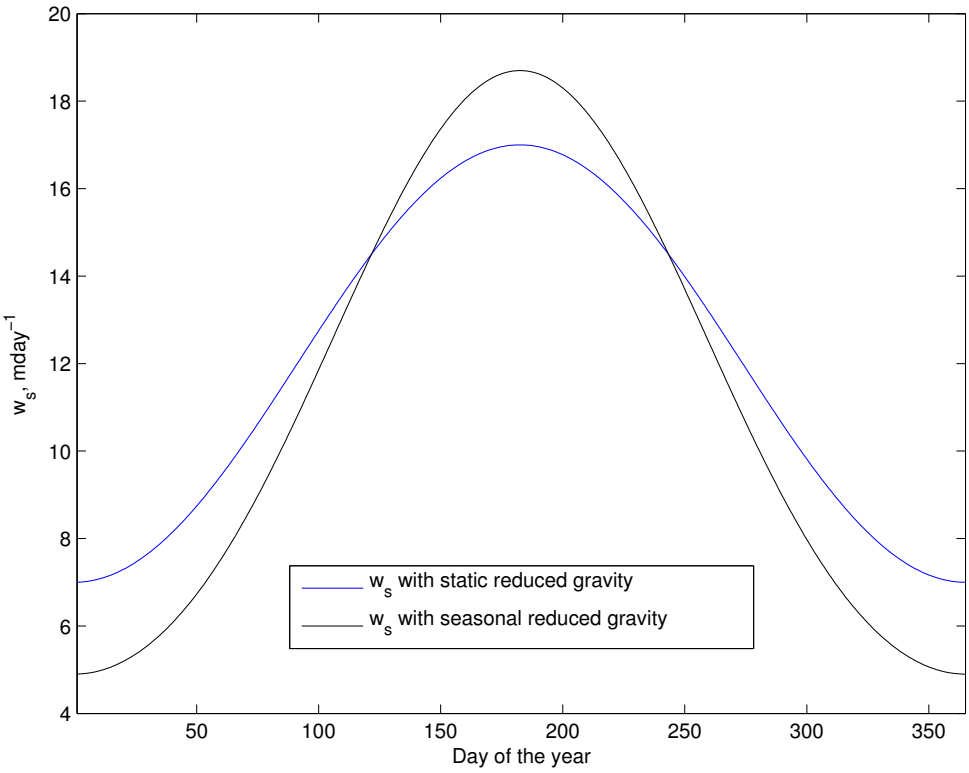


Figure 89: Influence of reduced gravity (g') upon the settling speed ($w_s$) of marine particles.

As described in the above assumptions made in the settling speed calculation, it can be proposed that use of these assumptions would not act against the observed variability but instead, the variability would in reality have a larger amplitudinal dynamic but within the same seasonal phase (Figure 89).

## 22.3 Semi-diurnal and spring-neap variability

Due to the low frequency of observations, the expected minimum period of dc/du calculation and estimation of the settling speed, would be over a spring-neap cycle of approximately 14.5 days. However, it is proposed that there would be variability in the settling speed within this 14.5 day period (Figure 90).

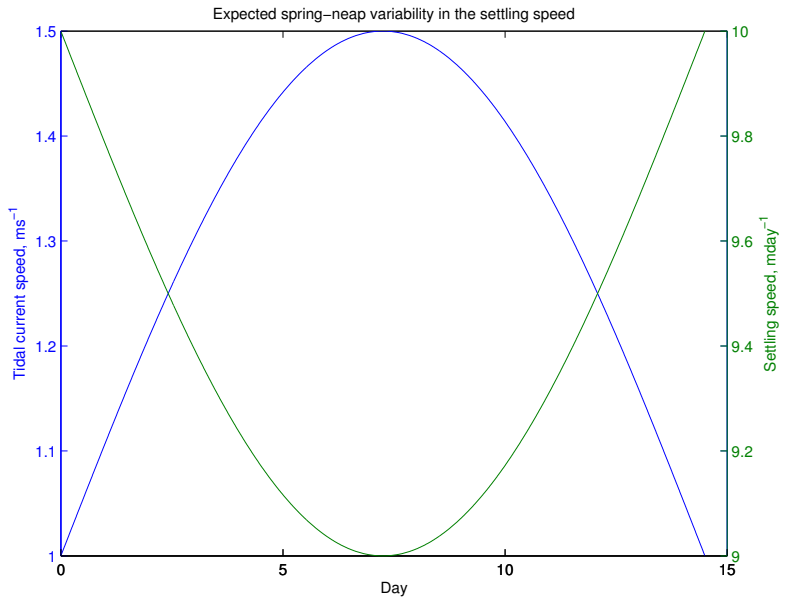


Figure 90: Proposed settling speed induced by the spring-neap tidal cycle.

Verney et al. (2011) described floc formation over a semi-diurnal tidal cycle, estimating lower floc diameters during the flood and ebb tides, with peaks during the slack tides. Increases in floc size have been shown to correspond with an increased rate of settling (Manning & Dyer, 1999; Soulsby et al., 2013). Similar to that of Verney et al. (2011), van der Lee (2000) described floc variation and settling speed over an ebb flood cycle, with floc size and settling peaking during the slack periods between ebb and flood. As such it can be expected that the settling speed would follow a similar variation to that predicted by Verney et al. (2011), peaking in settling speed during the slack tide and dropping on the flood and ebb tides (Figure 91).

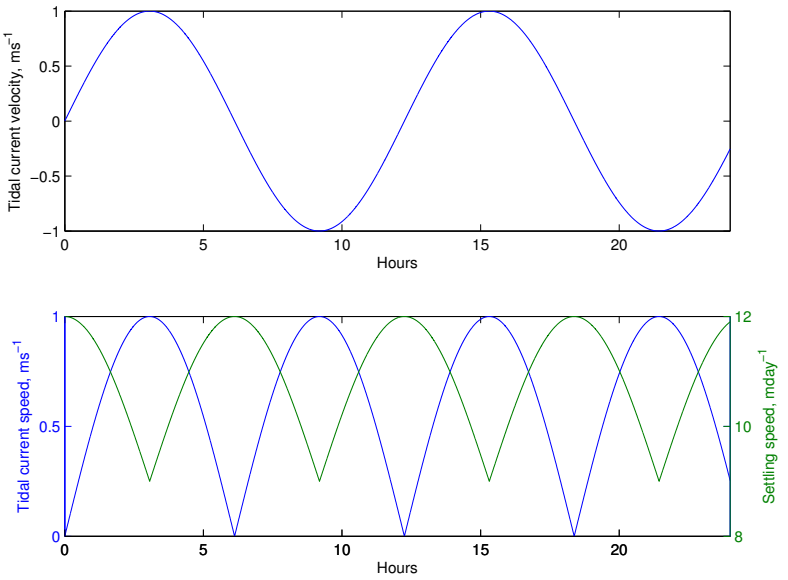


Figure 91: Approximated settling speed variability over a semi-diurnal tidal cycle (Verney et al., 2011), excluding flood-ebb tidal asymmetry.

The spring-neap variation would modulate the turbulent shearing observed over a semi-diurnal tide. Thus, on a spring tide, where tidal currents would be largest and turbulent shearing greatest, the floc size would be lower than on the neap tide during less turbulent shearing. The settling speed can thus be proposed to vary in the form where it is lowest during the spring tide and highest during the neap tide, with the ebb and flood variability on top of this.

Using the dc/du method (Equation 20.5) may not be possible to analyse semi-diurnal variability with present satellite limitations, which normally allow for only one image each day of a location. It is possible that with advancements in geostationary satellites, that variability over a spring-neap cycle in settling speed may be explored. Within the region covered by this thesis (northwest European shelf), there are several locations which may provide two images for each day, where MODIS swath granules overlap.

The statistical modelling chapter of this thesis describes the application of data of MODIS-Terra, MERIS, VIIRS and SEVIRI which would be similarly applicable for this study. In addition to increasing frequency for analysis of the spring-neap cycles of settling speed, this

expansion would have the capability to examine semi-diurnal variability as proposed. Similarly, using multiple remote sensing datasets may aid in improving temporal and spatial resolution for future validation of this method.

## 22.4 Do Chlorophyll-a or sea surface temperature (SST) relate directly to particle settling speed?

In the statistical model of Rivier et al (2012) and the statistical modelling chapter of this thesis, Chlorophyll-a was used as an approximation of the photosynthetic productivity of the water column. The rationale for using this it to approximate flocculation and thus the influence of settling speed upon particles. Flocculation is catalysed by the EPS (extracellular polymeric substances) which are released during the degradation of phytoplankton following a bloom. It is has therefore been suggested that this may cause a delay in the effect of a peak in Chlorophyll-a upon the level of EPS and thus the rate of particle settling. In addition, assuming Chlorophyll-A represents flocculation does not take account of the influence of turbulent shearing upon floc size which may occur during the winter, causing a drop in the settling speed. To counter this, Rivier et al. (2012) proposed the use of the sea surface temperature as a representation of flocculation throughout the year, highest in the summer an lowest in the winter. Figure 92 compares the estimation of the settling speed, to the sea surface temperature and Chlorophyll-a concentration at a location in the southern Irish Sea.

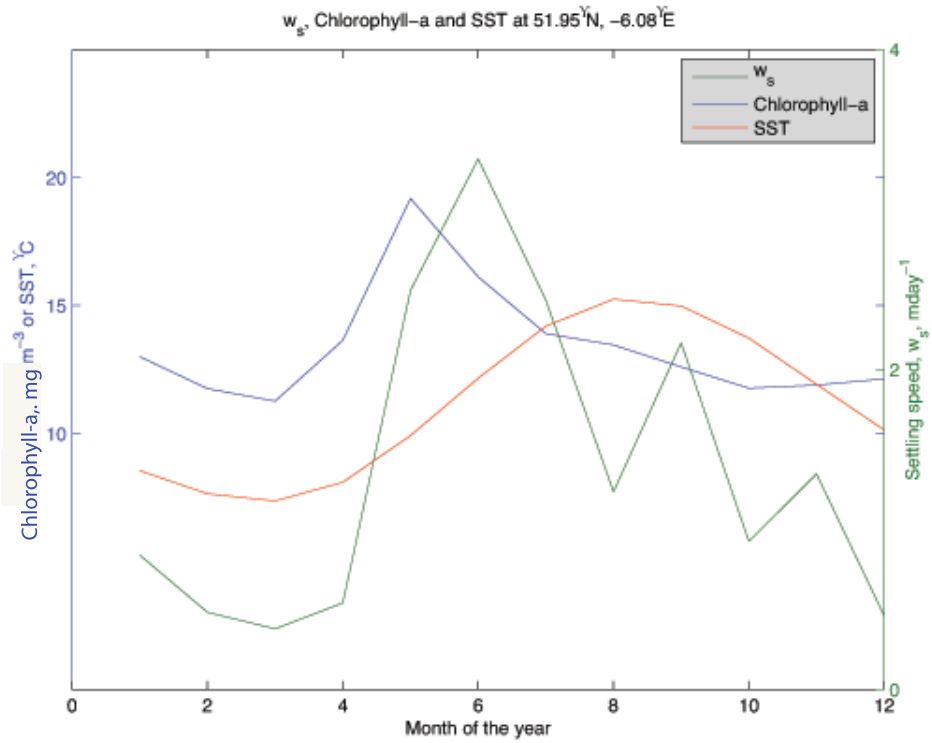


Figure 92: The estimated settling speed ($w_s$) alongside the sea surface temperature (SST) and Chlorophyll-a concentration at a location in the southern Irish Sea ($51.95°N, -6.08°E$).

Using the Chlorophyll-a concentration, the peak in May occurs approximately a month before that of the settling speed in June. This may represent the period of breakdown of phytoplankton and the time needed for the release of EPS into the water column. However, the sea surface temperature is shown to peak in August, with an additional peak noticeable in the settling speed in September. A potential avenue of future research could involve relating the importance of both the sea surface temperature and the Chlorophyll-a concentration to flocculative processes and settling speed.

## 22.5 Implications

There are several implications from the ability to provide a first estimate of the settling speed of the water column:

- Numerical models for sediment transport often require heavily parameterised estimates of settling speed (Baugh & Manning, 2007). This method provides estimations of settling speed for each month, allowing a mean estimation for the two inclusive spring-neap tidal cycles. Manning and Bass (2006) observed that as the populations of microflocs and macroflocs also change over a semi-diurnal tidal cycle, that the settling speed also varied by a factor of 5 over this period. Unfortunately, due to irregular daily observations from remote-sensing, it would not be possible to resolve variability at a semi-diurnal scale using this method. Despite this, the first order spring-neap variability from this method could be used to constrain the second order semi-diurnal variability in more precise estimations.
- Pollutant monitoring requires accurate understanding of the settling speed of pollutants (Aldridge et al., 2003). Although this study does not directly look at pollutant dispersion or pollutant transport, flocculated particles are known to often contain pollutants. When estimating the floc settling of pollutants in analysis of pollutant dispersion, estimates such as those described would provided valuable insight.

- Understanding the settling of marine flocs also has an important role in monitoring carbon sequestration with studies of Bianci (2011) and Bauer et al. (2013) describing the importance of flocculation in the sequestration of both inorganic and organic carbon. Bauer et al. (2013) estimated that flocculated coastal sediments account for 45% of the net carbon burial in shelf sea regions. Providing estimates of the rate of settling as those in this study alongside measurements of inorganic and organic carbon concentration could allow for future identification of the key areas of shelf seas responsible for this important pathway of carbon sequestration.
- Although not explored within this study, particle size alongside particle density are key factors controlling the settling speed of marine particles (see equation 3.1). Future analysis could expand upon this study with inclusions of estimates of particle size (van der Lee et al., 2009).

# Part VI

# Conclusions

The thesis centres upon methods to improve the monitoring of suspended material in coastal shelf seas. In addition to field observations looking at understanding assumptions made in remote-sensing algorithms, other chapters looked at utilising the present remote-sensing archive to develop statistical models and to test numerical simulations. This chapter summarises the main conclusions and future developments from the chapters in this thesis:

**Part III - Backscattering of light by marine particles**

- The mass-specific backscattering coefficient, $b_{b_p}*$, which is assumed constant in remote-sensing algorithms was shown to vary by over a factor of 4 in the field observations.
- Correlation between the concentration of total suspended solids and the mass-specific backscattering coefficient, $b_{b_p}*$, produced an $R^2$ value of 0.36. Although this is not a high value of $R^2$, it does present the possibility of iterative estimation of $b_{b_p}*$ in future remote-sensing algorithms. $b^*_{b_p}$ was shown to correlate with the mineral content, with an $R^2$ of 0.38, literature suggested this relationship to be due to the increase in the refractive index with mineral content. This was also proposed to be the main factor influencing the relationship between total suspended solids concentration and $b^*_{b_p}$, as the highest concentrations were observed to be more mineral.
- The mass-specific backscattering coefficient, $b_{b_p}*$ was shown to be dependent on the particle size, D50, with an $R^2$ of 0.43. Analysis alongside other observations suggested that this was less due to small particles being better scatterers and more due to small particles being highly mineral in the observation data set.

The results of this study were found to fit within those of Neukermans et al. (2012) and Bowers et al. (2014). The range of $b_{b_p}*$ and $Q_{b_b}$ values were less than those observed by Neukermans et al. (2012) but slightly higher than those observed by Bowers et al. (2013) for

$Q_{b_b}$. This study was shown to reinforce the role of particle size and cross-sectional area upon backscattering following from Neukermans et al. (2012) and Bowers et al. (2014) through the use of $Q_{b_b}$. Additionally, this study showed a statistically significant relationship between mineral content and $b^*_{b_b}$. The study found a new relationship between total suspended solids concentration and $b^*_{b_p}$, outlining the potential use in an iterative algorithm. The range of values observed were less than those of Neukermans et al. (2012), which may limit the wider applicability of the iterative algorithm as it is presently described. However, future inclusion of further data from a larger range of locations in the same iterative format may allow significant improvement upon the spatial and temporal performance of remotely-sensed algorithms for suspended sediment concentration.

**Part IV - Statistical analysis of remotely-sensed variability in suspended material concentration**

- Using only tides, it was possible to predict between 40% and 65% of the variability of the suspended matter concentration on the shelf.
- The inclusion of tides in model 2, improved the prediction of short-term wind-driven resuspension by 5%.
- The inclusion of Chlorophyll-a as a multiplicative factor provided expression of stratification in the model at stratifying locations. In areas, that did not stratify, this inclusion lowered the concentration representing the seasonal variability in settling speed expected.

The statistical model made significant improvements upon that of Rivier et al. (2012), expanding the area from the English Channel to the northwest European shelf and improving the performance of model 3. The chapter showed that the inclusion of a sine curve to represent the seasonal influence of each forcing (tides, wind and Chlorophyll-a) was highly beneficial. Model 1 was shown to represent both the general seasonal variability in the SPM concentration and also the spring-neap variability. Potential improvements were discussed in the use of multiple satellites and geostationary satellites to improve temporal coverage further.

Additionally, there is potential to improve the performance of the model further with river discharge data, especially in areas surrounding large rivers. The dependence upon the tidal coefficient in Rivier et al. (2012) greatly limited the spatial applicability of that model, however the use of a tidal model will allow the model in this study to be simply applied to other areas of the world.

**Part V - Numerical model of suspended sediment concentration**

- Using the simple numerical model with stratification and imposed seasonal settling speed, it was possible to achieve $R^2$ values between 0.6 and 0.8 in the Irish and Celtic Seas when compared with the remotely-sensed observations.
- The model was slightly less proficient in the English Channel, with $R^2$ values between 0.4 and 0.7.
- The performance of the model suggested it to be a reasonable alternative to more complex numerical simulations when computational performance is not sufficient.

Despite the simple, two-layer nature of the numerical model used, it was shown to perform well in representing the main features of the annual variation in SPM concentration. Settling speed ($w_s$) was shown to be a crucial controlling factor of the performance of the model, with significant improvement with the inclusion of an imposed seasonally-varying settling speed. Future improvements to this could include increased vertical resolution (from the two-layer form), increased temporal resolution (hourly) and the use of the estimated $w_s$ from Chapter VI to improve the representation of $w_s$ in the model.

**Part VI - Remote sensing of particle settling speed**

- Using the numerical formulation derived from Bowers (2003), it was possible to estimate the particle settling speed from remotely-sensed suspended matter concentration.
- Settling speeds estimated were at levels up to $60 m day^{-1}$ ($0.8 mm s^{-1}$), comparable to those observed of particles in laboratory experiments and using settling velocity tubes.
- This novel approach has the potential to provide first order estimates of settling speed

on a monthly timescale for uses such as the modelling of sediment transport, pollutant dispersion and carbon sequestration.

- It is suggested that the settling speed would also experience second order variability with varying properties over a spring-neap tidal cycle and indeed over a semi-diurnal tidal cycle, however, due to constraints of satellite temporal coverage, this method is unlikely to be sufficient at those higher temporal resolutions.

Chapter VI demonstrated an novel approach, to use remotely-sensed observations of SPM to estimate the settling speed $w_s$ of particles in the water column. Although laboratory and in-situ measurements exist of $w_s$, they are laborious and spatially and temporally sensitive. This method estimated values of $w_s$ which were within the range observed in-situ, reinforcing the validity of these preliminary results. This approach has the potential to allow large-scale surveying of $w_s$ using remote-sensing, which could be easily applied to other areas with similar tidal controls upon SPM. The chapter described the potential for validation using existing and future measurements of $w_s$, alongside higher resolution remote-sensing images. Using remote-sensing data such as that of SEVIRI was discussed as a possibility to use this same novel method to examine diurnal variability in $w_s$. Not only does information regarding the particle settling speed influence our understanding of sediment dynamics (improving upon present $w_s$ model parameterisation) but has impacts for wider fields such as pollutant monitoring and carbon sequestration.

## Part VII

# References


Ackroyd, D.R., Bale, A.J., Howland, R.J.M., Knox, S., Millward, G.E., & Morris, A.W. (1986). *Distributions and behaviour of Cu, Zn and Mn in the Tamar estuary.* Estuarine, Coastal and Shelf Science. **23**. 621-640.

Agrawal, Y.C. (2005). *The optical volume scattering function: temporal and vertical variability in the water column off the New Jersey coast.* Limnology & Oceanography. **50**(6). 1787-1794.

Agrawal, Y.C., McCave, I.N., & Riley, J.B. (1991). *Laser diffraction size analysis.* Principles, methods and applications of particle size analysis. Cambridge University Press.

Agrawal, Y.C., & Pottsmith, H.C. (2000). *Instruments for particle size and settling velocity observations in sediment transport.* Marine Geology. **168**. 89-114.

Agrawal, Y.C., Traykovski, P. (2001). *Particles in the bottom boundary layer: concentration and size dynamics through events.* Journal of Coastal Research. **106** (C5). 9533-9542.

Agrawal, Y.C., Whitmire, A., Mikkelsen, O.A., & Pottsmith, H.C. (2008). *Light scattering by random-shaped particles and consequences on measuring suspended sediments by laser diffraction.* Journal of Geophysical Research. **113** (C04023).

Aldridge, J., Kershaw, P., Brown, J., McCubbin, D., Leonard, K., & Young, E. (2003). *Transport of plutonium ($^{239/240}Pu$) and caesium ($^{137}Cs$) in the Irish Sea: comparison between observations and results from sediment and contaminant transport modelling.* Continental Shelf Research. **23** (9). 869-899.

Alldredge, A.L., Granata, T.C., Gotschalk, C.G., & Dickey, T.D. (1990). *The physical strength of marine snow and its implication for particle disaggregation in the ocean.* Limnology and Oceanography. **35** (7). 1415-1428.

Ardanuy, P.E., Han, D., & Salomensen, V. V. (1992). *The Moderate Resolution Imaging Spectrometer (MODIS) Science and Data System Requirements.* IEEE Transactions on Geoscience and Remote Sensing. **29** (1).

Asmala, E., Bowers, D.G., Autio, R., Kaartokallio, G., & Thomas, D.N. (2014). *Qualitative changes of riverine dissolved organic matter at low salinities due to flocculation.* Journal of Geophysical Research: Biogeosciences. **119** (10). 1919-1933.

Austin, R.W. (1974). *The remote sensing of spectral radiance from below the ocean surface.* In Jerlov, N.G., Steeman-Neilsen (Eds.). Optical aspects of oceanography. Academic Press, New York. p389-413.

Aznay, O., & Santer, R. (2009). *MERIS atmospheric correction over coastal waters: validation of the MERIS aerosol models using AERONET.* International Journal of Remote Sensing. **30** (18). 279-283.

Babin, M., Morel, A., Fournier-Sicre, V., Fell, F., & Stramski, D. (2003). *Light scattering properties of marine particles in coastal and open ocean waters as related to the particle mass concentration.* Limnology and Oceanography. **48**(2). 848-859.

Babin, M., Stramski, D., Ferrari, G.M., Claustre, H., Bricaud, A., Obolensky, G., & Hoepffner, N. (2003b). *Variations in the light absorption coefficients of phytoplankton, non-algal particles, and dissolved organic matter in coastal waters around Europe.* Journal of Geophysical Research. **108** (C7).

Balch, W.M., Gordon, H.R., Bowler, B.C., Drapeau, D.T., & Booth, E.S. (2005). *Calcite carbonate budgets in the surface global ocean based on MODIS data.* Journal of Geophysical Research. **110** (C07001).

Bale, A.J., & Morris, A.W. (1987). *In situ measurement of particle size in estuarine waters.* Estuarine, Coastal and Shelf Science. **24**. 253-263.

Bauer, J.E., Cai, W-J., Raymond, P.A., Bianchi, T.S., Hopkinson, C.S., & Regnier, P.A.G. (2013). *The changing carbon cycle of the coastal ocean.* Nature. **504**. 61-70.

Baugh, J.V., & Manning, A.J. (2007). *An assessment of a new settling velocity parameterisation for cohesive sediment transport modelling.* Continental Shelf Research. **27** (13). 1835-1855.

Behrenfeld, M.J., Westberry, T.K., Boss, E.S., O'Malley, R.T., Siegel, D.A., Wiggert, J.D., Franz, B.A., McClain, C.R., Feldman, G.C., Doney, S.C., Moore, J.K., Dall'Olmo, G., Milligan, A.J., Lima, I., & Mahowald, N. (2009). *Satellite-derived fluorescence reveals global physiology of ocean phytoplankton.* Biogeosciences. **6**. 779-794.

Bianci, T.S. (2011). *The role of terrestrially derived organic carbon in the coastal ocean: A changing paradigm and the priming effect.* Proceedings of the National Academy of Sciences of the United States of America. **108** (49). 19473-19481.

Binding, C.E., Bowers, D.G., & Mitchelson-Jacob, E.G. (2001). *An algorithm for the retrieval of suspended sediment concentrations in the Irish Sea from SeaWiFS ocean colour satellite imagery.* International Journal of Remote Sensing. **19**.

Binding, C.E., Bowers, D.G., & Mitchelson-Jacob, E.G. (2005). *Estimating suspended sediment concentrations from ocean colour measurements in moderately turbid waters; the impact of variable particle scattering properties.* Remote Sensing of Environment. **94** (3). 373-383.

Bloesch, J. (1994). *A review of methods used to measure sediment resuspension.* Hydrobiologia. **284** (1). 13-18.

Blumer, H. (1925). *Strahlungsdiagramme kleiner dielektrischer Kugeln.* Zeitschrift für Physik. **32** (119).

Bonneton, P., Bonneton, N., Parisot, J-P., & Castelle, B. (2015). *Tidal bore dynamics in funnel-shaped estuaries.* Journal of Geophysical Research. C010267.

Boss, E., Pegau, W.S., Lee, M., Twardowski, M., Shybanov, E., Korotaev, G., & Baratenge, F. (2004a). *Particulate backscattering ratio at LEO 15 and its use to study particle composition and distribution.* Journal of Geophysical Research. **109** (C01014).

Boss, E., Stramski, D., Bergmann, T., Pegau, W.S., & Lewis, M. (2004b). *Why should be*

*measure optical backscattering?*. Oceanography. **17** (2).

Boss, E., & Pegau, W.S. (2001). *Relationship of light scattering at an angle in the backward direction to the backscattering coefficient*. Applied Optics.**40**. 5503-5507.

Bowers, D.G., & Mitchelson-Jacob, E.G. (1996). *Inherent optical properties of the Irish Sea determined from underwater irradiance measurements*. Estuarine, Coastal and Shelf Science. **43**. 433-447.

Bowers, D.G., Gaffney, S., White, M., & Bowyer, P. (2002). *Turbidity in the southern Irish Sea*. Continental Shelf Research. **22**. 2115-2126.

Bowers, D.G. (2003). *A simple turbulent energy-based model of fine suspended sediments in the Irish Sea*. Continental Shelf Research. **23**. 1495-1505.

Bowers, D.G., & Binding, C.E. (2006). *The optical properties of mineral suspended particles: a review and synthesis*. Estuarine, Coastal and Shelf Science. **67**. 219-230.

Bowers, D.G., Binding, C.E., & Ellis, K.M. (2007). *Satellite remote sensing of the geographical distribution of suspended particle size in an energetic shelf sea*. Estuarine, Coastal and Shelf Science. **73**. 457-466.

Bowers, D.G. (2013). *Optical techniques in studying suspended sediments, turbulence and mixing in marine environments*. In: Watson, J., & Zielinski. Subsea optics and imaging. Woodhead Publishing. 213-240.

Bowers, D.G., Hill, P.S., & Braithwaite, K.M. (2014). *The effect of particulate organic content on the remote sensing of marine suspended sediments*. Remote Sensing of Environment. **114**. 172-178.

Braithwaite, K.M., Bowers, D.G., Nimmo-Smith, W.A.M., & Grahmam, G.W. (2012). *Controls on floc growth in an energetic tidal channel*. Journal of Geophysical Research Oceans. **117** (C02024).

Brenon, I., & Le Hir, P. (1999). *Modelling the turbidity maximum in the Seine Estuary (France): Identification of formation processes*. Estuarine, Coastal and Shelf Science. **49**.

525-544.

Bunt, J.A.C., Larcombe, P., & Jago, C.F. (1999). *Quantifying the response of optical backscatter devices and transmissometers to variation in suspended particulate matter.* Continental Shelf Research. **19**. 1199-1220.

Calvet, L., & Fisher, A. (2001). *Forecasting multifractal volatility.* Journal of Econometrics. **105** (1). 27-58.

Calvet, L.E., & Fisher, A.J. (2004). *How to forecast long-run volatility: regime switching and the estimation of multifractal processes.* Journal of Financial Econometrics. **2** (1). 49-83.

Campanelli, A., Pascussi, S., Betti, M., Grilli, F., Marini, M., Pignatti, S., & Guicciardi, S. (2017). *An empirical ocean colour algorithm for estimating the contribution of coloured dissolved organic matter in north-central western Adriatic Sea.* Remote Sensing. **9** (180).

Cao, C., Xiong, J., Blonski, S., Liu, Q., Uprety, S., Shao, X., Bai, Y., & Weng, F. (2013). *Suomi NPP VIIRS sensor data record verification, validation, and long-term performance monitoring.* Journal of Geophysical Research: Atmospheres. **118** (20).

Carder, K.L., Chen, F.R., Lee, Z.P., Hawes, S.K., & Cannizzaro, J.P. (2003). *Case 2 Chlorophyll a. Algorithm theoretical basis document.* In M.O.S. Team (Ed.), Vol. ATBD 19 Version 7. College of Marine Sciences, University of South Florida.

Carper, G.L., & Bachmann, R.W. (1984). *Wind resuspension of sediments in a prarie lake.* Canadian Journal of Fisheries and Aquatic Sciences. **41**. 1763-1767.

Casey, H.J. (1935). *About bedload movement.* PhD Dissertation, Technischen Hochschule, Berlin, Germany.

Chen, S., & Eisma, D. (1995). *Fractal geometry of in situ flocs.* Netherlands Journal of Sea Research. **32**. 173-182.

Costello, D.K., Carder, K.L., & Hou, W. (1995). *Aggregation of diatom bloom in a mesocosm: bulk and individual particle optical measurements.* Deep Sea Research Part II: topical studies in oceanography. **41** (1). 29-45.

Cox, C., & Munk, W. (1954). *Measurement of the roughness of the sea surface from photographs of the sun's glitter.* Journal of the Optical Society of America. **44** (11).

Curran, K.J., Hill, P.S., Milligan, T.G., Mikkelsen, O.A., Law, B.A., Durrieu de Madron, X., & Bourrin, F. (2007). *Settling velocity, effective density, and mass composition of suspended sediment in a coastal bottom boundary layer, Gulf of Lions, France.* Continental Shelf Research. **27**. 1408-1421.

Darwin, G.H. (1879). *Philosophical transactions of the Royal Society, London.* **170** (1).

Davis, A. (2012). *Lecture Notes.* OSX-3006: Sediment Dynamics. School of Ocean Sciences, Bangor University.

Di Natale, F., Erto, A., Lancia, A., & Musmarra, D. (2011). *Mercury adsorption on granular activated carbon in aqueous solutions containing nitrates and chlorides.* Journal of Hazardous Materials. **192**. 1842-1850.

Doxaran, D., Leymarie, E., Nechad, B., Dogliotti, A., Ruddick, K., Gernez, P., & Knaeps, E. (2016). *Improved correction methods for field measurements of particulate light backscattering in turbid waters.* Optics Express. **24** (4).

Dushaw, B.D., Egbert, G.D., Worcester, P.F., Cornuelle, B.D., Howe, B.M., & Metzger, K. (1997). *A TOPEX/POSEIDON global tidal model (TPXO.2) and barotropic tidal currents determined from long-range acoustic transmissions.* Progress in Oceanography. **40**. 337-367.

Dyer, K.R. (1986). *Coastal and Estuarine Sediment Dynamics.* Wiley Sons, Chichester, UK.

Dyer, K.R., & Manning, A.J. (1999). *Observation of the size, settling velocity and effective density of flocs, and their fractal dimensions.* Journal of Sea Research. **41** (1-2). 87-95.

Egbert, G.D., Bennett, A.F., & Foreman, M.G.G. (1994). *TOPEX/POSEIDON Tides estimated using a global inverse model.* Journal of Geophysical Research. **99** (24). 821-852.

Egbert, G.D., & Erofeeva, S.Y. (2002). *Efficient inverse modeling of barotropic ocean tides.* Journal of Atmospheric and Ocean Technology. **19**. 183-204.

Egbert, G.D., Erofeeva, S.Y., & Ray, R.D. (2010). *Assimilation of Altimetry Data for Nonlin-*

*ear Shallow-water Tides: Quarter-diurnal tides of the Northwest European Shelf.* Continental Shelf Research. **30** (6). 668-679.

Eisma, D. (1986). *Flocculation and de-flocculation of suspended matter in estuaries.* Netherlands Journal of Sea Research. **20** (2-3). 183-199.

Eisma, D. (1993). *Suspended matter in the aquatic environment.* Springer-Verlag, Berlin. 324 pp.

Eisma, D., Kalf, J., & Veenhuis, M. (1980). *The formation of small particles and aggregates in the Rhine Estuary.* Netherlands Journal of Sea Research. **14**. 172-191.

Eisma, D., Bernard, P., Cadee, G.C., Ittekot, V., Kalf, J., Laane, R., Martin, J.M., Mook, W.G., Put, A., & van Schuhmaker, T. (1991). *Suspended-matter particle size in some west-European estuaries: part 2: a review of floc formation and breakup.* Netherlands Journal of Sea Research. **28**. 215-220.

Elliott, A.J., & Clarke, T. (1991). *Seasonal stratification in the northwest European shelf seas.* Continental Shelf Research. **11**. 467-492.

Elliott, A.J., Clarke, T., & Li, Z. (1991). *Monthly distributions of surface and bottom temperature in northwest European shelf seas.* Continental Shelf Research. **11** (5). 453-466.

Ellis, K.M., Bowers, D.G., & Hones, S.E. (2004). *A study of the temporal variability in particle size in a high energy regime.* Estuarine, Coastal and Shelf Science. **61**. 311-315.

Ellis, K.M., Binding, C.E., Bowers, D.G., Simpson, J.H. (2008). *A model of turbidity maximum maintenance in the Irish Sea.* Estuarine, Coastal and Shelf Science. **76**. 765-774.

ESA (2017). *Facts and figures, Sentinel-3.*
Available at: textit$http://www.esa.int/Our_Activities/Observing_the_Earth/Copernicus/Sentinel-3/Facts_and_figures$ [Accessed 27 June 2017].

Evers-King, H., Martinez-Vicente, V., Brewin, R.J.W., Dall'Olmo, G., Hickman, A.E., Jackson, T., Kostadinov, T.S., Krasemann, H., Loisel, H., Röttgers, R., Roy, S., Stramski, D., Thomalla, S., Platt, T., & Sathyhendranath, S. (2017). *Validation and intercomparison of*

*ocean colour algorithms for estimating particulate organic carbon in the oceans.* Frontiers of Marine Science. **4** (251).

Feldman, G.C. (2017). *An overview of SeaWiFS and the SeaStar Spacecraft.* Available at: *https* : *//oceancolor.gsfc.nasa.gov/SeaWiFS/SEASTAR/SPACECRAFT.html* [Accessed 13 June 2017].

Flory, E. N., Hill, P.S., Milligan, T.G., & Grant, J. (2004). *The relationship between floc area and backscatter during a spring phytoplankton bloom.* Deep-Sea Research I. **51**. 213-223.

Font, J., Camps, S., Borges, A., Martín-Neira, M., Boutin, J., Reul, N., Kerr, Y.H., Hahne, A., & Mecklenburg, S. (2010). *SMOS: The challenging sea surface salinity measurement from space.* Proceedings of the IEEE. **98** (5).

Frazier, S. (2017). *MODIS WEB.* Available at: *https* : *//modis.gsfc.nasa.gov/about/specifications.php* [Accessed 12 June 2017].

Froidefrond, J.M., Lavender, S., Labordes, P., Herbland, A., & Lafon, V. (2002). *SeaWiFS data interpretation in a coastal area in the Bay of Biscay.* International Journal of Remote Sensing. **23**. 881-904.

Fugate, D.C., & Friedrichs, C.T. (2003). *Controls on suspended aggregate size in partially mixed estuaries.* Estuarine, Coastal and Shelf Science. **58**. 389-404.

Gans, R. (1925). *Strahlungsdiagramme ultramikroskopischer Teilchen.* Annalen der Physik. **381** (1). 29. Gibbs, R.J. (1985). *Estuarine flocs: their size, settling velocity and density.* Journal of Geophysical Research. **90** (C2). 3249-3251.

Gill, A.E. (1982). *Atmosphere-ocean dynamics.* Academic Press, Oxford. 662pp.

Gohin, F., Druon, J.N., & Lampert, L. (2002). *A five channel chlorophyll concentration algorithm applied to SeaWiFS data processed by SeaDAS in coastal waters.* International Journal of Remote Sensing. **23**. 1639-1661.

Gohin, F., Loyer, S., Lunven, M., Labry, C., Froidefrond, J-M., Delmas, D., Huret, M., & Herbland, A. (2005). *Satellite-derived parameters for biological modelling in coastal waters:*

*illustration over the eastern continental shelf of the Bay of Biscay.* Remote Sensing of Environment. **95**. 29-46.

Gohin, F. (2011). *Annual cycles of Chlorophyll-a, non-algal suspended particulate matter, and turbidity observed from space and in-situ in coastal waters.* Ocean Science. **7**. 705-732.

Gohin, F., Bryère, P., & Griffiths, J. W. (2015). *The exceptional surface turbidity of the North-West European shelf seas during the stormy 2013 - 2014 winter: Consequences for the initiation of the phytoplankton blooms?* Journal of Marine Systems. **148**. 70-85.

Gordon, D.C. (1970). *A microscopic study of organic particles in the North Atlantic Ocean.* Deep Sea Research. **17**. 175-185.

Gordon, H.R., & McCluney, W.R. (1975). *Estimation of the depth of sunlight penetration in the sea for remote sensing.* Applied Optics. **14** (2).

Gordon, H.R., Brown, O.B., & Jacobs, M.M. (1975). *Computed relationships between the inherent and apparent optical properties of a flat homogeneous ocean.* Applied Optics. **14** (2).

Gordon, H.R., Brown, O.B., Evans, R.H., Brown, J.W., Smith, R.C., Baker, K.S., & Clark, D.K. (1988). *A semi-analytic model of ocean colour.* Journal of Geophysical Research. **93** (10). 10909-10924.

Gordon, H.R., & Wang, M. (1994). *Retrieval of water-leaving radiance and aerosol optical thickness over the oceans with SeaWiFs: A preliminary algorithm.* Applied Optics. **33**. 443-452.

Graham, G.W., Davies, E.J., Nimmo-Smith, W.A.M., Bowers, D.G., & Braithwaite, K.M. (2012). *Interpreting LISST-100X measurements of particles with complex shape using digital in-line holography.* Journal of Geophysical Research. **117** (C05034).

Green, M.O., & Coco, G. (2014). *Review of wave-driven sediment resuspension and transport in estuaries.* Reviews of Geophysics. **52** (1). 77-117.

Guillou, N., Rivier, A., Chapalain, G., & Gohin, F. (2016). *The impact of tides and waves on near-surface suspended sediment concentrations in the English Channel.* Oceanologia. **74**.

Gupta, P., Christopher, S.A., Wang, J., Gehrig, R., Lee, Y., & Kumar, N. (2006). *Satellite remote sensing of particulate matter and air quality assessment over global cities.* Atmospheric Environment. **40** (30). 5880-5892.

Häkanson, L., & Jansson, M. (1983). *Principles of lake sedimentology.* The Blackburn Press. 332 pp.

Harmel, T., & Chami, M. (2016). *Estimation of daily photosynthetically active radiation (PAR) in presence of low to high aerosol loads: application to OLCI-like satellite data.* Optical Express. **24** (22).

Harris, J.E. (1977). *Characterization of suspended matter in the Gulf of Mexico - II - Particle size analysis of suspended matter from deep water.* Deep Sea Research. **24**. 1055-1061.

Harvey, J.G. (1968). *The flow of water through the Menai Straits.* Geophysical Journal Of The Royal Astronomic Society. 15. 517-528.

Hatcher, A., Hill, P.S., & Grant, J. (2001). *Optical backscatter of marine flocs.* Journal of Sea Research. **46**. 112.

Hergert, W., & Wreidt, T. (2012). *The Mie Theory.* Springer Series in Optical Sciences. **169**.

Herndl, G.J., & Reinthaler, T. (2013). *Microbial control of the dark end of the biological pump.* Nature Geoscience. 6. 718-724.

Hirleman, E.D. (1987). *Optimal scaling of the inverse Fraunhofer diffraction particle sizing problem: The linear system produced by quadrature.* Particle Characterization. **4**. 128-133.

Howarth, M.J. (1998). *The effect of stratification on tidal current profiles.* Continental Shelf Research. **18** (11).

Hu, C., Lee, Z., & Franz, B. (2012). *Chlorophyll-a algorithms for oligotrophic oceans: a novel approach based on three-band reflectance difference.* Journal of Geophysical Research: Oceans. **117** (C1).

Hunter, K.A., & Liss, P.S. (1979). The surface charge of suspended particles in estuarine and coastal waters. Nature. 282. 823-825.

Hurd, D.C., & Spencer, D.W. (1991). Marine Particles: Analysis and Characterization. Geophysical Monograph Series. American Geophysical Union.

Isao, K., Hara, S., Terauchi, K., & Kogure, K. (1990). Role of sub-micrometre particles in the ocean. Nature. 345. 242-244.

IOCCG. (2010). *Atmospheric correction for remotely-sensed ocean colour products.* Wang, M. (ed.). Reports of the International Ocean-Colour Coordinating Group. **10**. Dartmouth, Canada.

Jalón-Rojas, I., Schmidt, S., & Sottolichio, A. (2015). *Turbidity in the fluvial Gironde Estuary (southwest France) based on 10-year continuous monitoring: sensitivity to hydrological conditions.* Hydrological Earth Sciences. 19. 2805-2819.

James, I.D. (2002). *Modelling pollution dispersion, the ecosystem and water quality in coastal waters: a review.* Environmental Modelling & Software. **17** (4). 363-385.

Jarvis, P., Jefferson, B., Gregory, J., & Parson, S.A. (2005). *A review of floc strength and breakage.* Water Resources. **39** (14). 3121-3137.

Jerrold, D.W. (1919). *Douglas Jerrold's Wit.* Bartlett's Familiar Quotations. **10**. Bartleby.

Jonasz, M., & Fournier, G.R. (2007). *Light scattering by particles in water.* Theoretical and Experimental Foundations. Elsevier.

Khelifa, A., & Hill, P.S. (2006). *Models for effective density and settling velocity of flocs.* Journal of Hydraulic Research. **44** (3). 390-401.

Kirk, J.T.O. (2011). *Light and Photosynthesis in Aquatic Ecosystems.* Cambridge University Press, England.

Klimpel, R.C., & Hogg, R. (1986). *Effects of flocculation conditions on agglomerate structure.* Journal of Colloid and Interface Science. **113**. 121-131.

Koglin, B. (1977). *Assessment of the degree of aggregation in suspension.* Powder Technology. **17**. 219-227.

Kramer, H. (1932).*Modellgeschiebe und schleppkraft.* PhD Dissertation, Technischen Hochschule, Dresden, Germany.

Kramer, H. (1935). *Sand mixtures and sand movement in fluvial models.* Transactions of the American Society of Civil Engineers. **100** (1). 798878

Kranck, K., & Milligan, T.G. (1988). *Macroflocs from diatoms: in situ photography of particles in Bedford Basin, Nova Scotia.* Marine Ecology. **44**. 183-189.

Kranenburg, C. (1994). *On the fractal structure of cohesive sediment aggregates.* Estuarine, Coastal and Shelf Science. **39**. 451-460.

Kutser, T., Metsamaa, L., Strömbeck, N., & Vahtmäe, E. (2006). *Monitoring cyanobacterial blooms by satellite remote sensing.* Estuarine, Coastal and Shelf Science. **67** (1-2). 303-312.

Lafite, R. (2001). *Impact de la dynamique tidale sur le transfert de sédiments fins.* PhD Thesis, *Université* de Rouen, France.

Lanzoni, S., & Seminara, G. (2002). *Long term evolution and morphodynamic equilibrium of tidal channels.* Journal of Geophysical Research. **107** (C13001).

Le, C.F., Li, Y.M., Zha, Y., Sun, D., & Yin, B. (2009). *Validation of a quasi-analytical algorithm for highly turbid eutrophic water of Meiliang Bay in Taihu Lake, China.* IEEE Transactions of Geoscience and Remote Sensing. **47** (8).

Lee, Z.P., Carder, K.L., Hawes, S.H., Steward, R.G., Peacock, T.G., & Davis, C.O. (1994). *A model for interpretation of hyperspectral remote-sensing reflectance.* Applied Optics. **33**. 5721-5732.

Lee, Z.P., Carder, K.L., & Arnone, R.A. (2002). *Deriving inherent optical properties from water color: a multiband quasi-analytical algorithm for optically deep waters.* Applied Optics. **41** (27). 5755-5772.

Lee, Z.P., Du, K.P., & Arnone, R. (2005). *A model for diffuse attenuation coefficient of downwelling irradiance.* Journal of Geophysical Research. **110**(C02016).

Levy, R.C., Remer, L.A., & Dubovik, O. (2007). *Global aerosol optical properties and appli-*

*cation to Moderate Resolution Imaging Spectroradiometer aerosol retrieval over land.* Journal of Geophysical Research: Atmospheres. **112** (D13).

Lunau, M., Lemke, A., Dellwig, O., & Simon, M. (2006). *Physical and biogeochemical controls of microaggregate dynamics in a tidally affected coastal ecosystem.* Limnology and Oceanography. **51**. 847-859.

Maffione, R.A., & Dana, D.R. (1997). *Instruments and methods for measuring the backward-scattering coefficient of open waters.* Applied Optics. **29**. 4658-4665.

Malarkey, J., Jago, C.F., *Hübner*, R., & Jones, S.E. (2013). *A simple method to determine the settling velocity distribution from settling velocity tubes.* Continental Shelf Research. **56**. 8289.

Manning, A.J. (2004). *Observations of the properties of flocculated cohesive sediment in three western European estuaries.* Sediment Transport in European Estuaries. Journal of Coastal Research. **SI 41**. 90-104.

Manning, A.J., & Bass, S.J. (2006). *Variability in cohesive sediment settling fluxes: observations under different estuarine tidal conditions.* Marine Geology. **235** (1). 177-192.

Manning, A.J., & Dyer, K.R. (1999). *A laboratory examination of floc characteristics with regard to turbulent shearing.* Marine Geology. **160**. 147-170.

Manning, A.J., & Dyer, K.R. (2002). *The use of optics for the in-situ determination of flocculated mud characteristics.* Journal of Optics A: Pure and Applied Optics. Institute of Physics. **4** (S71-S81).

Manning, A.J., Friend, P.L., Prowse, N., & Amos, C.L. (2007). *Estuarine mud flocculation properties determined using an annular mini-flume and the LabsFLOC system.* Continental Shelf Research. **27**. 1080-1095.

Manning, A.J., & Schoellhamer, D.H. (2013). *Factors controlling floc settling velocity along a longitudinal estuarine transect.* Marine Geology. **345**. 266-280.

Mantovanelli, A., & Ridd, P.V. (2006). *Devices to measure settling velocities of cohesive*

*sediment aggregates: A review of the in situ technology.* Journal of Sea Research. **56**. 199226.

Maritorena, S., Siegel, D.A., & Peterson, A.R. (2002). *Optimization of a semi-analytical ocean color model for global-scale applications.* Applied Optics. **41**(15). 2705-2714.

Matthews, T., Murphy, C., Wilby, R.L., & Harrigan, S. (2014). *Stormiest winter on record for Ireland and U.K.* Nature Climate Change. **4**. 738-740.

McNown, J.S., & Malaika, J. (1950). *Effects of particle shape on settling velocities at low Reynolds numbers.* AGU Transactions. **31** (1).

Meyer, R.A. (1979). *Light-scattering from biological cells - dependence of backscatter radiation on membrane thickness and refractive-index.* Applied Optics. **18**. 585-588.

Mie, G. (1908). *Annalen der Physik.* **330** (3). 377.

Mikes, D., Verney, R., Lafite, R., & Belorgey, M. (2004). *Controlling factors in estuarine flocculation processes: experimental results with material from the Seine Estuary, northwestern France.* Journal of Coastal Research. **41**. 82-89.

Mitchell, C., Cunningham, A., & McKee, D. (2014). *Remote sensing of shelf sea optical properties: evaluation of a quasi-analytical approach for the Irish Sea.* Remote Sensing of Environment. **143**. 142-153.

Mobley, C.D., Gentili, B., Gordon, H.R., Jin, Z., Kattawar, G.W., Morel, A., Reinersman, P., Stamnes, K., & Stavn, R. (1993). *Comparison of numerical models for the computation of underwater light fields.* Applied Optics. **32** (36). 7484-7504.

Mobley, C.D. (1994). *Light and Water - Radiative Transfer in Natural Waters.* Academic, San Diego, California.

Mobley, C.D. (2001). *Radiative transfer in the ocean.* Encyclopaedia of Ocean Sciences. Elsevier, New York.

Mobley, C. D., Zhang, H., & Voss, K.J. (2003). *Effects of optically shallow bottoms on upwelling radiances: Bidirectional reflectance distribution function effects.* Limnology and Oceanography. **48**. 337345.

Mobley, C.D. & Sundman, L.K. (2008). *Hydrolight 5 Ecolight 5 technical documentation.* Sequoia Scientific.

Mobley, C.D., Chai, F., Xiu, P., & Sundman, L.K. (2015). *Impact of improved light calculations on predicted phytoplankton growth and heating in an idealized upwelling-downwelling channel geometry.* Journal of Geophysical Research Oceans. **120**. 875-892.

Morel, A. (1974). *Optical properties of pure water and pure sea water.* In Jerlov, N.G., & Steeman-Nielsen, E. Optical Aspects of Oceanography. Academic Press, New York.

Morel, A., Voss, J.V., & Gentilli, B. (1995). *Bidirectional reflectance of oceanic water: a comparison of modelled and measured upward radiance.* Journal of Geophysical Research. **100**. 143-151.

Morel, A., & Prieur, L. (1977). *Analysis of variations in ocean color.* Limnology and Oceanography. **22** (4). 709-722.

Morel, A., Gentili, B., Claustre, H., Babin, M., Bricaud, A., Ras, J., & Tiéche, F. (2007). *Optical properties of the "clearest" natural waters.* Limnology & Oceanography. 52 (1). 217-229.

NASA. (2016). *Moderate Resolution Imaging Spectrophotometer.*
Available at: *https://modis.gsfc.nasa.gov/data/* [Accessed 11/04/15].

NASA EOSDIS (2016). *EOSDIS Worldview.*
Available at: *https://worldview.earthdata.nasa.gov/* [Accessed 25/05/15].

Nechad, B., Ruddick, K.G., & Park, Y. (2010). *Calibration and validation of a generic multisensor algorithm for mapping of total suspended matter in turbid waters.* Remote Sensing of Environment. **114**. 854-866.

Neukermans, G., Loisel, H., Mériaux, X., Astoreca, R., & McKee, D. (2012). *In situ variability of mass-specific beam attenuation and backscattering of marine particles with respect to particle size, density and composition.* Limnology & Oceanography. **57**(1). 124-144.

Neukermans, G., Ruddick, K.G., & Greenwood, N. (2012b). *Diurnal variability of turbid-*

*ity and light attenuation in the southern North Sea from the SEVIRI geostationary sensor.* Remote Sensing of Environment. **124**. 564-580.

Oishi, T. (1990). *Significant relationship between the backward scattering coefficient of sea-water and the scatterance at 120 degrees.* Applied Optics. **29**. 4658-4665.

Ody, A., Doxaran, D., Vanhellemont, Q., Nechad, B., Novoa, S., Many, G., Bourrin, F., Verney, R., Pairaud, I., & Gentil, B. (2016). *Potential of high spatial and temporal ocean colour satellite data to study the dynamics of suspended particles in a micro-tidal river plume.* Remote Sensing in Coastal Environments. **8** (3).

Owen, M.W. (1976). *Determination of the settling velocities of cohesive muds.* HR Wallingford Report No. IT. **161**. 18 pp.

Petus, C., Chust, G., Gohin, F., Doxaran, D., Froidefrond, J-M., & Sagarminaga, Y. (2010). *Estimating turbidity and total suspended matter in the Adour River plume (South Bay of Biscay) using MODIS 250-m imagery.* Continental Shelf Research. **30**. 379-392.

Pingree, R.D., & Griffiths, D.K. (1978). *Tidal fronts on the Shelf Seas around the British Isles.* Journal of Geophysical Research. **83**.

Pope, R.M., & Fry, E.S. (1997). *Absorption spectrum (380-700nm) of pure water, II: Integrating cavity measurements.* Applied Optics. **36** (33). 8710-8723.

Preisendorfer, R.W. (1976). *Hydrological Optics I-VI.* U.S. Department of Commerce, NOAA, Hawaii, USA.

Rast, M., Bezy, J.L., & Bruzzi, S. (2010). *The ESA Medium Resolution Imaging Spectroradiometer MERIS a review of the instrument and its mission.* International Journal of Remote Sensing. **20** (9).

Ray, R.D., Egbert, G.D., & Erofeeva, S.Y. (2010). *Tide predictions in shelf and coastal waters: status and prospects* in Coastal Altimetry, Vignudelli, S., Kostianoy, A., Cipollini, P., & Benveniste, J. Springer.

Reeve, D., Chadwick, A., & Fleming, C. *Coastal engineering: process, theory and design*

*practice*. SPON Press, Taylor & Francis Group, England.

Reynolds, A., Stramski, D., & Neukermans, G. (2016). *Optical backscattering by particles in Arctic seawater and relationships to particle mass concentration, size distribution, and bulk composition*. Limnology and Oceanography. **61**. 1869-1890.

Rippeth, T.R., Lincoln, B.J., Kennedy, H.A., Palmer, M.R., Sharples, J., & Williams, C.A.J. (2014). Impact of vertical mixing on sea surface pCO2 in temperature seasonally stratified shelf seas. Journal of Geophysical Research: Oceans. 119 (6). 3868-3882.

Rivier, A., Gohin, F., Bryére, P., Petus, C., Guillou, N., & Chapalain, G. (2012). *Observed vs. predicted variability in non-algal suspended particulate matter concentration in the English Channel in relation to tides and waves*. Geo-Marine Letters. **32**. 139-151.

Safak, I. (2016). *Variability of bed drag on cohesive beds under wave action*. Water. **8** (131).

Safak, I., Allison, M.A., & Sheremet, A. (2013). *Floc variability under changing turbulent stresses and sediment availability on a wave energetic muddy shelf*. Continental Shelf Research. **53**. 1-10.

Sambrotto, R.N. (2014). Ocean Chemistry: Biogeochemical regimes in focus. Nature Geoscience. 7. 862-863.

Sandwell, D.T., & Agreen, R.W. (1984). *Seasonal variation in wind speed and sea state from global satellite measurements*. Journal of Geophysical Research. **89** (C2). 2041-2051.

Saulquin, B., Fablet, R., Mercer, G., Demarcq, H., Mangin, A., & d'Andon, O.H.F. (2014). *Multiscale event-based mining in geophysical time series: characterization and distribution of signifcant time-scales in the sea surface temperature anomalies relatively to ENSO periods from 1985 to 2009*. IEEE Journal of Selected Topics in Applied Earth Observation and Remote Sensing.

Saulquin, B., Fablet, R., Ailliot, P., Mercier, G., Doxaran, D., Mangin, A., & d'Andon, O.H.F. (2015). *Characterization of time-varying regimes in remote sensing time series: application to the forecasting satellite-derived suspended matter concentrations*. IEEE Journal of Selected

Topics in Applied Earth Observation and Remote Sensing. **8** (1).

Sequoia. (2017). *Hydrolight-Ecolight 5.1.* Sequoia Reports. Available at *http* : *//www.sequoiasci.com/wp−content/uploads/*2013/07/*HE*5*description.pdf* [Accessed on 27th July 2017].

Shettle, E.P., & Fenn, R.W. (1979). *Models for the aerosols of the lower atmosphere and effects of humidity variations on their optical properties.* Environmental Research Paper. Air Force Geophysics Laboratory, Hanscom, Optical Physics Division.

Shields, A. (1936).*Anwendung der Ähnlichkeitsmechanik und Turbulenzfo auf die Geschiebebewegung.* Mitteilungen der *Preußischen* Versuchsanstalt *für* Wasserbau und Schliffbau. **26**. Berlin.

Sholkovitz, E.R. (1976). *Flocculation of dissolved and inorganic matter during the mixing of river water and sea water.* Geochimica et Cosmochimica Acta. **40**. 831845.

SHOM. (2000). *Courants de marée et hauteurs deau: La Manche de Dunkerque a Brest.* Service Hydrographique et Océanographique de la Marine, Brest. 564-UJA.

Simpson, J.H., & Hunter, J.R. (1974). *Fronts in the Irish Sea.* Nature. **1250**. 404-406.

Simpson, J.H., Allen, C.M., & Morris, N.C.G. (1978). *Fronts on the continental shelf.* Journal of Geophysical Research. **83**. 4607-4614.

Simpson, J.H., & Bowers, D.G. (1979). *Shelf sea fronts' adjustments revealed by satellite IR imagery.* Nature. **280**. 648-651.

Simpson, J.H., & Bowers, D.G. (1981). *Models of stratification and frontal movement in shelf seas.* Deep Sea Research. **28A**. 727-738.

Simpson, J.H., & Bowers, D.G. (1984). *The role of tidal stirring in controlling the seasonal heat cycle in shelf seas.* Annales Geophysicae. **2**. 411-416.

Simpson, J.H., & Brown, J. (1987). *The interpretation of visible band imagery of turbid shallow seas in terms of the distribution of suspended particles.* Continental Shelf Research. **7**. 1307-1313.

Simpson, J.H. (1998). *Tidal processes in shelf seas.* The Sea **10**.

Slade, W., & Boss, E. (2015). Spectral attenuation and backscattering as indicators of average particle size. Applied Optics. **54** (24).

Smith, R.C., & Baker, K. (1981). *Optical properties of the clearest natural waters (200-800nm).* Applied Optics. **20** (2).

Soulsby, R.L., Manning, A.J., Spearman, J., & Whitehouse, R.J.S. (2013). *Settling velocity and mass settling flux of flocculated estuarine sediments.* Journal of Marine Geology (2013).**339**. 1-12;

Stillinger, D.C., Helland, K.N., & van Atta, C.W. (1983). *Experiments on the transition of homogeneous turbulence to internal waves in a stratified fluid.* **131**. 91-122.

Sullivan, J.M., Twardowski, M.S., Donaghay, P.L., & Freeman, S.A. (2005). *Use of optical scattering to discriminate particle types in coastal waters.* Applied Optics. **44**. 1667-1680.

Stewart, C., & Thomson, J.A.J. (1997). *Vertical distribution of butyltin residues in sediments of British Columbia harbours.* Environmental Technology. **18**. 1195-1202.

Stramski, D., Boss, E., Bogucki, D., & Voss, K.J. (2004). *The role of seawater constituents in light backscattering in the ocean.* Progress in Oceanography. **61**. 27-50.

Stramski, D., Babin, M., & Woźniak, S.B. (2007). *Variations in the optical properties of terrigenous mineral-rich particulate matter suspended in seawater.* Limnology and Oceanography. **52** (6). 2418-2433.

Sullivan, J.M., Twardowski, M.S., Donaghay, P.L., & Freeman, S.A. (2005). *Use of optical scattering to discriminate particle types in coastal waters.* Applied Optics. **44**. 1667-1680.

Sullivan, J.M., & Twardowski, M.S. (2009). *Angular shape of the oceanic particulate volume scattering function in the backward direction.* Applied Optics. **48**. 6811-6819.

Sullivan, J.M., Twardowski, M.S., Ronald, J., Zaneveld, V., & Moore, C.C. (2013). *Chapter 6, Measuring optical backscattering in water.* Light Scattering Review 7, Radiative Transfer and Optical Properties of Atmosphere and Underlying Surface. S Praxis Books.

Sydor, M., & Arnone, R. (2002). *Effect of suspended particulate and dissolved organic matter on remote sensing of coastal and riverine waters.* Applied Optics. **36**. 6905-6912.

Tambo, N., & Watanabe, Y. (1979). *Physical characteristics of flocs I, The floc density function and aluminium floc.* Water Research. **13**. 409-419.

Tassan, S. (1992). *An improved in-water algorithm for the determination of chlorophyll and suspended sediment concentration from Thematic Mapper data in coastal waters.* International Journal of Remote Sensing. **6**.

Thill, A., Moustier, S., Garnier, J-M., Estournel, C., Naudin, J-J., & Bottero, J-Y. (2001). *Evolution of particle size and concentration in the Rhone river mixing zone: influence of salt flocculation.* Continental Shelf Research. **21**. 2127-2140.

Thorpe, S.A. (2005). *The Turbulent Ocean.* Cambridge University Press, England.

Thorne, P.D., Vincent, C.E., Hardcastle, P.J., Rehman, S., & Pearson, N. (1991). *Measuring suspended sediment concentration using acoustic backscatter devices.* Marine Geology. **98**. 7-16.

Topliss, B.J., Almos, C.L., & Hill, P.R. (1989). *Algorithms for remote sensing of high concentration, inorganic suspended sediment.* International Journal of Remote Sensing. **6**.

Twardowski, M., Boss, E., Macdonald, J.B., Pegau, W.S.,Barnard, A.H., & Zaneveld, J.R.V. (2001). *A model for estimating bulk refractive index from the optical backscattering ratio and the implications for understanding particle composition in case I and case II waters.* Journal of Geophysical Research. **106** (14). 129-142.

Uncles, R.J., Joint, I., & Stephens, J.A. (1998). *Transport and retention of suspended particulate matter and bacteria in the Humber-Ouse estuary, UK, and their relationship to hypoxia and anoxia.* Estuaries. **21**. 597-612.

van der Lee, W.T.B. (2000). *Temporal variation of floc size and settling velocity in the Dollard estuary.* Continental Shelf Research. **20**. 1495-1511.

van der Lee, E., Bowers, D.G., & Kyte, E. (2009). *Remote sensing of temporal and spatial*

*patterns of suspended particle size in the Irish Sea in relation to the Kolmogorov microscale.* Continental Shelf Research. **29**. 1213-1225.

van Leeuwen, S., Tett, P., Mills, D., & van der Molen, J. (2015). *Stratified and non-stratified areas in the North Sea: Long-term variability and biological and policy implications.* Journal of Geophysical Research: Oceans. **120**.

van Leussen, W. (1994). *Estuarine Macroflocs and their Role in Fine-grained Sediment Transport.* PhD Thesis, University of Utrecht, Netherlands.

van Rijn, L.C. (1984). *Sediment transport, part II: suspended load transport.* Journal of Hydraulic Engineering. **110** (11). 1613-1641.

Verney, R., Brun, C.J., Lafite R., Deloffre, J., & Taylor, J. (2006). *Tidally-induced shear stress variability above intertidal mudflats in the macrotidal Seine estuary.* Estuaries and Coasts. **29** (4). 653-664.

Verney, R., Lafite, R., & Brun-Cottan, J-C. (2009). *Flocculation potential of estuarine particles: the importance of environmental factors and of the spatial and seasonal variability of suspended particulate matter.* Estuaries and Coasts. **32** (4). 678-693.

Verney, R., Lafite, R., Brun-Cottan, J-C., & Hir, P.L. (2011). *Behaviour of a floc population during a tidal cycle: laboratory experiments and numerical modelling.* Continental Shelf Research. **31**. S64-S83.

Wang, M., & Bailey, S. (2001). *Correction of the sun glint contamination on the SeaWiFS ocean and atmosphere products.* Applied Optics. **40**. 4790-4798.

Wang, M., Knobelspeisse, K.D., & McClain, C.R. (2005). *Study of the Sea-Viewing Wide Field-of-View Sensor (SeaWiFS) aerosol optical property data over ocean in combination with the ocean colour products.* Journal of Geophysical Research. **110**. D10S06.

Werdell, P.J., & Bailey, S.W. (2005). *An improved in-situ bio-optical data set for ocean color algorithm development and satellite data product validation.* Remote sensing of environment. **98** (1).

Werdell, P.J., Franz, B.A., Bailey, S.W., Feldman, G.C., Boss, E., Brando, V.E., Dowell, M., Hirata, T., Lavender, S.J., Lee, Z-P., Loisel, H., Maritorena, S., Mélin, F., Moore, T.S., Smyth, T.J., Antoine, D., Devred, E., d'Anton, O.H.F., & Mangin, A. (2013). *Generalized ocean color inversion model for retrieving marine inherent optical properties.* Applied Optics. **52** (10).

Werner, S.R., Beardsley, R.C., & Williams III, A.J. (2003). *Bottom friction and bed forms on the southern flank of Georges bank.* Journal of Geophysical Research. **108** (C11).

WETLabs. (2013). *BB9 Specification Sheet.* WETLabs documentation. WETLabs.

WETLabs. (2016). *ECO triplet datasheet.* WETLabs documentation. WETLabs.

Winterwerp, J.C. (1998). *A simple model for turbulence induced flocculation of cohesive sediment.* Journal of Hydraulic Research. **36** (3). 309-326.

Winterwerp, J. C. (2002). *Scaling parameters for high-concentration mud suspensions in tidal flows.* Proceedings in Marine Science. **5**. 171186.

Winterwerp, J.C. (2006). *Stratification effects by fine suspended sediments at low, medium, and very high concentrations.* Journal of Geophysical Research: Oceans. **111** (C5).

Zanke, U.C.E. (2003). *On the influence of turbulence on the initiation of motion.* International Journal of Sediment Research. **18** (1). 17-31.

Zibordi, G. Mélin, F., & Berthon, J-F. (2006). *Comparison of SeaWiFS, MODIS and MERIC radiometric products at a coastal site.* Geophysical Research Letters. 33. L06617.

Zhang, X.D., Hu, L.B., Twardowski, M.S., & Sullivan, J.M. (2009). *Scattering by solutions of major sea salts.* Optics Express. **17**. 19580-19585.